La borsa di dottorato è stata cofinanziata con risorse del Programma Operativo Nazionale Ricerca e Innovazione 2014-2020 (CCI 2014IT16M2OP005), Fondo Sociale Europeo, Azione I.1 "Dottorati Innovativi con caratterizzazione Industriale"







University of Naples Federico II Ph.D. program in Ingegneria Strutturale, Geotecnica e Rischio Sismico THESIS FOR THE DEGREE OF DOCTOR OF PHILOSOPHY

Stochastic Domain Reduction Method for the Definition of Underground Space Seismic Demand: the CERN LHC Point 5 case study

by Ugo Carmando

Advisor: Prof. Eng. Antonio Bilotta Co-Advisor: Dr. Eng. Marco Andreini

2025



Scuola Politecnica e delle Scienze di Base





SCUOLA POLITECNICA E DELLE SCIENZE DI BASE
DIPARTIMENTO D STRUTTURE PER L'INGEGNERIA E L'ARCHITETTURA

Hi miei nonni

Ugo, *Hss*unta, Giuseppe ed Anna

Un porto sicuro nei giorni di tempesta



Stochastic Domain Reduction Method for the Definition of Underground Space Seismic Demand: the CERN LHC Point 5 case study

Ph.D. Thesis presented

for the fulfillment of the Degree of Doctor of Philosophy in Ingegneria Strutturale, Geotecnica e Rischio Sismico

by

Ugo Carmando



Approved as to style and content by

Prof. Eng. Antonio Bilotta, Advisor

Dr. Eng. Marco Andreini, Co-Advisor

Università of Naples Federico II Ph.D. Program in Ingegneria Strutturale, Geotecnica e Rischio Sismico XXXVI cycle - Chairman: Prof. Iunio Iervolino



www.dist.unina.it/dottorati-di-ricerca/dottorati

Candidate's declaration

I hereby declare that this thesis submitted to obtain the academic degree of

Philosophiæ Doctor (Ph.D.) in Ingegneria Strutturale, Geotecnica e Rischio

Sismico is my own unaided work, that have not used other than the sources

indicated, and that all direct and indirect sources are acknowledged as

references.

Parts of this dissertation have been published in international journals

and/or conference proceedings (see list of the author's publications at the end

of the thesis).

Napoli, 23/05/2025

Ugo Carmando

6



Contents

A	bstract		11
S	intesi in l	ingua italiana	13
A	cknowled	dgements	15
L	ist of Fig	ures	20
L	ist of Tal	oles	32
1	Introd	luction and thesis layout	35
2	Seismi	ic behaviour of underground structures	42
	2.1 T	Tunnels and underground structures	43
	2.1.1	Design and construction approaches	45
	2.1.2	Tectonic aspects	50
	2.1.3	Fundamental geotechnical concepts	52
		The importance of considering the soil-structure interaction 8	on (SSI)
	2.2.1	Underground structures: seismic response mechanisms	60
	2.2.2 of the	Underground structures: analytical and numerical invesseismic response	C
	2.3 N	Main regulatory applications	74
3	Model	lling methodology	78
	3.1 S	trategy of numerical modelling: issues and goals	81
	3.1.1	Numerical modelling issues in soil-tunnel interaction	86
	3.1.2	Finite Element Modelling (FEM)	92
	3.2 A	Advanced Modelling	100
	3.2.1	Real – ESSI Simulator: a framework	101
	3.2.2	The Domain Reduction Method (DRM)	108
	3.2.3	Reasons for employing DRM	117
	3.2.4	DRM application to the case study	119

	3.3	The Uncertainties Treatment problem employing the Latin
	Hypercu	be Sampling algorithm
4	A case 129	e study: the Large Hadron Collider project at Point 5 at CERN
		The European Organization for Nuclear Research: historical notes nework
	4.2	The Geneva Basin: geographical and geological frameworks 138
	4.3	Seismic hazard and site response
	4.4 I	Point 5: geotechnical investigations
	4.4.1	Soils
	4.4.2	The Molasse
	4.4.3	LHC case study: geotechnical model
	4.5	The underground structures at Point 5: an overview
	4.5.1	Construction method and rock support
	4.5.2	UXC 55 Experimental cavern: construction sequence 168
	4.5.3	UXC 55 Experimental cavern: the CMS detector
		Preliminary study for seismic assessment of the underground at Point 5
	4.6.1	FE model description
	4.6.2	Seismic input motions and analyses setup
	4.6.3	Results and comments: the Friuli earthquake (1976) 190
	4.6.4	Results and comments: the other input motions
		Evaluation of the seismic behaviour of the underground facilities eal – ESSI Simulator
	4.7.1 comm	Real-ESSI verification on the free-field response: results and ents
	4.7.2	Real-ESSI verification on CMS cavities: results and comments 200
5	Uncer	rtainties treatment
	5.1 I	LHC seismic stations
	5.2	The earthquake event of 1st November 2022214

8	Autho	or's publications	280
7	Refer	ence List	268
6	Conc	lusions and future developments	262
	5.4.2	Results and comments	259
	5.4.1	Evaluation of the displacements and accelerations	254
	5.4	LHS application to DRM model: second comparison	251
	5.3.2	Results and comments	239
	5.3.1	Evaluation of the displacements and accelerations	229
	5.3	LHS application to DRM model: first comparison	223



Abstract

The European Organisation for Nuclear Research (CERN) is a research centre of international relevance continuously upgrading its extensive underground facilities to cope with the need for new and more complex experiments. CERN underground structures composed of a complex network of linear and circular particle accelerators, which are characterized as the most powerful and unique of its type in the world.

Such a complex underground infrastructure lies in the Geneva basin, characterized by crystalline basement rocks and formations of Triassic, Jurassic and Cretaceous ages. It is filled with sedimentary deposits, the so called Molasse, which is overlain by Quaternary glacial moraines.

The site is classified as a zone of moderate seismicity and the underground structures were designed against a "standard" seismic risk, that corresponds to the importance category II according to Eurocode 8.

This dissertation proposes to address the seismic behaviour of underground structures, with particular focus on tunnels and subterranean facilities, specifically focusing on the emblematic case study of the Large Hadron Collider (LHC) hosting the CMS underground cavities, at CERN's Point 5 site.

The advanced numerical techniques applied, combined with a robust uncertainty analysis, define several probabilistic scenarios and highlight how realistic variations in soil mechanical properties and cavity support parameters significantly influence structural dynamic responses.

Such methodology provide a baseline for further investigations to be conducted within a thorough assessment of the seismic response of the CMS cavities, by better understating how the seismic motions vary through site layers and can affect the hosted equipment and installations inside them, contributing to more accurate estimations of the structural safety and the functional integrity requirements of these latter, which are unique in their kind and permit a continuous improvement of the human understanding of how the nature of the universe works.

Keywords: Underground Structures, Advanced Finite Element Modelling, Domain Reduction Method, Seismic Input Motion, Stochastic Dynamic Analysis, Uncertainty Treatment.



Sintesi in lingua italiana

L'Organizzazione europea per la ricerca nucleare (CERN) è un centro di ricerca di rilevanza internazionale che aggiorna continuamente le sue vaste strutture sotterranee per far fronte alla necessità di esperimenti nuovi e più complessi. Le strutture sotterranee del CERN sono composte da una complessa rete di acceleratori di particelle lineari e circolari, che sono caratterizzati come i più potenti e unici del loro genere al mondo. Un'infrastruttura sotterranea così complessa si trova nel bacino di Ginevra, caratterizzato da rocce basali cristalline e formazioni di età triassica, giurassica e cretacea. È piena di depositi sedimentari, la cosiddetta Molassa, che è ricoperta da morene glaciali quaternarie. Il sito è classificato come zona di sismicità moderata e le strutture sotterranee sono state progettate contro un rischio sismico "standard", che corrisponde alla categoria di importanza II secondo l'Eurocodice 8.

Questa tesi si propone di affrontare il comportamento sismico delle strutture sotterranee, con particolare attenzione ai tunnel e alle strutture sotterranee, concentrandosi specificamente sul caso di studio emblematico del Large Hadron Collider (LHC) che ospita le cavità sotterranee del CMS, presso il sito Punto 5 del CERN.

Le tecniche numeriche avanzate applicate, combinate con una solida analisi dell'incertezza che definisce diversi scenari probabilistici ed evidenzia come variazioni realistiche nelle proprietà meccaniche del terreno e nei parametri di supporto della cavità influenzino significativamente le risposte dinamiche strutturali, forniscono una base di partenza per ulteriori indagini da condurre nell'ambito di una valutazione approfondita della risposta sismica delle cavità CMS, comprendendo meglio come i moti sismici variano attraverso gli strati del sito e possono influenzare le apparecchiature e le installazioni ospitate al loro interno, contribuendo a stime più accurate della sicurezza strutturale e dei requisiti di integrità funzionale di queste ultime, che sono unici nel loro genere e consentono un continuo miglioramento della comprensione umana di come funziona la natura dell'universo.

Parole chiave: Strutture Sotterranee, Modellazione avanzata agli Elementi Finiti, Metodo di Riduzione del Dominio, Segnale Sismico in ingresso, Analisi Dinamica Probabilistica, Trattamento delle Incertezze.



Acknowledgements

Sto ancora imparando

[Michelangelo, all'età di 87 anni]

Ed eccomi qui, seduto a questa scrivania, pronto a dedicarmi alla parte forse più importante del mio lavoro di tesi. Non ho intenzione di essere sbrigativo né tantomeno approssimativo, ma voglio prendermi tutto il tempo necessario per annotare qualche mia riflessione e, soprattutto, menzionare tutte le persone a me care, parenti ed amici, che hanno contribuito ad arricchire questo viaggio.

Se è vero che non conta la meta, quanto soprattutto il viaggio che si è fatto per raggiungerla, non posso che essere profondamente grato a tutti coloro che mi sono stati vicino, tanto nei momenti spensierati e festosi, quanto nelle avversità, di fronte alle quali inevitabilmente ci si ritrova nell'intraprendere un lungo viaggio. Ma andiamo con ordine.

Il dottorato di ricerca ha rappresentato la mia prima vera sfida personale e professionale. Nel momento in cui ho deciso di iniziare questo percorso, forse non ero del tutto preparato a ciò cui sarei andato incontro, anche perché provenivo da un ambiente formativo da cui ho appreso conoscenze non pienamente confacenti alla preparazione necessaria al conseguimento di tutte le attività proposte dal dottorato.

Inizialmente, un grande entusiasmo misto ad una grande curiosità mi hanno pervaso al punto di voler approfondire molti aspetti e saperi a volte anche totalmente nuovi, ma con il passare dei mesi e degli anni, a questo entusiasmo si è sostituito un senso di inadeguatezza ed incapacità.

Ci sono stati momenti difficili da affrontare, non posso negarlo, e momenti di profondo sconforto. Più e più volte ho pensato di rinunciare ed abbandonare tutto, ma molteplici pensieri ricorrevano frequentemente nella mia testa, pensieri del tipo: se sei riuscito a laurearti brillantemente, perché mai non dovresti riuscire a completare questo percorso? Perché ti poni dei limiti e pensi che non ce la farai mai? Perché ti senti inadeguato ed incapace? Perché ti fai divorare dall'ansia? Perché ti senti insicuro?

Col tempo, ho iniziato a capire che le sfide vanno affrontate nel migliore dei modi possibili, mettendoci tutto l'impegno, e che i momenti difficili vanno presi di petto e superati. Questo vuol dire crescere, maturare, prepararsi alla vita ed alle innumerevoli prove che essa ci presenta.

Oggi, posso dire di essere più tranquillo, ma ho capito che la sfida più grande è quella di credere più in sé stessi e nelle proprie capacità. C'è ancora

molta strada da fare ma, intanto, posso dire di aver acquisito un bagaglio umano e culturale inestimabili che mi condurranno all'inizio di un nuovo capitolo della mia vita, per poi poter cogliere, un giorno, quell'opportunità che mi consenta di sfruttare appieno questo arricchimento.

Rivolgendomi all'aspetto più specificatamente accademico, non posso che ringraziare il mio Tutor, Prof. Antonio Bilotta, ed il prof. Emilio Bilotta, per il loro supporto e la disponibilità ad aiutarmi laddove avessi bisogno di chiarimenti e delucidazioni su determinate tematiche da approfondire.

Ringrazio moltissimo il mio Tutor al CERN, Marco Andreini (non posso scrivere Dr. Andreini altrimenti mi rimprovera!). Il periodo semestrale trascorso al CERN ha segnato una svolta per me. Sono stati mesi speciali, perché ho avuto modo di conoscere e rapportarmi a persone di diversa nazionalità, apprendere nuove usanze e nuovi costumi, ma soprattutto nuovi saperi. Marco è stato fondamentale in questo percorso, ho avuto la fortuna di confrontarmi con la sua sterminata preparazione tecnica ed ho potuto contare sulla sua collaborazione per affrontare le problematiche che giorno dopo giorno si presentavano.

Ora però, è doveroso dedicare un pensiero a tutte le persone con le quali, in questi anni, ho intrecciato rapporti di amicizia, talvolta speciali, e grazie ai quali ho vissuto momenti che resteranno impressi nel mio cuore, così come tutti coloro che sono supporto e sostegno per me da sempre.

Un ringraziamento speciale va al mio grande amico Antonio Fumai (alias T.V. (INFR) FUMAI Ing. Antonio, PhD). Non basterebbe una tesi intera per raccontare gli innumerevoli momenti trascorsi insieme, a partire dal primo giorno del corso di Dinamica delle Strutture a cui abbiamo preso parte, sino ad oggi. Da semplici colleghi di studio, col passare del tempo, tra la pagina di un libro e la preparazione di una qualche esercitazione, è nata una sincera amicizia ed un rapporto di complicità tale da poterlo considerare un fratello maggiore. Quante serate abbiamo passato qui, all'università, a studiare ed a confrontarci di continuo sui più svariati argomenti, e quanti momenti conviviali vissuti insieme, inclusi i pranzi/cene a casa mia che, a detta sua, lo hanno spesso distrutto (ma non è vero, la mia cucina è light!). La sua esperienza nel mondo del lavoro, la sua smisurata preparazione e un'innata curiosità che lo portano a spaziare da un argomento ad un altro hanno rappresentato, per me, un momento di vera formazione, più di quanto avessi potuto apprendere durante il dottorato, e di questo gli sono infinitamente grato. Non sono mancati momenti in cui, tra uno spunto di riflessione ed un altro, ha sempre voluto spronarmi a fare meglio e ad infondermi sicurezza, ed anche per questo lo ringrazio. Ad Antonio riconosco una grande umiltà nell'aiutare gli altri nei momenti di difficoltà, e ne ammiro la costante volontà di mettersi in gioco e di saper affrontare, con impegno e perseveranza, tutte le sfide che gli si presentano, fino al raggiungimento degli obiettivi prefissati.

A questo punto, non posso non ringraziare un altro grande amico che ho incontrato lungo il cammino e che, insieme ad Antonio, ha rappresentato parte fondamentale del mio percorso: sto parlando di Ciccio (alias Dr. Francesco Colella). Persona di grande spessore intellettuale, con lui ho trascorso momenti altrettanto speciali, da una parte costellati di innumerevoli ritardi (arrivo tra 10 – 15 minuti = arrivo tra 2 ore), ma dall'altra vissuti con pienezza ed allegria. Quante serate passate ad ammirare il patrimonio architettonico del centro storico, tra palazzi e chiese, col solo intento di capire quanti monolocali potessero venir fuori e, quindi, dare puntualmente sfogo al suo vero animo da immobiliarista. A Ciccio riconosco una smisurata bontà d'animo, e il suo mettersi al servizio degli altri lo rendono una persona genuina, sincera ed affidabile.

Un'altra persona cui tengo molto ringraziare è Fabiana Zizzi. Ancor prima che Ciccio entrasse nelle nostre vite, con Antonio e Fabiana abbiamo vissuto momenti impagabili. Anche Fabiana ha dovuto fare il battesimo del fuoco, assaggiando la mia cucina, e puntualmente, ogni volta mi dava (e mi dà tuttora) consigli su come cucinare qualcosa di più leggero! Più e più volte ho avuto modo di attingere dalla sua vastissima preparazione, comprendente anche tematiche legate al mio percorso iniziale, e non sono mancate occasioni in cui una serata a cena si trasformava in un interessante dibattito su un aspetto piuttosto che su un altro, rendendo il tutto piacevole e stimolante.

Un ringraziamento particolare va anche a Ciro Napolitano, un collega ed amico conosciuto per caso qui all'università e con cui ho stretto un bel rapporto di amicizia. Tra un caffè preso al distributore e qualche incontro fugace nei rispettivi uffici, non sono mancati momenti di confronto, in cui l'uno dispensava consigli per l'altro, uniti a momenti di allegria e convivialità.

Ringrazio i miei colleghi di ufficio Chiara, Alessandro, Carmine, Antonio Mudadu, Tommaso e Giulio. Ogni giorno trascorso con loro si è rivelato essere non solo un'opportunità di dialogo e confronto profondamente costruttivi per me, ma soprattutto un momento per stare tutti insieme, in cui organizzarci al volo per andare a mangiare una pizza oppure chiacchierare di cose che non riguardassero esclusivamente il lavoro.

Ringrazio i miei amici universitari storici Federica, Carla e Ruben per il loro supporto. Abbiamo iniziato tutti insieme il percorso di studi in Architettura, ed oggi, a distanza di anni, anche se presi da mille impegni lavorativi, non manca occasione in cui rivederci, trascorrere un po' di tempo tutti insieme e, ogni tanto, ricordare i bei tempi in cui studiavamo all'università, quando ci districavamo tra un esame di laboratorio ed un altro, tra la correzione di un progetto e la corsa alle stampe frenetica. Momenti che appartengono alla nostra storia e che ci porteremo dietro sempre. Non mancano, ovviamente, i momenti in cui torniamo al presente e parliamo dei problemi legati alla nostra vita lavorativa ed alle future decisioni da prendere.

Ultimi, ma mai ultimi, ringrazio profondamente i miei genitori Riccardo e Maria Pia. La loro incrollabile fiducia ed il continuo sostegno hanno rappresentato il vero incentivo a non mollare mai. Mi hanno rassicurato, quando mi mostravo preoccupato. Mi hanno consigliato, quando avevo qualche dubbio. Mi hanno appoggiato, quando era il momento di fare una scelta. Dedico principalmente a loro questo traguardo e spero di non deludere mai le loro aspettative.

Per finire, ringrazio tutta la mia famiglia. Anche se la fine di questo mio percorso è segnato da qualche pesante assenza, non posso che rivolgere a tutti il mio ringraziamento per aver sempre creduto in me e per essersi sempre preoccupati che tutto andasse per il meglio.

Talvolta, la forza per proseguire ed andare avanti la si prende proprio dall'affetto e dalla stima che gli altri ripongono in te.

Grazie a tutti, Ugo



List of Figures

Figure 2.1.1 General design aspects for New Austrian Tunnelling Method
(NATM). [2]
Figure 2.1.2 Tunnel built with NATM. [3]
Figure 2.1.3 Example of full-face and different choices of partial
excavations. The numbers indicate the sequence of the excavation's stages.
[4]
Figure 2.1.4 Scheme of the double – shield TBM. [4]
Figure 2.1.5 Strain in a ductile material can be decomposed into elastic and
plastic components. The elastic component of strain obeys Hooke's law at all stress levels [6]
Figure 2.1.6 Concept of Associated and Non-Associated Flow Rule [7] 55
Figure 2.1.7 The Mohr–Coulomb failure criteria and Mohr's circle. The
failure criterion represents the linear envelope that is obtained from a plot of
the shear strength τ of a material versus the applied normal stress σ , where ϕ
is the angle of friction, considering also cohesion c [8]
Figure 2.1.8 Shear strength. [9]
Figure 2.2.1 Simplified deformation modes of underground structures
subjected to seismic waves. ([16] [15] modified after Norman in [19]) 61
Figure 2.2.2 Simplified model to evaluate flexibility ratio for rectangular
structures. [15] [20]
Figure 2.2.3 Importance of the shear stresses at the perimeter of the structure
on the deformation mode. ([15] modified after [21])
Figure 2.2.4 Simplified frame analysis models, (a) concentrated force, (b)
triangular distribution (modified after [20]). [16]
Figure 2.2.5 Simplified equivalent static method for the transversal seismic
analysis of (a) rectangular and (b) circular tunnels; δ_{ff} : free – field seismic ground deformation, p_s : seismic earth pressures on the side – walls of the
rectangular structure, τ_s : seismic shear stresses around the perimeter of the
tunnel, Ws: weight of overburden soil, Fs: inertial forces of overburden soil,
W_T : weight of tunnel, F_S : inertial forces of tunnel, K_x , K_y normal and shear
soil springs along the perimeter of the tunnel lining (redrawn after [15]). [16]
67
Figure 2.2.6 Detailed equivalent static analysis: (a) distributed inertial loads
(b) imposed ground distortions at the boundaries (agg ground acceleration at

free-field, F _{inertia} : equivalent to ground acceleration inertial body force) [16].
Figure 2.2.7 Simplified equivalent static analysis method for tunnels, (a) transversal, (b) longitudinal analysis [25]
Figure 2.2.9 Comparison between the two different estimations of (a) γ , (b) G and (c) D. [26]
Figure 2.2.10 Analyzed numerical models. [26]
Figure 2.2.11 Numerical vs. experimental response spectra of pseudo-
acceleration. [26]
Figure 3.1.1 Numerical modelling process: flowchart
Figure 3.1.2 Stress release factor as a function of the distance from tunnel
face [28]
Figure 3.1.3 a) Convergence-confinement method; b) temporary and
permanent lining [28]
Figure 3.1.4 Example of distribution of axial thrust, shear force and bending
moments in a tunnel segment [32]
Figure 3.1.5 Modelling strategies for soil-tunnel interaction issues 91 Figure 3.1.6 Characteristic stiffness – strain behaviour of soil with typical
strain ranges for laboratory tests and structures [38]
Figure 3.1.7 Reduction of secant shear modulus with shear strain [36] 95
Figure 3.1.8 HS – small model: hysteretic behaviour (on the left) and
damping ratio evaluated as a function of cyclic shear strain (on the right)
[37]
Figure 3.1.9 Rayleigh damping formulations with (a) single control
frequency and (b) two control frequencies [39]
Figure 3.1.10 Schematic representation of the β -method for the analysis of
NATM tunnels in PLAXIS software [33]
Figure 3.2.1 Real-ESSI Simulator: 3D slice model realized in Gmsh 102
Figure 3.2.2 Real – ESSI Simulator: mesh layout obtained in Gmsh 103
Figure 3.2.3 Real-ESSI Simulator: Windows Subsystem for Linux 104
Figure 3.2.4 Real-ESSI Simulator: analysis phase. 105
Figure 3.2.5 Real-ESSI Simulator: Post-processing phase
Figure 3.2.6 Real-ESSI Simulator: Post-processing results visualized in Paraview
Figure 3.2.7 Large physical domain with the source of load Pe(t) and the
local feature (soil – foundation – structure system) [41]

Figure 3.2.8 Simplified large physical domain with the source of load Pe (t)
and without the local feature (free-field conditions) [41]
Figure 3.2.9 DRM: a single layer of elements between Γ and Γ e is used to
create Peff for a section of 8-node-brick elements [41]
Figure 3.2.10 Characterization of the damping layer around DRM layer [45].
Figure 3.2.11 One-dimensional site-response analysis [47]
Figure 3.2.12 DRM methodology: from large to smaller domain
Figure 3.2.13 FE model developed to verify the free-field response 121
Figure 3.2.14 Ricker wavelet: a) horizontal acceleration and b) horizontal
displacement time histories
Figure 3.2.15 Time histories of horizontal accelerations at the ground surface
for two different values of numerical damping: a) $\gamma = 0.5$; b) $\gamma = 1.0$
Figure 3.3.1 Samples as the probabilistic means of intervals: LHS-mean
scheme [50]
Figure 3.3.2 Latin cube, two variables and five realizations. The 5 x 2 matrix
(a) determines the plan illustrated in (b) [52]
Figure 4.1.1 Timeline containing the chronological construction process of
CERN underground structures
Figure 4.1.2 Layout of the existing tunnel structures that host the LEP\SPS
beam accelerator at the Franco-Swiss border [57]
Figure 4.1.3 Layout of the underground structures that host the LHC project:
definition of Point 1 (ATLAS), Point 5 (CMS), Point 2 (ALICE) and Point 8
(LHCb) sites. [58]
Figure 4.1.4 Layout of the underground structures that host the High
Luminosity - LHC project: definition of the infrastructures added (blue) 136
Figure 4.1.5 Top: study boundary (red polygon) showing the main
topographical and geological structures, LHC (blue line) and FCC tunnel
trace (brown line). Bottom: 3D not-to-scale schematic of the underground
structures [59]
Figure 4.2.1 Geographic map of the western Switzerland and surrounding
France with indication of wells and seismic lines available in the area of
study. A cross-section A-A' is considered in Moascariello [60] 138
Figure 4.2.2 Mesozoic-Cenozoic structural scheme of the Greater Geneva
Basin illustrating: a) SW-NE Mesozoic lows associated with underlying
Permo-Carboniferous basins at the front thrust of the Salève ridge and
Subalpine/Prealpine units. b) Zones affected by the NNW-SSE trending
wrench fault systems crossing the Geneva Basin and Bornes Plateau: (I)

Vuache; (II) Cruseilles; (III) Le Coin; (IV) Arve. c) Top Mesozoic structural
highs (H) and lows (L) associated with underlying Permo-Carboniferous
Figure 4.2.3 Geological section crossing the Geneva Basin from SE to NW summarizing the key stratigraphic and structural elements present in the basin [60].
Figure 4.2.4 Summary stratigraphy of the Swiss Plateau in the Geneva Basin area [60]
Figure 4.4.2 Vertical section made at Shaft PX54 showing the positioning of the LHC beam in respect to the positioning of the UXC55 experimental cavity
Figure 4.4.3 Point 5: stratigraphic profile from reference geotechnical investigations up to caverns' depth (on the left) and a shear wave velocities comparison between [55] and calibration done by means of PLAXIS software.
Figure 4.4.4 Calibration of HS-small stiffness degradation curves and damping parameters against the available curves in the literature for the Geneva basin [70]
Figure 4.5.1 Point 5: 3D model representing the underground facilities as part of the old LEP accelerator (white) and the civil structures as part of the LHC project [72].
Figure 4.5.2 Point 5: 3D model representing LHC underground facilities, compared to LEP existing structures
rigure 4.5.5 Point 5: access by means of Pivi54 and PA56 Snafts 1/21 [6]

Figure 4.5.4 Point 5: type section of Experimental and Service caverns [69].
Figure 4.5.5 HL-LHC at Point 5: scheme of the underground structures 163
Figure 4.5.6 CMS plan view and its upper drainage gallery
Figure 4.5.8 Sequence of the excavation for the UXC55 Experimental cavern
Figure 4.5.9 UXC55 Experimental cavern: excavation sequence
Figure 4.5.10 UXC55 Experimental cavern: arc inverts' excavation sequence
Figure 4.5.11 UXC55 Experimental cavern: arc inverts' excavation sequence.
Figure 4.5.12 UXC55 Experimental cavern: linings construction sequence
Figure 4.5.13 Particles of the Standard Model of Particle Physics [78] 173 Figure 4.5.14 A schematic of the LHC at CERN's accelerator complex in
Geneva at the border of Switzerland and France [78]
Figure 4.5.16 Compact Muon Solenoid Detector: section view
Figure 4.5.17 An exploded view of the CMS detector layout with labelled sub-detectors [78]
Figure 4.6.1 LHC project: layout of the Point 5 model built in Plaxis 2D [40]
Figure 4.6.2 Plaxis 2D: effective principal stresses in free field lithostatic conditions [40]
Figure 4.6.3 Plaxis 2D: effective principal stresses in post – cavities conditions [40]
Figure 4.6.4 Plaxis 2D: main plastic calculation stages of the underground cavities: a) free – field conditions; b) pillar construction; c) USC55 Service
cavern excavation; d) UXC55 Experimental cavern excavation
Figure 4.6.6 Spectro-compatibility [82]
the related Fourier spectrum (on the right) [40]
Figure 4.6.8 Centre Italy earthquake (2016): acceleration time history (on the left); the related Fourier spectrum (on the right)

Figure 4.6.9 Iceland earthquake (2000): acceleration time history (on the
left); the related Fourier spectrum (on the right)
Figure 4.6.10 Iceland earthquake (2000): acceleration time history (on the
left); the related Fourier spectrum (on the right)
Figure 4.6.11 Iceland earthquake (2008): acceleration time history (on the
left); the related Fourier spectrum (on the right)
Figure 4.6.12 PSA response spectra
Figure 4.6.13 PSA values along vertical arrays, related to Friuli signal, in
significative points of the model [40]
Figure 4.6.14 PSA values along horizontal arrays, related to Friuli signal, in
significative points of the model [40]
Figure 4.6.15 PSA values for the considered seismic inputs at different
locations [40]
Figure 4.7.1 Comparison between model built by PLAXIS (top) and Real –
ESSI (bottom) [53]
Figure 4.7.2 Acceleration time histories and related Fourier spectra of Friuli
earthquake of 1976 (top), Ricker Wavelet (centre) and event recorded at
CERN on November 1°, 2022 (bottom), respectively
Figure 4.7.3 Free-field conditions: acceleration time history observed at
ground level as results of the three-software adopted, by applying Ricker
Wavelet at the surface base [53]
Figure 4.7.4 CMS cavities: section type
Figure 4.7.5 Comparison between PLAXIS and Real-ESSI models: results in
terms of acceleration time histories by applying Ricker Wavelet [53] 201
Figure 4.7.6 Comparison between PLAXIS and Real-ESSI models: results in
terms of acceleration time histories by applying Ricker Wavelet [53] 202
Figure 4.7.7 Amplification functions observed for free-field conditions (top)
and with the presence of CMS cavities (bottom) [53]
Figure 5.1.1 Position of the seismic stations [86]211
Figure 5.1.2 Convention for alignment of the underground stations [86] 212
Figure 5.1.3 Point 5: location of the CERN5 sensors (green) in the CMS
cavern area [86]
Figure 5.2.1 Earthquake event of 1 st November 2022: PGA distribution [87].
Figure 5.2.2 Horizontal components of the CERN5 underground acceleration
(left) and CERNS surface acceleration time histories (right), with indication
of bracketed duration considered

Figure 5.2.3 Horizontal components of CERN5 underground accelerations
(left) and CERNS surface accelerations (right) time histories: bracketed
durations
Figure 5.2.4 Horizontal components of CERN5 underground displacements
(left) and CERNS surface displacements (right) time histories: bracketed
durations
Figure 5.2.5 Earthquake event of 1 st November 2022: seismic stations
distribution and related accelerograms recorded [88]
Figure 5.2.6 Earthquake event of 1 st November 2022: North-South
component of the maximum acceleration of the sole volume waves recorded
in the first second in CERN stations (blue) and the PGA recorded in surface
stations (red) [88]
Figure 5.2.7 Horizontal components of CERNS surface acceleration (left)
and displacement (right) time histories properly attenuated
Figure 5.2.8 DRM methodology applied to the model realized in Real – ESSI
Simulator
Figure 5.3.1 DRM model: displacement time history, in [m] unit, recorded at
the ground surface (top) and at the UXC55 cavity basement (bottom), by
employing the parameters of Tables 11-12 and applying the deconvolution
considering CERNS input at the ground surface
Figure 5.3.2 Vs profiles generated by LHS algorithm by implementing Vs
mean profile
Figure 5.3.3 DRM section model highlighting the Vs mean profile and all the
fifteen profiles associated to the fifteen analyses within the first simulations
process. 228
Figure 5.3.4 DRM model: comparison between displacement time histories
recorded by CERNS surface station and five "comparable" results recorded at
ground surface. 231
Figure 5.3.5 DRM model: comparison between displacement time histories
recorded by CERN5 underground station and five "comparable" results
recorded at the UXC55 cavity basement. 231
Figure 5.3.6 DRM model: comparison between displacement time histories
recorded by CERN5 underground station and five "comparable" results
recorded at the UXC55 cavity basement. 232
Figure 5.3.7 DRM model: comparison between displacement time histories
recorded by CERNS surface station and all the fifteen output results recorded
at ground surface

Figure 5.3.8 DRM model: comparison between displacement time histories
recorded by CERN5 underground station and all the fifteen output results
recorded at the UXC55 cavity basement
Figure 5.3.9 DRM model: comparison between acceleration time histories
recorded by CERNS surface station and five "comparable" results recorded at
ground surface. 235
Figure 5.3.10 DRM model: comparison between acceleration time histories
recorded by CERN5 underground station and five "comparable" results
recorded at the UXC55 cavity basement
Figure 5.3.11 DRM model: comparison between acceleration time histories
recorded by CERN5 underground station and five "comparable" results
recorded at the UXC55 cavity basement
Figure 5.3.12 DRM model: comparison between acceleration time histories
recorded by CERNS surface station and all the fifteen output results recorded
at ground surface
Figure 5.3.13 DRM model: comparison between acceleration time histories
recorded by CERN5 underground station and all the fifteen output results
recorded at the UXC55 cavity basement
Figure 5.3.14 Definition of the impedance ratio between adjacent layers. 239
Figure 5.3.15 DRM section model showing the variation of the seismic
impedance ratios, as depth changes, calculated at the interface between one
soil layer and another. 242
Figure 5.3.16 Vs profiles compared for the central packet of soil layers in S3
and S8 simulations
Figure 5.3.17 Comparison between S3 and S8 simulations in terms of
impedance and damping ratios
Figure 5.3.18 DRM model: comparison between displacement time histories
recorded by CERNS, S3 and S8 simulations at ground surface, by
substituting in S3 the damping ratios considered for S8
Figure 5.3.19 DRM model: comparison between displacement time histories
recorded by CERN5, S3 and S8 simulations at UXC55 cavity basement, by
substituting in S3 the damping ratios considered for S8
Figure 5.3.20 DRM model: comparison between displacement time histories
recorded by CERNS, S3 and S8 simulations at ground surface, by
substituting in S3 the damping ratios considered for S8
Figure 5.3.21 DRM model: comparison between displacement time histories
recorded by CERN5, S3 and S8 simulations at UXC55 cavity basement, by
substituting in S3 the damping ratios considered for S8

Figure 5.3.22 DRM model: comparison between acceleration time histories
recorded by CERNS, S3 and S8 simulations at ground surface, by
substituting in S3 the damping ratios considered for S8
Figure 5.3.23 DRM model: comparison between acceleration time histories
recorded by CERN5, S3 and S8 simulations at UXC55 cavity basement, by
substituting in S3 the damping ratios considered for S8
Figure 5.3.24 DRM model: comparison between acceleration time histories
recorded by CERN5, S3 and S8 simulations at UXC55 cavity basement, by
substituting in S3 the damping ratios considered for S8
Figure 5.3.25 DRM model: comparison between displacement time histories
recorded by CERNS, S3 and S8 simulations, by substituting in S8 the
damping ratios considered for S3
Figure 5.3.26 DRM model: comparison between displacement time histories
recorded by CERN5, S3 and S8 simulations, by substituting in S8 the
damping ratios considered for S3
Figure 5.3.27 DRM model: comparison between acceleration time histories
recorded by CERNS, S3 and S8 simulations, by substituting in S8 the
damping ratios considered for S3
Figure 5.3.28 DRM model: comparison between acceleration time histories
recorded by CERN5, S3 and S8 simulations, by substituting in S8 the
damping ratios considered for S3
Figure 5.4.1 Vs mean profile defined for the second analysis process and
compared to the previous one
Figure 5.4.2 DRM section model highlighting the Vs mean profile and all the
fifteen profiles associated to the fifteen analyses within the second
simulations process
Figure 5.4.3 DRM model: comparison between displacement time histories
recorded by CERNS surface station and all the fifteen output results recorded
at ground surface
Figure 5.4.4 DRM model: comparison between displacement time histories
recorded by CERN5 underground station and all the fifteen output results
recorded at the UXC55 cavity basement
Figure 5.4.5 DRM model: comparison between displacement time histories
recorded by CERN5 underground station and all the fifteen output results
recorded at the UXC55 cavity basement
Figure 5.4.6 DRM model: comparison between acceleration time histories
recorded by CERNS surface station and all the fifteen output results recorded
at ground surface

Figure 5.4.7 DRM model: comparison between acceleration time histories
recorded by CERN5 underground station and all the fifteen output results
recorded at the UXC55 cavity basement
Figure 5.4.8 DRM model: comparison between acceleration time histories
recorded by CERN5 underground station and all the fifteen output results
recorded at the UXC55 cavity basement
Figure 5.4.9 Impedance ratios: comparison between first and second process
analyses
Figure 5.4.10 DRM section model showing the variation of the seismic
impedance ratios, as depth changes, calculated at the interface between one
soil layer and another

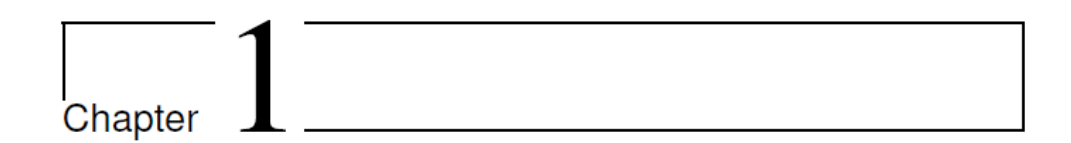


List of Tables

Table 1 Material characteristics and their statistical distribution parameter	S.
Table 2 LHC Point 5: definition of Rayleigh damping [40]	183
Table 3 LHC Point 5: mechanical properties and model parameters for the	2
different layers, after [55] and employed in [40]	184
Table 4 LHC Point 5: mechanical properties for cavities' linings and for	
massive concrete pillar	184
Table 5 Seismic records selected [40].	185
Table 6 Seismic records properties.	185
Table 7 Seismic input motions: filtering and baseline corrections.	186
Table 8 Mechanical properties defined for different soil layers in both	
software.	196
Table 9 Mechanical properties defined for cavities' walls and for the conc	rete
pillar in Real - ESSI	200
Table 10 Coordinates of the CERN seismic stations.	.211
Table 11 Earthquake event of 1st November 2022: summary description	214
Table 12 Earthquake event of 1 st November 2022: CERNS and CERN5	
seismic data [88]	218
Table 13 LHS: probability distributions of the input parameters (soils and	
rock)	223
Table 14 LHS: probability distributions of the input parameters (concrete	
linings and basements).	
Table 15 LHS: recalibration of the probability distributions for the soils at	
rock parameters	227
Table 16 LHS: recalibration of the probability distributions for the soils at	nd
rock parameters, done as the mean of the five analyses with better results	
obtained in the first analysis process.	252







1 Introduction and thesis layout

In recent years, several researchers carried out analytical and numerical studies concerning various aspects of the behaviour of underground structures under seismic excitations in different ground conditions.

Understanding the seismic behaviour of underground structures is essential to assess the response of critical equipment for scientific experiments, such as those housed in the cutting-edge infrastructure of the European Organisation for Nuclear Research (CERN), one of the world's largest research centres, whose purpose is to continuously upgrade its extensive underground facilities to cope with the need for new and more complex experiments.

The latter is located at the border between France and Switzerland and consists of linear and circular accelerators of nuclear particles, including the Large Hadron Collider complex (LHC), consisting of a 27-kilometer ring of superconducting magnets with several accelerating structures to boost the energy of the particles along the way.

Such complex houses the Compact Muon Solenoid (CMS) detector at its Point 5, where there are two large shafts, two 100 m deep major parallel caverns, with a total span of 50 m, separated by a 7 m wide and 28 m high concrete pillar, and a system of secondary tunnels and caverns.

This dissertation proposes to address the seismic behaviour of underground structures, with particular focus on tunnels and subterranean facilities, specifically focusing on the emblematic case study of the Large Hadron Collider (LHC), at CERN's Point 5 site, more specifically of the CMS underground cavities.

The study demonstrated how the combined application of advanced numerical methodologies, such as the Domain Reduction Method (DRM), and

high – performance software like the Real-ESSI Simulator, facilitates an accurate representation of complex phenomena characterizing soil-structure interaction (SSI).

The advanced numerical techniques applied, combined with a robust uncertainty analysis defining several probabilistic scenarios and highlighting how realistic variations in soil mechanical properties and cavity support parameters significantly influence structural dynamic responses, provide a baseline for further investigations to be conducted within a thorough assessment of the seismic response of the CMS cavities, by better understating how the seismic motions vary through site layers and can affect the hosted equipment and installations inside them, contributing to more accurate estimations of the structural safety and the functional integrity requirements of these latter, which are unique in their kind and permit a continuous improvement of the human understanding of how the nature of the universe works. This dissertation s structured as follows:

In Chapter 2, an overview of the tunnels and underground structures in general and, more in detail, a focus on the seismic behaviour of the underground structures, as discussed in several works taken by the literature, were presented, exploring various aspects influencing seismic performance, starting from the most relevant design and construction methodologies used in modern engineering practice, and highlighting the importance of integrating tectonic considerations into these processes.

Furthermore, fundamental geotechnical concepts were introduced, given their significant influence on the dynamic response of underground structures, particularly when soil-structure interaction is considered. In this context, existing regulatory frameworks and their practical implications for underground infrastructure were critically reviewed, revealing areas of potential improvement in current standards and guidelines.

- In Chapter 3, a detailed description of the numerical modelling methodology, adopted in this thesis, is presented.

As proposed in literature, numerical modelling appears an essential tool for academic and scientific purposes and to explain a project to stakeholders and the public in real-world applications.

Research on soil-structure interaction, among others, have been carried out for a long time by different approaches, such as analytical methods, laboratory measurements and, more recently, numerical modelling and hybrid experimental and numerical modelling.

Numerical models are even more useful the better they represent the real problem, but this is not always possible, due to lack of adequate instrumentation required for long simulations of large domains, so an increasing processing power of personal computers and the use of high-performance computer (HPC) facilities become an essential prerequisite.

All the advantages and limitations offered by adopting a numerical modelling process are presented, as well as all the phases underlying the execution of such a process are described.

A focus on the issues related to soil – tunnels interaction has been reported, highlighting all the methods describing the possible approaches to be adopted to better understand such issues, up to focusing, in more detail, on the major FEM methods adopted in the literature and applied in the present study.

Specifical reference was made to the adoption of an FE software employed, named PLAXIS, showing its peculiarities, as well as describing the advantages and motivations inherent in the adoption of a further modelling methodology, the DRM, highlighting its greater applications.

A further overview on advanced modelling has been presented, focusing on the use of a software with high – performance capabilities, namely Real-ESSI Simulator, showing its operation process and basic architecture, from a model conception to its realization.

Subsequently, a detailed description of the DRM methodology, as well as the application of this latter to the case study, were respectively presented, showing its peculiarities and subjecting the proposed model to a validation process aimed at highlighting the most powerful and useful features of DRM.

Concluding, a theoretical description of the Latin Hypercube Sampling technique, employed to adequately characterize the uncertainties treatment problem, was presented.

- In Chapter 4, an historical framework inherent the chronological evolution of CERN, starting from its foundation to the future infrastructures to be realized, as well as the geological characterization of the Geneva basin were presented, with reference to the several stratigraphic modifications succeeded by the passage of the various geological eras.

Moreover, after presenting the seismic hazard of the area in which CERN is located, that is, according to Eurocode 8, classified as a zone of moderate seismicity and the underground structures were designed against a "standard" seismic risk, that corresponds to the importance category II, a detailed description of the geotechnical investigations at the Point 5 was presented, also on the basis of consequent simplification taken by previous literature studies.

The underground facilities within the LHC complex are carefully described, with a major attention to the main experimental cavern (UXC55), highlighting its design and construction chronological sequence, as well as to the installations characterizing CMS detector, through a basic description of the detector's functioning, as well as its main constituent structural components.

All the results inherent in modelling and simulation of the behaviour of underground structures located within the LHC complex, when subjected to seismic excitations, are presented to preliminarily define seismic safety requirements for sensitive infrastructure and facilities located within the tunnels and caverns.

Results obtained by means the execution of fully dynamic analyses carried out by PLAXIS software and, subsequently, the results obtained using the advanced FE software Real-ESSI Simulator, were reported, focusing on comparison results between the operating methodologies offered by these latter, in order to validate such methodologies and to evaluate, in addition, a dynamic response, by applying different seismic input motions, for the conditions with and without cavities, respectively, in terms of amplification functions.

In Chapter 5, a large discussion regarding the application of the Latin Hypercube Sampling technique on the case study, highlighting its potentials and advantages, is presented.

LHS technique is framed as a sampling approach working along the lines of Monte Carlo simulation, a powerful tool which is frequently used to analyse random phenomena.

In a random problem, statistical or probabilistic information is desired for a random output, which depends upon random input variables, fields, and processes.

In Monte Carlo simulation, these random input quantities are represented by sets of deterministic numbers called realizations, observations, or samples. Monte Carlo simulation is robust, simple to use, and generally faster than full probabilistic approaches, and therefore is often used to solve random problems and to validate other analysis techniques, but cannot be applied to time-consuming problems, as it requires many simulations (repetitive calculation of responses).

A small number of simulations can be used to gain an acceptable level of accuracy for the statistical characteristics of the response using the LHS sampling technique. This latter was employed to define all the possible uncertainties related to the random choice of the geotechnical and mechanical parameters defining the properties of soils, rocks and cavities' materials.

Through a series of analyses, several probabilistic scenarios were studied in which the displacements and accelerations, with reference to the point located at the base of the experimental cavity UXC55, showed a variation, sometimes significant, depending on the above properties and, above all, on the type of seismic signal considered.

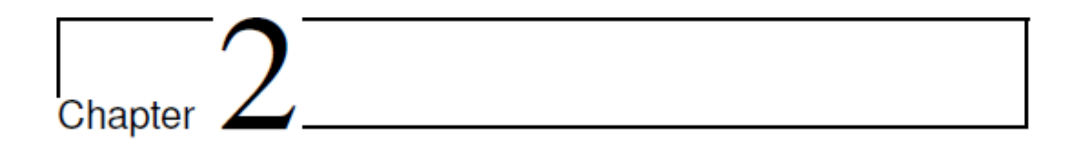
In this context, a first data set containing all the random variables chosen on the basis of several parameters as the uncertainty weight and the probability distribution functions, has been produced. All the results were reported, describing all the possible causes that produced a high level of uncertainty, highlighted in terms of very high amplifications of the responses in terms of displacements and accelerations that may produce conditions of serious damage due to the nature of the systems

Chapter 1: Introduction and thesis layout

and equipment present in the cavities and, therefore, may negatively affect the safety requirements and structural integrity.

A second data set was produced on the basis of the mean values of all the analyses that, in the first stage, produced appreciable results, since the state of uncertainty around the variables recalibrated had less effects, in terms of large amplifications, on the responses produced.





2 Seismic behaviour of underground structures

Underground structures, tunnels, subways, metro stations and parking lots, are crucial components of the built environment and transportation networks. Considering their importance for life saving and economy, appropriate seismic design is of prior significance.

Focusing on tunnels, they were invented by man in the Stone Age to initially mine orebodies and have then been improved over the centuries to satisfy a large variety of economic, military and social needs. In the Roman Age, numerous tunnels were constructed as aqueducts, to remove waste waters, as well as to drain wet areas and to allow a way through mountains.

In the Renaissance Age, Leonardo da Vinci accurately studied the potential of tunnels for solving transportation problems in the urban areas and improving urban liveability: by designing his ideal city after the plague that caused an enormous number of fatalities in Milan, he promoted the use of the underground space for the transport of goods and for the supply pf clean water and removal of wastewater.

Today, the use of underground tunnels, in both urban and extra – urban areas, is aimed to cross natural obstacles, to improve the transport networks and for a wide number of applications: their resiliency and durability, compared to other surface infrastructures, allow them to be protected against natural hazards such as floods, rockfalls, earthquakes and atmospheric actions. [1]

2.1 Tunnels and underground structures

Tunnelling represents the engineering process that, by means of the removal of large volumes of soil and rocks from their original underground position, allows the creation of an underground void characterized by one prevalent dimension and a predefined cross section. The final product of the process consists in obtaining a tunnel that is capable of fulfilling, over a prescribed period, the provision of necessary maintenance works, and the specific use for which it was planned and designed. This goal is achieved by considering a set of predefined constraints, strictly related to the specific site and by minimizing both the time and the costs of construction. With time, several solutions have been introduced to make the excavation safer for workers, by progressively reducing their number thanks to an efficient mechanization of the process; to safely excavate in more and more variable and poor or potentially dangerous geological environments; to reduce costs and construction time; to improve the durability of the works; to improve construction sustainability.

Tunnel engineering requires:

- an optimal merging of the design phase processes,
- the management of the construction/technological phases,
- a good knowledge of how the various techniques have been implemented in similar case histories.

For a long time, tunnelling has been seen as an art: both designers and builders had to be capable of accepting and dealing with the unpredictability of both geological and geotechnical conditions. They had to tailor their tunnel design to the current needs, these being discovered during construction and often evolving with each advancing step. Any inadequacy of their knowledge implied that the tunnel design would develop only during the tunnel construction. Today, no client is willing to accept the amount of time and the costs that would be needed to build tunnels without the help of a modern design approach, as well as modern excavation and supporting techniques. Although today's tunnels are larger, longer and deeper, the main challenge of designers and construction engineers is managing the complexity of tunnelling within defined costs and time, by correctly checking:

the stability of both face and cavity,

Chapter 2: Seismic behaviour of underground structures

- settlements induced by the excavation,
- safety during construction and operations,
- the quality of the final product,
- the feasibility of the construction process influenced by the hydrothermos-chemo-mechanical behaviour of the natural soils and rock mass formations to be excavated.

Today, a modern tunnel design protocol must be based on suitably detailed geological and geotechnical studies, since numerical codes and sophisticated constitutive relationships allow, in most geological and geotechnical environments, reliable three-dimensional stress-strain analyses of the excavated soil/rock mass to be performed. [1]

2.1.1 Design and construction approaches

During the past decades, different approaches have been used for design and construction, strictly linked to the upgrading and development of design tools, and excavations and means of support in conventional excavation. Starting from the traditional excavation by drilling and blasting in rock masses, the evolution of design and excavation techniques in more complex and poor ground has been great.

From the late 1800s, the Sequential Excavation Method was used: this multi-drift tunnel construction technique was based on the design concept that a smaller excavation volume was easier to support by employing the poor supporting means available at that time.

In the 1950s, the New Austrian Tunnelling Method (NATM) was introduced: this uses partialized face excavation (Figure 2.1.2, Figure 2.1.3) and suggests multiple methods of excavation and means of support, to be tailored to the rock mass classification. Tunnels with variables shapes and geometries can be excavated, depending on the tunnel's final use. This took good advantage of the use of shotcrete and bolts as readily available supports for excavation. As a general design philosophy for NATM, the essential aspects for design are illustrated in Figure 2.1.1. The operations related to it have to guarantee the permanent stability of the tunnel, without creating risks to workers or damage to the objects that exist around the tunnel area, above and below the surface, or to the environment. Its basic principles are:

- Excavation, i.e. the detachment of the soil or rock mass from the tunnel core using mechanical tools or explosives and the removal of the material at the face. In this phase, the prevention of disintegration of rock mass, as well as the security that the additional stresses developing during excavation are received by the rock mass, become aspects of fundamental importance.
- Stabilization of the created cavity. The stabilization process includes
 the use of the first phase supports (also called primary or temporary
 supports), realized as shotcrete linings, generally installed in the
 newly created span by the excavation process, and of auxiliary
 measures (rock or soil reinforcements usually installed ahead of the

tunnel face and/or around the tunnel. Monitoring of the behaviour of the rock-tunnel system becomes fundamental to observe the stabilization process and intervene with appropriate construction measures if necessary. In this context, the auxiliary measures must stabilize the free span created by the excavation, helping to correctly control the redistribution of the stresses around the tunnel and managing displacements of the tunnel boundaries and the tunnel face. That said, rigid supports should be avoided to allow stresses to build up in the rock mass, just as the deformation of rock mass should be kept below the critical level, especially when disintegration and loosening phenomena are possible.

• The long-term stabilization of the tunnel by means of the final support (secondary shotcrete lining).

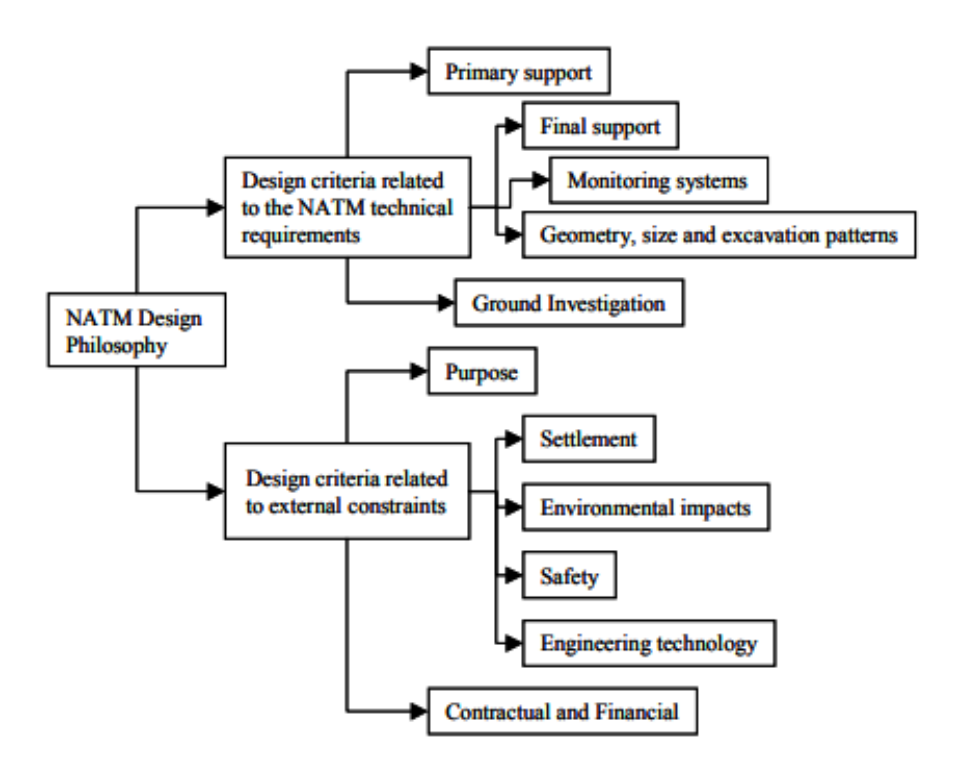


Figure 2.1.1 General design aspects for New Austrian Tunnelling Method (NATM). [2]

Chapter 2: Seismic behaviour of underground structures

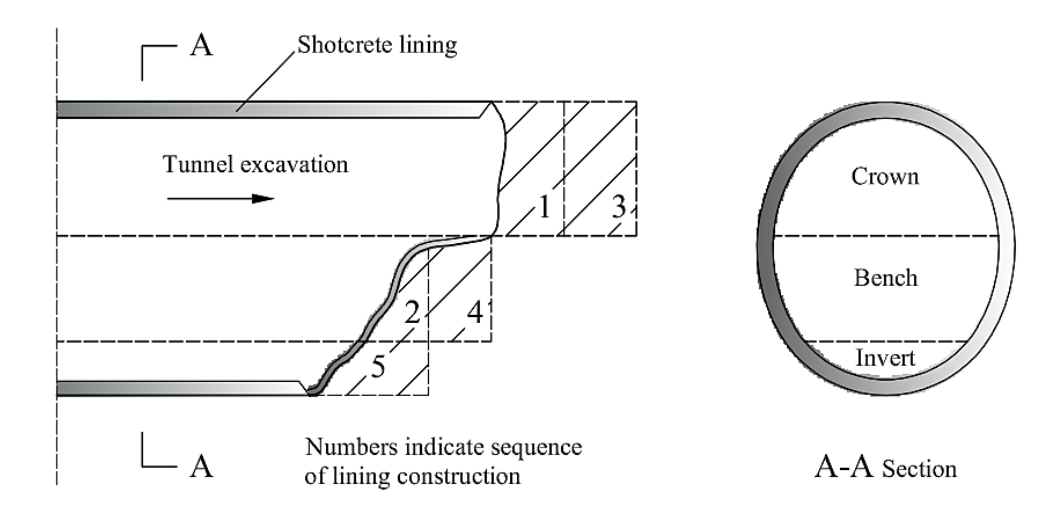


Figure 2.1.2 Tunnel built with NATM. [3].

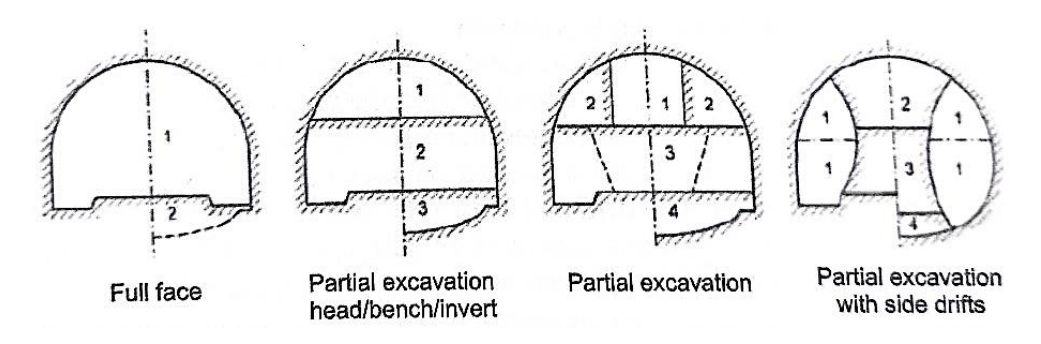


Figure 2.1.3 Example of full-face and different choices of partial excavations. The numbers indicate the sequence of the excavation's stages. [4]

In Italy, since the 1980s, the systematic use of pre-confinement and presupport interventions, also named pre - reinforcement interventions, ahead of the tunnel face has become standard and has evolved in a design approach named Analysis of Controlled Deformation in Rocks and Soils, or ADECO-RS. According to this approach, the unsupported, always full-face, tunnel coreface mechanical response (forecast of extrusions, pre-convergences and convergences) has to be three-dimensionally studied, the excavation operations and supports have to be designed by performing three-dimensional analyses considering and using the core-face, improved if necessary by means of an adequate pre-confinement and/or reinforcement actions/interventions, as a stabilization tool, the monitoring, to be carried out during and after construction, has to be designed, and during construction, the design has to be updated (according to the project), by considering monitoring data in terms of deformation phenomena of core-face, cavity and ground level. This approach has widely been used for the construction in Italy and all around the world of more than a thousand kilometres of underground infrastructures. This also ensures reliable design predictions in terms of construction times and costs and improves the safety of workers. The wide use of this approach has pushed forward the development of new technologies and equipment, to install reinforcing elements in the core-face also for large lengths and boosted the excavation of tunnels with a full section. The greater the need for tunnel construction to deal with difficult stress – strain situations, the more important it is to operate with nearly circular full-face excavation rather than in a partialized face: this allows the invert lining to be built close to the excavation face and therefore a full round structural section to be achieved close to the tunnel face, better controlling the rock mass deformation. The extrusive phenomenon of the core-face is directly responsible for the evolution of the subsequent cavity convergence phenomena, and therefore of the tunnel's stability. The convergence is thus the last stage of the deformation response due to excavation, which begins upstream of the excavation face, due to the extrusive behaviour of the core, and then evolves into pre-convergence, which can increase the and amplify the convergence downstream of the tunnel face itself.

At the same time, since the 1970s, there has been great development of the use of full-face TBMs (Tunnel Boring Machine) (Figure 2.1.4).

These started from gripper TBMs, able to excavate stable rock masses, and evolved to shielded TBMs, which are also able to apply pressure at the face to counterbalance the water pressure and the soil pressure by means of different types of fluids. The excavation by means of shielded TBMs allows control of the deformation around the tunnel both at the face (with the applied pressure in the bulk chamber) and at the cavity, with the immediate support action of the shield and of the continuous installation of the full round segment lining, put in place inside the shield tail, close to the tunnel face. [1]

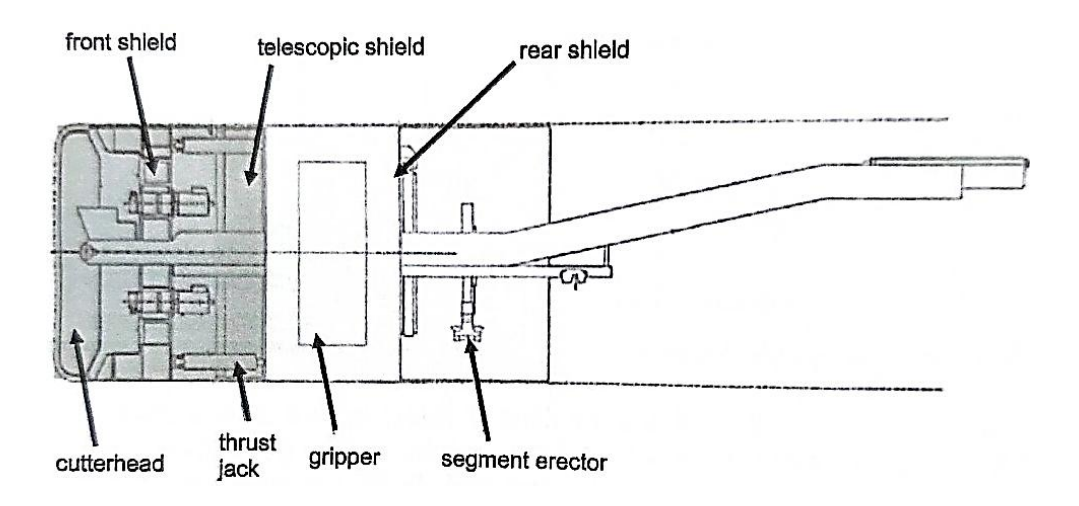


Figure 2.1.4 Scheme of the double – shield TBM. [4]

2.1.2 Tectonic aspects

The behaviour of rocks and soils being excavated depends on many factors, among which the most important are certainly the geological and hydrogeological ones.

The construction of tunnels, in fact, involves solutions to many complex technical problems depending on the geological and geoenvironmental conditions of the area in which the work must be realized.

Before the excavation, the ground is in equilibrium under its original state of stress. The excavation modifies this state of stress by generating a stress deviation around the cavity, with stress concentration close to the boundary surfaces of the cavity. As a result, the ground undergoes deformations in order to reach a new equilibrium condition dependent on several aspects as the depth of excavation, the shape and the dimension of the cavity, the excavation method and the geological features of the site, since during excavation, the natural ground is removed, so becomes essential to carefully know the geomorphological and tectonic features of the site.

The behaviour of the mass being excavated essentially depends on three main aspects: the lithological nature determining the mechanical characteristics of the rock matrix; the structural feature governing the mechanical properties of the mass itself; the state of the stress existing before the excavation.

Focusing on tectonic issues, the lithosphere is subdivided into plates that may converge, diverge or scroll side by side, involving several geological effects as volcanism and earthquakes. In this context, tunnelling can be heavily influenced in a tectonically active area, so a stress state depends on the plate kinematics. Brittle tectonic structures as faults are generated by divergent movements, while folds frequently develop when movements are convergent. Several conditions influence either brittle or ductile deformations, as the type of stress state (compression, tensile and shear); the physical and mechanical behaviour of the rocks; temperature and pressure conditions.

Fractures and faults are determined by brittle deformations of the earth's crust; more in detail, fractures are caused by stresses exceeding the rock strength, and a fault is a fracture characterized by a significant displacement (slip) of the two sides of the faut plane. The main challenges to be faced when

an underground excavation crosses fault rocks are the face instabilities and the achievement of high radical convergences.

On the other hand, folds are the result of plastic deformation of the earth's crust due to compression stresses. In tunnelling, they can involve residual stresses, especially at high depths, as well as dissymmetrical loads and lithological heterogeneity.

For these reasons, to predict the behaviour of the material during excavation, it's essential to collect data related to the:

- Geometry: inventory of all brittle or ductile structures.
- Kinematics: evaluation of the displacements and movements that lead to change of position, orientation, size and/or shape of rock bodies
- Dynamics: reconstruction of the nature and orientation of the stresses producing the deformation.

Such tectonic aspects, together with other conditions, become of fundamental importance when framed within the seismicity. Generally, underground structures show a much lower seismic vulnerability than surface infrastructures, as they are usually flexible enough to withstand the strains imposed by the surrounding soil without reaching their breaking point.

Moreover, tunnel mass is small compared to the mass of surrounding ground, and the confinement of the tunnel by the ground allows to significantly damp out the seismic perturbation. Despite their good seismic behaviour, violent seismic events may become hazardous for underground works, especially if the surrounding ground is affected by liquefaction phenomena or displacements along faults.

The vulnerability of underground structures to earthquakes depends on:

- The stiffness of rocks and soils.
- Tectonic setting.
- Tunnel depth (damage extent usually decreases with depth).
- Tunnel size (the larger the section, the greater the seismic vulnerability).
- Section type (with or without invert).

For these reasons, it's necessary to evaluate the seismicity of the area of interest for an underground excavation and to define the relationship between the seismicity and the geological and tectonic setting of the area [5].

2.1.3 Fundamental geotechnical concepts

The definition of design solutions, as well as the performance of a tunnel during the construction phase and under operating conditions, pass through the definition of a geotechnical model, thanks to which the process of geotechnical investigation and characterization of the ground volume involved, is conduced.

Such model is defined starting from the geological model, to describe the nature and the origin of the soil layers and rock masses, and proceed to the definition of the geotechnical units, i.e. a description of the geometrical layout, with possible spatial variability, that could or could not coincide with the geological units identified before, and their characterization from a physical-mechanical point of view.

In this context, the knowledge of geotechnical concepts necessary for understanding the mechanical behaviour of soils and rocks, by means of appropriate theories and constitutive models, becomes essential, in order to have an overview of the tensional state present in the ground being excavated, to be able to predict deformation phenomena resulting from it, and to provide the possible risks related to the excavation and construction phases, within the more general soil-tunnel interaction.

The mechanical behaviour of soils and rocks investigated passes through the elasticity and plasticity theories. More in detail, elasticity allows to define a simple constitutive model for describing a material mechanical behaviour assuming the stress tensor (σ_{ij}) to be a single-valued function of the strain sensor (ε_{ii}) .

$$\sigma_{ij} = f(\varepsilon_{ij}) \tag{1}$$

The strain history does not affect the stress state, and the material deformation is fully reversible after cyclic stress paths. The law underlying this assumption is Hooke's law (Figure 2.1.5):

$$\sigma_{ii} = E_{ii} \left(\varepsilon_{ii} \right) \tag{2}$$

employed for the definition of a linear-elastic model and an isotropic elasticity, if the material behaviour is independent of the loading direction. Such model involves two basic elastic parameters, i.e. Young's modulus E and Poisson's ratio ν .

The shear modulus, G, is defined as a combination of the previous two parameters:

$$G = \frac{E}{2(1+v)} \tag{3}$$

The stiffness of a material affects its response to stress change in terms of strain. Formally, it is expressed by a stiffness matrix [D] that relates the strain increments, $\delta \varepsilon$, to the stress increments, $\delta \sigma$:

$$\{\delta\sigma_{ij}\} = [D] \cdot \{\delta\varepsilon_{ij}\} \tag{4}$$

The stress – strain behaviour of the soil is not linear; hence, stiffness changes with the strain level and accordingly the elements of the stiffness tensor change. When the stress-strain curve is non-linear, two stiffness values can be defined: the secant or the tangent stiffness. In terms of shear modulus:

$$G_s = \frac{\tau}{\gamma} \text{ (secant shear stiffness)} \tag{5}$$

$$G_t = \frac{\delta \tau}{\delta y} \text{ (tangent shear stiffness)} \tag{6}$$

The dependency of stiffness (either secant or tangent) on the strain level is generally represented by employing a plot of the normalized stiffness modulus (with respect to its maximum value, exhibited at very small strain) as a

function of strain. A typical curve in terms of normalized shear modulus, G/G_0 , varying with shear strain γ , is shown in the Chapter 3 (Figure 3.1.6).

The range in which different laboratory tests can characterize the soil stiffness at different strain levels is shown in the figure. At the same time, the typical range of strain mobilized in geotechnical construction process is also identified. In most cases, the level of shear strain involved in tunnelling falls between 0.01% and 1%.

The plasticity theory assumes that beyond a given stress threshold, defined by means of the yield function, plastic/irreversible strains, remaining after loading – unloading, can develop. In case yield surface coincides with the failure envelope, the term perfectly plastic is used. Elastic – plastic models assume the yield function to coincide with the boundary of the elastic locus and, when inside the yield function the mechanical response is assumed to be rigid, the model is defined rigid perfectly plastic. In the elastic – plastic models, the strain rate tensor $(\dot{\varepsilon_{ij}})$ can be decomposed into two additive components: elastic $(\dot{\varepsilon_{ij}})$ and plastic strain rates $(\dot{\varepsilon_{ij}})$.

$$\dot{\varepsilon_{ij}} = \dot{\varepsilon_{ij}}^e + \dot{\varepsilon_{ii}}^p \tag{7}$$

Within the yield surface, the material behaves as elastic, while, once it is reached (yielding), a plastic strain rate develops. The direction of the plain strain rate tensor is defined by means of the flow rule (Figure 2.1.6), according to which the increment in the plastic strain vector is normal to an additional function, i.e. the plastic potential. If the yield function and the plastic potential coincide, the plastic strain increments are normal to the yield surface, and the flow rule is called associated. In case the yield function does not evolve, the term perfect plasticity is used; otherwise, the evolution of the yield function is called plastic hardening; in case of its evolution is governed by the accumulation in plastic strains, it's called strain hardening. When a progressive shrinkage of the yield surface takes place, the term strain softening is employed. An isotropic material exhibits the same behaviour along any direction. However, soil deposition and layering, rock bedding and discontinuities may affect the mechanical properties the ground along different directions, making the mechanical behaviour of the geomaterial anisotropic. In

this case, the same stress change can produce very different strain increases if applied along different directions.

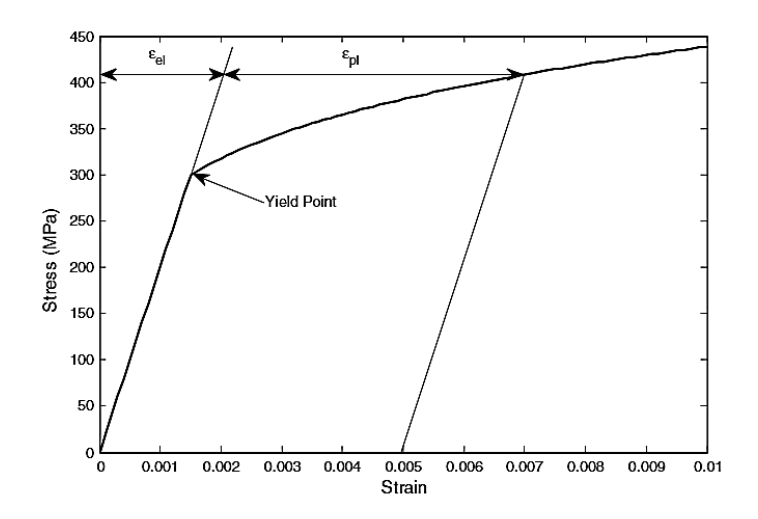


Figure 2.1.5 Strain in a ductile material can be decomposed into elastic and plastic components. The elastic component of strain obeys Hooke's law at all stress levels [6].

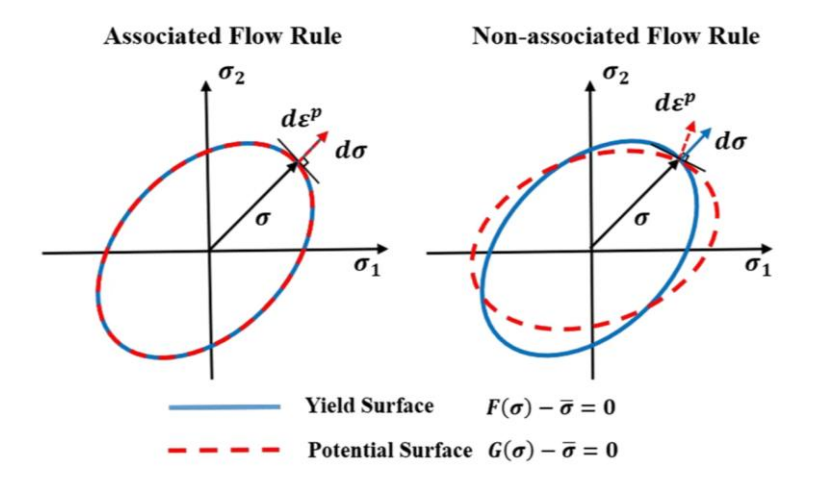


Figure 2.1.6 Concept of Associated and Non-Associated Flow Rule [7].

In soils, strength represents the ability of a material to carry stress. More in detail, the shear stress τ can reach a limiting value, τ_f , that cannot be exceed (failure). This is called shear strength and, according to the Mohr-Coulomb failure criterion (Figure 2.1.7) is defined by the sum of two contributions: one independent of stresses (cohesion) and the other proportional to the effective normal stress σ_n acting on the failure plane (friction):

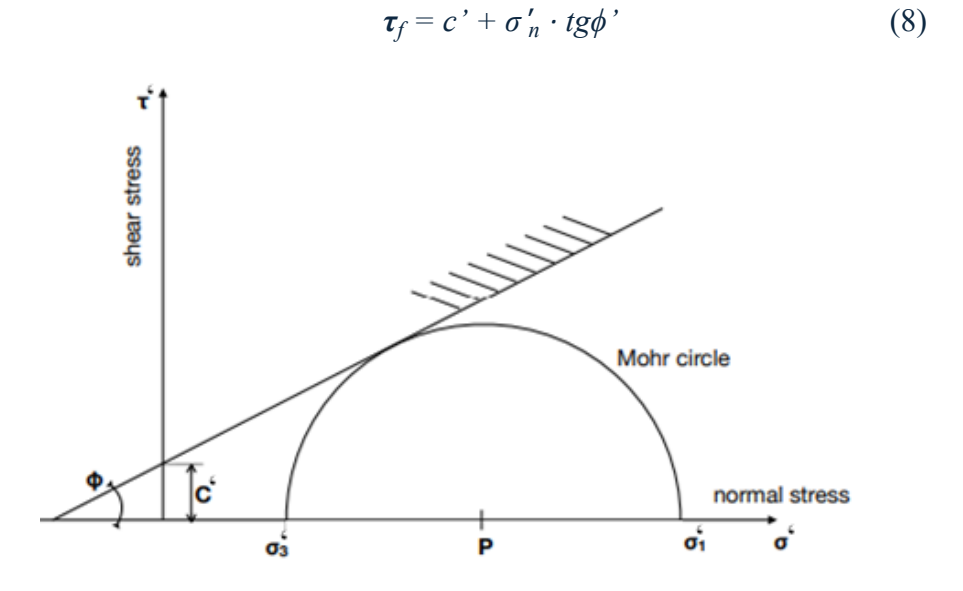


Figure 2.1.7 The Mohr–Coulomb failure criteria and Mohr's circle. The failure criterion represents the linear envelope that is obtained from a plot of the shear strength τ of a material versus the applied normal stress σ , where ϕ is the angle of friction, considering also cohesion c [8].

For cemented soils and rocks some tensile strength, commonly put in relation to shear strength parameters c (cohesion) and ϕ (angle of shear strength or friction angle) is also available. Since many soils are unbonded, the effective cohesive term is in most cases just the consequence of interpreting as linear the actual non – linear strength criterion under long-term (drained) conditions. Under strain-controlled conditions, soil specimens at large strains exhibit a stationary response, characterized by no change in stresses and

volume, and it's called critical. In case of very dense granular soils and overconsolidated fine-grained soils, i.e. a soil subjected to a previous history of loading and unloading, this state is reached after a peak in stresses.

Two parameters should be defined: one at peak, c_p and ϕ , and the other at the critical state, c_{cs} and ϕ_{cs} . The latter set is independent of the initial state of the soil. The cohesive term at the critical state, c_{cs} , can be assumed null; the friction angle further reduces with a very large shear strain. Such a state is called residual, and the corresponding lower value of friction angle is named residual friction angle ϕ_r .

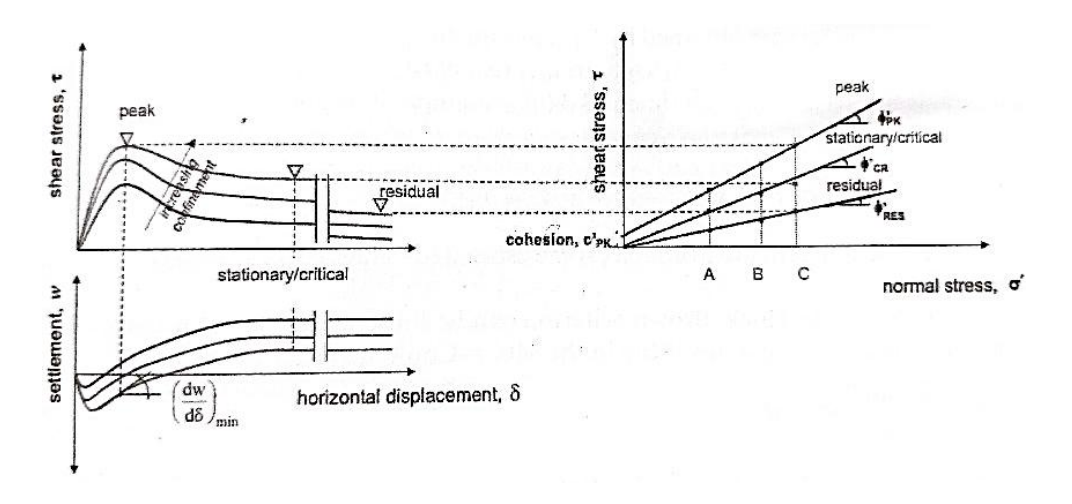


Figure 2.1.8 Shear strength. [9]

Since the excess pore water pressure generated by the perturbation in the short term, in the undrained conditions, it's hard to be computed, there is a common practice formulating the strength criterion in terms of total stresses:

$$\tau_f = c_u \tag{9}$$

Where c_u is the so-called undrained shear strength. Since it is related to an equivalent single-phase formulation of the continuum, c_u depends on the state of soil and cannot be considered an intrinsic parameter of the material.

2.2 The importance of considering the soil-structure interaction (SSI)

Considering SSI in design of various structures is a rarity. This is because of inadequately laid SSI provisions in design codes.

Depending on structure-to-soil stiffness contrast, SSI may turn either beneficial or detrimental to structural response during a seismic event.

For instance, as observed in presence of 2015 Nepal Earthquake by Badry and Satym in [10], the irregularity in the structure, such as an asymmetry in its geometry, led to detrimental effects greatly precisely intensified by considering SSI.

Similarly, noticeable instances include the collapse of Hanshin Expressway Route 3 (Fukae section) in 1995 Kobe Earthquake as investigated by Mylonakis and Gazetas in [11].

Aydemir in [12] studied soil-structure interaction effects on structural parameters for stiffness degrading systems built on soft soil sites and found smaller strength reduction factors for interacting systems than those for corresponding fixed-base systems. This implies that neglecting SSI may result in an unconservative design. Further he observed the importance of considering stiffness degradation in an SSI analysis for stiff structures. Negative post-yield stiffness resulting from P-delta effect (known as negative strain hardening) also detrimentally affects seismic response in terms of lower strength reduction factors and higher inelastic displacement demands.

A case in which the traditional belief of SSI being beneficial to seismic response of structures is observed by Ciampoli and Pinto in [13], where considering SSI in inelastic response of bridge piers exhibits a reduced ductility demand at an expense of a slight increase in top displacement demand. They identified two input parameters: wave parameter and slenderness parameter. While wave parameter represents soil-to-structure stiffness contrast, slenderness parameter is purely geometrical property of structure.

It can therefore be observed that there is a need to consider SSI in design of inelastic structures. Considering huge capital required, importance of connectivity in post-disaster situations and magnitude of hazards involved,

inclusion of SSI in design of bridges, dams, wind turbines and nuclear reactors is of paramount importance, as observed by Anand and Satish Kumar in [14].

Focusing on the underground structures, during its lifetime they may experience a non – negligible evolution of their stress and strain state due to either hydro-thermos-chemo-mechanical coupled process or accidental loads. Although underground structures, more specifically tunnels, have traditionally been considered less susceptible to earthquake perturbations than aboveground structures, several cases in which typical damages, including lining cracks, portal failures, concrete lining spalling, groundwater ingress, exposed and buckled reinforcements, are reported in De Prisco et al. [1].

In most cases, the damage occurring to underground structures during earthquakes is due to the lack of consideration of appropriate seismic loads in design and during construction. Differently for above-ground structures, the seismic behaviour of underground structures is determined mostly by the loads induces by the surrounding ground, while the inertial forces are generally of secondary importance, due to their specific geometrical and conceptual features.

Although it is not yet possible to accurately evaluate the seismic earth pressures and the seismic shear stresses around a tunnel or on the sidewalls of a deep underground structures and making yet several hypotheses on the evaluation of the applied shaking loadings, which may not reflect the real loading conditions during a strong earthquake excitation, several methods are proposed in literature to address the complexity of the problem, as observed in Pitilakis and Tsinidis [15] Tsinidis et al.[16]

The seismic response of an underground structure is highly affected by the soil-structure interaction (SSI) effects that take place during ground shaking.

Hence, the properties of the surrounding ground and its response during ground shaking, the geometrical features and burial depth of the tunnel, the soil to tunnel relative stiffness, the soil-tunnel interface characteristics, as well as the ground motion characteristics are especially important parameters that affect the response, as described in Pitilakis and Tsinidis [15], Hashash et al. [17] and Kawashima [18].

2.2.1 Underground structures: seismic response mechanisms

In seismic areas, underground structures should be designed to respond to ground shaking and ground failure.

The underground structures response to ground shaking represents a typical soil-structure interaction (SSI) problem. During a strong earthquake, in fact, ground shaking due to wave propagation and permanent ground displacements due to lateral spreading, landslides and fault rupture significantly affect such structures. The inertia of the surrounding soils is much higher than the inertia of the structure itself; consequently, the response of the embedded structure is dominated by the response of the surrounding soil and the transient ground deformations.

By considering a simple rectangular structure embedded or simply founded on the ground as an indicative example, when travelling seismic waves joint an underground structure, they "forced" it to deform in various modes, both in the longitudinal and transverse direction. Seismic waves with soil particle movement parallel to the underground structure (e.g. tunnel) axis, result in axial deformation (compression-extension), whereas soil movement perpendicular to the tunnel axis causes longitudinal bending. Shear waves propagating upwards from the bedrock may cause the deformation modes presented in Figure 2.2.1 showing ovaling or racking effects for circular and rectangular cross-sections respectively.

The interaction between the underground structures and the surrounding soil is related to two crucial parameters, i.e.:

• the relative flexibility of the structure and the ground.

In this case, the soil deformation in the proximity of the structure, which in general is not elastic, imposes displacement constraint on the structure's cross-section. Yet, due to the stiffness difference between the two media, the structure does not follow the imposed ground deformation.

A relatively rigid structure will resist to the seismic ground deformations, while a flexible structure will follow the ground distortions. For a very flexible structure the structural distortion may be even higher than the free field ground deformation.

Chapter 2: Seismic behaviour of underground structures

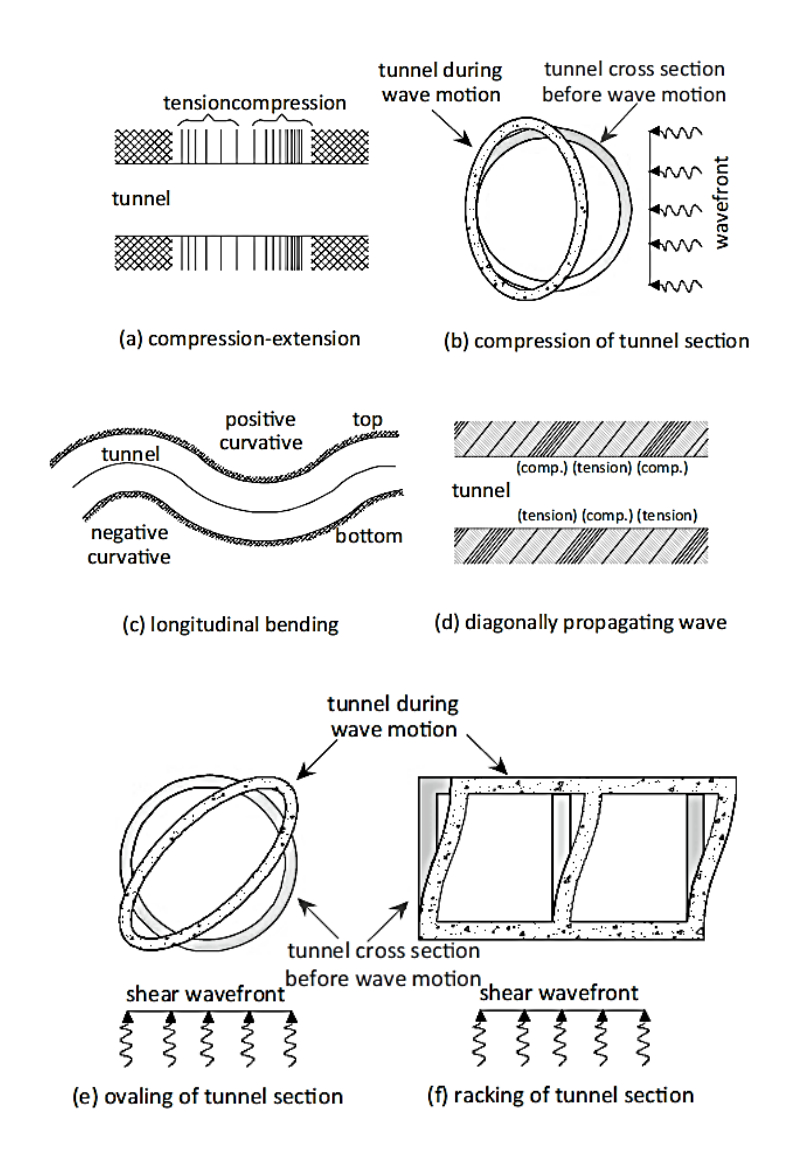


Figure 2.2.1 Simplified deformation modes of underground structures subjected to seismic waves. ([16] [15] modified after Norman in [19])

The overall seismic behaviour of the structure depends on the properties of the surrounding soil, which are not constant during strong excitation, and the inertial properties of the structure itself. The soil to structure relative flexibility is expressed through the so-called flexibility ratio F.

Such value is closely related to the expected stress level on the structure and specifically relates to transverse actions on the tunnel.

- F \rightarrow 0: The structure is rigid and will not display any type of deformation.
- F < 1: the structure is stiffer than the surrounding soil, thus the structural deformation level will be smaller than the free-field deformation level.
- F = 1: the structure and the surrounding soil share the same level of stiffness, so the tunnel will follow the free-field deformation.
- F > 1: the racking deformation of the structure is amplified compared to the free-field deformations. To this end, a crucial point for the seismic evaluation of an underground structure is the proper estimation of the flexibility ratio. For circular tunnels, assuming elastic behaviour, the flexibility ratio can be computed, using the following analytical formulation:

$$F = \frac{E_s (1 - v_l^2) R^3}{6 E_l I_l (1 + v_s)}$$
 (10)

Where E_s is the soil elastic modulus, ν_s is the soil Poisson ratio, E_l is the lining elastic modulus, ν_l is the lining Poisson ratio, I_l is the lining moment of inertia (per meter), and R is the circular tunnel radius. For rectangular structures (Figure 2.2.2) the flexibility ratio is estimated according to Wang and Munfakhz in [20] as:

$$F = \frac{G_M W}{SH} \tag{11}$$

Where G_M is the soil shear modulus, W is the width of the structure, H is the height of the structure and S is the required force to cause a unit racking deflection of the structure, estimated through a simple static elastic frame analysis.

Rigid structures can exhibit rocking movement along the structure's vertical line of symmetry, while for flexible structures vertical shear and inward deformations of the sidewalls and the slabs may be observed. To this end, the invert slab and the roof are not always moving and deformed as a simple "shear beam". Rocking or inward deformations of the structure are clearly observed theoretically; rocking modes or inward deformation modes, which prove the emerging need to consider seriously the SSI effects in the seismic design.

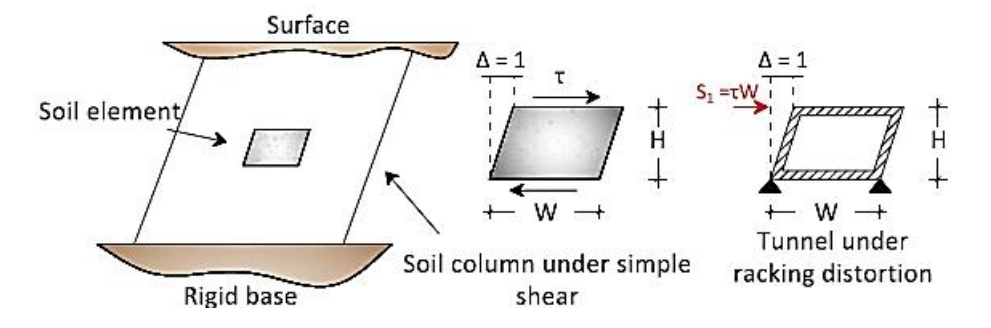


Figure 2.2.2 Simplified model to evaluate flexibility ratio for rectangular structures. [15] [20]

• The interface characteristics between the structure and the surrounding soil.

The interface characteristics between the structure lining and the surrounding soil affect considerably the seismic behaviour of the system.

The development of the shear stresses is supposed to reduce to a minimum the in-plane vertical shear deformation of the structure and it's rocking, forcing it to deform predominantly in "horizontal shear" (Figure 2.2.3).

While a "strong" interface, capable to accommodate high shear stresses with limited deformations, results in high stresses on the lining, implying, for a stiff structure, that the displacements of the surrounding soil are constrained, the soil deformations around the structure are low and the shear modulus

degradation is limited, a "weaker" interface, on the contrary, will transmit on the same stiff structure smaller shear stresses.

The reduced constraint on the soil mass will result in larger shear deformations in the interface, which may even produce a slip along the interface. The slip will produce higher concentration of stresses, higher strains and consequently a further degradation of the soil shear modulus, causing larger deformations in the surrounding soil and high normal stresses at the interface. Hence the potential to develop considerable soil displacements will be increased, although the capability to transmit them in terms of shear to the structure will be small. To this end, the soil-structure relative stiffness and the interface characteristics are interrelated and may have opposite effects on the structure's response.

In general, the complex soil to structure relative flexibility, usually expressed in terms of the flexibility ratio, and the interface seismic behaviour have a paramount effect on the dynamic response of an underground structure, and both are changing with the seismic excitation as they depend on the soil shear modulus and strength, which depend on the ground strains attaint and the soil non-linear behaviour.

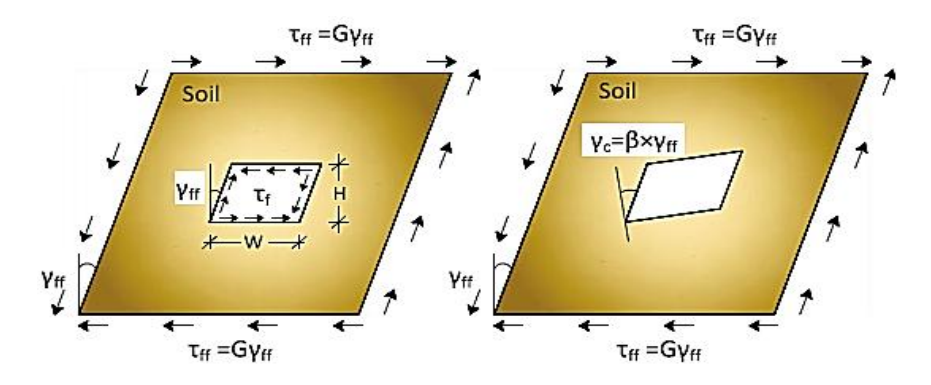


Figure 2.2.3 Importance of the shear stresses at the perimeter of the structure on the deformation mode. ([15] modified after [21])

2.2.2 Underground structures: analytical and numerical investigation of the seismic response

Understanding of the seismic behaviour of underground structures and, more in detail tunnels, has continuously improved, by means of the introduction of rational methods of analysis, based on the interpretation of observations from the response of actual structures during seismic events, as well as laboratory testing. Such methods, in the form of analytical solutions, simplified pseudo-static analyses, and numerical tools, are becoming standard practice for new tunnels in seismic areas, as well as for the retrofit of existing tunnels that are vulnerable to seismic effects.

Analytical solutions were proposed by many researchers to estimate the seismic internal forces of tunnels' linings, under certain assumptions and conditions, e.g. elastic response of the soil and the tunnel lining, and simulation of seismic loading in quasi-static fashion, among others.

Even though analytical solutions are formed using relatively strict assumptions and simplifications, they are useful, relatively fast and easy to use for preliminary seismic design of tunnels. Hence, they are widely utilized in preliminary design stages. The seismic design basis for underground structures was first laid out by St John and Zahrah in [22] whose solutions provided a very useful tool for practicing engineers to estimate the seismic behaviour of tunnels under ground shaking in both longitudinal and transversal directions.

Penzien in [21] proposed closed-form solutions for the seismic analysis of deep rectangular and circular tunnels, with the seismic loading being simulated in a simplified way as a uniform shear-strain distribution, τ_{ff} , imposed on the soil boundaries of the soil-tunnel system, away from the tunnel. (Figure 2.2.3)

However, Penzien's solutions neglect the effect of the normal stresses developed during loading along the soil-tunnel interface.

Analytical solutions typically assume linear elastic behaviour of the soil and, therefore, they do not account implicitly for the strain-dependent soil shear modulus. Bobet et al. in [23] incorporated this shear modulus reduction by using an iterative procedure to adjust the shear modulus of the ground depending on the level of shear strain until the convergence of shear strain was reached.

The applicability of the analytical solutions is limited by the assumptions that the soil response is always considered to be linear elastic, so the solutions are generally more accurate only when the ground experiences small deformations. The reached results should, in most cases, be validated by numerical simulations, which represent better the seismic tunnel-ground interaction phenomena.

Due to the distinct deformation modes of tunnels and the associated potential levels of damage induced by ground shaking in the longitudinal and transverse directions, the seismic analysis of tunnels is commonly decoupled in the two directions, employing methods of analysis of different complexity.

In the transverse direction, it is quite common to simplify the analysis using an equivalent static procedure. For instance, for rectangular tunnels one may use the method proposed by Wang and Munfakhz in [20] which implies a simplified static analysis of the tunnel's lining frame (Figure 2.2.4).

The seismic distortion of the tunnel (δ_{str}) is obtained from the "free-field" ground distortion at the tunnel depth (δ_{ff}), multiplied by the racking ratio, R, to account for the soil-tunnel interaction effects. In turn, the racking ratio is related to the flexibility ratio, F, the latter expressing the relative stiffness of the tunnel with respect to the surrounding ground.

Upon determination of the structural racking distortion, δ_{str} , this is imposed on the lining frame either as an equivalent static load (P) atop corner of the frame or as a pressure distribution (p) on the side walls of the frame.

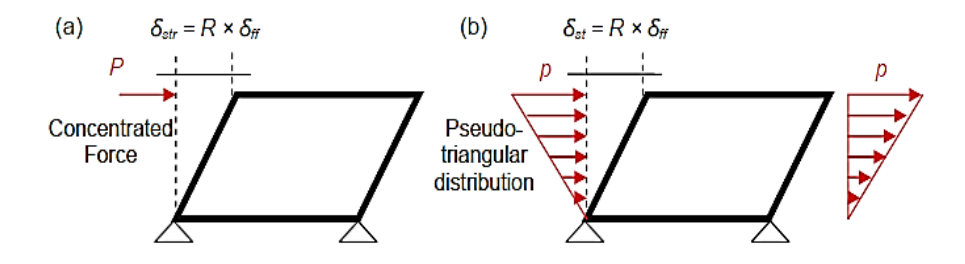


Figure 2.2.4 Simplified frame analysis models, (a) concentrated force, (b) triangular distribution (modified after [20]). [16]

A tunnel may also be analysed in the transversal direction using a framespring model (Figure 2.2.5). In this case, the structure is modelled with beam elements, while the soil is simulated via "appropriate" springs. The equivalent seismic loading is statically introduced in terms of: (i) equivalent inertial static loads (caused by the structure and the overburden soils mass), (ii) seismic shear stresses along the perimeter of the structure and (iii) seismic earth pressure or ground deformations, imposed on the sidewalls of the structure.

The introduction of the soil springs makes it very difficult, if not impossible, to account for the soil stress redistributions effect on the earth pressures and shear stresses around the tunnel.

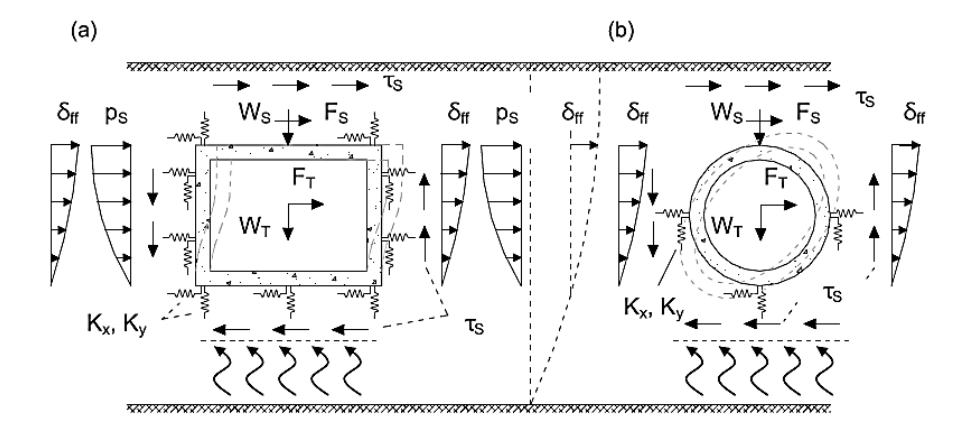


Figure 2.2.5 Simplified equivalent static method for the transversal seismic analysis of (a) rectangular and (b) circular tunnels; δ_{ff}: free – field seismic ground deformation, p_s: seismic earth pressures on the side – walls of the rectangular structure, τ_s: seismic shear stresses around the perimeter of the tunnel, W_S: weight of overburden soil, F_S: inertial forces of overburden soil, W_T: weight of tunnel, F_S: inertial forces of tunnel, K_x, K_y normal and shear soil springs along the perimeter of the tunnel lining (redrawn after [15]). [16]

To avoid the problems associated with the simulation of the ground by means of springs, numerical methods that treat the surrounding ground as a continuum have been developed. Within the "pseudo-static seismic coefficient deformation method" as described by Jeremy Hung et al. in [24], the soil-tunnel configuration is simulated via a 2D numerical model. The seismic load is introduced statically, as an equivalent inertial body force throughout the entire numerical model, corresponding to the ground free-field acceleration

amplification profile. (Figure 2.2.6) The acceleration profile may be derived through a separate one-dimensional site response analysis of the soil deposit (linear, equivalent linear or non-linear). Such method is applicable to both circular and rectangular tunnels.

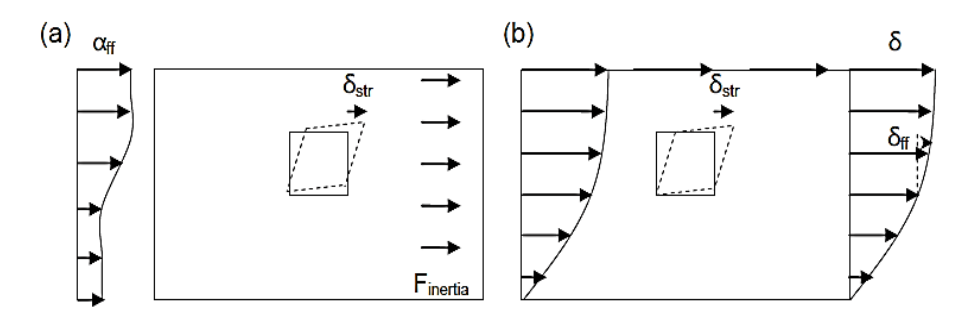


Figure 2.2.6 Detailed equivalent static analysis: (a) distributed inertial loads (b) imposed ground distortions at the boundaries (aff: ground acceleration at free-field, F_{inertia}: equivalent to ground acceleration inertial body force) [16].

As an alternative to this method, the equivalent seismic load is introduced as a ground deformation pattern on the numerical model boundaries, corresponding to the free-field ground response. A procedure of analysis in which the equivalent seismic load is introduced statically in terms of displacement time histories, within a pseudo-static time history analysis, was recommended. The displacement time histories are computed for each depth through a 1D seismic soil response analysis and applied in the 2D numerical model statically through a stepping procedure.

Modelling the tunnel as a beam on elastic springs have been proposed for the seismic analysis of tunnels in the longitudinal direction. In this type of analyses, referred to as to "simplified equivalent static analyses" or "simplified dynamic analyses", according to ISO 23469 in [25], the "seismic load" is applied to the springs as an equivalent static ground deformation that may account for the spatial variation of the ground motion (Figure 2.2.7). A parameter that may affect significantly the computed response is the distance between the springs, which depends on the predominant wavelength and, therefore, on the frequency range of interest.

Chapter 2: Seismic behaviour of underground structures

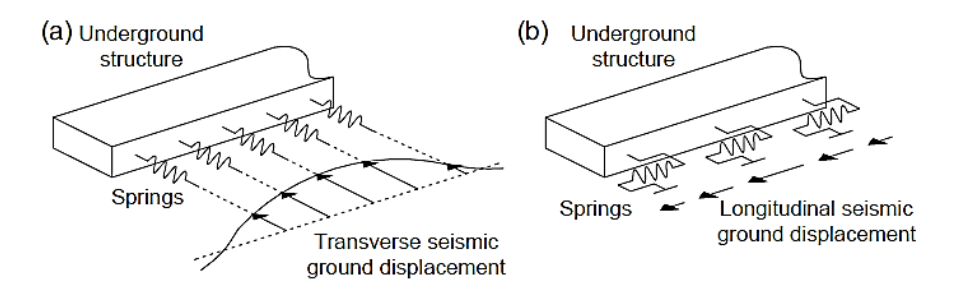


Figure 2.2.7 Simplified equivalent static analysis method for tunnels, (a) transversal, (b) longitudinal analysis [25].

Like the simplified equivalent static analysis is the simplified dynamic analysis. In this case, the seismic loading is introduced in terms of displacement time histories that may account for the spatial variation of the seismic ground motion. This method permits to model efficiently complex mechanical properties. A crucial issue for the implementation of the above methods is the adequate estimation of the soil impedance functions (springs and dashpots).

Recent studies have examined the accuracy of the simplified methods of analysis described above by comparing their predictions against the results of full dynamic analyses, as well as experimental data from centrifuge tests.

For instance, in Lanzano et al. [26] the results of centrifuge tests in terms of mobilized shear stiffness and damping ratio on reduced scale models of a circular tunnel, physically modelled by an aluminum-copper alloy tube (Figure 2.2.8), were back-calculated from the experimental results.

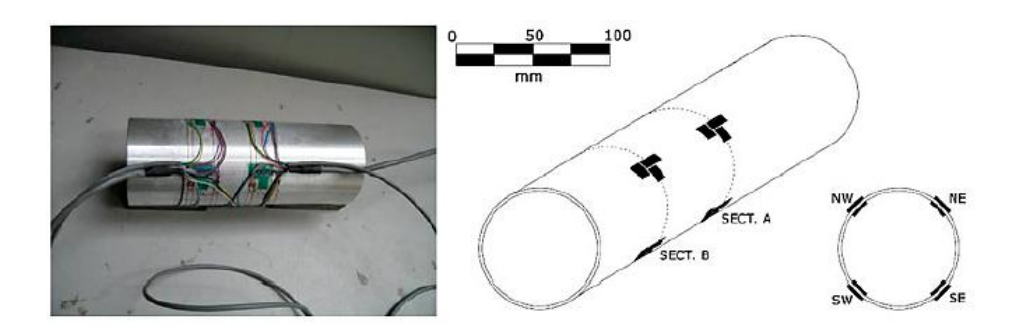


Figure 2.2.8 Aluminium alloy tube and drawing of strain gauges layout [26].

Two procedures were used to back-figure the mobilized shear stiffness and damping ratio from the centrifuge tests: one was based on the interpretation of the spectral ratio between surface and bottom accelerometric signals and the other on the shear stress-strain cycles during each event. (Figure 2.2.9) shows a reasonably good agreement between the two methods.

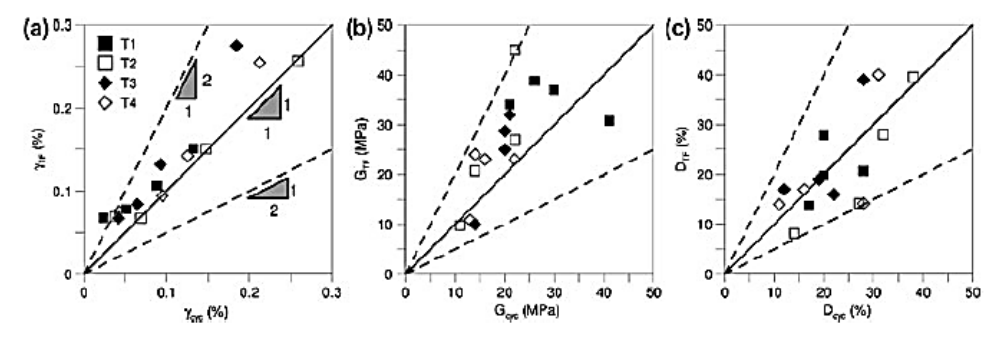


Figure 2.2.9 Comparison between the two different estimations of (a) γ , (b) G and (c) D. [26]

The degree of uncertainty of both procedures is increasingly high at the lowest strain levels, where the input signal was most affected by high frequency noise, although time histories were filtered for high frequencies before each integration step. The scatter of the parameters derived from the stress-strain loops is related to the back-calculation procedure, which determines the shear strain by numerical manipulation (time integration and spatial derivation) of the recorded accelerations. Due to the characteristics of

the input signals, which were pseudo-harmonic, the procedure based on the spectral ratio allowed for results of lower reliability than the interpretation of cycles. Therefore, only the latter was used to back-figure the mobilized stiffness and damping for the numerical and analytical predictions.

In this context, equivalent linear viscoelastic dynamic analyses of the coupled ground-tunnel system undergoing shaking were performed by the FE code PLAXIS 2D to adequately reproduce the geometry of centrifuge models (Figure 2.2.10).

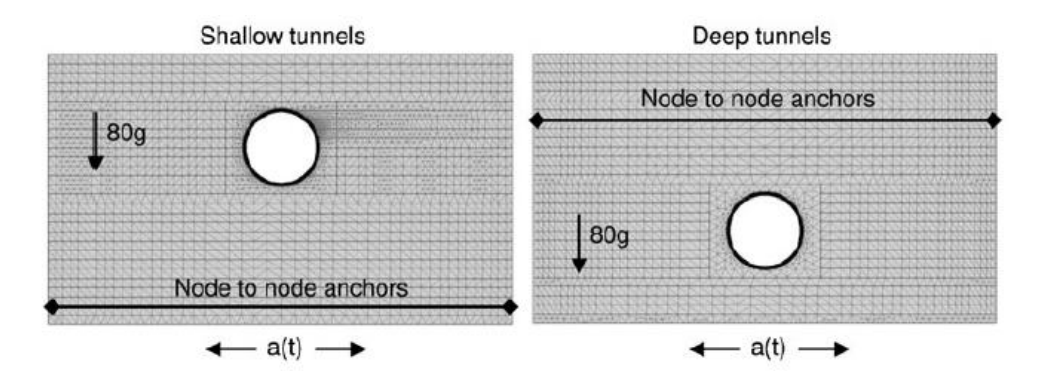


Figure 2.2.10 Analyzed numerical models. [26]

In the numerical simulations carried out, the soil was intentionally modelled as linear viscoelastic and homogeneous, by assuming the shear stiffness G and the damping ratio D constant with depth and corresponding to the values backfigured from the τ - γ cycles. On average, the predicted shear strains result higher than experimental ones, since the computed accelerations sometimes overestimate measurements (Figure 2.2.11). The figure shows the difficulties which may arise in back figuring such values, because of the pseudo-harmonic shape of the input signal.

Focusing on the tunnel interface conditions, the stiffness reduction factor of the ground-lining interface (R_{inter}) was back-calculated to be used in numerical analyses to provide a reliable estimate of the transient changes of hoop force. The comparison of experimental and numerical results in terms of transient changes of internal forces in the lining was satisfactory both in terms of bending moment and of hoop force.

Generally speaking, on the soil-tunnel relative stiffness, the soil-tunnel interface condition adopted in the dynamic and equivalent static analyses, as well as the simulation of the non-linear response during ground shaking, equivalent static analyses tend to either underestimate or overestimate the computed seismic lining forces of the examined tunnels or culverts, compared to full dynamic analyses, with the differences reaching 20-40%.

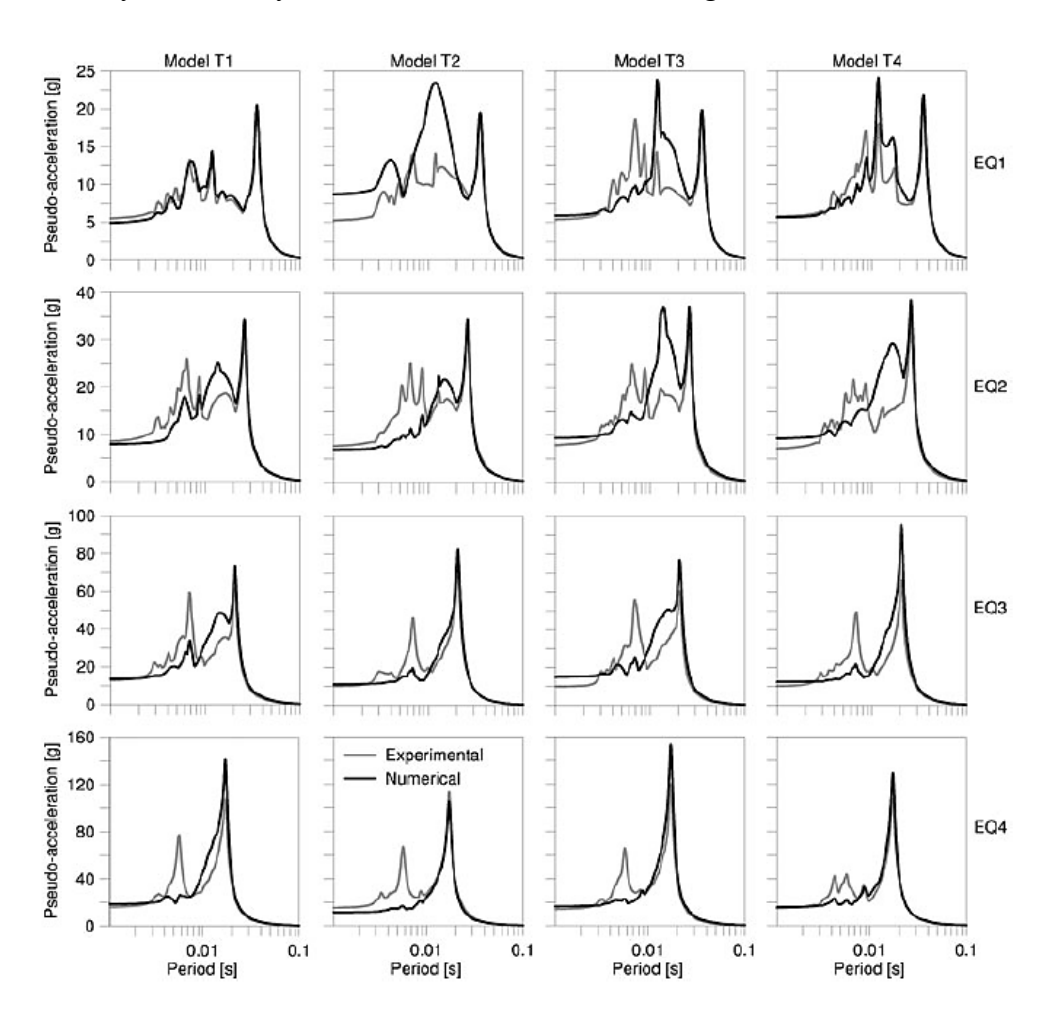


Figure 2.2.11 Numerical vs. experimental response spectra of pseudo-acceleration. [26]

Analytical solutions and simplified methods of analysis are extremely useful for preliminary design purposes. However, for more thorough predictions, full dynamic analyses, employing numerical models, may be needed. A full dynamic time history analysis of the coupled soil-tunnel configuration is potentially the most accurate method for the seismic analysis of tunnels [24] [25].

Different numerical approaches have been reported in the technical literature, for the investigation of tunnel response, for design, or for back - calculation of the observed dynamic behavior of tunnels in field or in the laboratory. Numerical analyses can inherently describe the kinematic and inertial aspects of soil-structure interaction, while they can adequately simulate complex geometries and heterogeneities of the soil deposit, as well as the effects of other existing structures, the latter located in the near area.

Using appropriate constitutive laws, it is possible to model the non-linear behavior of the soil, the structure and the soil-structure interface, as shown in Bilotta et al. 2014 [27] where several sets of numerical analyses were performed with different constitutive models and numerical codes to predict the behavior of a set of centrifuge models of tunnels under seismic loading.

The comparison among the numerical results has shown that the amplification of ground acceleration is relatively well matched by very different constitutive models, provided that the model is able to mobilize a shear stiffness and a damping ratio in the soil layer, which are close to those mobilized in the centrifuge test. On the other hand, the calculation of shear strain is pretty much affected by constitutive behavior, since a significant accumulation of plastic shear strain, which may have occurred in the physical model during shaking, could be underestimated by numerical analysis.

As better discussed in the next Chapter, 2D or 3D numerical codes, based on the Finite Element (FE) or the Finite Difference (FD) method, are the most used for calculations involving buried structures in a continuous medium, i.e. soil and rock, while the Discrete Element Method (DEM) has been employed for analyses of discontinuous media, i.e. fractured rock.

2.3 Main regulatory applications

The current design codes are based on the employment of both the ultimate limit state (ULS) approach and partial factors of safety, accounting for the uncertainties associated with both material parameters and applied actions. The limit states to be considered are related to both soil/rock failure (e.g. tunnel face collapse) and structural element failure.

The ULS approach was originally conceived for structural design where, in most of the cases, actions applied on structural elements can be treated as input data. On the contrary, in most of the geotechnical problems and particularly in tunnelling, the actions applied on structural elements are calculated by solving a soil-structure interaction problem. Therefore, internal actions in structural elements (i.e. axial and shear forces and bending moment) are to be determined by employing "coupled approaches", (either simplified, such as the convergence-confinement method, or numerical, as explained in the Chapter 3), taking into consideration both the soil domain and the structural elements. Only in same special cases, for instance when a single detached rock blocks interacts with the lining, internal actions in structural elements can be calculated without solving a soil-structure interaction ("uncoupled approach").

The design codes (e.g. EC8), for the verification of structural elements in soil-structure interaction problems, allow the introduction of partial coefficients on the effects of the actions, i.e. on the internal actions in the structural elements. This implies that:

- The internal actions in the structural elements are evaluated by employing either coupled or uncoupled approaches without the introduction of partial factors of safety on both material strength properties and actions.
- Subsequently, the internal actions are increased by using partial factors. The structural verification is performed by also applying partial factors on structural material strength.

On the contrary, for the evaluation of ULS only related to soil/rock mass failures (for instance unsupported cavity/face collapse), numerical analyses can be performed reducing the characteristic soil strength properties and by not imposing any amplification of actions. [28]

Focusing on EN 1998 Eurocode 8 [29], the latter was introduced to enhance the safety and resilience of buildings in seismic – prone regions, providing a comprehensive framework for engineers and architects to ensure structures withstand the forces unleashed during earthquakes. Its purpose is to ensure that in the event of earthquakes: (i) human lives are protected; (ii) damage is limited; (iii) structures important for civil protection remain operational.

The random nature of the seismic events and the limited resources available to counter their effects are such as to make the attainment of these goals only partially possible and only measurable in probabilistic terms.

The extent of the protection that can be provided to different categories of buildings, which is only measurable in probabilistic terms, is a matter of optimal allocation of resources and is therefore expected to vary from country to country, depending on the relative importance of the seismic risk with respect to risks of other origin and on the global economic resources.

Eurocode 8 also addresses the importance of designing structures with a level of ductility, allowing them to undergo controlled deformations without catastrophic failure. This ductile behaviour is crucial for dissipating seismic energy and preventing sudden collapses, thus enhancing the overall resilience of the structure.

Eurocode 8 establishes clear structural performance requirements. These requirements delineate the expected behaviour of structures during seismic events, specifying factors such as lateral displacement limits and deformation capacities. By providing quantifiable benchmarks, the code enables engineers to assess and validate the seismic performance of a structure against predetermined criteria. Additionally, it introduces the concept of performance levels, categorizing structures based on their intended function and the consequences of failure.

Eurocode 8 is subdivided in six parts numbered from EN 1998-1 to EN 1998-6. Among these, EN 1998-5 establishes the requirements, criteria, and rules for the siting and foundation soil of structures for earthquake resistance.

It covers the design of different foundation systems, the design of earth retaining structures and soil-structure interaction under seismic actions.

The complex topic of soil-structure interaction is addressed involving many dynamic and geotechnical factors, explained by means of key aspects:

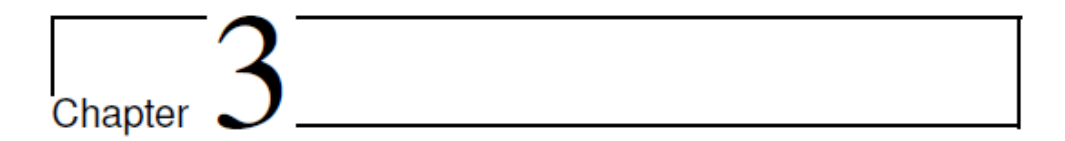
• the modelling of dynamic response, describing how during an earthquake, the soil movement induces forces in the structure, but

- the structure's response can also influence the soil-behaviour. The combination of these effects is analysed through coupled models.
- the non-linear behaviour of the soil, since the soil does not behave linearly during an earthquake, but it's necessary considering the non-linear behaviour of the latter, which can lead to phenomena such as liquefaction or amplification of seismic waves under certain geotechnical conditions.
- The soil amplification effects, i.e. how the vibrations generated by the earthquake are intensified as they propagate through the soil and reach the structure, increasing the loading on the structure itself. It is therefore essential to consider the soil class (e.g., rigid soil, semirigid, or soft soil) to determine how seismic waves propagate and are transmitted to the structure.
- The bearing capacity of the soil and its elastic deformation to be determined while considering the interaction between the soil and the structure.
- The type of the soil to be modelled, since it may behave anomalously during an earthquake, negatively influencing the stability of the structure. In such cases, soil-structure interaction is critical and needs to be carefully considered.

Such theoretical guidelines characterizing the Part 5 of EN-1998, explained by means of proper formulations and mathematical expressions, contribute to properly model both the soil and the structures so that their interaction can ensure the safety and stability of structures themselves during an earthquake.

<u>Chapter 2: Seismic behaviour of underground structures</u>





3 Modelling methodology

As currently specified in the literature, numerical modelling appears an essential tool for academic and scientific purposes and to explain a project to stakeholders and the public in real-world applications.

Research on soil-structure interaction, among others, have been carried out for a long time by different approaches, such as analytical methods, laboratory measurements and, more recently, numerical modelling and hybrid experimental and numerical modelling.

Until the 1970s, the first two approaches (analytical solutions and physical modelling) were the only ones widely used. At that time, physical modelling techniques were widely used in different fields.

Since then, the great advances made in computer technology, especially since the 1980s, e.g., improving information processing and enabling large amounts of data to be stored, have made possible the use of mathematical models of greater complexity, leading to the widespread use of numerical modelling to the detriment of the other two approaches.

There are three important steps in the numerical modelling of any physical process: (i) problem definition, (ii) mathematical model, and (iii) computer simulation. The first natural step is to define an idealization of a problem of interest in terms of a set of relevant quantities to be measured. The second step of the modelling process is to represent such idealization of physical reality by a mathematical model, by means of the governing equations of the problem. After the selection of an appropriate mathematical model, together with suitable boundaries and initial conditions, one can proceed to its solution, as demonstrated in Péiro and Sherwin in [30].

Numerical models are even more useful the better they represent the real problem, but this is not always possible, due to lack of adequate instrumentation required for long simulations of large domains, so an increasing processing power of personal computers and the use of high-performance computer (HPC) facilities become an essential prerequisite.

In the present Chapter, an overview on the numerical modelling methodology, adopted for the present study, is described. More in detail:

- in Section 3.1 and its subsections, all the advantages and limitations offered by adopting a numerical modelling process, are presented, as well as all the phases underlying the execution of such a process are described. A focus on the issues related to soil-tunnels interaction has been reported, highlighting all the methods describing the possible approaches to be adopted to better understand such issues, up to focusing, in more detail, on the FEM methods adopted in the literature, as also illustrated in the previous chapter, and applied in the present study. Specifically, reference was made to the adoption of an FE software employed, called PLAXIS, showing its peculiarities, as well as describing the advantages and motivations inherent in the adoption of a further modelling methodology, namely the DRM, highlighting its potential applications.
- In Section 3.2 and its subsections, an overview on advanced modelling has been presented, focusing on the use of a software with high performance capabilities, namely Real-ESSI Simulator, showing its operation process and basic architecture, in terms of model conception and construction. Subsequently, a theoretical overview of the DRM methodology, as well as the application of this latter to the case study, were respectively presented, showing its peculiarities and subjecting the proposed model to a validation process aimed at highlighting the most powerful and useful features of DRM and demonstrating the correct implementation of the data necessary for the correct operation of the software.
- In Section 3.3, a theoretical overview on the Latin Hypercube Sampling technique, employed to adequately characterize the uncertainties treatment problem, was presented and described in

Chapter 3: Modelling methodology

more detail in chapter 5 where the results dictated by the application of this algorithm are shown.

3.1 Strategy of numerical modelling: issues and goals

The term "modelling" refers to a representation of a physical system, commonly undertaken by means of physical or numerical models. While physical modelling regards the experimental representation of a natural phenomenon usually at a smaller scale in a laboratory, numerical modelling is the mathematical representation of the physical processes included in a natural phenomenon, based on certain assumptions, as reported in Vyzikas and Greaves [31].

Since physical modelling is often limited to scaled models, whose results could contain uncertainties, the need for using sophisticated numerical tools have led to an increase in the application of numerical models for many problems which are generally not subjected to scaling effects. If compared to the physical model testing, the numerical modelling presents relevant strengths, such as a low cost, since costly facilities are not required, as well as the employment of a high density of flow field data capable of offering an integrated point of view of the problem examined. A weakness, on the other hand, could be represented by the lack of adequate instrumentation required for long simulations of large domains, so an increasing processing power of personal computers and the use of high-performance computer (HPC) facilities become an essential prerequisite.

Numerical modelling comprises three distinct steps (Figure 3.1.1):

• Step 1: a pre-processing phase includes all the necessary preliminary actions and decisions before executing a numerical simulation. It deals with the problem setting, by defining the geometry of the computational domain, the physical phenomena to be simulated and the numerical methods that will be employed for the discretization of the equations and the numerical solution. Once the geometry is accurately designed, it must be discretized into several computational nodes, by means of a mesh carefully generated. The number of nodes determines a computational cost related to the accuracy level to be achieved in a numerical simulation, so a computational mesh can be "structured", if it is characterized by a regular distribution of nodes in each axis, and "unstructured", if the

nodes are arbitrarily distributed in the domain. The solution of the interior domain is defined by governing equations, while at the borders and on the embedded structures in the domain, boundary conditions must be applied. These conditions are important as they establish the relationship between different variables in the surrounding and the internal boundaries of the computational domain. Similarly, initial conditions define the variables' values in the domain and on the boundaries at the beginning of the simulations. The correct definition of the boundary conditions is crucial for realistic simulations and accurate initial conditions can make the simulation more efficient.

- Step 2: in a modelling process, the governing equations represent a means with which physical phenomena are idealized through a mathematical model. After an appropriate selection of such model, together with suitable boundary and initial conditions, a numerical solution can be determined by introducing several discretization techniques. Listed below are the three classical methods:
 - The finite difference method (FDM), introduced by Euler in the eighteenth century, is because the time and space continuum have to be discretized into a finite number of discrete grid points. The value of a variable at a given point is calculated by a certain number of neighbouring points. Only one equation is solved per grid point with only one unknown variable, which is the same unknown variable at all the neighbouring cells. The accuracy of the FDM can therefore be first-order, second-order or higher depending on the omitted terms of the approximation. Additionally, the values of the variables can be computed at locations other than the grid points, by interpolation. Apart from accuracy, the FDM should be characterized by consistency, convergence and stability. Consistency requires the authentic representation of the governing equations by the FDM for capturing the physical behaviour of the problem.

Convergence refers to the ability of the FDM schemes to approach the true solution of the problem, guaranteed by continuous refinement of the mesh and decrease of the time step. Stability refers to the augmentation of errors in the numerical solution of transient problems that can 'blow up' the simulation, if the errors become larger than the actual computed values of the variables. This method can be applied on any grid, but it is mainly used for structured grids, because the regularity of structured grids facilitates the implementation of the FDM and makes it work very efficiently, while unstructured grids or complex geometries might raise important issues, making this method impractical for many practical engineering applications.

- The finite volume method (FVM) is a discretization method for solving the governing equations by transforming them into algebraic equations around a control volume, i.e. subdivisions of the computational domain that do not overlap. Each computational volume is represented by a computational cell, which has a node at the centre, where the variables are computed, and vertices and edges that connect it with the neighbouring cells. A considerable advantage of FVM is the ability to accommodate any type of grid, making it applicable for domains of high complexity.
- The finite element method (FEM) was historically used for structural and solid mechanics. In FEM, the computational domain is subdivided into several elements that are related to computational nodes. The characteristic distinguishing FEM from the other methods is that it employs variational methods in order to minimize the error between the approximated numerical solution and the true solution. In FEM formulation, differential-type boundary conditions for transient problems and algebraic type boundary conditions for steady-state problems can be considered. That makes the

Chapter 3: Modelling methodology

FEM very efficient, since it can incorporate higher-order accuracy, and it is flexible implementing different boundary conditions. Another important skill is to handle complex geometries, including structured or unstructured grids consisting of triangular or quadrilateral elements.

• Step 3: post-processing refers to the last step of numerical modelling, performed after the numerical computation is complete, and it is a crucial part of the numerical process, since it allows for visualization and interpretation of the results produced by the numerical model. Post – processing allows for better understanding the computational results thanks to informative and illustrative figures. The increasing availability of processing power and storage has led to the employment of more advanced solvers, complex mesh structures and the ability to handle millions of computational nodes per numerical simulation. In general, it represents an essential part of the numerical modelling procedure, so tools are being specifically designed to read complex data and visualize them in the most efficient way.

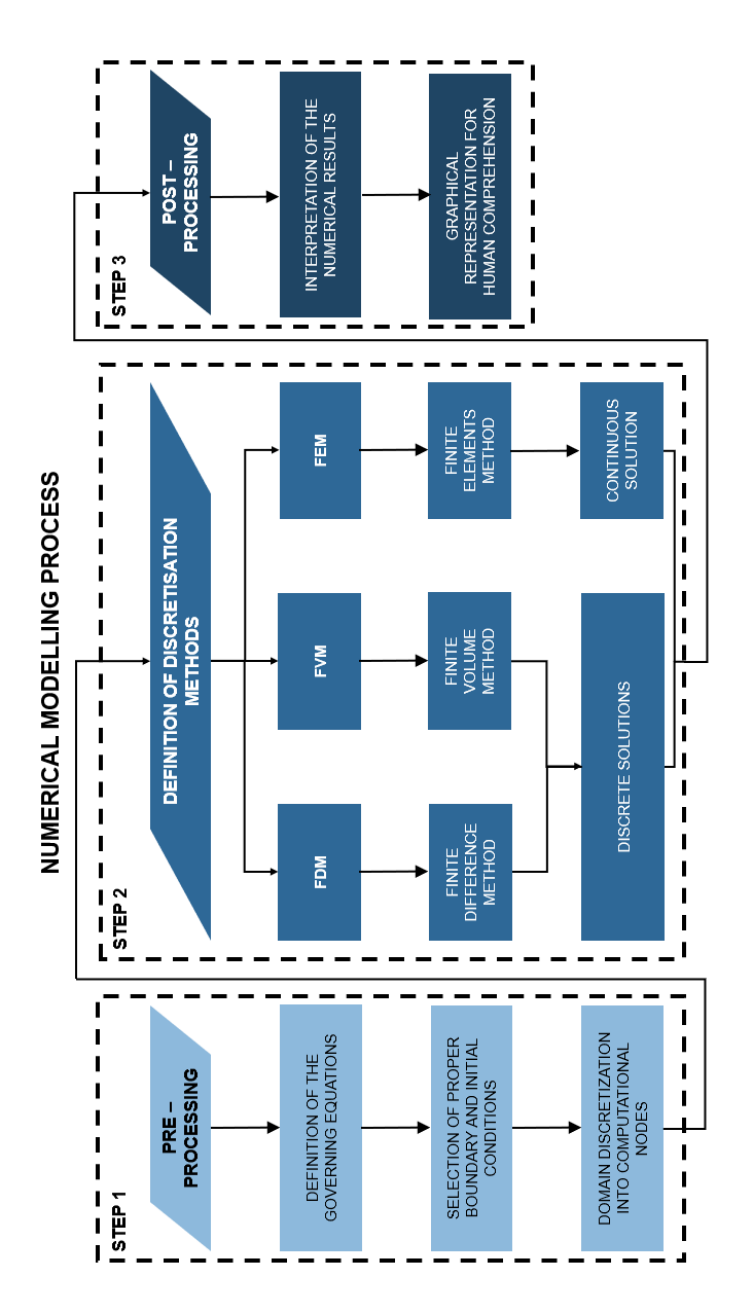


Figure 3.1.1 Numerical modelling process: flowchart.

3.1.1 Numerical modelling issues in soil-tunnel interaction

Soil-tunnel interaction phenomena involve several issues, starting from the excavation techniques, moving on the code regulations, empirical methods for preliminary analyses and to current numerical techniques for a detailed representation of all stages of such phenomenon (Figure 3.1.5), as reported in Terzi and Manolis in [32]

Empirical methods are based on observations and measurements, as directly experienced and transferred from one practitioner to another. They have important advantages such as simplicity, speed of execution and economy of use. Their application during the concept design phase must be always followed by regular inspection, as well as monitoring of deformations during tunnel construction. At the same time, it is necessary to consider some disadvantages such as the level of safety in the support design is unknown, there is little or no guidance on the appropriate timing of support installation, and the effects of natural or man – made adjacent structures are not considered. Empirical methods have historically been applied to more traditional construction processes, among which it is worth mentioning the New Austrian Tunnelling Method (NATM), as described in Karakus and Fowell in [2].

On the other hand, the soil-tunnel interaction study can be further addressed by the application of closed – form analytical methods that are generally two-dimensional idealizations. In this perspective, the choice of employing a continuum or discontinuum-based approach is mandatory.

Continuum methods provide information regarding the stress and strain field created after the excavation and lining of a hole in a stressed continuum. The distribution of both stresses and strains around a tunnel assumed to be infinitely long, and the related displacement field, can be easily derived for a medium by the elastic behaviour, by means the primary basic assumptions: (i) circular tunnel cross-section; (ii) uniform state of stress; (iii) plane stress conditions (considering tunnel sections far from the tunnel face); (iv) initial isotropic state of stress; (v) elastic lining; (vi) absence of slipping between soil and tunnel. These conditions are characterized by axial symmetry, and the state of stress/strains of any point around a tunnel depends only on the radial distance r from the tunnel centre (Figure 3.1.2). To also consider the non-linearity of the mechanical behaviour of soils, as well as an elastic-perfectly

plastic of the medium, the available continuum analytic models contemplate other assumptions such as geometrical non-linearities, pore-pressure changes, non-circular tunnels and arbitrary cross-sections.

One of the most popular analytical methods is based on the convergenceconfinement (GRC) describing the response of the rock / soil domain during the tunnel excavation, as well as the interaction between rock / soil and temporary or permanent support [28]. By considering a deep circular tunnel, constructed by using full-face excavation techniques, under plain strain asymmetric conditions, a hydrostatic fictitious pressure q_t is applied to the inner contour of a circular tunnel to account for the excavation advancement. It depends on the distance from the tunnel face and on the strength properties of the ground and can be defined as a percentage of the natural state of stress S, assumed isotropic, through so-called "stress release factor" λ. The presence of a circular support, installed at a certain distance from the tunnel face and progressively loaded by the stress release of the ground by a pressure applied at its extrados, can be also accounted for. In the convergence-confinement, two curves are defined, given respectively by the relationship between the applied fictitious pressure q_t and the radial displacement u_r at the tunnel inner contour, and the support reaction curve (SRC) expressing the relationship between the pressure applied at the lining extrados and the corresponding radial convergence. The solution to the soil-tunnel interaction is obtained in a simplified way by imposing equilibrium and compatibility between the two subsystems and is provided graphically by the intersection of the two curves in the plane q_t - u_r . By means of this intersection, the equilibrium of the tunnel / lining is achieved: as evident in Figure 3.1.3, the higher the stress release at the time of support installation (i.e. the distance of the tunnel face when the support is installed), the lower is the pressure on the support and the higher is the final tunnel convergence. The stand-up time, the admissible convergence and the maximum pressure admissible on the support to guarantee it reacts elastically must be accounted for when choosing the installation time.

The GRC is linear for an elastic medium, while in case of elastic – plastic materials, it is composed by a first linear elastic branch, followed by a non-linear one, associated with the development of irreversible strains.

For SRC, a typical linear elastic relation is represented by:

$$q_t = k_s \cdot \left(\frac{u_r}{r_0} - \frac{u_0}{r_0}\right) \tag{12}$$

where k_s is the equivalent radial support stiffness, r_0 is the tunnel radius, and u_0 is the tunnel convergence that already occurred at the instant of time of lining installation.

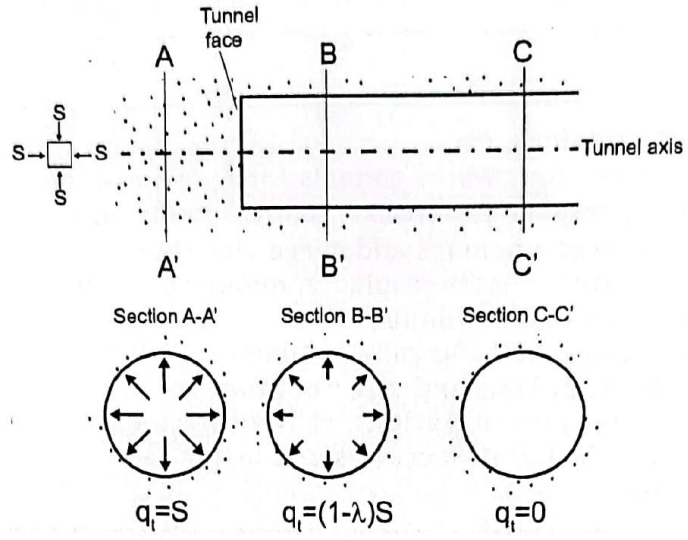


Figure 3.1.2 Stress release factor as a function of the distance from tunnel face [28].

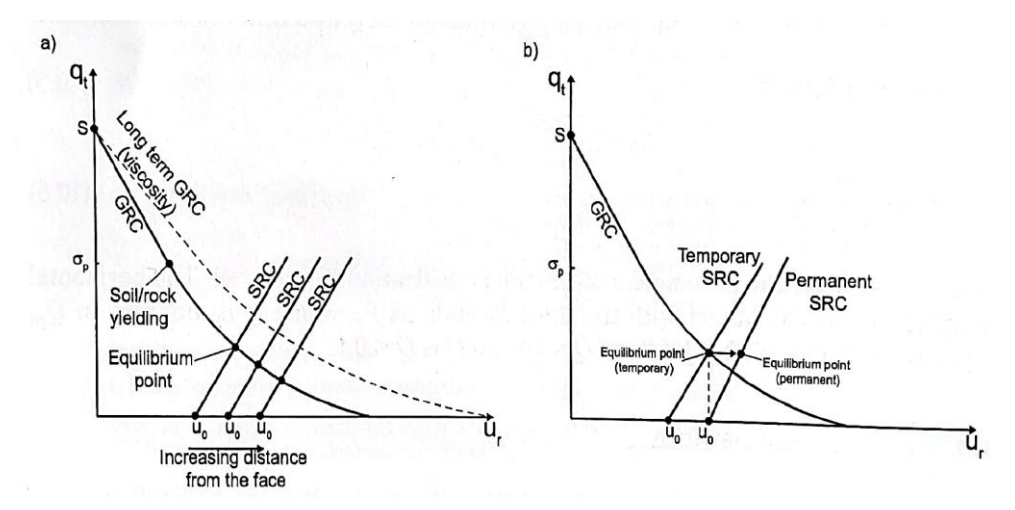


Figure 3.1.3 a) Convergence-confinement method; b) temporary and permanent lining [28].

In presence of discontinuities systems in rock mass which can originate potential unstable rock blocks, the design of stabilizing support (rock bolts and shotcrete) can be based on a LEM analysis, i.e. in adopting the limit equilibrium method. It is a simplified approach aimed at the assessment of a safety factor related to the probability for the system to fail. It is a function of geometry, mechanical properties and hydraulic conditions. The first step of LEM is the definition of a set of failure mechanisms, consisting in rigid blocks interacting along interfaces, where plastic strains develop. For each mechanism, the factor of safety is determined by imposing the balance of momentum and by introducing the safety factor as a reduction coefficient to the material shear strength necessary to reach failure conditions. Among all these calculated values, the best approximation of the system factor of safety is the minimum one.

To correctly model complex structures, geological conditions, constitutive behaviour and construction sequences, numerical approaches, as FEM (Finite Elements Method) and FDM (Finite Difference Method) can be employed. These methods can simulate, under bi-dimensional and tri-dimensional conditions, the tunnel support by employing structural elements such as beams and shells located all around the excavation boundary. Numerical analyses provide the state of stress induced by the ground in the lining, in terms of axial thrust (N), shear force (V) and bending moment (M) values (Figure 3.1.4), taking rigorously the ground response to both boundary conditions and time effects into account, as well as are capable of dealing with material and geometrical non – linearities which determine the mechanical behaviour of the soil-tunnel system [32]. In 2D analyses, the stress release at the time of support installation (both temporary and permanent linings) is obtained by using the GRC.

The selection of numerical methods of analysis depends on various factors, such as: (i) software availability; (ii) type of soil medium; (iii) analysis stage (preliminary or design); (iv) data availability. By focusing on the choice of FEM software, as described in the next chapter, PLAXIS represents a useful tool with which different stages can be modelled and the stress release along the excavation boundary is simulated as a function of tunnel advance and excavation sequences. In this context, the presence of a first-phase lining is usually neglected when the final lining is installed, and this is numerically simulated by deactivating the first-phase lining in the stage in which the

secondary one is activated. Whatever the method used for estimating the stresses induced in the support by the ground is, their compatibility with the mechanical characteristics of the support must be verified according to the current regulations (See Chapter 2).

Based on the above, tunnel design is a challenging task, which is best addressed by the combined implementation of empirical, analytical and numerical methods, each with its own strength and limitations.

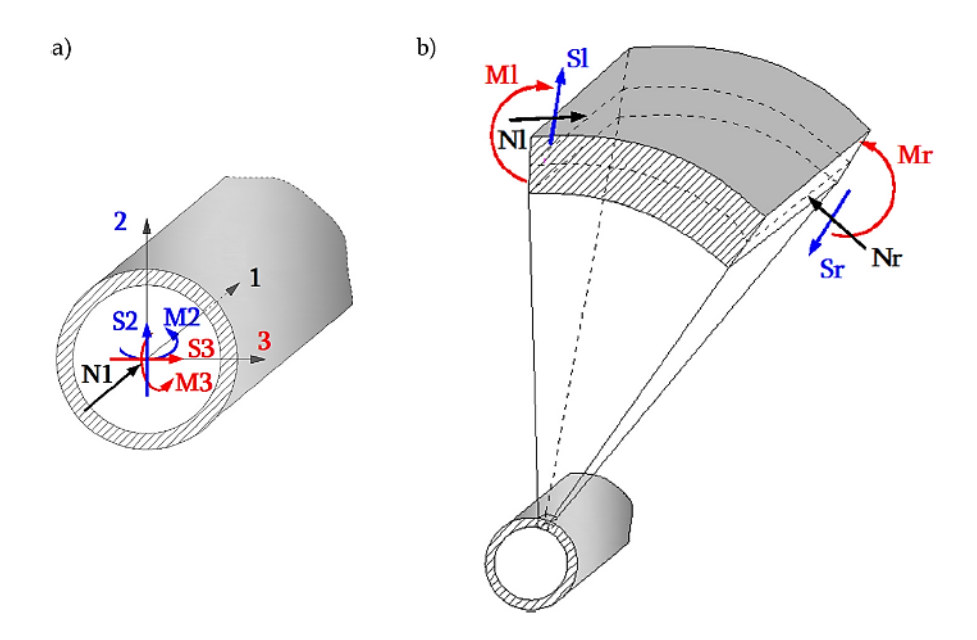


Figure 3.1.4 Example of distribution of axial thrust, shear force and bending moments in a tunnel segment [32].

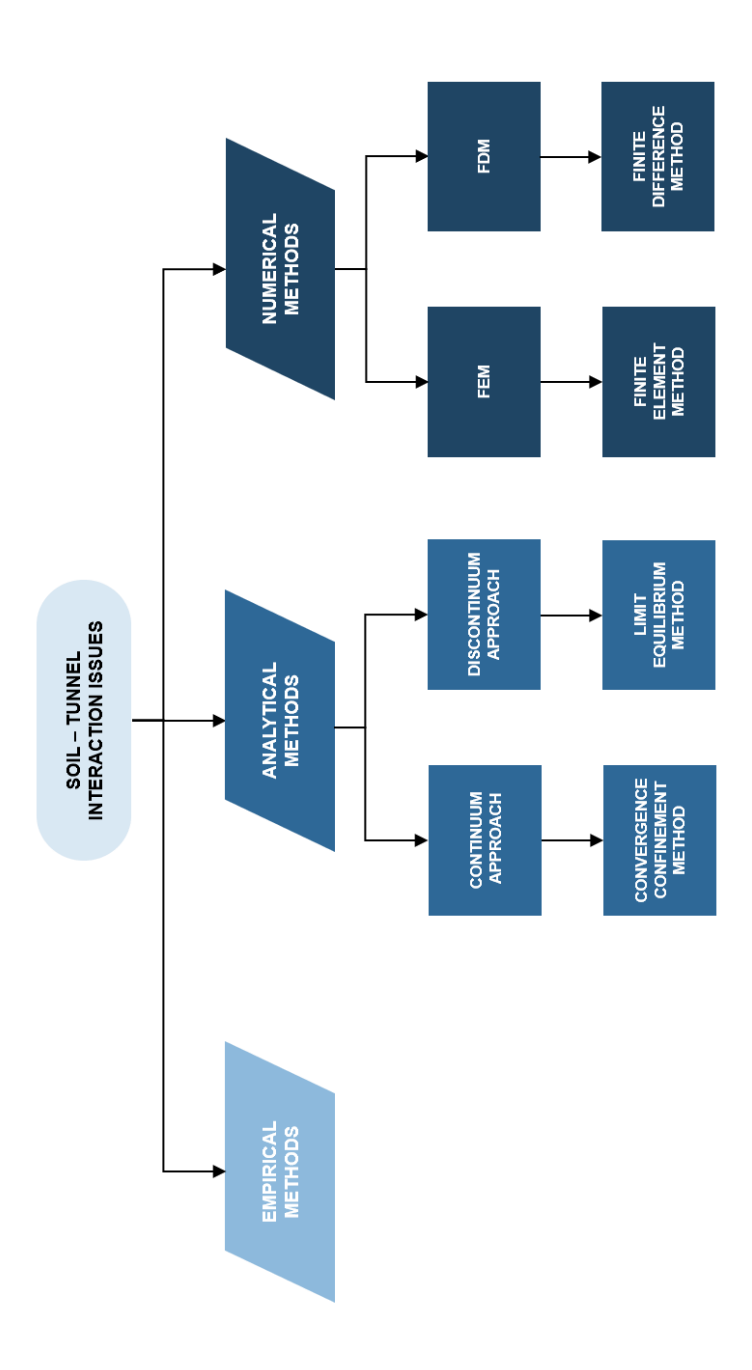


Figure 3.1.5 Modelling strategies for soil-tunnel interaction issues.

3.1.2 Finite Element Modelling (FEM)

Based on what was highlighted in Chapter 2, the use of FEM codes has become very common. The most widely used software in several applications in the literature is PLAXIS, a Finite Elements software package for two- or three-dimensional analyses of deformation, stability, dynamics and groundwater flow in geotechnical engineering and rock mechanics, as carefully described in Brinkgreve in [33] and [34].

The input of soils and structures data, as well as construction stages, loads and boundary conditions are based on CAD drawing procedures, which allows for a detailed modelling of the geometry. While soil layers are modelled by means of boreholes, plates or shell elements can be employed to model structures embedded in the ground, and their mechanical behaviour may be chosen with respect to the degree of accuracy to be reached.

The mechanical behaviour of soils may be modelled as much with simple stress-strain relationships, as the Hooke's law of linear and isotropic elasticity, as more advanced models, such as the linear elastic perfectly plastic model knows as Mohr-Coulomb model, as described in the previous chapter, and other material models involving specific features such as stress – dependency of stiffness, strain – hardening/softening, anisotropy, creep, in order to simulate soils behaviour more realistically.

One of them, employed for the studies present in this thesis, is the Hardening Soil model with small – strain stiffness (HS-small) (Figure 3.1.6). This model is based on the PLAXIS Hardening Soil model, extended with an elastic overlay model to take into account the high stiffness at small strain levels. More in detail, the small – strain formulation comes from modulus reduction curves where a shear modulus, G, is plotted as a logarithmic function of the shear strain, γ , ranging from very small strain levels (vibrations) up to large strain levels, so with increasing strain amplitude, soil stiffness decays nonlinearly (Figure 3.1.7). The use of this model involves the addition of two parameters are needed to describe the variation of stiffness with strain, i.e. the initial or very small – strain shear modulus G_0 , and the shear strain level $\gamma_{0.7}$ at which the secant shear modulus G_s is reduced about 70% of G_0 . G_0 value generally ranges from around 10 times G_{ur} for soft soils, down to 2.5 times G_{ur} for harder types of soil, where:

Chapter 3: Modelling methodology

$$G_{ur} = E_{ur}/(2(1+v_{ur}))$$
 (13)

As the HS-small model is an overlay model, the tangent shear modulus is bounded by a lower limit, G_{ur} , of the original HS model. When combined with the HS model, the apparent shear modulus will reduce further due to plasticity.

As for the original HS model, plasticity occurs due to an isotropic shear hardening surface and an isotropic cap hardening surface.

The decay of the secant shear modulus depends on the amount of shear strain, and a good approximation is given by the Hardin-Drnevich relationship, proposed in [35]:

$$G_s = \frac{G_0}{I + |\frac{\gamma}{\gamma_r}|} \tag{14}$$

Where the threshold shear strain γ_r is quantified as:

$$\gamma_r = \frac{\tau_{max}}{G_0} \tag{15}$$

With τ_{max} being the shear stress at failure. More straightforward and less prone to error is the use of a smaller threshold shear strain. Gomes Correia et al. in [36] suggest using the shear strain $\gamma_r = \gamma_{0.7}$ at which the secant shear modulus G_s is reduced to about 70% of its initial value. Eq (14) can be rewritten as:

$$G_s = \frac{G_0}{I + \alpha \left| \frac{\gamma}{\gamma_0} \right|} \tag{16}$$

Where $\alpha = 0.385$.

When subjected to cyclic shear loading, the HS – small model presents a typical hysteretic behaviour, as showed in Figure 3.1.8. Starting from the small-strain shear stiffness, G_0 , the actual stiffness will decrease with increasing shear strain. Upon load reversal the stiffness will restart from G_0 and will decrease again until the next load reversal, according to Brinkgreve et al. in [37]

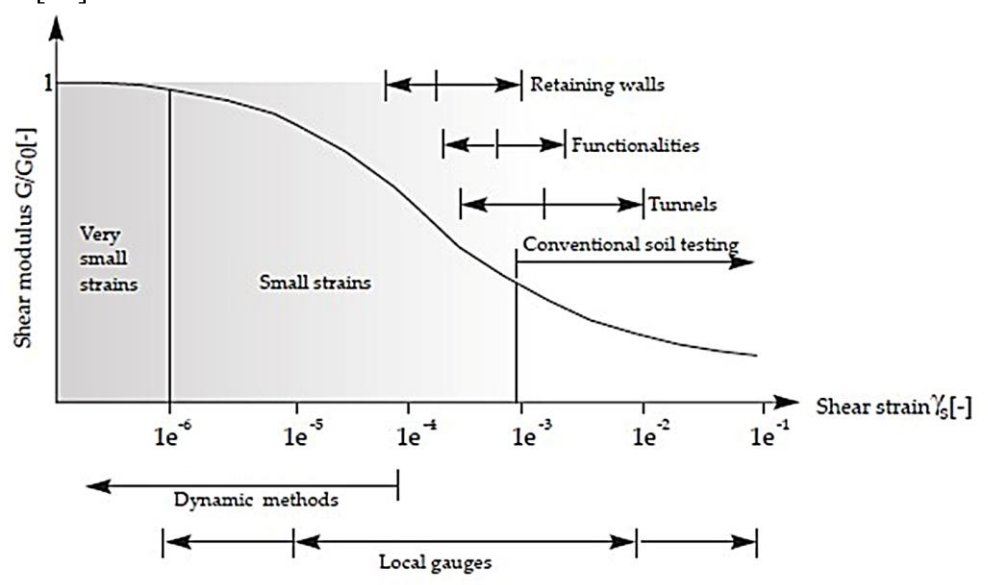


Figure 3.1.6 Characteristic stiffness – strain behaviour of soil with typical strain ranges for laboratory tests and structures [38].

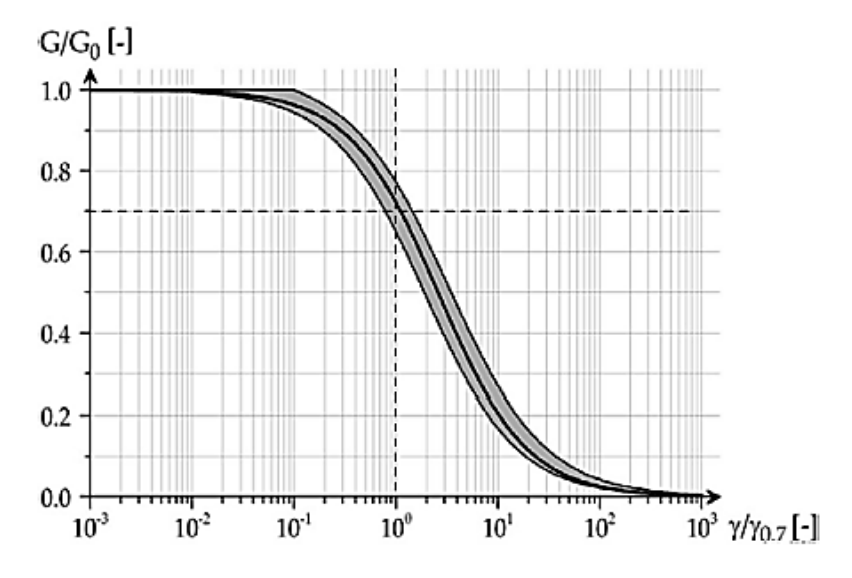


Figure 3.1.7 Reduction of secant shear modulus with shear strain [36].

The hysteretic damping ratio in the HS-small model only applies if the material behaviour remains elastic, and the shear modulus decreases according to the small-strain formulation. As soon as G_{ur} is reached the damping does not further increase. On the other hand, as soon as (hardening) plasticity occurs, the observed damping will further increase.

By considering the damping ratio as a function of the cyclic shear strain γ_r for different values of $\gamma_{0.7}$ and different G_0 / G_{ur} ratios, a lower $\gamma_{0.7}$ gives more damping, or damping occurs at smaller shear strain. A variation of G_0 / G_{ur} only leads to a different maximum damping ratio, regardless the selected value of $\gamma_{0.7}$. When the difference between G_0 and G_{ur} (i.e. the difference between the upper bound and lower bound G-value) is larger, the maximum damping is also larger. Since damping ratio is purely based on the stress-strain relationship, it is independent from the loading frequency, so time-independent.

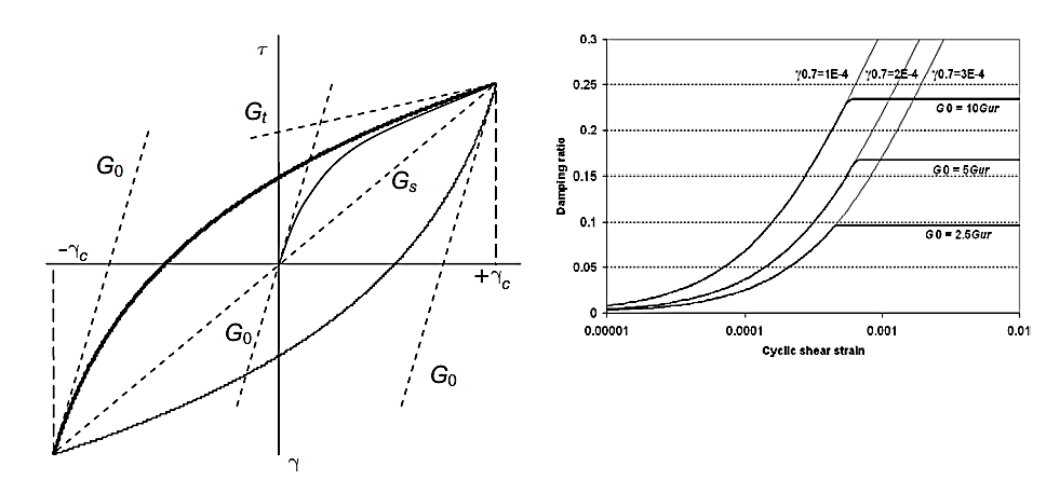


Figure 3.1.8 HS – small model: hysteretic behaviour (on the left) and damping ratio evaluated as a function of cyclic shear strain (on the right) [37].

Besides the hysteretic material damping, it can be modelled in general by means of Rayleigh damping (Figure 3.1.9). This latter provides additional viscous damping, since it contributes to the velocity term in the dynamic equation by taking a portion of mass ($\alpha_R M$) and a portion of stiffness ($\beta_R K$), where M is the mass matrix, K is the stiffness matrix and α_R and β_R are the Rayleigh coefficients:

$$[C] = \alpha_R [M] + \beta_R [K]$$
 (17)

When using HS-small model, the amount of damping that is obtained depends on the amplitude of the strain cycles. Considering very small vibrations, such model doesn't show material damping as well as numerical damping, whereas real soils still show a bit of viscous damping. Hence, additional damping is needed to model realistic damping characteristics of soils in dynamics calculations. In contrast to hysteretic damping, Rayleigh damping is frequency dependent. Hence, before selecting the Rayleigh

coefficients to arrive at a particular damping ratio, a range of target frequencies must be selected in accordance with the natural frequency of the system and the dominant load frequency.

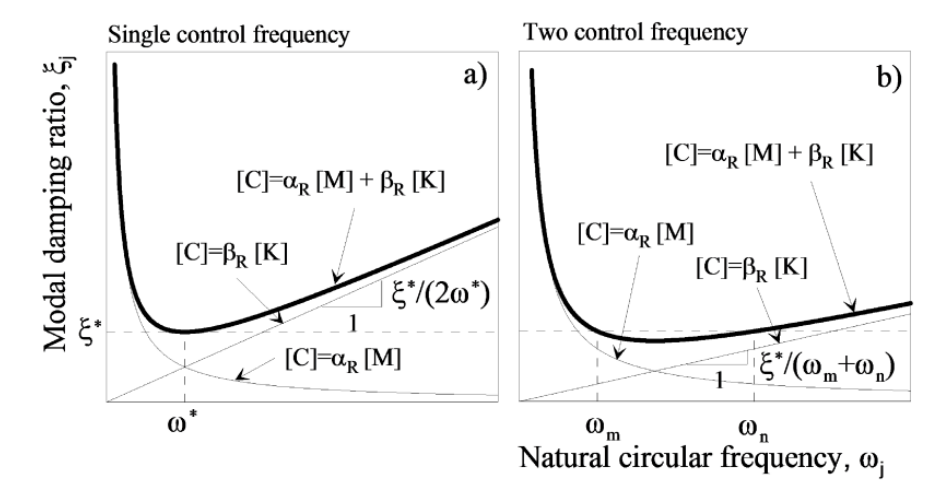


Figure 3.1.9 Rayleigh damping formulations with (a) single control frequency and (b) two control frequencies [39].

Once the geometrical process is complete, one can proceed with the generation of a mesh and definition of the construction stages.

For a numerical stability of the calculation, mesh must have a good quality, reached via accuracy that is proportional to the number of elements introduced into the discretization. The accuracy of the solution is obtained by considering a correct size of the finite elements: they should be small enough, especially in those areas where significant changes in stress or strain can be expected during the analysis, calibrating adequately a coarseness factor, but this will lead to a very large calculation time. A general rule for optimizing discretization, as stated in U. Carmando et al. in [40], is to provide three to four points to describe the semi-wavelength of vibration of an element of thickness h and velocity V_s . This condition implies that if f_{max} is the maximum significant frequency of the seismic input, the maximum thickness h_{max} to be assigned to the element must be:

$$h_{max} = \frac{\lambda}{6 \div 8} = \frac{V_s}{(6 \div 8) f_{max}} \tag{18}$$

In PLAXIS, different types of loads could be defined to represent a determined load level in each construction stage, within the staged construction phase, to adequately simulate the material removal by progressively decreasing both the stiffness and the weight of the excavated material, so at the end of the process, the corresponding elements can be "switched off".

For the case study, the NATM method was employed to simulate the construction process of the tunnels with a sprayed concrete lining. The major point in such an analysis is to account for the three-dimensional arching effect that occurs within the soil and the deformations that occur around the unsupported tunnel face. More in detail, the so-called convergence confinement method or β -method (Figure 3.1.10), according to which the initial stresses p_k acting around the location where the tunnel is to be constructed are divided into a part $(1-\beta)$ p_k that is applied to the unsupported tunnel and a part β pk that is applied to the supported tunnel. The way this process works in PLAXIS is:

- Phase 1: an initial stress field is generated and eventual external loads, that are present before the tunnel is constructed, are applied.
- Phase 2: by considering a tunnel with different excavations sections, each excavations section may have a different level of deconfinement, so without the activation of the tunnel lining, each tunnel clusters are de -activated and a deconfinement value of $1-\beta$ can be applied.
- Phase 3: For each soil cluster inside the tunnel, the lining must be activated, checking that the deconfinement of the soil clusters is set to 100%.

Chapter 3: Modelling methodology

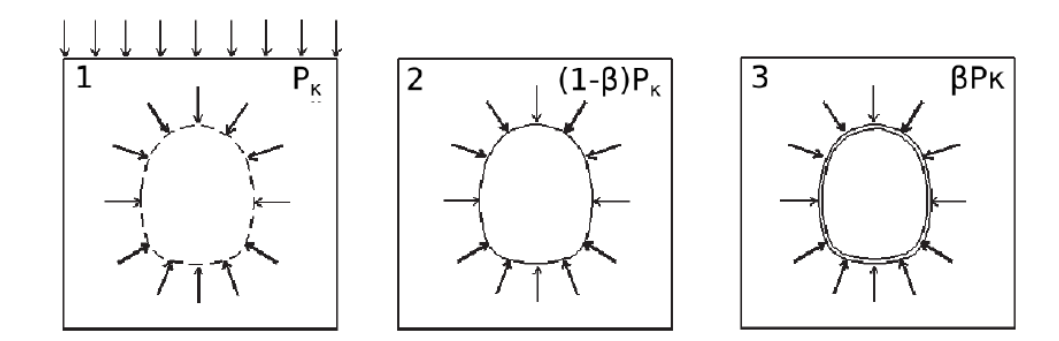


Figure 3.1.10 Schematic representation of the β -method for the analysis of NATM tunnels in PLAXIS software [33].

3.2 Advanced Modelling

In engineering practice, the modelling process is a key step in understanding and subsequently solving real problems. Proper execution of such process, as measured by a high degree of fidelity in the results resulting from the analyses performed, goes through adherence to a hierarchy of sophistication of a model, so to gain a better understanding of model behaviour, the transition from simple to more sophisticated models is highly encouraged.

In this context, Real-ESSI Simulator, as stated in Jeremic et al. in [41] allows analysis of a full hierarchy of models, from very simple 2D models to very sophisticated 3D models. For example, a building model can start as a simple beam or a simple frame on a fixed base. Next, an analyst can add wall, plate and shell elements, and later springs for foundation modelling, all linear elastic. Next, material models for parts of the soil-structure system could be changed from a linear elastic to nonlinear, inelastic behaviour, and simple loads could be applied to test the model.

By increasing step by step the level of detail, a good level of understanding of the model behaviour, as well as a sensitivity of model response to various simplified or sophisticated modelling options, various material behaviour, various loads, will be reached. It can happen, in fact, that the use of very sophisticated models, without model verification and gradual understanding of model behaviour through an adequate hierarchy, lead to results that are difficult to understand and that can sometimes be wrong due to use of wrong modelling details. Potential errors can be due to approximations and simplifications that must be understood before simulation results can be used for design and assessment. Finally, once the analyst has fully mastered all the intrinsic aspects of modelling, a sophisticated, realistic model, with realistic loading, using all the available Real-ESSI Simulator modelling and simulation features, will be employed.

3.2.1 Real – ESSI Simulator: a framework

The Real-ESSI Simulator (Realistic, Modelling and Simulation of Earthquakes, and/or Soils, and/or Structures and their Interaction) is a powerful FE software developed by University of California, Davis, US, in the person of Prof. Boris Jeremic, and has been conceived with the aim of characterizing not only the design and the assessment of the static behaviour of civil engineering objects, including buildings, bridges, roads, dams, power plants, tunnels, but also to perform dynamic simulations with high computational costs when they are excited by seismic inputs, in order to understand how much these structures are influenced by the behaviour of the surrounding soil and, therefore, accurately predict the dynamics of the soil-structure interaction systems [41].

A domain specific language (DSL) described by Abell et al. in [42] is appropriately designed with a primary goal of developing FEA models and interfacing them with various Real – ESSI functionalities. More in detail, all base variables are implemented as physical quantities, that is, all variables have a unit associated with it, except for those variables which have no relevant unit. This unit awareness approach provides an additional layer of security to FEA calculations forces to carefully think about units.

A targeted study of this software for understanding the underlying architecture has been done at CERN, by exploiting the high-performance computing resources available there and correctly employing a WSL (*Windows Subsystem for Linux*), a compatibility system thanks to which one can work in a non-isolated "parallel" Linux environment.

Real - ESSI execution process is divided into three main phases:

• Pre – processing defined by Sinha et al. in [43] (Figure 3.2.1): a geometric model was developed by Gmsh, a finite element mesh generator in which a *.geo* file is initially provided by defining all the geometric characteristics in terms of points, lines, surfaces and volumes. Subsequently they were imprinted in a *.msh* file, with which a regular mesh has been created by employing 8 – node – brick elements and converted from Gmsh to Real – ESSI DSL format in *gmESSI*, an efficient pre-processing tool, with the primary aim of making Gmsh with various Real-ESSI functionalities. The

translator basically provides some strict syntax for naming physical and entity group concept of Gmsh which provides *gmESSI* information about the elements or (nodes) on which the translation operates (Figure 3.2.2). The size of the mesh elements varies between 3 and 4 m: this variability is related to geometric modelling and is compatible with the frequency content of the accelerograms employed for subsequent analyses.

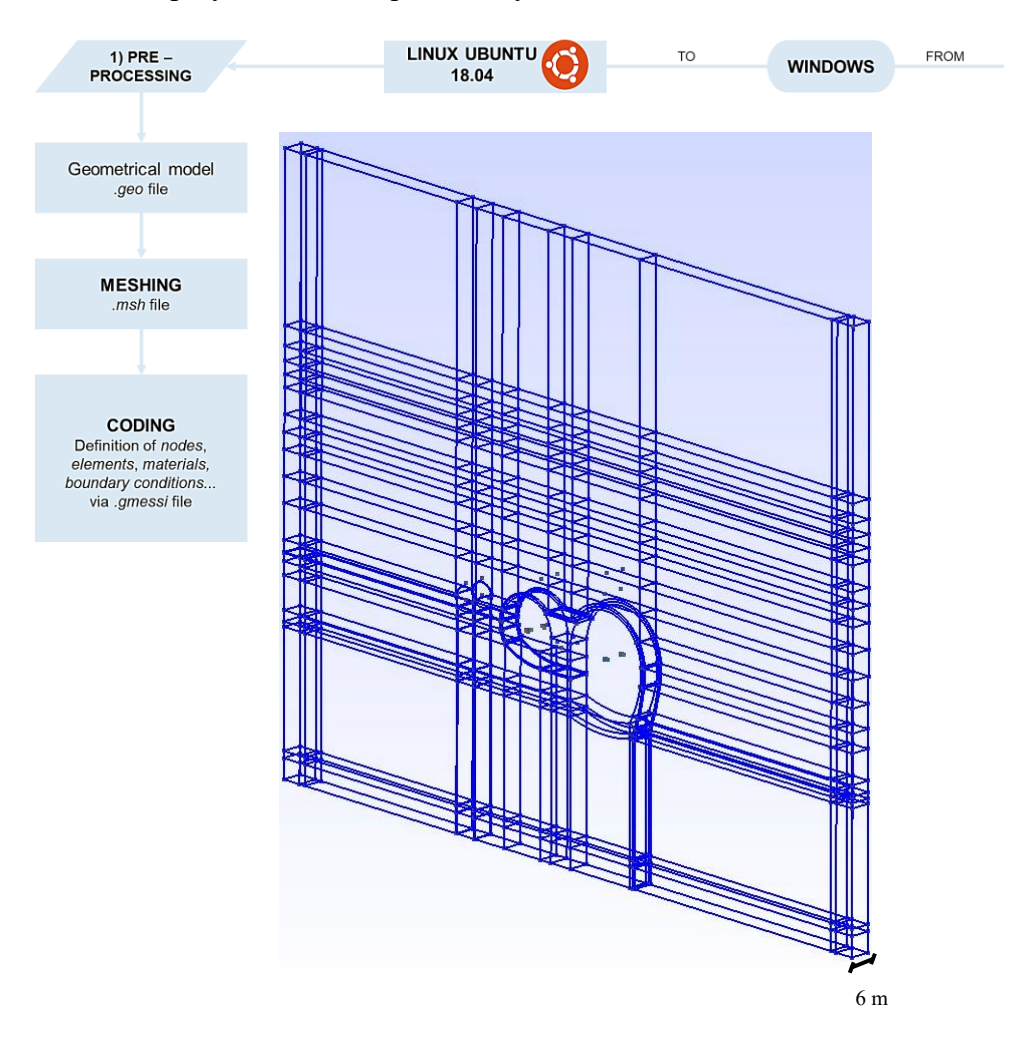


Figure 3.2.1 Real-ESSI Simulator: 3D slice model realized in Gmsh.

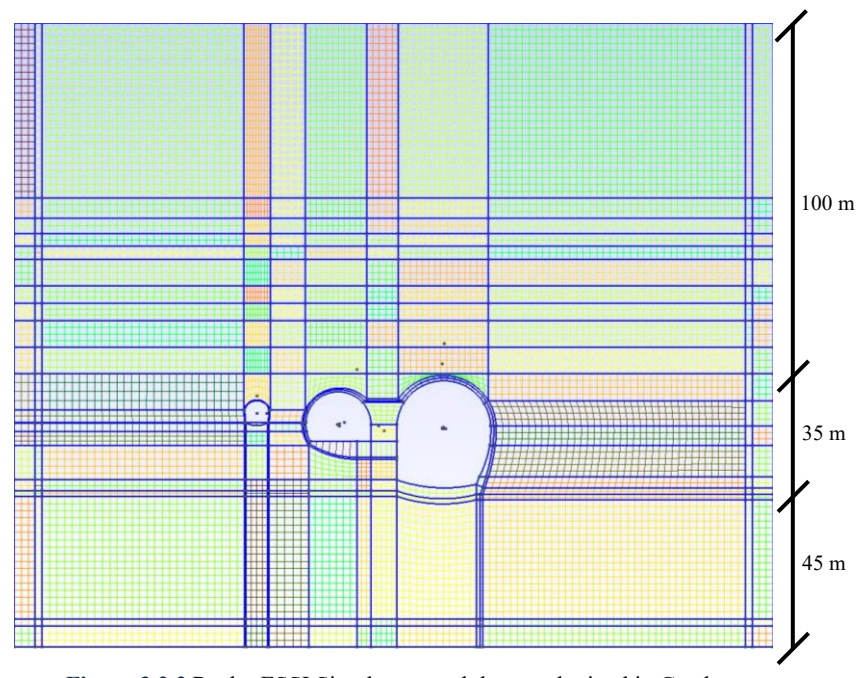


Figure 3.2.2 Real – ESSI Simulator: mesh layout obtained in Gmsh.

WSL (Figure 3.2.3): in the second phase, once *gmESSI* translated the commands operated on mesh (.msh) file to different ESSI input containing some important information mainly regarding model's statics, by means of (node, element, load, main, damping, boundary conditions, wave field, materials) (.fei) files and once put them in the user-defined directory, including mesh (.msh) file, all the commands regarding the definition of the static and dynamic phases, more specifically parameters such as the self-weight to be considered, the Rayleigh damping, the numerical damping provided by the Newmark integrator, were defined in the main.fei file and the analysis has been started. At the end of the simulation, output files with .feioutput extension were produced for each analysis stage and contain the information about the model mesh, nodal displacements, elements output, boundary conditions, material tags (Figure 3.2.4).

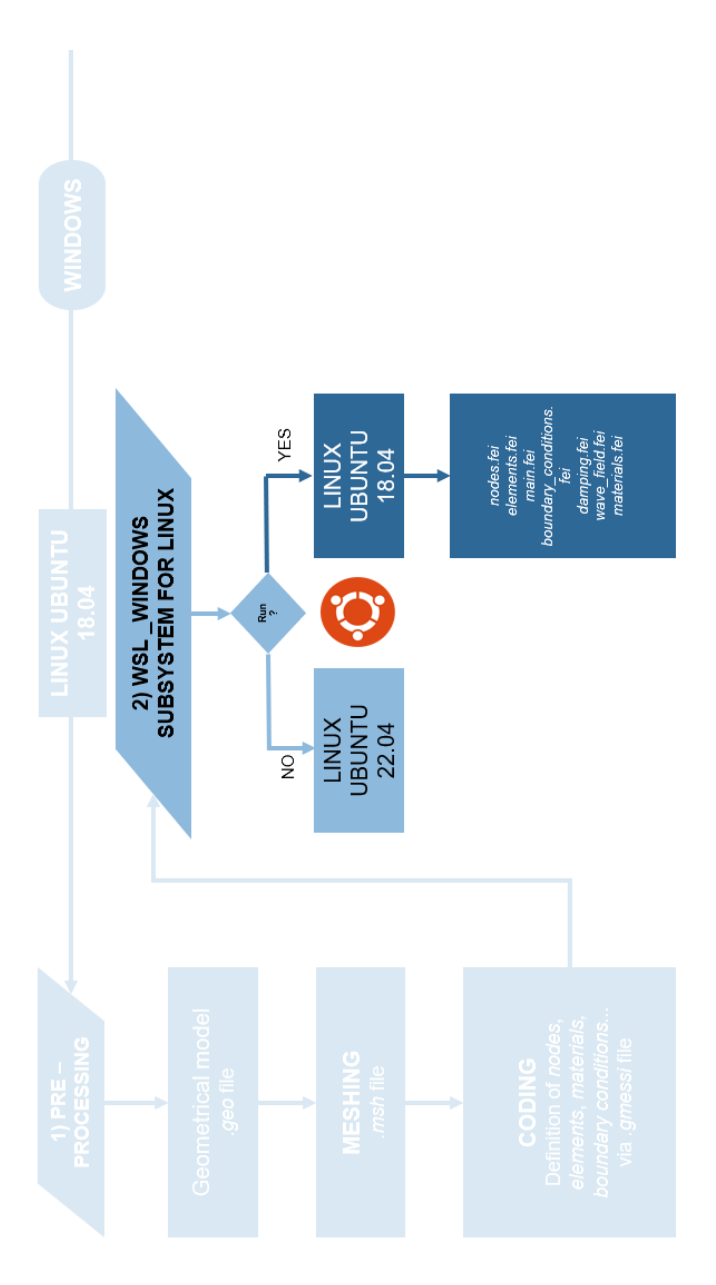


Figure 3.2.3 Real-ESSI Simulator: Windows Subsystem for Linux.

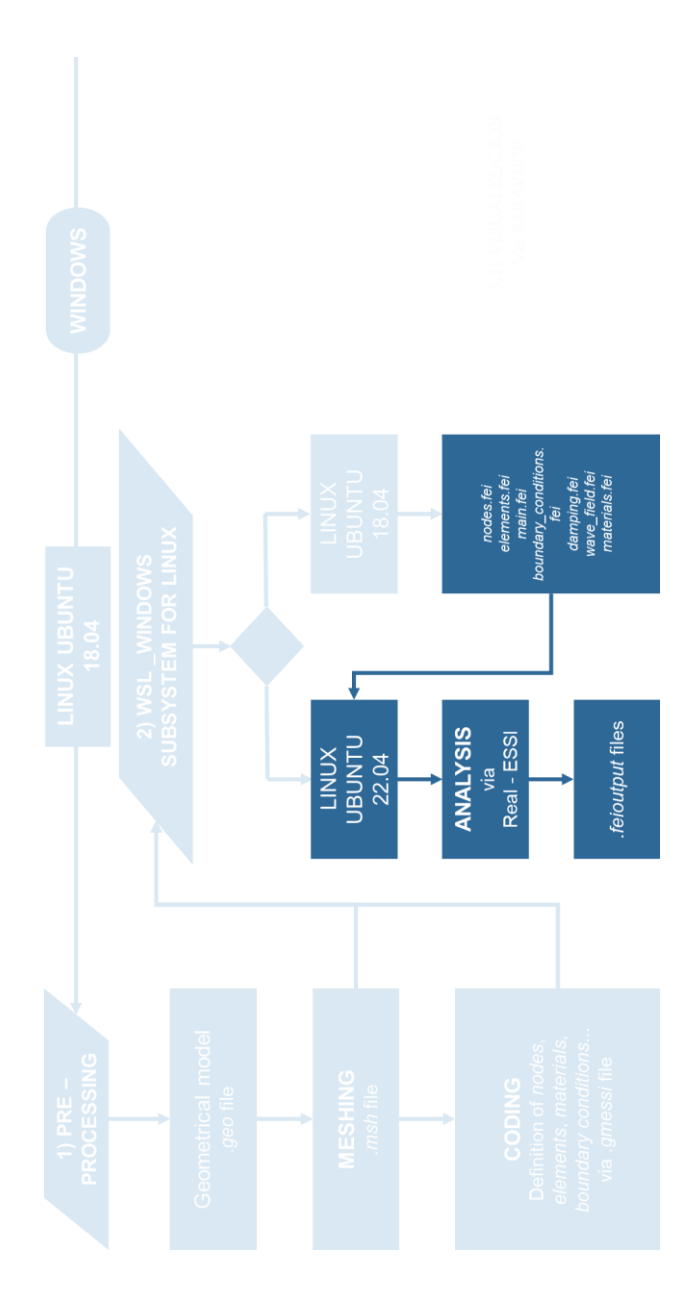


Figure 3.2.4 Real-ESSI Simulator: analysis phase.

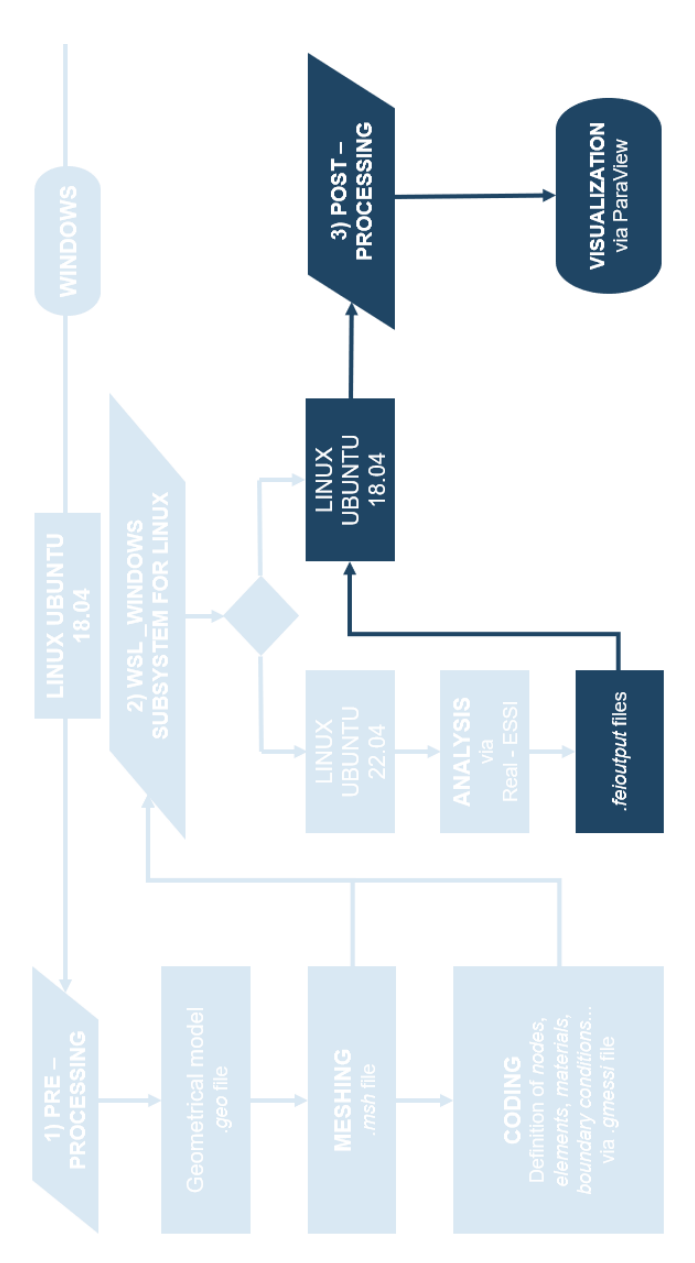


Figure 3.2.5 Real-ESSI Simulator: Post-processing phase.

• Post-processing [44] (Figure 3.2.5): once output files were produced, a powerful multi-platform data analysis and visualization program available as an open source, named ParaView, has been employed to visualise results, by means of *PVESSIReader*, a plugin that integrates Real-ESSI Simulator output to ParaView for visualization (Figure 3.2.6). It has several visualization features to visualize stresses, eigen modes, relative displacements, boundary conditions.

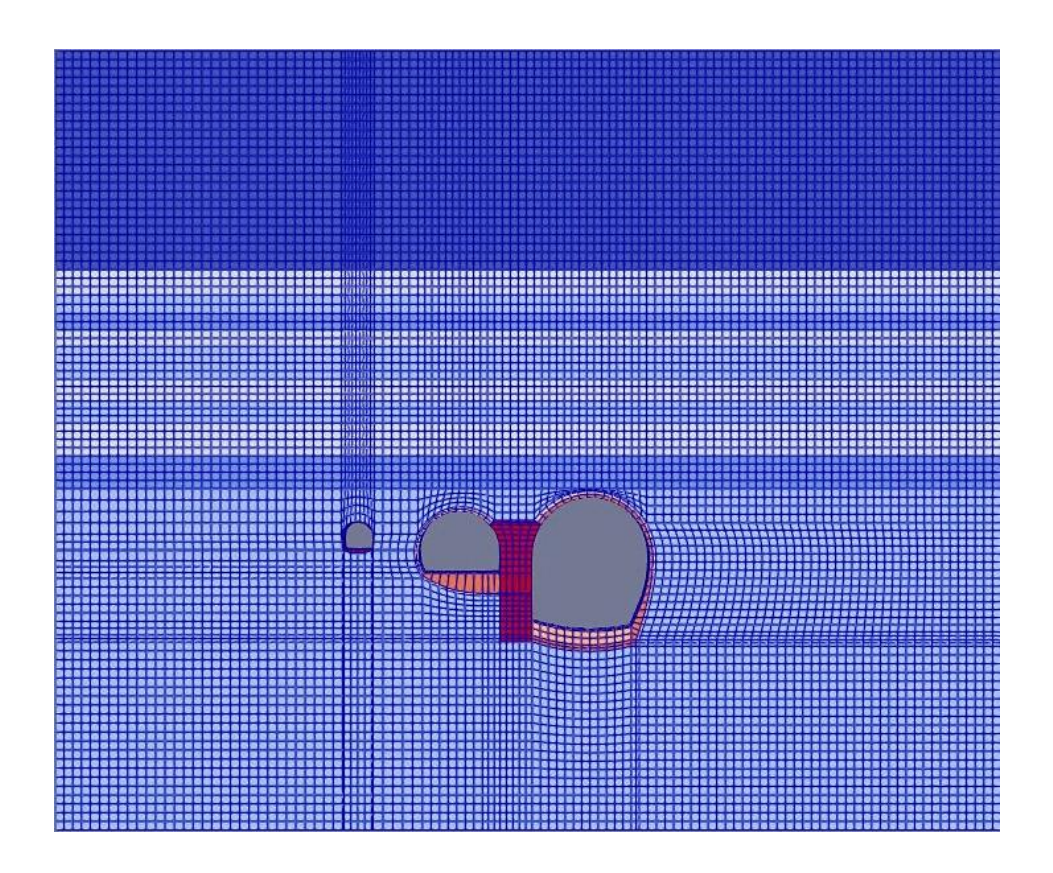


Figure 3.2.6 Real-ESSI Simulator: Post-processing results visualized in Paraview.

3.2.2 The Domain Reduction Method (DRM)

A summary explanation according to Bielak et al. in [45], Yoshimura et al. in [46] and in [41], for better understanding the main Domain Reduction Method features, is reported below.

DRM was conceived as a procedure aimed at reducing a large computational domain, encompassing fault, rock, soil and the structure, to a much smaller domain, encompassing only local soil and the structure.

The formulation of this method concerned the treatment of a problem in which a semi-infinite seismic region containing localized geological features such as sedimentary valleys and ridges as well as seismically active faults, under earthquake excitations, was considered. The source of disturbance is a known time history of a force field $P_e(t)$ and is far away from a local feature which is dynamically excited by $P_e(t)$ (Figure 3.2.7).

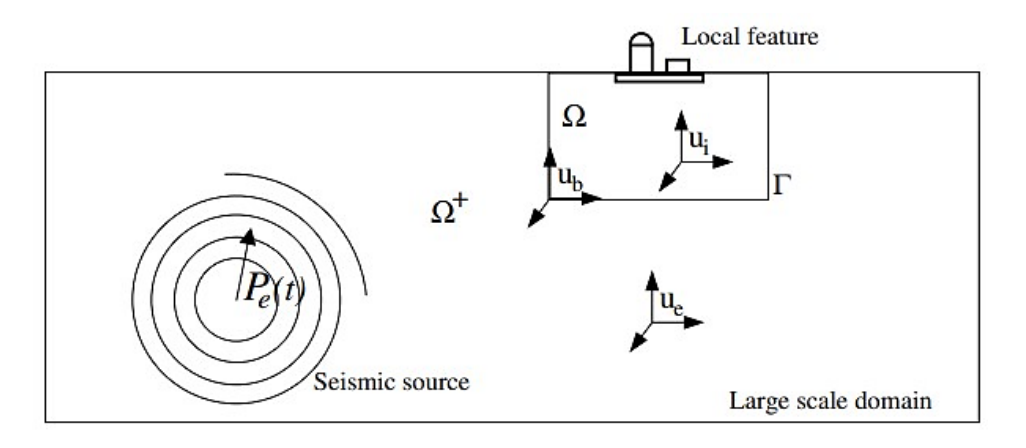


Figure 3.2.7 Large physical domain with the source of load Pe(t) and the local feature (soil – foundation – structure system) [41].

Since analysing the soil-structure interaction of a large seismo-geological model would require great computational efforts, the problem could be solved by understanding how a smaller zone around the local feature of interest can be separated from it, in such a way that the seismic excitation effects are limited in that zone. In order to propagate consistently the dynamic forces $P_e(t)$, a simple domain with Γ boundary needed to be considered, that is the influence of local feature (bridge, building, tunnel) is temporarily taken out and has to be replaced with a much simpler geometry and material (Figure 3.2.8).

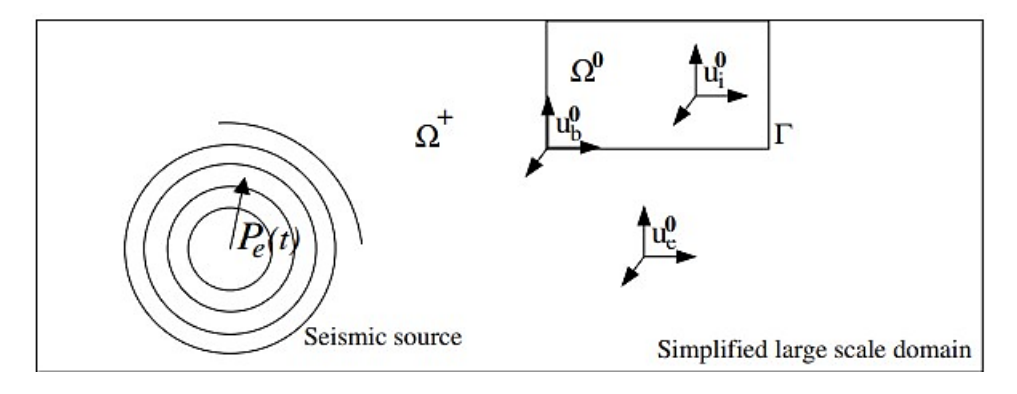


Figure 3.2.8 Simplified large physical domain with the source of load Pe (t) and without the local feature (free-field conditions) [41].

By means of this simplification, propagating the dynamic forces to the boundary becomes much easier. On the basis of this operation, the domain inside the boundary Γ is named Ω_0 . The rest of the large-scale domain, outside boundary Γ , is then named Ω_+ . The outside domain Ω_+ is still the same as in the original model, while the change, simplification, is done on the domain inside boundary Γ . The displacement fields for exterior, boundary and interior of the boundary Γ are u_e , u_b and u_i , respectively, on the original domain.

The equations of motions for the complete system can be written as:

$$[M] \cdot \{\ddot{u}\} + [K] \cdot \{u\} = \{P_e\}$$

$$(19)$$

If written for each domain (interior, boundary and exterior of Γ) separately, the equations assume the following form:

$$\begin{bmatrix} M_{ii}^{\Omega} & M_{ib}^{\Omega} & 0 \\ M_{bi}^{\Omega} & M_{bb}^{\Omega+} + M_{bb}^{\Omega+} & M_{be}^{\Omega+} \\ 0 & M_{eb}^{\Omega+} & M_{ee}^{\Omega+} \end{bmatrix} \begin{pmatrix} \ddot{u}_{i} \\ \ddot{u}_{b} \\ \ddot{u}_{e} \end{pmatrix} + \begin{bmatrix} K_{ii}^{\Omega} & K_{ib}^{\Omega} & 0 \\ K_{bi}^{\Omega} & K_{bb}^{\Omega+} + K_{be}^{\Omega+} \\ 0 & K_{eb}^{\Omega+} & K_{ee}^{\Omega+} \end{bmatrix} \begin{pmatrix} u_{i} \\ u_{b} \\ u_{e} \end{pmatrix} = \begin{pmatrix} 0 \\ 0 \\ P_{e} \end{pmatrix}$$
(20)

In these equations, the matrices M and K are mass and stiffness matrices respectively, the vectors \ddot{u} and u denote the nodal accelerations and displacements sub vectors, the subscripts i, e, and b are referencing nodes in either the interior or exterior domain or on their common boundary, respectively, while the superscripts Ω and Ω_+ reference domains to which matrices belong. The previous equation can be separated if the compatibility of displacements and equilibrium is respected. The resulting two equations of motion are:

$$\begin{bmatrix} M_{ii}^{\Omega} & M_{ib}^{\Omega} \\ M_{bi}^{\Omega} & M_{bb}^{\Omega} \end{bmatrix} \begin{Bmatrix} \ddot{u}_{i} \\ \ddot{u}_{b} \end{Bmatrix} + \begin{bmatrix} K_{ii}^{\Omega} & K_{ib}^{\Omega} \\ K_{bi}^{\Omega} & K_{bb}^{\Omega} \end{bmatrix} \begin{Bmatrix} u_{i} \\ u_{b} \end{Bmatrix} = \begin{Bmatrix} 0 \\ P_{b} \end{Bmatrix}, \quad \text{in}\Omega$$
(21)

$$\begin{bmatrix} M_{bb}^{\Omega+} & M_{be}^{\Omega+} \\ M_{eb}^{\Omega+} & M_{ee}^{\Omega+} \end{bmatrix} \begin{Bmatrix} \ddot{u}_b \\ \ddot{u}_e \end{Bmatrix} + \begin{bmatrix} K_{bb}^{\Omega+} & K_{be}^{\Omega+} \\ K_{eb}^{\Omega+} & K_{ee}^{\Omega+} \end{bmatrix} \begin{Bmatrix} u_b \\ u_e \end{Bmatrix} = \begin{Bmatrix} -P_b \\ P_e \end{Bmatrix}, \quad \text{in}\Omega^+$$
(22)

Compatibility of displacements is maintained automatically since both equations contain boundary displacements u_b (on boundary Γ), while the equilibrium is maintained through action – reaction forces P_b .

In order to simplify the problem, an auxiliar problem in which the exterior region and the material therein, as well as the dynamic force source, are identical with those of the original problem, is defined. The interior domain is significantly simplified and denoted as Ω_0 , as well as the localized feature is

removed. In this case, the displacement field (interior, boundary and exterior, respectively) and action-reaction forces are denoted by u_i^0 , u_b^0 , u_e^0 and P_b^0 .

The entire simplified domain Ω_0 and Ω_+ is now easier to analyse. The equations of motion in Ω_+ for the auxiliary problem can now be written as:

$$\begin{bmatrix} M_{bb}^{\Omega+} & M_{be}^{\Omega+} \\ M_{eb}^{\Omega+} & M_{ee}^{\Omega+} \end{bmatrix} \begin{Bmatrix} \ddot{u}_{b}^{0} \\ \ddot{u}_{e}^{0} \end{Bmatrix} + \begin{bmatrix} K_{bb}^{\Omega+} & K_{be}^{\Omega+} \\ K_{eb}^{\Omega+} & K_{ee}^{\Omega+} \end{bmatrix} \begin{Bmatrix} u_{b}^{0} \\ u_{e}^{0} \end{Bmatrix} = \begin{Bmatrix} -P_{b}^{0} \\ P_{e} \end{Bmatrix}$$
(23)

Since there was no change to the exterior domain Ω_+ (material, geometry and the dynamic source are still the same), the mass and stiffness matrices and the nodal force Pe are the same as in Equations (21) and (22).

Previous Equation (22) can be employed to obtain the dynamic force P_{e} :

$$P_{e} = M_{eb}^{\Omega +} \ddot{u}_{b}^{0} + M_{ee}^{\Omega +} \ddot{u}_{e}^{0} + K_{eb}^{\Omega +} u_{b}^{0} + K_{ee}^{\Omega +} u_{e}^{0}$$
(24)

The total displacement u_e can be expressed as the sum of the free-field displacement u_e^0 due to the background structure and the residual displacement field w_e due to the local feature, that is the relative displacement field with respect to the reference free field conditions:

$$u_e = u_e^0 + w_e \tag{25}$$

By substituting the Equation (25) in (20):

Chapter 3: Modelling methodology

$$\begin{bmatrix} M_{ii}^{\Omega} & M_{ib}^{\Omega} & 0 \\ M_{bi}^{\Omega} & M_{bb}^{\Omega+} + M_{be}^{\Omega+} & M_{be}^{\Omega+} \\ 0 & M_{eb}^{\Omega+} & M_{ee}^{\Omega+} \end{bmatrix} \begin{Bmatrix} \ddot{u}_{i} \\ \ddot{u}_{b} \\ \ddot{u}_{e}^{0} + \ddot{w}_{e} \end{Bmatrix} + \begin{bmatrix} K_{ii}^{\Omega} & K_{ib}^{\Omega} & 0 \\ K_{bi}^{\Omega} & K_{bb}^{\Omega+} + K_{be}^{\Omega+} \\ 0 & K_{eb}^{\Omega+} & K_{ee}^{\Omega+} \end{bmatrix} \begin{Bmatrix} u_{i} \\ u_{b} \\ u_{e}^{0} + w_{e} \end{Bmatrix} =$$

$$\begin{pmatrix} 0 \\ 0 \\ P_{e} \end{pmatrix}$$

which, after moving the free field motions u_e^0 to the right-hand side, becomes:

$$\begin{bmatrix} M_{ii}^{\Omega} & M_{ib}^{\Omega} & 0 \\ M_{bi}^{\Omega} & M_{bb}^{\Omega} + M_{bb}^{\Omega+} & M_{be}^{\Omega+} \\ 0 & M_{eb}^{\Omega+} & M_{ee}^{\Omega+} \end{bmatrix} \begin{cases} \ddot{u}_{i} \\ \ddot{u}_{b} \\ \ddot{w}_{e} \end{cases} + \begin{bmatrix} K_{ii}^{\Omega} & K_{ib}^{\Omega} & 0 \\ K_{bi}^{\Omega} & K_{bb}^{\Omega+} + K_{be}^{\Omega+} \\ 0 & K_{eb}^{\Omega+} & K_{ee}^{\Omega+} \end{bmatrix} \begin{cases} u_{i} \\ u_{b} \\ w_{e} \end{cases} =$$

$$\begin{cases} 0 \\ -M_{be}^{\Omega+} \ddot{u}_{e}^{0} - K_{be}^{\Omega+} u_{e}^{0} \\ -M_{ee}^{\Omega+} \ddot{u}_{e}^{0} - K_{ee}^{\Omega+} u_{e}^{0} + P_{e} \end{cases}$$

$$(27)$$

By substituting Equation (24) in (27), the right-hand side can now be written as:

$$\begin{bmatrix} M_{ii}^{\Omega} & M_{ib}^{\Omega} & 0 \\ M_{bi}^{\Omega} & M_{bb}^{\Omega+} + M_{bb}^{\Omega+} & M_{be}^{\Omega+} \\ 0 & M_{eb}^{\Omega+} & M_{ee}^{\Omega+} \end{bmatrix} \begin{bmatrix} \ddot{u}_{i} \\ \ddot{u}_{b} \\ \ddot{w}_{e} \end{bmatrix} + \begin{bmatrix} K_{ii}^{\Omega} & K_{ib}^{\Omega} & 0 \\ K_{bi}^{\Omega} & K_{bb}^{\Omega+} + K_{be}^{\Omega+} \\ 0 & K_{eb}^{\Omega+} & K_{ee}^{\Omega+} \end{bmatrix} \begin{bmatrix} u_{i} \\ u_{b} \\ w_{e} \end{bmatrix} = \begin{bmatrix} 0 \\ -M_{be}^{\Omega+} \ddot{u}_{e}^{0} - K_{be}^{\Omega+} u_{e}^{0} \\ M_{eb}^{\Omega+} \ddot{u}_{b}^{0} + K_{eb}^{\Omega+} u_{b}^{0} \end{bmatrix}$$

$$(28)$$

The vector on the right-hand side of (28) represents the seismic effective nodal force vector P^{eff} for the dynamic source forces Pe. In other words, the dynamic force Pe was consistently replaced by the effective force P^{eff} :

$$P^{eff} = \begin{cases} P_i^{eff} \\ P_b^{eff} \\ P_e^{eff} \end{cases} = \begin{cases} 0 \\ -M_{be}^{\Omega +} \ddot{u}_e^0 - K_{be}^{\Omega +} u_e^0 \\ M_{eb}^{\Omega +} \ddot{u}_b^0 + K_{eb}^{\Omega +} u_b^0 \end{cases}$$
(29)

Several aspects regarding this method can be examined:

• The Equation (29) shows that the effective nodal forces P^{eff} involve only the sub-matrices M_{be} , K_{be} , M_{eb} , K_{eb} . These matrices vanish everywhere except the single layer of finite elements in domain Ω_+ adjacent to Γ . The significance of this is that the only wave-field (displacements and accelerations) needed to determine seismic effective nodal forces P^{eff} is that obtained from the auxiliary problem at the nodes that lie on and between boundaries Γ and Γ_e , as shown in Figure 3.2.9. In order to determine the intensity of forces P^{eff} , it is necessary to know the values of accelerations \ddot{u}_0 and displacements u_0 only for those nodes characterizing the so-called DRM layer.

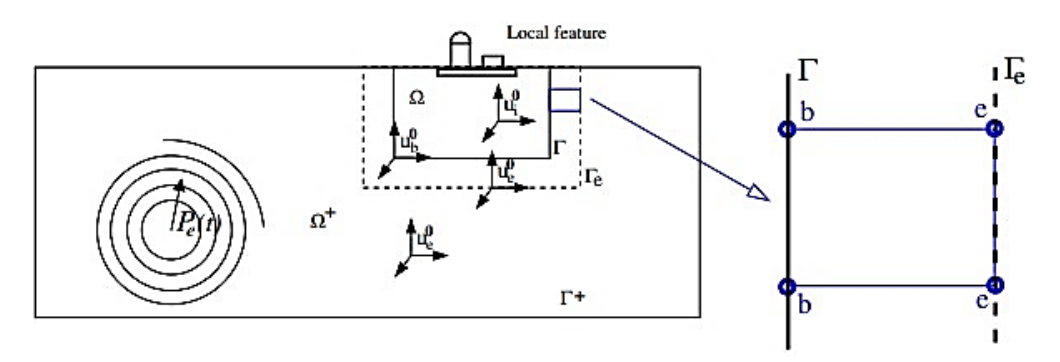


Figure 3.2.9 DRM: a single layer of elements between Γ and Γ e is used to create P^{eff} for a section of 8-node-brick elements [41].

The unknown values in (28) are the displacements of the nodes on the boundaries Γ and Γ_e . For the outside soil subdomain Ω_+ i.e., part of the soil beyond the boundary Γ_e , the "residual" displacement field w_e is the relative displacement field with respect to the primary displacement field u_0 (free-field displacements) and is obtained by solving (28). In the soil-structure interaction analyses, attention is focused on the structure and the foundation soil, so by providing appropriate supports (including fixities and damping) at some distance from the boundary $\Gamma_{e,}$ into Ω_{+} region, the "residual" displacements have no practical significance and the behaviour of the full model (outside Γ_e into Ω_+ region) can be neglected. In this way, large models can be reduced in size until to a smaller subdomain Ω_+ around DRM layer, i.e. the subdomain between the boundaries Γ_e and Γ^+ . A sufficiently high damping level should be adopted for the material of the reduced subdomain Ω_+ , in order to prevent the occurrence of spurious seismic waves that can be generated by waves from the inside subdomain passing through the outside subdomain, hitting the model boundary, and being reflected to the inside subdomain and structure. The reduced outside soil subdomain Ω_+ with pronounced material damping is called Damping layer (Figure 3.2.10).

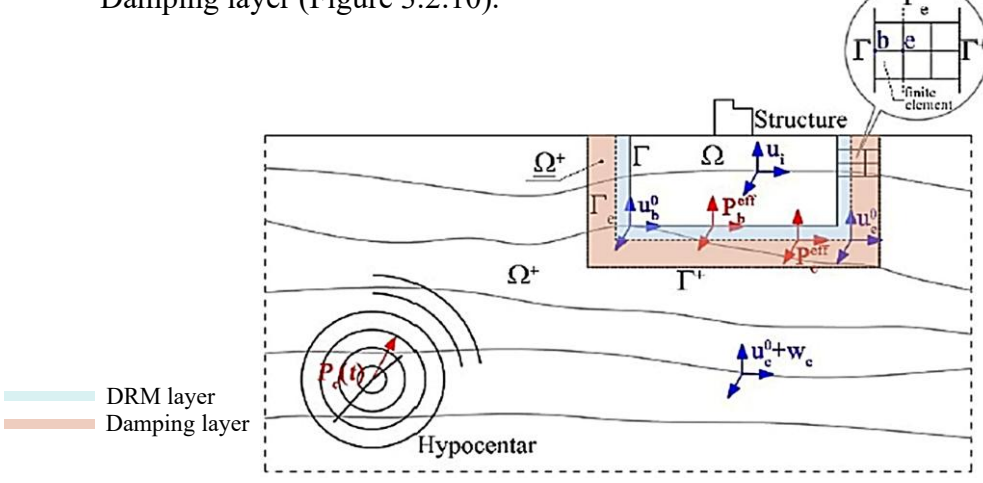


Figure 3.2.10 Characterization of the damping layer around DRM layer [45].

- Inside the Ω domain, the assumption that the material is linear elastic is not necessary as the DRM is not relying on the principle of superposition. The latter is generally applied for linear elastic solids and structures but, in this case, it is only valid for the soil that is located at a sufficiently large distance from the structure, i.e. for the outside soil subdomain Ω_+ , not of interest in the soil structure analysis. Inside Γ_e , instead, materials can be assumed linear or nonlinear, elastic or inelastic. This makes the DRM a very powerful method for analysis of soil foundation structure systems.
- Since the nodal forces P^{eff} consistently replace the effects of the seismic source, all appropriate (real) seismic waves are properly (analytically) modelled, including body (SV, SH, P) and surface (Rayleigh, Love...) waves.

In the DRM, the input accelerograms and their corresponding displacement recordings can be used in different ways to determine the values of accelerations and displacements of all nodes of the DRM layer.

Most site – response analyses are carried out by adopting one – dimensional methods, based on the following assumptions reported in Bolisetti and Whittaker in [47]:

- the soil profiles consist of overlapping horizontal layers;
- the soil layers are homogeneous along the horizontal plane;
- the ground motion incident on the soil deposit is in the form of vertically propagating shear waves.

However, the soil deposits that do not conform to these assumptions need to be analysed using multi-dimensional methods. The one-dimensional method represents the most – widely used in practice and involves the excitation of a soil-profile using the horizontal component of a ground motion, calculating the response of the individual soil layers, and for each point of them the values of one, two or all three components of the accelerations \ddot{u}_0 or displacements u_0 , during an earthquake, are determined. In addition to the correct analysis to be performed, another important aspect to be defined is the position of the reference point, which is assumed to be the place of the registration of the input accelerograms (Figure 3.2.11). An upward wave propagation analysis, named convolution, typically involves the input of a rock outcrop motion (ground

motion recorded at a nearby, outcropping bedrock) at the soil - bedrock interface.

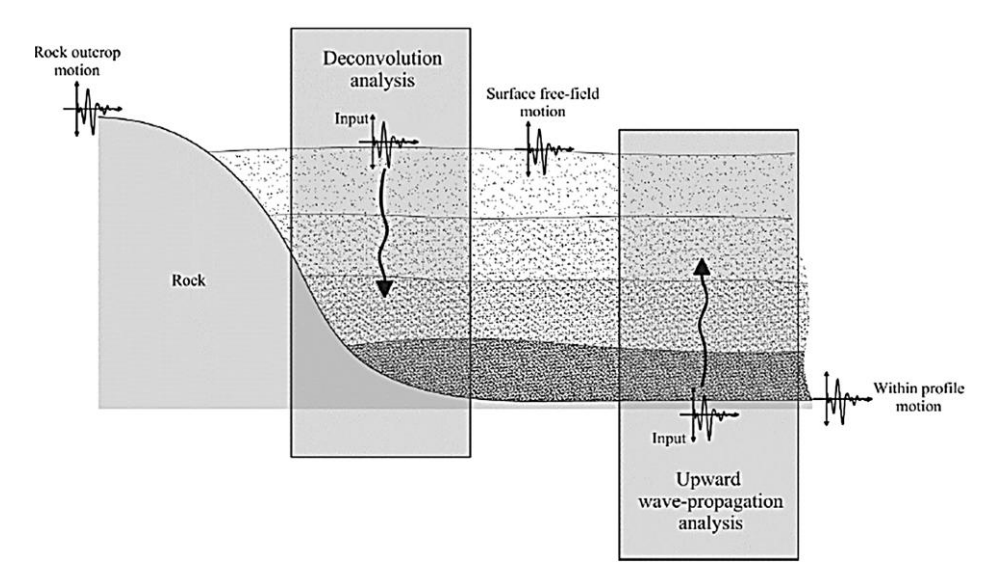


Figure 3.2.11 One-dimensional site-response analysis [47].

If the ground motion at depth is available from recorded data (termed as a within-profile ground motion), it is directly input at the base of the soil profile while assuming rigid properties for the bedrock. Starting from the bedrock, a response at the topmost layer is finally calculated to better highlight how much the dynamic response, which depends on the total mobilized stiffness, which in turn is a function of the level of deformation associated with an input of given intensity, is amplified or not, as per PLAXIS settings. Conversely, when such data are not available, even because there are no accelerometer stations at a certain depth, close to bedrock depth, as well as there may be numerical uncertainties and/or related to unclear stratification of the deposit under study, the convolution becomes difficult to apply.

By focusing on DRM methodology within Real-ESSI Simulator, instead, a process called deconvolution is proposed, i.e. a downward wave propagation analysis in which the surface free-field motion is the input at the topmost layer of the soil, and the response of underlying layers is then calculated.

3.2.3 Reasons for employing DRM

When simulating earthquake ground motion of a site with a significant topographic extent by employing numerical methods such as the finite element method, a large computational domain is usually required to mimic the theoretically infinite soil domain. According to a FEM method approach, the maximum grid size of a finite element model is proportional to the shear wave velocity of the material and inversely proportional to the highest relevant frequency of the excitation. This maximum grid size is usually small compared to the whole computation domain. Given that, a finite element model simulating seismic wave propagation will need to be meshed into numerous elements and nodes. Because of this, the analysis of a rational 3D soil-structure interaction finite element model is still an extremely time-consuming process. Likewise, most of existing methods employed to input seismic motions into FEM models cannot properly model all three components of body waves as well as always present surface waves.

There exists a method that is based on rational mechanics and can model both body and surface seismic waves input with high accuracy, by allowing at the same time the employment of a reduced computational domain into a finite-size model with artificial boundaries modelled in order to prevent unnecessary reflection waves from the edge of the numerical model and to increase the speed of analysis execution. This method is called Domain Reduction Method (DRM).

As better highlighted in the next section, such finite element methodology is a very suitable tool for the analyses of dynamic soil-structure interaction because allows modelling complex models that contain the earthquake source, i.e. the fault, as well as the wave propagation paths, and local geological and topographical structures, simulating a real seismic excitation. Defining this latter implies the determination of displacements and/or accelerations values obtained by processing the seismo-geological model of the location of interest, i.e. the wider area to which the location belongs, but models of this type are very rare.

On the other hand, some alternative solutions imply the use of appropriate recordings of previous earthquake, more specifically recordings of free-field ground motions for the location (area), where the analysed object is located:

Chapter 3: Modelling methodology

this aspect represents a very favourable circumstance for implementing the DRM, because it becomes possible to operate a technique better explained later and called deconvolution by which, starting with an input recorded at the surface, it is possible to evaluate the effects at certain depths, unlike in other FE software such as the aforementioned PLAXIS, in which, instead, the input is imposed at the base of the model, with its effects in terms of amplifications can be evaluated at the surface.

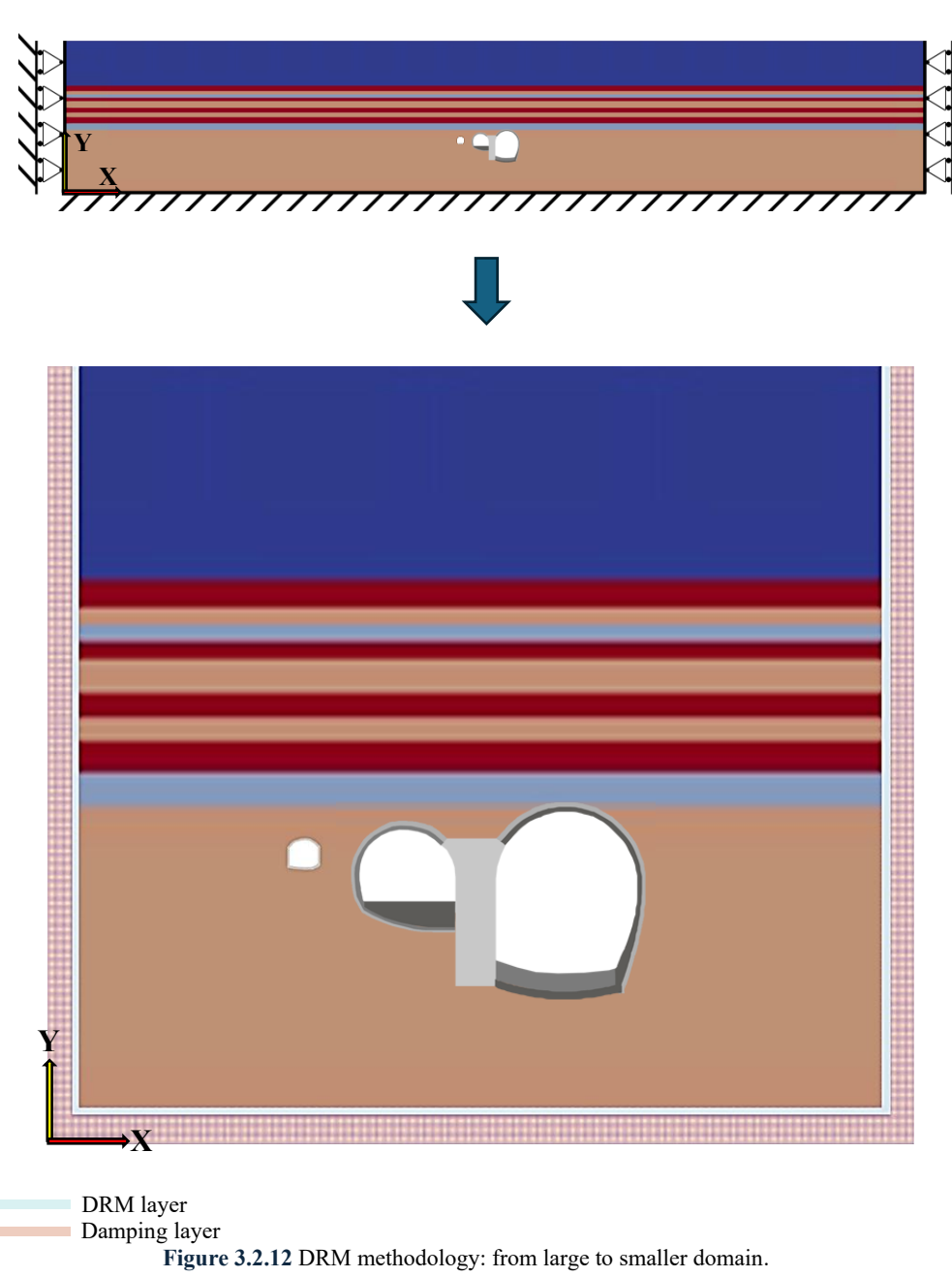
In this context, if unscaled or scaled recordings are available for a location of interest, they can be used as input data for DRM, i.e., as so-called input accelerograms. Otherwise, appropriate scaled or unscaled recordings of previous earthquakes downloaded from several databases, as ESM (Engineering Strong Motion Database) are used as input accelerograms for the DRM.

3.2.4 DRM application to the case study

To highlight the most powerful and useful features of DRM and to show it effectiveness of modelling soil – structure seismic response, a FE model was built via Real-ESSI and a seismic input motion is inserted, in order to create a wave field that will result in a targeted motion at the ground surface, and to generate a free – field wave field, by performing the deconvolution of such input down to the bedrock and then creating "effective" forces for the DRM elements.

For the present study, as properly explained in the Chapter 4, HL-LHC Point 5 at CERN is modelled using 8-node elastic solid brick elements (2D modelling with 3D elements, i.e. a 3D slice). According to the methodology aforementioned, a large computational domain including the local geological feature has been reduced to a much smaller domain that only includes local soil profile and structures, using appropriate boundary and initial conditions, surrounded by a DRM layer, which is in turn surrounded by a damping layer (Figure 3.2.12). Concerning the boundary conditions, all degrees of freedom of the lateral and bottom surfaces of the damping elements are fixed. In addition, since a one-component ground motion excitation is employed (i.e. vertically propagating horizontal shear waves), the soil elements nodes are allowed to move horizontally. An important consideration must be done for the damping elements, which purpose is to damp out any waves generated by the oscillations of the structures therein, by applying high values of Rayleigh viscous damping on such inciting waves.

In the phase of model verification and validation, to demonstrate the effective positioning of a point of control on the ground surface and apply the deconvolution, a free-field condition is considered (Figure 3.2.13). For this condition, being the structures removed, the damping elements remain inactive, as there are no radiated waves entering in their domain, so no Rayleigh damping has assigned them [48]. The input motion employed for the free – field verification is Ricker pulse, with duration of 7 s, the maximum frequency equal to 2 Hz and a peak ground acceleration of 0.1 g (Figure 3.2.14).



Chapter 3: Modelling methodology

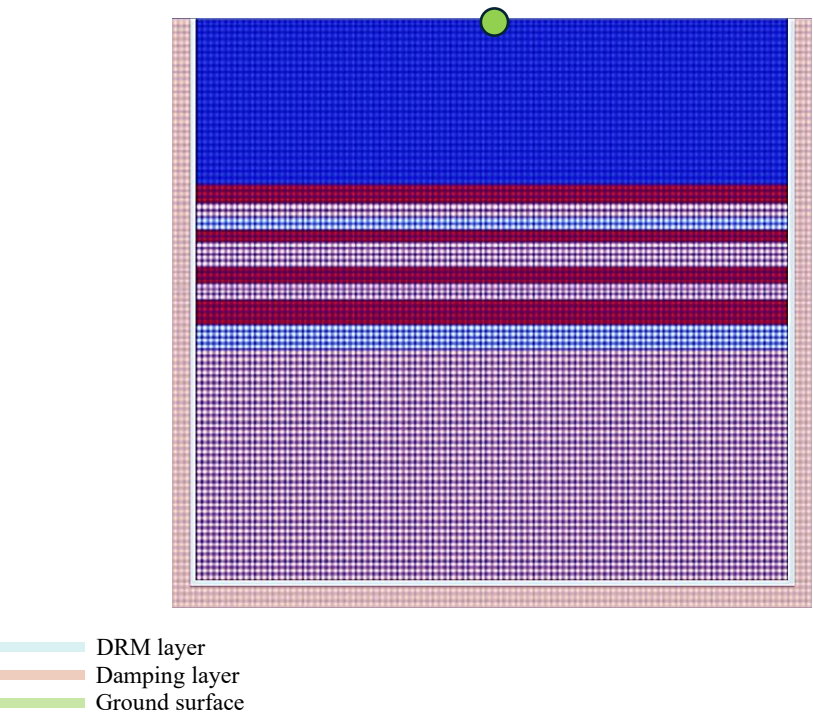


Figure 3.2.13 FE model developed to verify the free-field response.

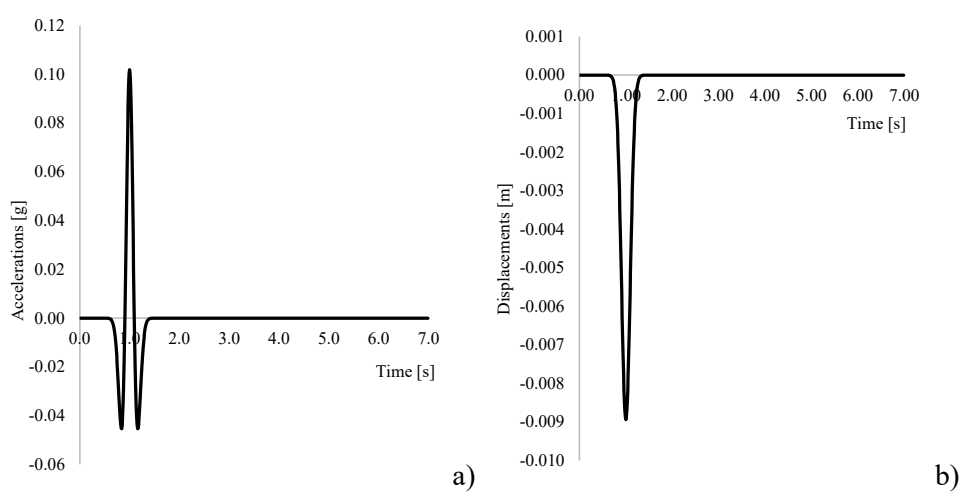


Figure 3.2.14 Ricker wavelet: a) horizontal acceleration and b) horizontal displacement time histories.

By considering a Rayleigh damping to each soil layer equal to 2% but keeping the damping elements inactive, the free-field verification showed that the excitation at the ground surface is, indeed, the targeted Ricker pulse. Different cases highlight how the ground surface acceleration time histories changed by changing the numerical damping implemented by means of the parameter γ of the Newmark integration method [49]. The formulation of the time integration constitutes an important factor for the stability and accuracy of the calculation process. In this context, the coefficients γ and β determine a stable solution when:

$$\gamma \ge 0.5$$

$$\beta \ge 0.25 \cdot (0.5 + \beta)^2$$
(30)

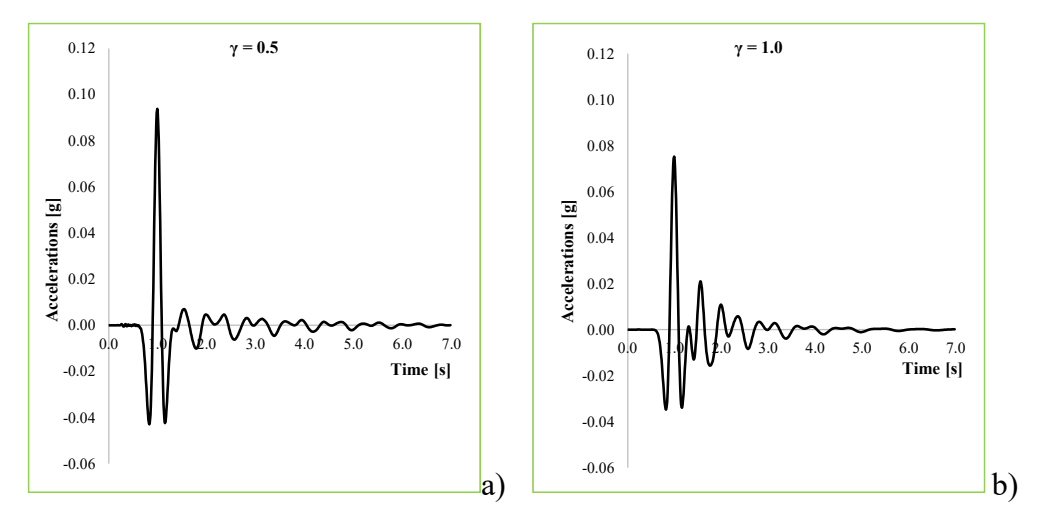


Figure 3.2.15 Time histories of horizontal accelerations at the ground surface for two different values of numerical damping: a) $\gamma = 0.5$; b) $\gamma = 1.0$.

Results show that in the absence of numerical damping ($\gamma = 0.5$), the targeted Ricker wavelet appears "contaminated" by spurious oscillations after the main pulse. A further increase to $\gamma = 1.0$ leads to an improper reproduction of the main pulse and to more prominent spurious oscillations (Figure 3.2.15).

3.3 The Uncertainties Treatment problem employing the Latin Hypercube Sampling algorithm

Within the numerical simulations, particularly for this study, all required geo-mechanical parameters were calibrated to perform analyses capable of producing responses that consider the uncertainty provided by a random choice of the same, according to a statistical approach, thus treating or imposing statistical correlations between the basic random input variables, as reported in Vořechovský and Novák in [50].

In this context, a solution could be represented by using the stratified sampling technique Latin Hypercube Sampling (LHS), a special type of Monte Carlo numerical simulation according to which a small number of simulations (from ten to hundreds) can be used to gain an acceptable level of accuracy for the statistical characteristics of the response and can be employed for both simple and very complicated computational model.

A deterministic function Y = g(X), representing a computational model, must be considered, with $Y \in \mathbb{R}$ and $X \in \mathbb{R}^{Nvar}$ defined as a random vector of N_{var} marginals, i.e. input random variables describing uncertainties, with $g(\cdot)$ that can be expensive to evaluate. The information on the random vector is limited to marginal probability distributions and the target correlation matrix T:

$$\boldsymbol{T} = \begin{pmatrix} X_{1} & X_{2} & \cdots & X_{N_{var}} \\ X_{1} & I & T_{1,2} & \cdots & T_{1,N_{var}} \\ \vdots & I & \cdots & \vdots \\ \vdots & \vdots & \ddots & \vdots \\ X_{N_{var}} & sym. & \cdots & \cdots & I \end{pmatrix}$$
(31)

The procedure is to draw N_{sim} (number of simulations) realizations of X and compute the same number of output realizations of Y using the model $g(\cdot)$.

Since $g(\cdot)$ can be expensive to compute it, pays to use a more advanced sampling scheme, i.e. the LHS algorithm. It is suitable for statistical and sensitivity calculations, and one of its strengths is its optimal coverage of a space with many variables with a minimum number of samples.

The first stage of LHS is to generate samples for each variable which represent the variable's probability distribution. The domain of each variable is divided into equiprobable disjunct intervals, and one sample is chosen from each interval. The current practice is to choose samples directly from the following cumulative distribution function:

$$x_{i,j} = F_i^{-1} \left(\frac{\pi_i(j) - 0.5}{N_{sim}} \right)$$
 (32)

where $x_{i,j}$ represents the *j*th realization of *i*th random variable X_i ($i = 1, ..., N_{var}$); $\pi_i(I), ..., \pi_i(N_{sim})$ is a random permutation of 1, ..., N_{sim} ; F_i^{-1} is the inverse of the target cumulative distribution function for variable X_i ; N_{sim} is the number of simulations, i.e. the number of realizations for each random variable. If F_i is continuous, then each of the N_{sim} equiprobable subintervals $j = 1, ..., N_{sim}$ for X_i is represented by one value $x_{i,j}$.

Mckay et al. in [51] showed that such a sample selection reduces the sampling variance of the statistics of g (**X**) when g (·) is monotone in each of the inputs. In the unbiased version, the Latin Hypercube Sample is generated by replacing the number 0.5 in Eq. (32) by U_j^i , where U_j^i is a uniformly distributed random variable over the interval [0; 1), independent of the permutations π_i (this sampling selection is called LHS-random).

However, one can criticize such a reduction of the sample selection to the midpoints within intervals (interval medians). This objection deals mainly with samples of the tails of PDF, which mostly influence the sample variance. To better enable the simulated variables to have the correct means and variances, and therefore better represent the random variables' marginal probability density functions, the sampling of interval mean values was proposed by means the following rule:

Chapter 3: Modelling methodology

$$x_{i,j} = \frac{\int_{\xi_{i,j-1}}^{\xi_{i,j}} x f_i(x) dx}{\int_{\xi_{i,j-1}}^{\xi_{i,j}} f_i(x) dx} = N_{sim} \int_{\xi_{i,j-1}}^{\xi_{i,j}} x f_i(x) dx$$
(33)

where f_i is the probability density function (PDF) of variable X_i and the integration limits (right bounds for *j*th realizations) are:

$$\xi_{i,j} = F_i^{-1} \left(\frac{j}{N_{sim}} \right) \text{ with } j = 1, ..., N_{sim}$$
 (34)

By using this scheme, named LHS-mean (Figure 3.3.1), samples represent one-dimensional marginal PDF better in terms of the distance of the point estimators from the exact statistics. In particular, the mean value is achieved exactly (the analytical expression preserves the mean) and estimated variance is much closer to that of the target.

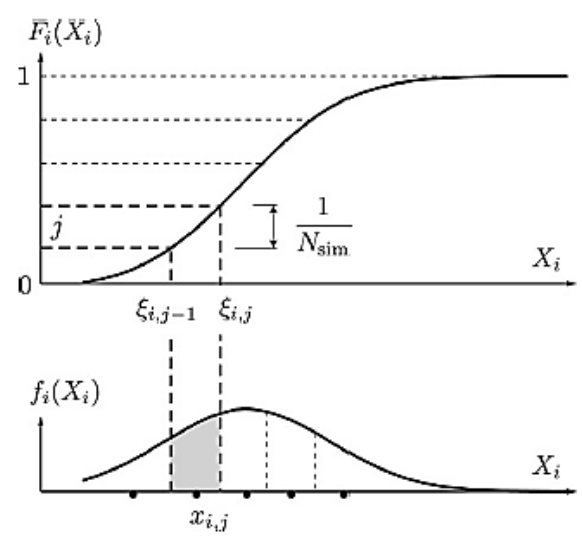


Figure 3.3.1 Samples as the probabilistic means of intervals: LHS-mean scheme [50].

For some PDFs, the integral Eq. (33) can be solved analytically. In the case that the solution of the primitive is impossible or difficult, it is necessary to use an additional effort: numerical solution of the integral. However, such an increase in computational effort is worthwhile especially when N_{sim} is very small. Samples selected by both Eqs. (32) and (33) are almost identical except for the values in the tails of PDFs. Therefore, one can use the more advanced scheme Eq. (33) only for the tails, since tail samples mostly influence the estimated variance of the sample set. Generally, regularity of sampling (the range of distribution functions is stratified) ensures good sampling and consequently good estimation of statistical parameters of response using a small number of simulations.

An explanatory example of sampling plan for two input variables and five realizations, taken by Olsson et al. in [52], is shown below (Figure 3.3.2). Let N denote the required number of realizations and K the number of random variables. The sampling space is then K – dimensional. An $N \times K$ matrix \mathbf{P} , in which each of the K columns is a random permutation of 1, ... N, and an $N \times K$ matrix \mathbf{R} of independent random numbers from the uniform (0,1) distribution are established. These matrices form the basic sampling plan, represented by the matrix \mathbf{S} as:

$$\mathbf{S} = \frac{1}{N} (\mathbf{P} - \mathbf{R}) \tag{35}$$

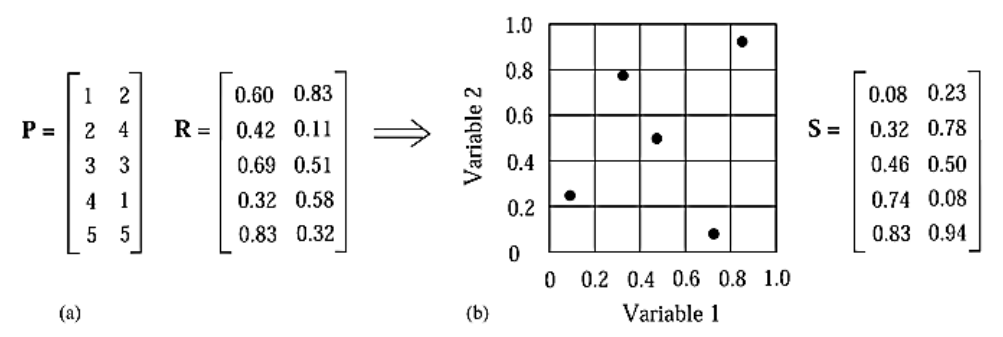


Figure 3.3.2 Latin cube, two variables and five realizations. The 5 x 2 matrix (a) determines the plan illustrated in (b) [52].

Chapter 3: Modelling methodology

For the present study, to correctly perform all the experimental analyses, which will be discussed in more detail in Chapter 5, the variables defined for soils, rock and concrete were the specific weight γ , Young' modulus E, Poisson coefficient ν and damping ratio ξ , respectively. For concrete, in addition to them, the mean cylindrical strength f_{cm} was defined.

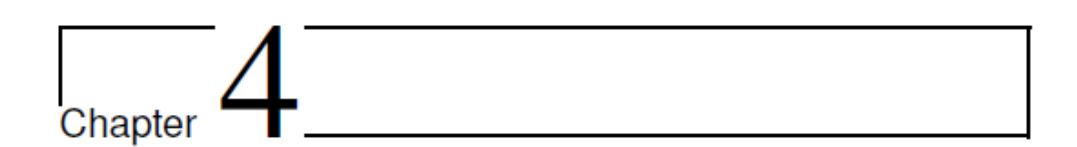
The uncertainty of the correlation matrix has been considered by suitable weights based on the expert judgement. For the soils and rock, the weight has been set equal to 5, while for the concrete a reasonable value equal to 3 has been considered. Moreover, the material properties are described through probability density functions, more specifically log-normal distributions (LN) were chosen for E, γ and ξ variables, while for the Poisson coefficient ν , a Beta distribution was chosen, because of its limited value.

		Uncertainty	Lower	Upper
Variables	Distribution	weight	Bound	Bound
γ_{soil}	LN	5	0	Inf
E_{soil}	LN	5	0	Inf
V _{soil}	Beta [0,0.5]	3	0	0.5
ξsoil	LN	5	0	Inf
$\gamma_{\rm conc}$	LN	5	0	Inf
f_{cm}	LN	5	0	Inf
V _{conc}	Beta [0,0.5]	3	0	0.5
ξconc	LN	5	0	Inf

Table 1 Material characteristics and their statistical distribution parameters.

Chapter 3: Modelling methodology





4 A case study: the Large Hadron Collider project at Point 5 at CERN

Physicists and engineers at CERN use the world's largest and most complex scientific instruments to study the basic constituents of matter-fundamental particles. Subatomic particles are made to collide together at close to the speed of light. The process gives us clues about how the particles interact and provides insights into the fundamental laws of nature.

The instruments used at CERN are purpose-built particle accelerators and detectors. Accelerators boost beams of particles to high energies before the beams are made to collide with each other or with stationary targets. Detectors observe and record the results of these collisions.

- In Section 4.1, an historical description containing the chronological evolution of CERN infrastructures was presented, starting from its foundation to the future developments.
- In Section 4.2, a geographical and geological framework of the Geneva basin was presented, with reference to the several stratigraphic modifications succeeded by the passage of the various geological eras.
- In Section 4.3, a focus on the seismic hazard of the area in which CERN is located, was highlighted, with a reference to the French main regulatory applications.
- In Section 4.4, a focus on the geotechnical investigations at the Point 5 was presented, more specifically a detailed stratigraphical

- characterization and their consequent simplification based on previous literature studies.
- In Section 4.5 and its subsections, a focus on the underground structures located at Point 5 was presented. More specifically, a detailed description regarding the design and construction methods of such structures was presented, with reference to the main experimental cavity (UXC55 cavity) hosting the Compact Muon Solenoid Detector. A further in-depth study, more specifically in particle physics, was made of the type of particles studied, as well as a brief description of the CMS detector's operating process.
- In Section 4.6 and its subsections, a preliminary study for seismic assessment of the underground facilities at Point 5 was reported, with related results and comments, by means of several fully dynamic analyses done in the FE software PLAXIS. This study, presented at COMPDYN [40] focused on the estimation of the response of such large underground cavities when subjected to seismic excitations, i.e. different seismic input motions and, consequently, on a preliminary evaluation of their safety and structural integrity.
- In Section 4.7 and its subsections, a further study on the evaluation of the seismic behaviour of the underground facilities at Point 5, with related results and comments, was reported, using the advanced FE software Real-ESSI Simulator. This study, presented at the International Workshop on Computational Dynamic Soil -Structure Interaction [53], mainly focused on comparison results between the operating methodologies offered by PLAXIS and Real-ESSI, considering the same initial and boundary conditions and the same parameters adopted in the COMPDYN study, in order to validate such methodologies and to evaluate, in addition, a dynamic response, by applying different seismic input motions, for the conditions with and without cavities, respectively, in terms of amplification functions.

4.1 The European Organization for Nuclear Research: historical notes and framework

The European Laboratory for Particle Physics (CERN) (Figure 4.1.1) is the world's largest research laboratory for particle physics.

At an intergovernmental meeting of UNESCO in Paris in December 1951, the first resolution concerning the establishment of a European Council for Nuclear Research (in French Conseil Européen pour la Recherche Nucléaire) was adopted. Founded in 1954, the CERN laboratory facilities (both surface and underground) are based in the northwest suburb of Geneva at the Franco-Swiss border. The organization is sponsored by 24 member states, and hosts an international community of scientists, researchers, staff and students.

CERN underground structures composed of a complex network of linear and circular particle accelerators, which are characterized as the most powerful and unique of its type in the world. Particle accelerators are used to spin either the protons or electrons at extremely high energies near the speed of light, which are then allowed to collide at pre-defined locations creating new particles that is used to study the origin of matter. Collision points are defined at specific locations along the circumference of the accelerator within huge underground experimental caverns, which host the so-called particle detectors. These detectors are highly sophisticated equipment capable of measuring the energy, mass and charge of these newly created particles.

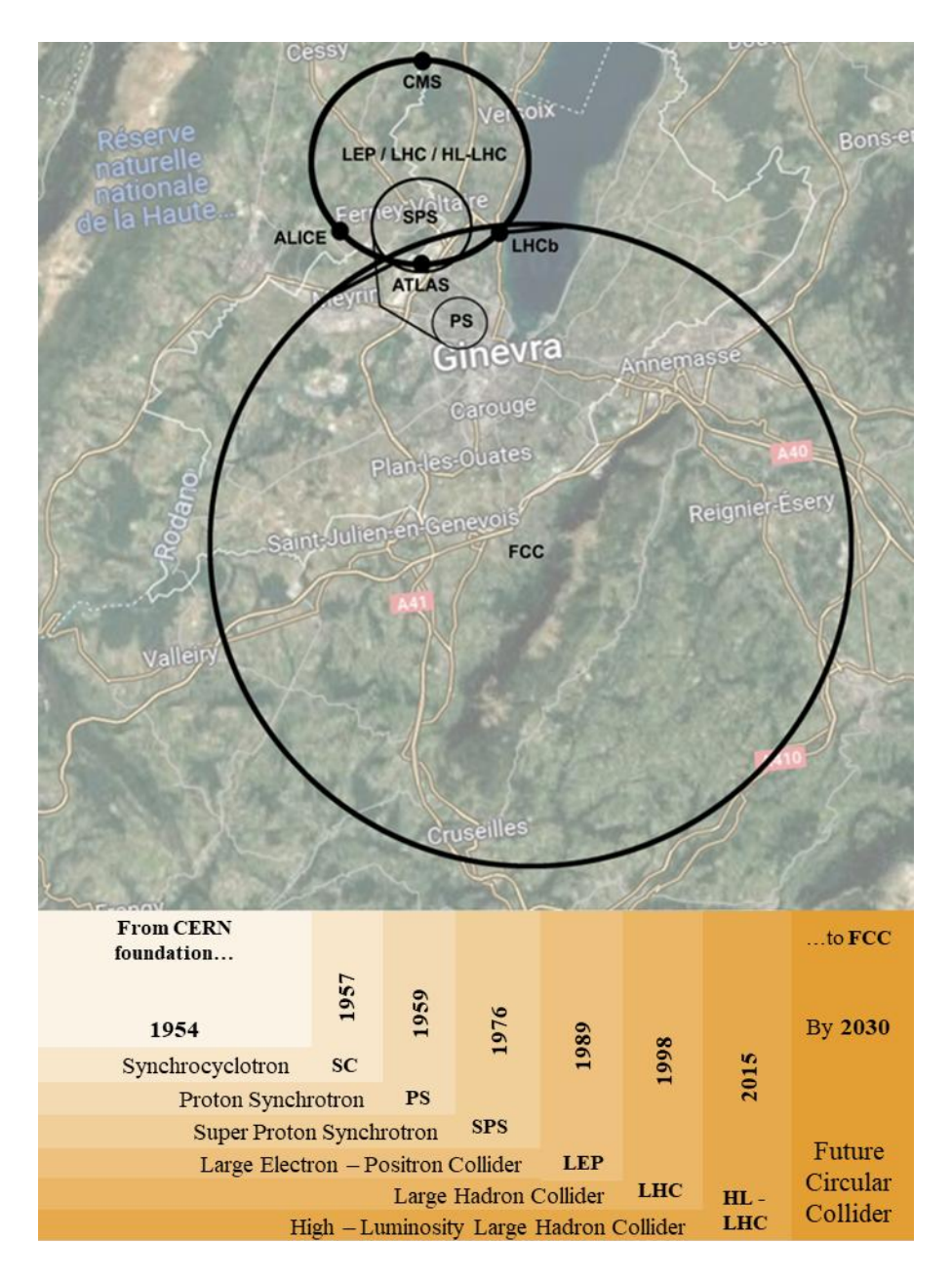


Figure 4.1.1 Timeline containing the chronological construction process of CERN underground structures.

Particle beam accelerators are hosted in tunnels at a depth between 50-100 m below ground level: the first particle accelerator was built in 1957, i.e. the *Synchrocyclotron* (SC). It was only in 1976 that CERN went underground with the *Super Proton Synchrotron* (SPS), a circular collider with a 7 km circumference; it was constructed using a TBM with an average depth of 40 m below the ground surface. The machinery was housed in caverns and access was provided by shafts. Since then, CERN has been extended multiple times.

In 1989, the *Large Electron – Positron Collider* (LEP) was built. It is a 27-km-long circular tunnel, making it the largest underground construction in Europe and one of Europe's longest tunnels at that time (Figure 4.1.2). [54] [55] [56] [57].

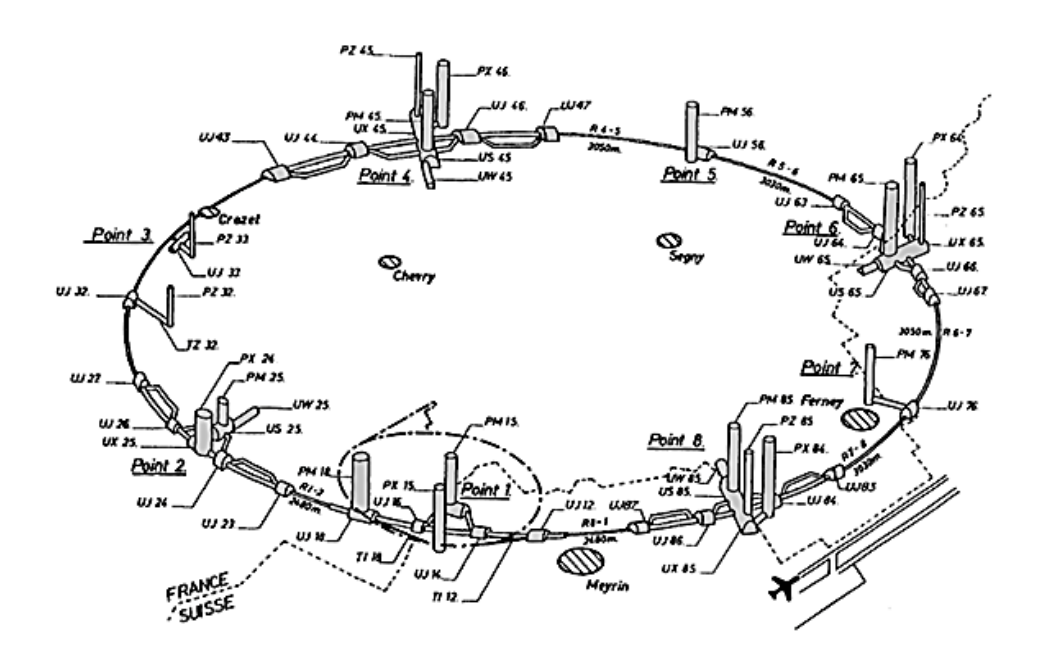


Figure 4.1.2 Layout of the existing tunnel structures that host the LEP\SPS beam accelerator at the Franco-Swiss border [57].

In 1998, The LEP was converted to the *Large Hydron Collider* (LHC) (Figure 4.1.3): the project utilizes the existing tunnel networks and surface facilities that were used to operate the physical experiments in the Large Electron Positron accelerator. This tunnel, which sits on average 100 m below the surface, was excavated using TBMs and one sector of drill & blast. Most of the tunnel was excavated in the variable sandstone layer known locally as molasse and a short sector was excavated in limestone using drill & blast. The tunnelling through the molasse layer was executed without any major problems and a maximum rate of 58.7 m per day was reached. However, approximately 3 km of tunnelling was required through the limestone at the foot of the Jura Mountain range, which proved more challenging. Even though continuous pilot borings were made ahead of the blast face, there was still a major geological incident where a water ingress with a rate of 100 l/s at a pressure of 8.5 bar occurred. In order to overcome the water flow, resin injections and drainage of the tunnel were required, resulting in an 8-month delay. The final breakthrough in the tunnel was achieved in February 1988.

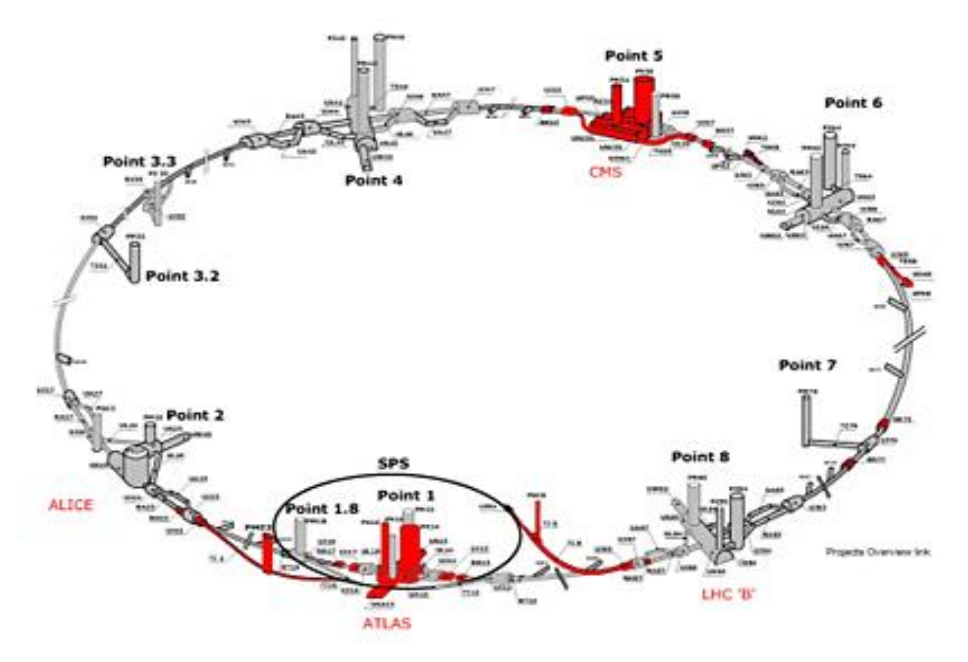


Figure 4.1.3 Layout of the underground structures that host the LHC project: definition of Point 1 (ATLAS), Point 5 (CMS), Point 2 (ALICE) and Point 8 (LHCb) sites. [58].

For the upgrade of the underground assets for the LHC, additional caverns and access shafts were constructed at Point 5 and Point 1 sites and accommodate ATLAS (A Toroidal LHC ApparatuS) and CMS (Compact Muon Solenoid) detectors, respectively. Inside the accelerator, two high-energy particle beams travel at close to the speed of light before they are made to collide. The beams travel in opposite directions in separate beam pipes – two tubes kept at ultrahigh vacuum. They are guided around the accelerator ring by a strong magnetic field maintained by superconducting electromagnets. The electromagnets are built from coils of special electric cable that operates in a superconducting state, efficiently conducting electricity without resistance or loss of energy. This requires chilling the magnets to -271.3°C – a temperature colder than outer space. For this reason, much of the accelerator is connected to a distribution system of liquid helium, which cools the magnets, as well as to other supply services. Thousands of magnets of different varieties and sizes are used to direct the beams around the accelerator. These include 1232 dipole magnets, 15 metres in length, which bend the beams, and 392 quadrupole magnets, each 5–7 metres long, which focus the beams. Just prior to collision, another type of magnet is used to "squeeze" the particles closer together to increase the chances of collisions. The particles are so tiny that the task of making them collide is akin to firing two needles 10 kilometres apart with such precision that they meet halfway. Shortly after, ALICE (Point 2) and LHCb (Point 8) were constructed, adding new caverns and tunnels to the existing facilities.

In 2015, the High Luminosity (*HiLumi*) project began with the construction of additional technical infrastructures for the two main detectors and will be operational in 2026 (Figure 4.1.4): it aims to crank up the performance of the LHC to increase the potential for discoveries after 2030. The objective is to increase the integrated luminosity by a factor of 10 beyond the LHC's design value. Luminosity is an important indicator of the performance of an accelerator; it is proportional to the number of collisions that occur in each amount of time. The higher the luminosity, the more data the experiments can gather to allow them to observe rare processes.

The HL-LHC construction works will be split into two existing experimental sites, the Point 1 for the ATLAS experiment, located in Switzerland, and the Point 5 for the CMS experiment, located in France, respectively. The underground structures required at each point consist of a

new shaft, a cryogenics cavern, radio frequency and power converter tunnels, service tunnels and linkage cores to the existing LHC infrastructure. New surface buildings and infrastructure range from small buildings for shaft access to large buildings for housing machinery critical to the operation of the upgraded technology.

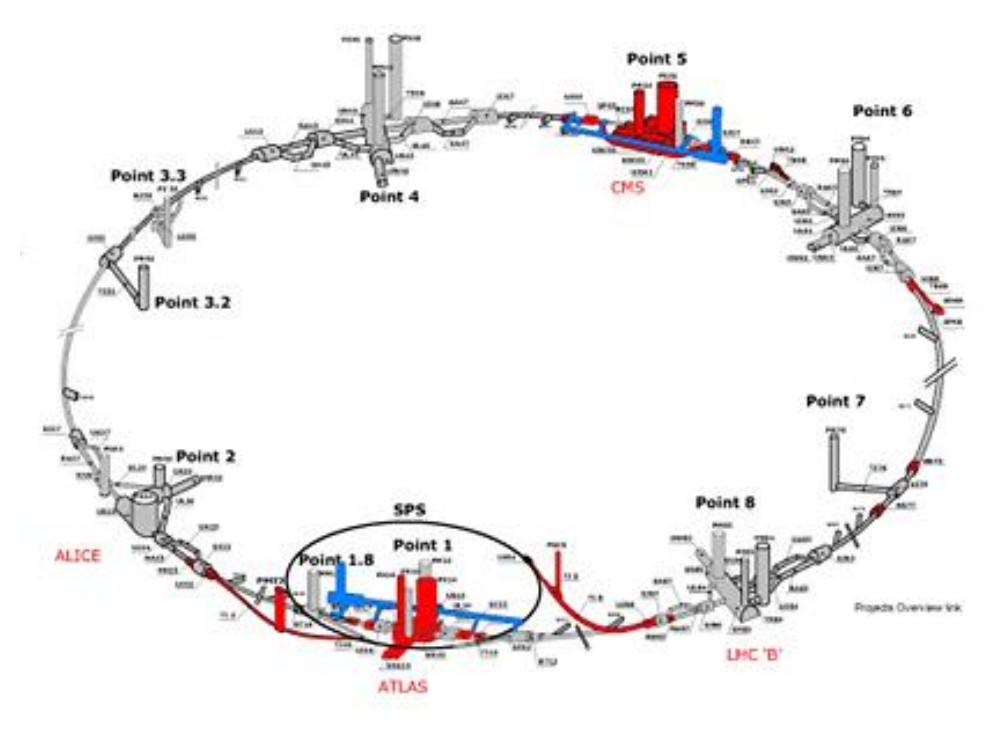


Figure 4.1.4 Layout of the underground structures that host the High Luminosity – LHC project: definition of the infrastructures added (blue).

By 2030, an upgrade of the particle accelerator complex will be developed by means of the construction of the *Future Circular Collider* (FCC) project: the principal structure of the FCC-hh collider is a quasi – circular tunnel composed of arc segments interleaved with straight sections with a diameter of 5.5 m and a circumference of 97.75 km (Figure 4.1.5) [59]. Approximately 8 km of bypass tunnels, 22 shafts, 14 large caverns and 12 new surface sites are also planned.



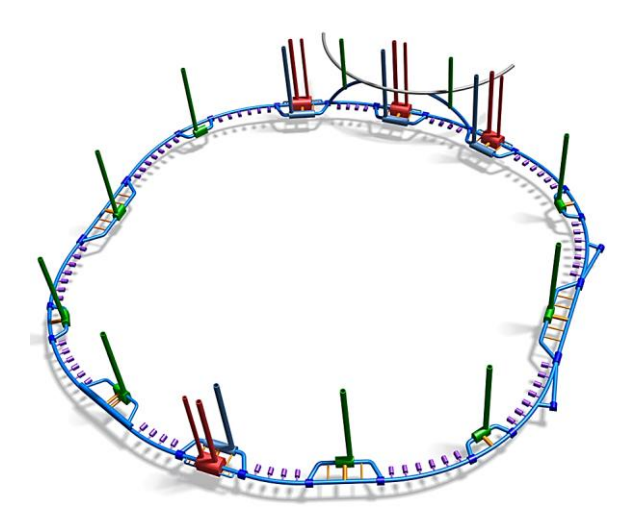


Figure 4.1.5 Top: study boundary (red polygon) showing the main topographical and geological structures, LHC (blue line) and FCC tunnel trace (brown line). Bottom: 3D not-to-scale schematic of the underground structures [59].

4.2 The Geneva Basin: geographical and geological frameworks

CERN site is located within the Geneva Basin, a Swiss French transnational zone located at the southwestern extremity of the North Alpine foreland molasses basin. (Figure 4.2.1). The Greater Geneva Basin extends over about 2.200 km² from the southwestern part of Lake Geneva nearby the city of Nyon toward the city of Annecy in France. It is delimited by mountains at North (Jura), West (Vuache) and South (Saleve), which were generated by tectonic structures uplifted during the final phases of the Alpine orogeny 5-10 million years ago. The basin consists of a low relief area confined between the Saleve Mountain to the SE and the folded Jura chain to the NW resulting from the interplay between tectonic deformation associated with the Alpine foreland emplacement and the profound landscape modifications associated with Pleistocene glaciations and subsequent post-glacial processes.

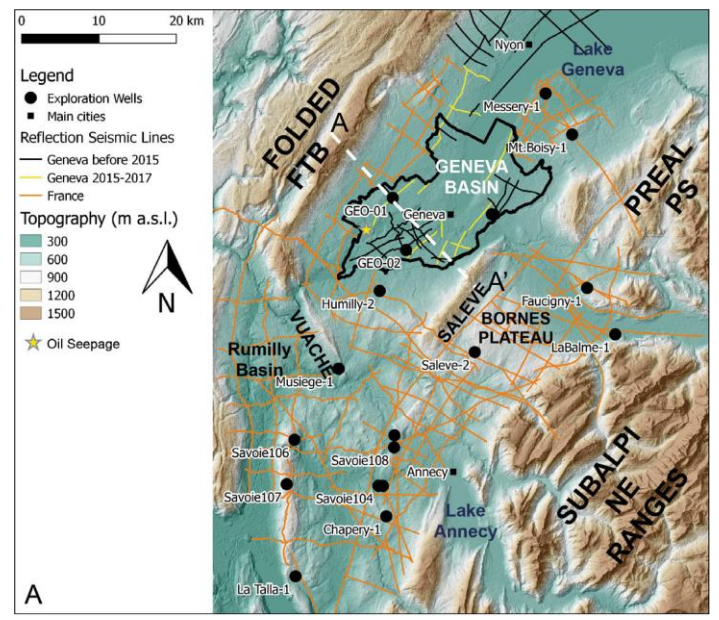


Figure 4.2.1 Geographic map of the western Switzerland and surrounding France with indication of wells and seismic lines available in the area of study. A cross-section A-A' is considered in Moascariello [60].

The geology of the basin, partly cropping out in the surround reliefs (Saleve Mt. to the SE, the Vuache Mt to the SW and the Jura to the NW) consists mostly of a thick Mesozoic sedimentary succession, made of evaporites at the base and a succession of thick carbonates and marls succession formed at the southern margin of the European continent on the northern margin of the Tethys Ocean. The Mesozoic sequence was deposited on top of a Palaeozoic crystalline basement with down-dropped graben filled with continental siliciclastic sediments of Permian and Carboniferous age because of the Variscan orogeny and rifting linked to post-orogenetic collapse (Figure 4.2.2).

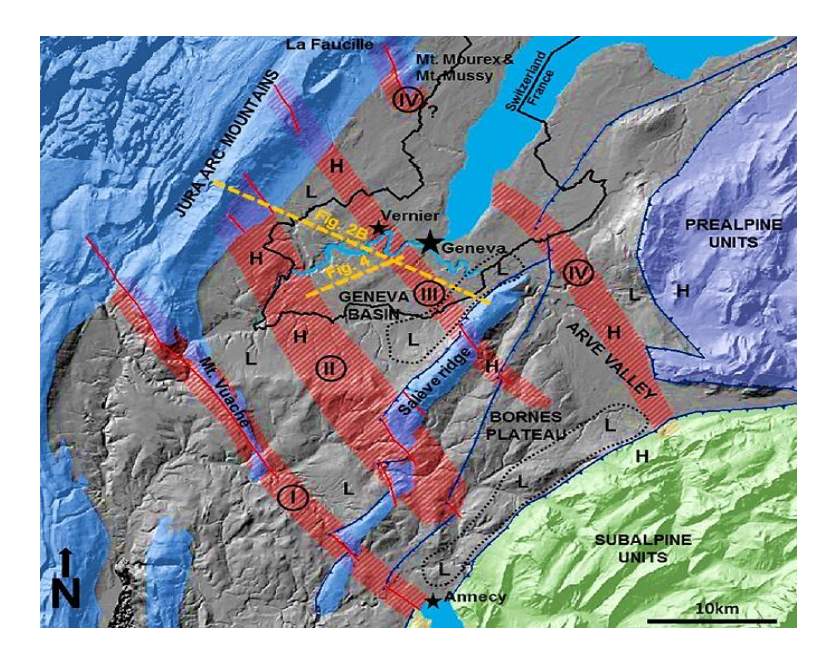


Figure 4.2.2 Mesozoic-Cenozoic structural scheme of the Greater Geneva Basin illustrating: a) SW-NE Mesozoic lows associated with underlying Permo-Carboniferous basins at the front thrust of the Salève ridge and Subalpine/Prealpine units. b) Zones affected by the NNW-SSE trending wrench fault systems crossing the Geneva Basin and Bornes Plateau: (I) Vuache; (II) Cruseilles; (III) Le Coin; (IV) Arve. c) Top Mesozoic structural highs (H) and lows (L) associated with underlying Permo-Carboniferous tectonics. [61]

The top of the Mesozoic sequence (Lower Cretaceous in age) is marked by a regionally extensive erosional surface which formed during the general uplift of the foreland basin during the Alpine compression. Above this surface, Oligocene siliciclastic Molasse are overlain by heterogeneous Quaternary glacial and glaciofluvial deposits. The generic stratigraphy of the Geneva Basin and surrounding area and synthetic geological profile across the Geneva Basin are shown in Figure 4.2.3. A short summary of the main stratigraphic element and their main paleogeographic and tectonic significance are summarized here below.

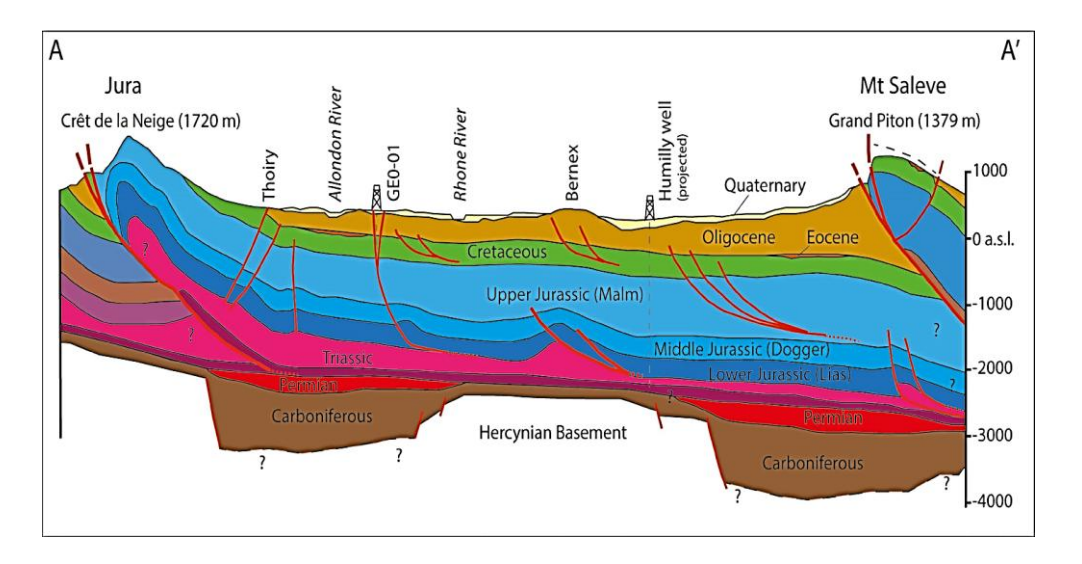


Figure 4.2.3 Geological section crossing the Geneva Basin from SE to NW summarizing the key stratigraphic and structural elements present in the basin [60].

The Geneva Basin lays over a crystalline basement resulted from the Palaeozoic Variscan orogeny (c.a. 480-250 Ma, Matte, 2001). The latter stages of this orogeny related to the continental collision between the Gondwana to the southeast and Laurentia-Baltica to the northwest, forming the supercontinent of Pangaea. After the main Variscan orogeny, the dextral translation of Gondwana and Laurussia and the reorganization of the asthenospheric flow patterns, caused the collapse of the orogeny and the thinning of the lithosphere and the setting of a trans tensional and tectonic regime together with a strong regional thermal subsidence. In the Geneva

Basin, predominantly NE-SW trending, elongated half-grabens were created. Sediments deposited during the Permian and Carboniferous were found locally in these structures in the Humilly-2 well in the Geneva Basin and other location in the Swiss Plateau, which consists of mainly lacustrine and fluvial deposits eroded from the crystalline basements. Under the humid conditions in the Carboniferous times, coal beds were formed, intercalating with the above deposits. No Permian sediments were observed yet in the Geneva Basin. However, their occurrence is possible as these were found in the deeper subsurface in the surrounding region (i.e. Noville-1 well). The top of the basement is characterized by an angular unconformity on which Triassic sediments were deposited.

The Triassic series, unconformably overlying the basement and Permo-Carboniferous rocks, is generally divided into three intervals, namely, the Buntsandstein (continental sandstone), Muschelkalk (marly limestones, anhydrites and dolomites) and Keuper (anhydrite, salt and shale). The Early to Middle Triassic (Buntsandstein to Muschelkalk) marks a marine transgression which formed a shallow epicontinental sea. The later deposition of dolomites and evaporites (Late Triassic, Keuper) suggests a restricted marine condition with limited connection to the Tethys. The Keuper evaporites are commonly thought to represent an important decollement layer which served in the later formation of the Jura fold and thrust belt (FTB). The Jurassic sequence starts with a marine transgression, marked by the marly limestones deposited during the Liassic (Lower Jurassic) and the Dogger (Middle Jurassic) in a distal marine environment. In this period (Toarcian), anoxic condition occurred enabling the accumulation and preservation of organic matter-rich marine deposits. The Upper Jurassic (Malm) was characterized by an important regional marine regression after which shallow carbonate platforms, with the accumulation of massive limestone and patch reefs occurred. The Early Cretaceous is characterized by a shallow and warm water environment, with several emersion-drowning episodes caused by low amplitude sea-level fluctuations. During this time, massive and bioclastic limestones with marly intervals were deposited. Subsequent wide marine transgression led to the deposition of pelagic chalk and limestones. These deposits were then completely eroded when the Geneva Basin came to emersion, which has caused the large-scale karstification in the Urgonian limestones.

According to Moscariello in [60] and Clerc et al. in [61], in early Cenozoic times (Eocene-Oligocene), the basement uplift associated with the Alpine orogeny genetically associated with the convergence of Eurasian and African plate, exhumed the uppermost Mesozoic series. The latter is therefore marked by a major unconformity which was estimated to have removed 1500-2000 m of sequence. Karsts and fractures on the top Mesozoic were filled with Eocene lateritic sediments and some reworked Aptian-Albian sediments. Sediments eroded from the rapidly uplifting Alps were deposited in the Geneva Basin, which was at a flexural foreland position at the time. In the Geneva Basin, the Lower Freshwater Molasse (LFM) which comprises alternations of sandstones and marls, directly onlaps the Early Cretaceous units or the Eocene lateritic sediments. The Upper Marine Molasse (UMM) and the Upper Freshwater Molasse (UFM) are not preserved in the Geneva Basin as they were either removed during the uplift of the Jura chain (Miocene-Pliocene) and/or the Pleistocene glacial advances or not deposited in this area. The Oligocene Molasse deposits are in fact overlain by Quaternary glacial, glacio-lacustrine and lacustrine sediments which account for a period punctuated by several episodes of glacial progradation and retreat. Following the last Glacial Maximum, the establishment of the present-day fluvial network shaped the landscape to the present configuration (Figure 4.2.4).

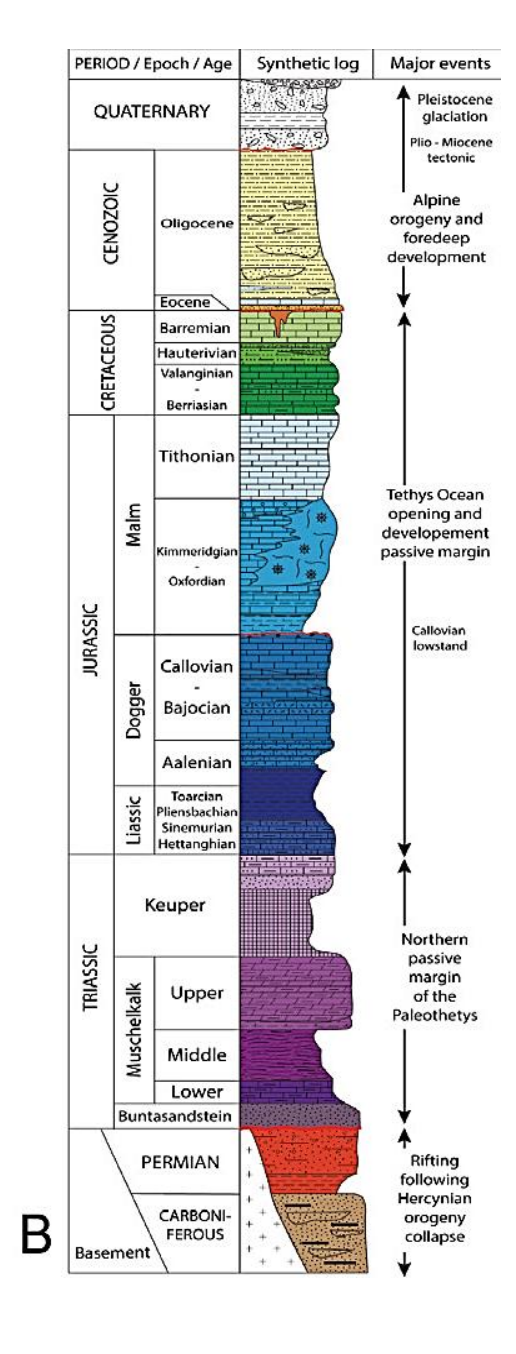


Figure 4.2.4 Summary stratigraphy of the Swiss Plateau in the Geneva Basin area [60].

4.3 Seismic hazard and site response

According to Antunes et al. in [62], a seismological setting of the Great Geneva Basin is presented. More in detail, two main sets of faults affect the GGB accommodating the NW–SE Alpine compression.

The first one consists of a series of thrust faults, NE–SW orientated, located in the Jura and in the subalpine Molasse that delineates the southeastern rim of the GGB. They are linked with the presence of reactivated Permo-Carboniferous lineaments.

The second set corresponds to sinistral strike-slip fault systems orientated NW–SE, laterally accommodating the NW–SE shortening (red area). From South to North, geological investigations identified 4 main fault areas, namely, Vuache, Cruseilles, Le Coin and Arve (Figure 4.3.1)

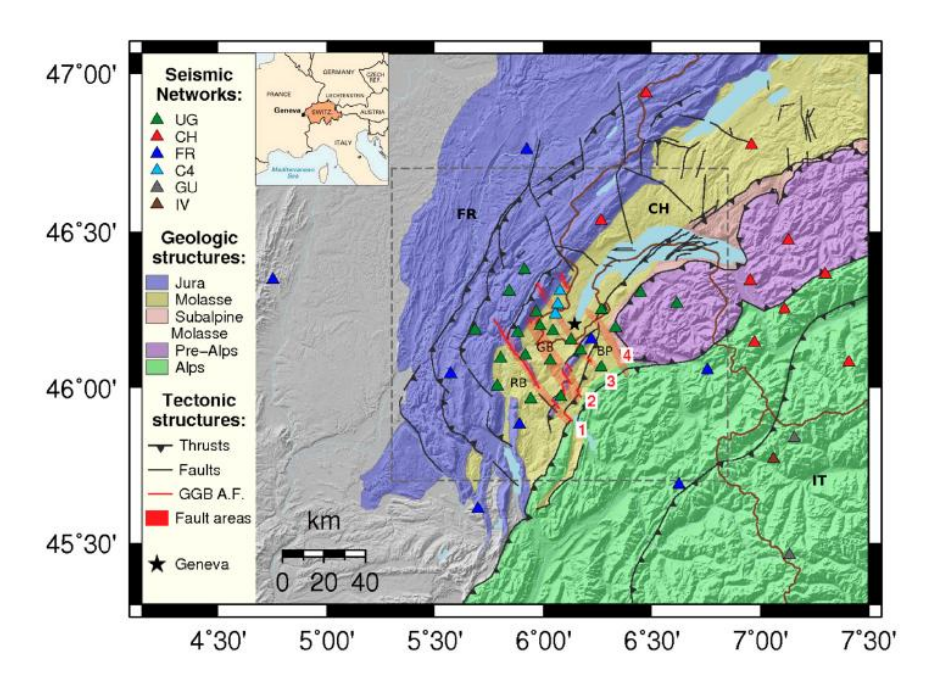


Figure 4.3.1 Simplified geological map of the region surrounding the Greater Geneva Basin (GGB) together with the red zones representing the 4 major fault areas in the GGB: 1, Vuache; 2, Cruseilles; 3, Le Coin and 4, Arve faults. The red lines represent the active fault segments in the fault area.

Despite the proximity to the tectonically active western Alpine front, little is known about the micro-seismic activity taking place in the GGB and surrounding regions.

Before 1975 the available earthquake information was based purely on historical documents mentioning shaking and infrastructure damage and allowed rough magnitude and intensity estimations. The location of these events is biased by the location of historical villages and the available written documentation. Such data must be considered with errors of several dozens of km (e.g. 20–50 km). Historical records show that the area was affected by seismic events with an intensity of up to about VII, as described in Fah et al. in [63]. The shores of Lake Geneva were flooded by at least one lake tsunami possibly caused by an earthquake in 563 AD. The largest seismic events occurred along the Vuache fault, a well mapped sinistral strike slip fault that accommodates the westwards rotation of the Alpine front.

Figure 4.3.2 displays the reported background seismicity from both historical (since 1500 until 1975, ECOS-09 catalogue), and instrumental seismic catalogues (from 1975 to 31st August 2016). [63]

From 1500 to 1850, 16 earthquakes were historically documented in the Canton of Geneva and nearby regions, with estimated intensities of IV-V that can be related to likely magnitudes of about 3–4, according to [63].

The Swiss Seismological Service (SED) has been operational since 1850 and reported 50 earthquakes in the region until 1975. After 1975, the seismic network of Switzerland was dense enough to obtain the reliable detection and location of earthquakes.

Until 2008, the magnitude displayed in the ECOS-09 catalogue corresponds to Moment magnitude (Mw), for a total of 146 earthquakes. After 2009, the magnitudes of the SED public catalogues are displayed as local magnitudes (Ml/MLh), and account for a total of 22 earthquakes. [63]

In 1996, an ML5.3 earthquake occurred at the southern tip of the Vuache fault, followed by an aftershock sequence referred to as the Epagny sequence. The source mechanism of the major event was a sinistral strike-slip. These events led to questioning whether the Vuache fault could generate strong magnitude events. [64]

Apart from this area, the seismicity in the GGB is rather diffuse. Most of the events occur within the first 15 km depth. The seismicity located at the northeastern-most part of the GGB is likely associated with the Alpine thrusts front, and to the south with the Vuache fault and thrusts at the Jura mountains.

A few events (<10) can be found near the Cruseilles and Arve faults indicating that these faults could also still be active.

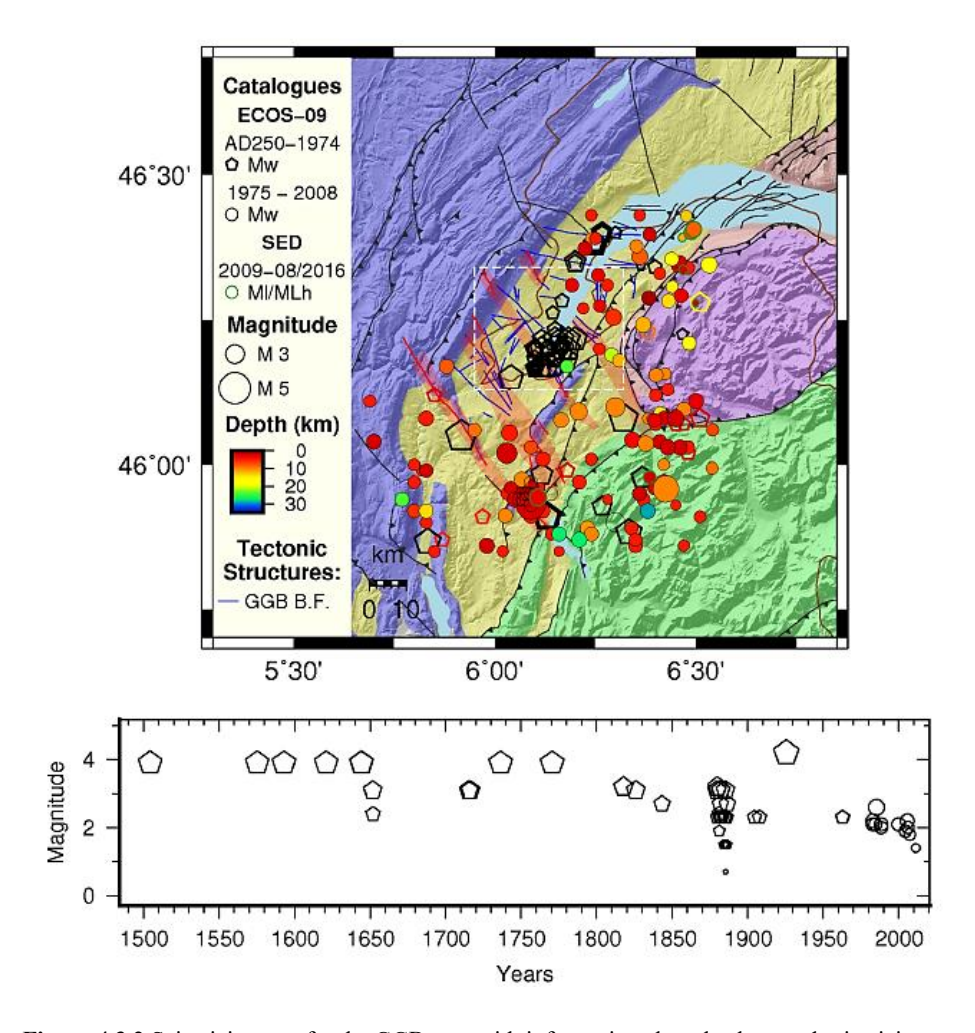


Figure 4.3.2 Seismicity map for the GGB area with information about background seismicity according to public catalogues. Historical seismicity is represented as black pentagons, the size corresponding to the estimated Mw. Instrumental seismicity is represented as circles, size representing Mw or ML (depending on the catalogue) and color representing the depth.

According to the *Décret du 13 septembre 2000* in [65] new constructions or constructions submitted to important modifications in seismic regions shall comply with the applicable seismic design requirements.

Located on the border between France and Switzerland, the seismic classification of the Point 5 site is based on the indications given in the *Décret du 22 octobre 2010* in [66], according to which:

- French territory is divided into five seismic zones from very low seismicity (zone 1) to strong seismicity (zone 5) (Figure 4.3.3Figure 4.3.3).
- Buildings, equipment and installations 'à risque normal' are those for which the consequences in the event of an earthquake are limited to an area within the vicinity, as well as buildings, equipment and installations for which the consequences in case of earthquake may have an impact outside the vicinity, due to explosions, pollution or fire, are classified 'à risque special'.

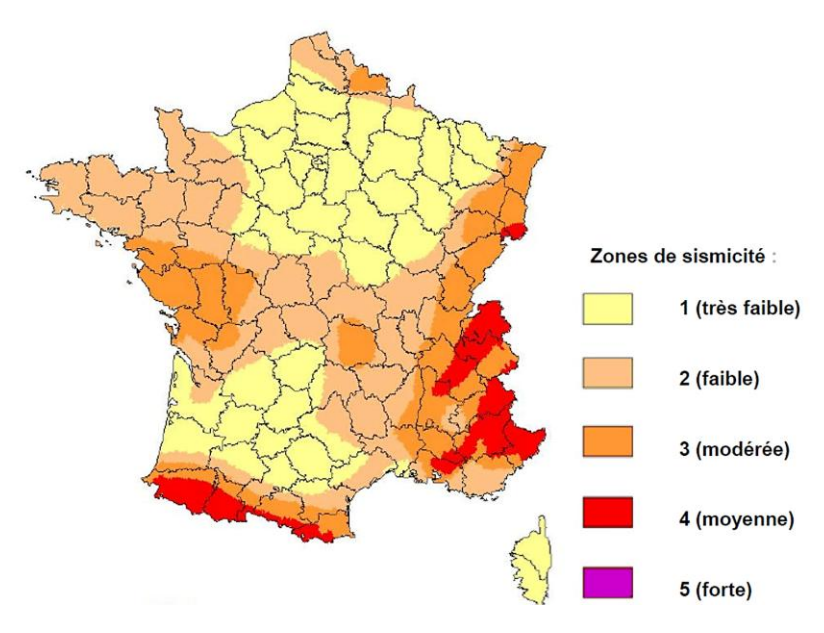


Figure 4.3.3 Seismic classification of French municipalities [67].

According to the *Arrêté du 22 octobre 2010* in [68], LHC point 5 is in zone 3 ("sismicitè modérée"), as shown in Figure 4.3.4, and the seismic action,

defined in terms of reference peak ground acceleration on type A ground, is about 0.090g, 0.112g, 0.135g and 0.159g respectively for return periods of 243, 475, 821 and 1303 years.

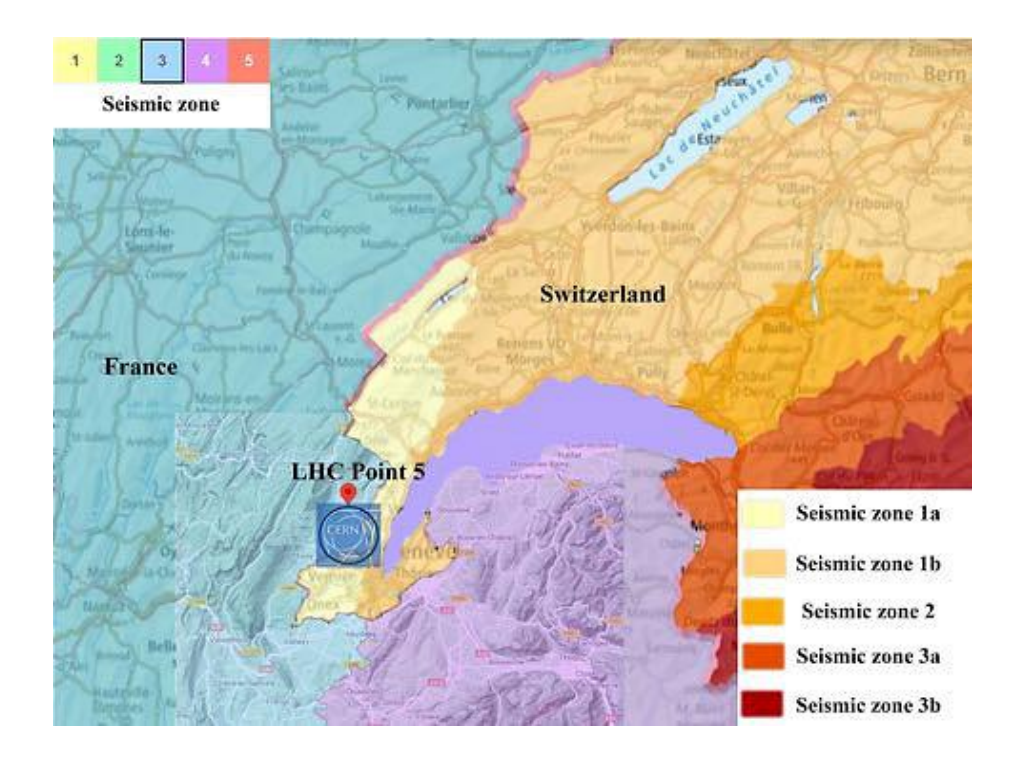


Figure 4.3.4 LHC ring: seismic classification and identification of Point 5 where CMS experiment is located.

4.4 Point 5: geotechnical investigations

At Point 5, the existing LEP tunnel is located predominantly within the molasse, at depths between 50 and 100 m below ground surface.

Geotechnical investigations carried out during several campaigns between 1995 and 2015 were used to define soil stratigraphy and geotechnical characterization of soils increasingly accurate [67].

The site investigation package during the 1996, within the design of the underground facilities characterizing the LHC project, involved drilling of 14 boreholes, denoted as "SLHC", distributed at various locations across the CMS site. During these drillings, seven boreholes (SLHC 30-36) were conducted to penetrate the molasse to the proposed cavern depth to investigate the detailed geology. Of these, four boreholes were selected to represent the lithological profile to the cavern depth.

The general soil profile at the Point 5 site can be described, from surface downward, as follows:

- a limited thickness (up to 7 m, generally less) of fill (put in place during the construction of the now existing buildings and facilities) and colluvial soils.
- glacial deposits, formed by fluvial-glacial soils resting on heterogeneous wurmian moraines. These deposits have overall thickness up to 50 m approximately.
- from the bottom of the morainic deposits to the investigated depth, red molasse (Chattian age, Tertiary) was encountered, which is typical in the Geneva basin.

4.4.1 Soils

More in detail [67], at Point 5 several geological and geotechnical units in the subsoil were identified (Figure 4.4.1):

- Cover soils reach a maximum thickness of 8 m:
 - heterogeneous fill: mainly formed of marl-sandstone molasse, moraines with varying content in cobbles and some sandy-gravelly layers.
 - *Colluvium*: mainly sandy silt (40-75 %), clayey (0-10 %), light brown to brownish, lumpy, blackish-stained, with pebbly or sandy thin beds, stiff to strong, quite plastic except when sandy.
- Fluvio glacial soils present an overall thickness quite variable, mostly estimated in the order of 5-10m:
 - Silty gravel: it's a heterogeneous, semi-cohesive, compact to very compact sandy (20-35 %), slightly clayey (< 10 %) gravel layer in abundant (10-15 %) silt paste; light brown, rich in round cobbles and boulders up to few decimetres' diameter (max observed diameter ~20cm, but larger diameter may be expected). The unit includes fine beds without cobbles and boulders, consisting of sandy silt or yellowish silty clay, with occasional organic traces, brownish, mostly weak, wet. Low permeability.
 - *Sandy gravels*: it's a heterogeneous layer, low or null cohesion very compact, overall pervious, consisting of sandy (20-40 %) slightly silty (<10 %) gravels, beige to greyish-beige, rich in round variable size cobbles, with some isolated boulders.
- Wurmian moraines have a typical overall thickness of 15-20m:
 - Silty-clayey moraine: slightly sandy, quite clayey (10-15 %) silt (40 -50 %), grey-beige to grey, massive, plastic, with few cobbles and small boulders; it's a generally very strong, almost impervious layer.
 - *Silty moraine:* sandy to gravelly, slightly clayey (<10 %) silt (30-40 %), grey to brownish-beige, massive, medium plastic, with frequent round cobbles and some small (maximum observed diameter 20cm) boulders. Very strong, very consistent, very little pervious.

- Silty-gravelly moraine: sandy (25-45%) gravel immersed in a generally high percentage of clayey (0-10%) silt (5-35 %), including frequent cobbles (typical diameter 6-8cm), stones and small boulders (maximum observed diameter 20cm, but larger diameters are to be expected), often grouped in layers. It's a very heterogeneous layer, which appears to be a transition material between the silty moraines and the morainic cobbles ("cailloutis"), with some characteristics of both. Very consistent, generally cohesive, little pervious.
- Ancient alluvial soils (deep morainic cobbles or "cailloutis") are discontinuous and reach a thickness of up to approximately 20 m: slightly to medium silty (2-20 %), sandy (15-25 %) gravels, grey or beige, including frequent cobbles (diameter 5-10 cm) and stones (frequent diameter 15cm, maximum observed diameter ~20 cm, but larger diameters are to be expected). It's a very dense, heterogeneous, overall pervious layer, though it shows neat differences with depth.

4.4.2 The Molasse

At the bottom of the morainic units lays the sedimentary tertiary molasse rock mass, where the underground structures under design are to be excavated.

The molasse can be described as soft rock and is composed of irregular alternations of several lithotypes, from marls to sandstones and marly limestones, of different grain-size grading with a thickness ranging from a few centimetres to a few metres and their stiffness can vary from one layer to another.

Based on lithology, three main "groups" can be distinguished within the molasse:

- The *marls* are micro fissured rocks with various amounts of clay (40-60% of illite, 20-25% of chlorite), calcite and quartz. They have smooth to slickenside closed and poorly cemented joints with a spacing smaller than 60 mm. These marls are subjected to swelling, slaking upon contact with air and water, and spalling. Three sub units were identified as follows:
 - Very weak marls mainly made from the diagenesis of highplasticity clays. It is characterized by numerous closed, polished, discontinuous and multi-directional micro-fissures, which give the rock isotropic characteristics. Its mineralogy gives it low stiffness and ductile behaviour. This marl is subjected to swelling, slaking upon contact with air, and spalling.
 - Weak marl is composed of laminated marl and is composed of 45-60% of clay, 15-30% of micro-crystalline quartz, and 20-30% of calcareous minerals. The micro-fissures are present but scares and are mostly in a single direction inferring an anisotropic structure to the unit. The weak marl is also subjected to swelling, slaking upon contact with air, and spalling.
 - Medium weak marl has similar proportion of clay (20-45%), quartz (20-40%) and calcite (20-30%). It is well cemented, which increases its strength and stiffness.

- The *sandstones* ("*grès*") are well-cemented silts and sands. The rock mass is homogeneous with a limited number of visible, rough and widely spaced joints and the spacing is usually greater than 1 m. It is mainly composed of feldspar and silica but can contain some clay and calcite in variable amounts. Three sub-units were identified as follows:
 - *Weak sandstone* is made of fine-grained poorly cemented granular materials with some clay.
 - Medium-strong sandstone is composed of well-cemented coarse-grained materials. It has good mechanical properties with rare discontinuities.
 - Strong sandstone has a composition similar to medium-strong sandstone but better-cemented grains with fewer discontinuities. [67]

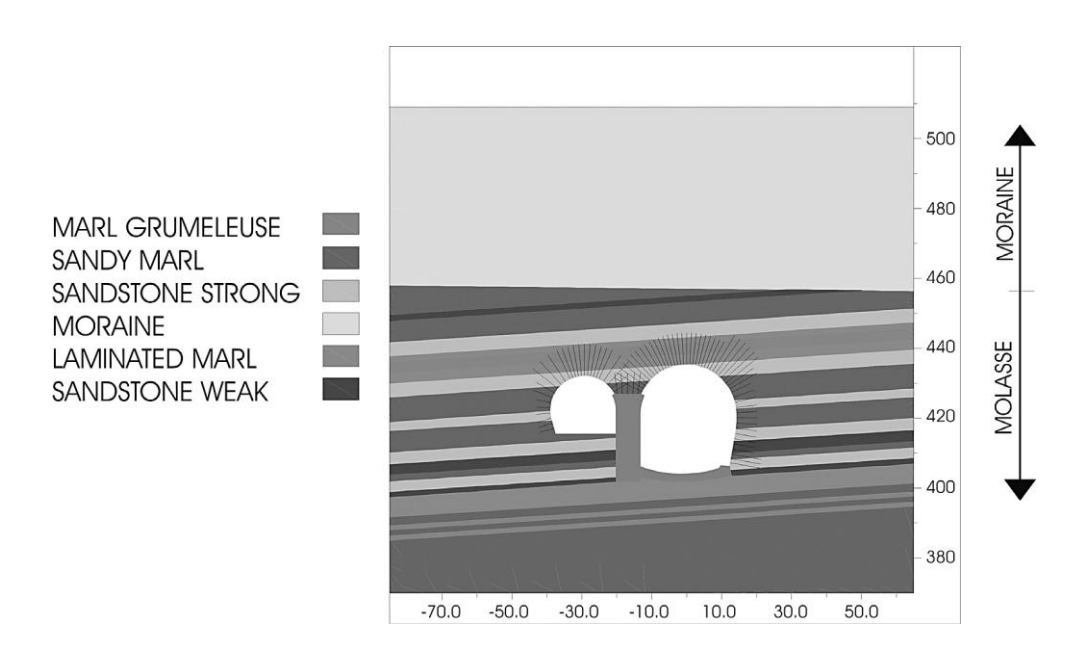


Figure 4.4.1 Point 5: two – dimensional model with geotechnical layers [69].

As discussed in more detail in Section 5.1 on LHC monitoring stations, the CERN infrastructure has a few accelerometer sensors whose measurements can be used to validate the numerical model.

More specifically, there is an accelerometer located inside the LHC tunnel, which is about 90 meters below ground level, i.e., in an area substantially outside the Molasse alternation layer.

To take this configuration into account in the validation phase, the positioning of the tunnel in the numerical model was modified from that shown in the survey shown in Figure 4.4.1 and in Figure 4.4.2.

In other words, to simulate more realistically the dynamic effects of the soil layers on the cavity response, it was chosen to place the numerical cavity below these layers, in a condition like that of the LHC tunnel where the survey is carried out to be used as a benchmark.

The cavity was then shifted downward about 30 meters (Figure 4.6.1), thus avoiding interference with wave propagation in the more superficial layers.

Of course, eventual three-dimensional modelling may also include the section of the LHC tunnel where the instrument is located, allowing the cavity to be represented at its true depth.

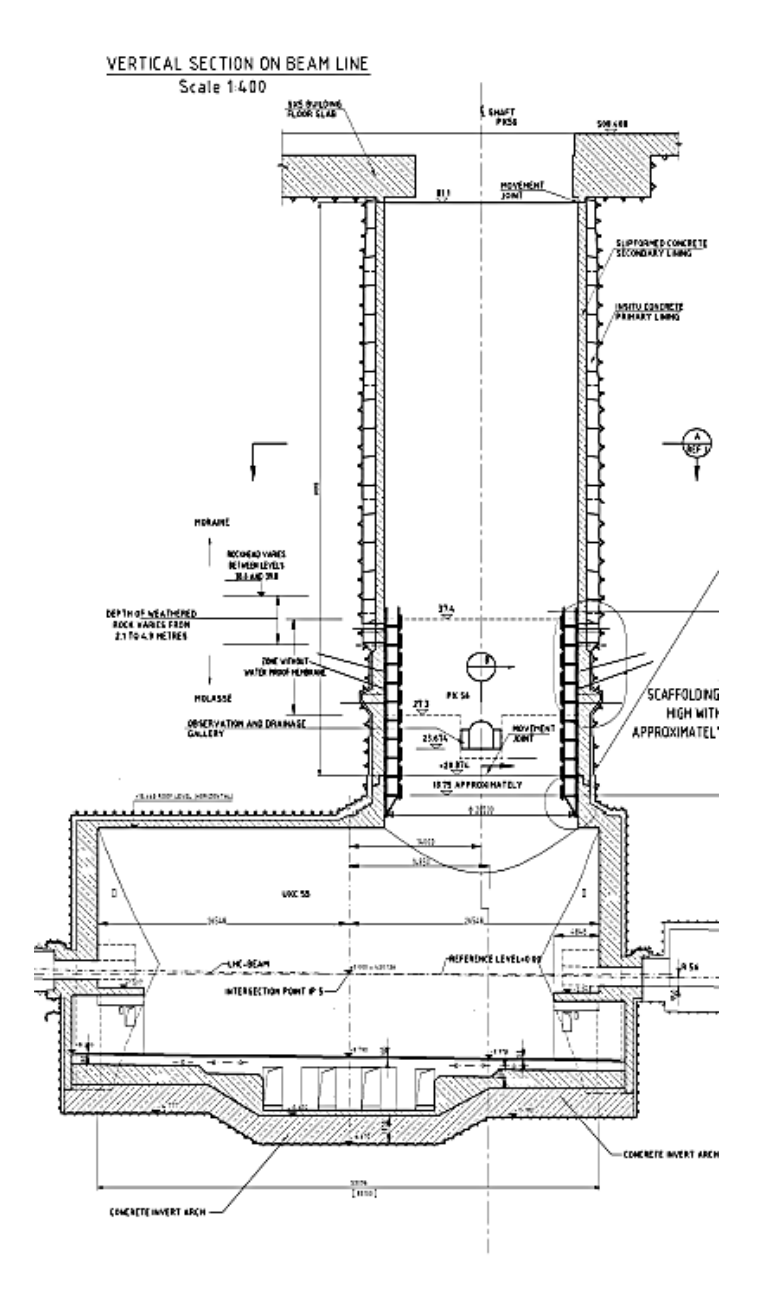


Figure 4.4.2 Vertical section made at Shaft PX54 showing the positioning of the LHC beam in respect to the positioning of the UXC55 experimental cavity.

4.4.3 LHC case study: geotechnical model

On the basis of previous studies [55], for modelling purposes the geological stratigraphy characterizing Point 5 site have been further simplified into three basic rock mass units and a homogeneous top moraine sedimentary deposit, to better represent the structural response within the existing ground conditions. For the sake of simplicity of the geotechnical model, and due to the relative importance of the molasse rock compared with the overlying moraine deposits, the moraine stratigraphy was simplified to a single layer with an average strength and deformation properties. On the other hand, the engineering behaviour of the molasse rock formation can be closely approximated to a stratified, horizontally bedded rock mass.

The rock mass surrounding the underground excavation is highly influenced by the degree of excavation disturbance and the extent of construction-induced over stresses.

A section type of soil layers profile has been idealized as follows (Figure 4.4.3):

- Upper Moraine deposits layer:
 - Thickness: 50 m.
 - \blacksquare 100 m/s < Vs < 400 m/s.
- Molasse rock layers having variable stiffness degree, more in detail:
 - Weak Molasse rock:
 - o Thickness: variable.
 - o Vs: 900 m/s.
 - Medium Strong Molasse rock:
 - Thickness: variable.
 - o Vs: 1200 m/s.
 - Strong Molasse rock:
 - o Thickness: variable.
 - o Vs: 1500 m/s.

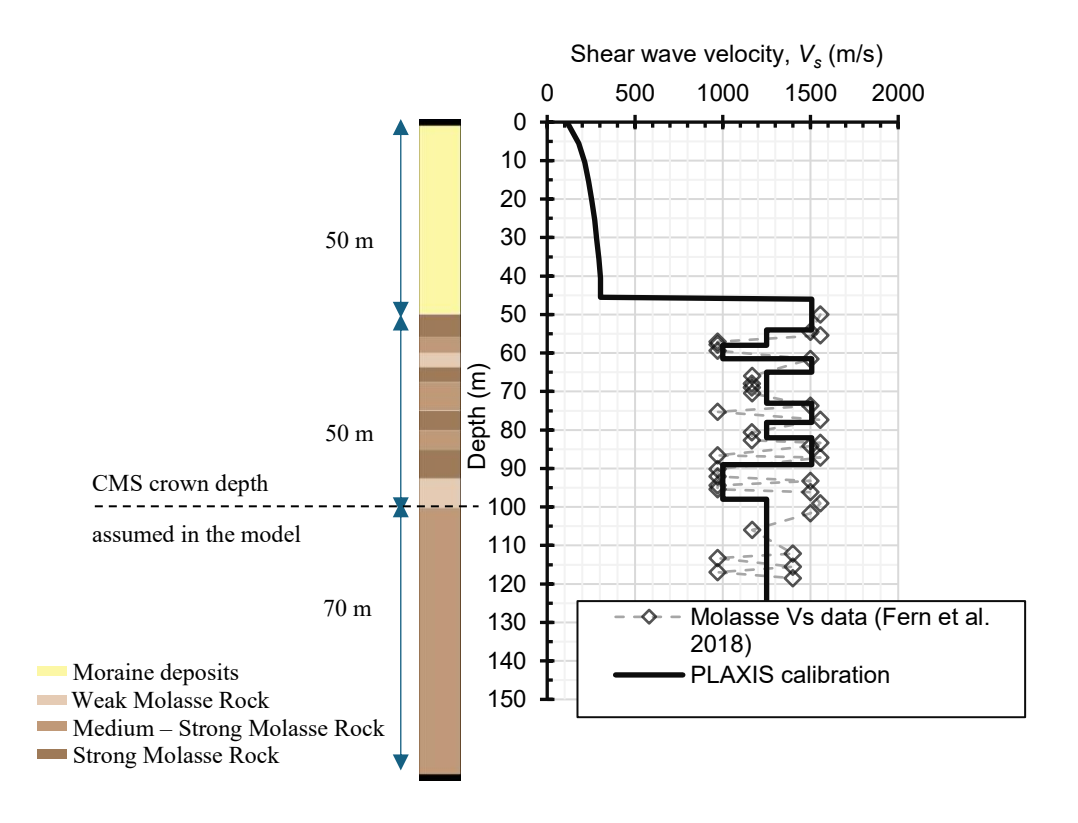


Figure 4.4.3 Point 5: stratigraphic profile from reference geotechnical investigations up to caverns' depth (on the left) and a shear wave velocities comparison between [55] and calibration done by means of PLAXIS software.

The constitutive behaviour of the successive rock and moraine layers were modelled using a Mohr-Coulomb failure criterion for the rock behaviour within PLAXIS software, i.e. a non-linear elastic-plastic isotropic hardening hysteretic model named Hardening Soil model with small strain stiffness (HS-small). This was selected as the strain range in which soil can be considered truly elastic, i.e. where recover from applied straining almost completely, is very small. With increasing strain amplitude, soil stiffness decays nonlinearly (Figure 4.4.4). According to [55] and [70] the shear modulus reduction curves

 (G_s / G_0) in the HS-small model were calibrated to achieve a reasonable agreement with the available degradation curves in the literature for the Geneva basin materials reported by [71]. This was manipulated by adjusting the shear strain at 70% of the initial shear modulus ($\gamma_{0.7}$) up to an appropriated value. Figure 4.4.4 compare the numerical HS-small stiffness degradation and damping parameters for the moraine and molasse rock against literature curves. On the basis of [55], the damping initial values assumed for Moraine deposits and Molasse rock were equal to 0.5% and 2.5% respectively.

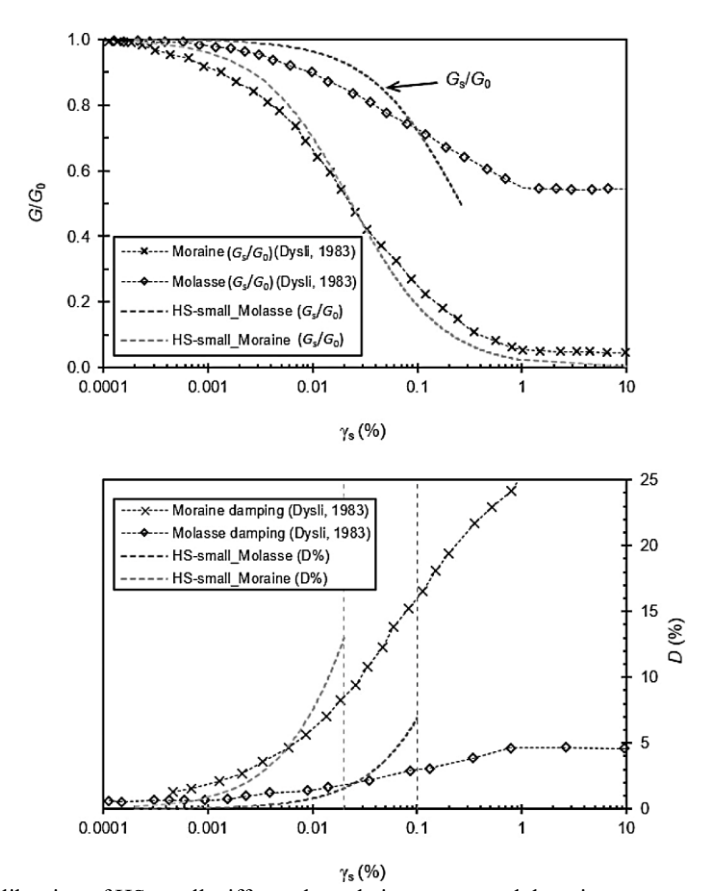


Figure 4.4.4 Calibration of HS-small stiffness degradation curves and damping parameters against the available curves in the literature for the Geneva basin [70]

4.5 The underground structures at Point 5: an overview

The Point Five site is in Cessy, a small village in the French side of the LHC. The ground surface lies at an elevation of 509 m above the Sea Level and slopes gently to the south-east. A single cavern (UJ56) and shaft (PM56) are already existing facilities as part of the old LEP accelerator, connected with the existing LEP tunnel. The underground structures at Point 5 consist of two large access shafts, the PX56 and PM54 with internal diameters of 20.4 m and 12.0 m, with several small service galleries, and enlarged tunnel connections to the existing LEP tunnel network (Figure 4.5.1, Figure 4.5.2, Figure 4.5.3).

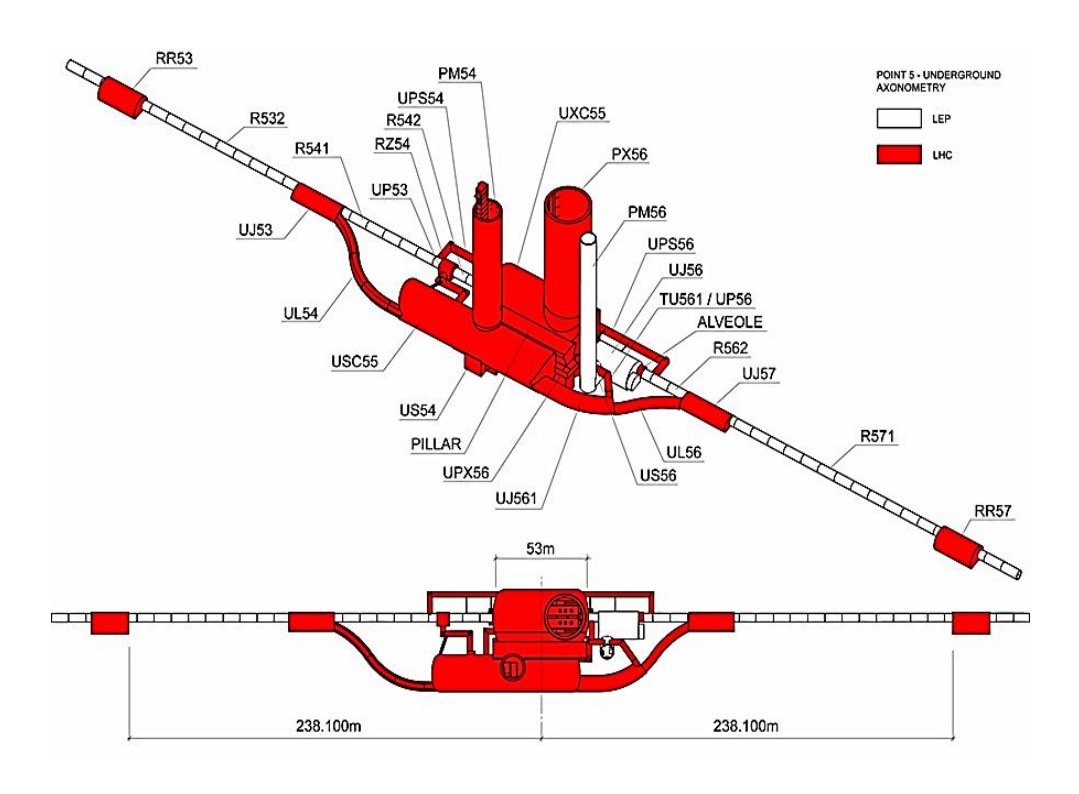


Figure 4.5.1 Point 5: 3D model representing the underground facilities as part of the old LEP accelerator (white) and the civil structures as part of the LHC project [72].

Two large parallel caverns have been added as part of the LHC project and are connected to the surface by two large diameter shafts: an Experimental Cavern UXC 55, which will later host the 15,000 tons CMS-Detector has a width of 27 m, a height of 34 m and a length of 53 m. The parallel-located Service Cavern USC 55 will later, among lots of other equipment, host the extensive computer site for control and evaluation of experiments. It has a width of 19 m, a height of 17 m and a length of 85 m (Figure 4.5.4). To reduce the total length of optical cables, required for data transfer between Experimental and Service caverns, it was a requirement by CERN to keep the distance between the two caverns to an absolute minimum, representing a major cost factor. Due to the total span of the cavern complex of more than 50 m a massive concrete pillar of 7 m width had to be designed to support loads induced by the wide spanned rock canopy [69].

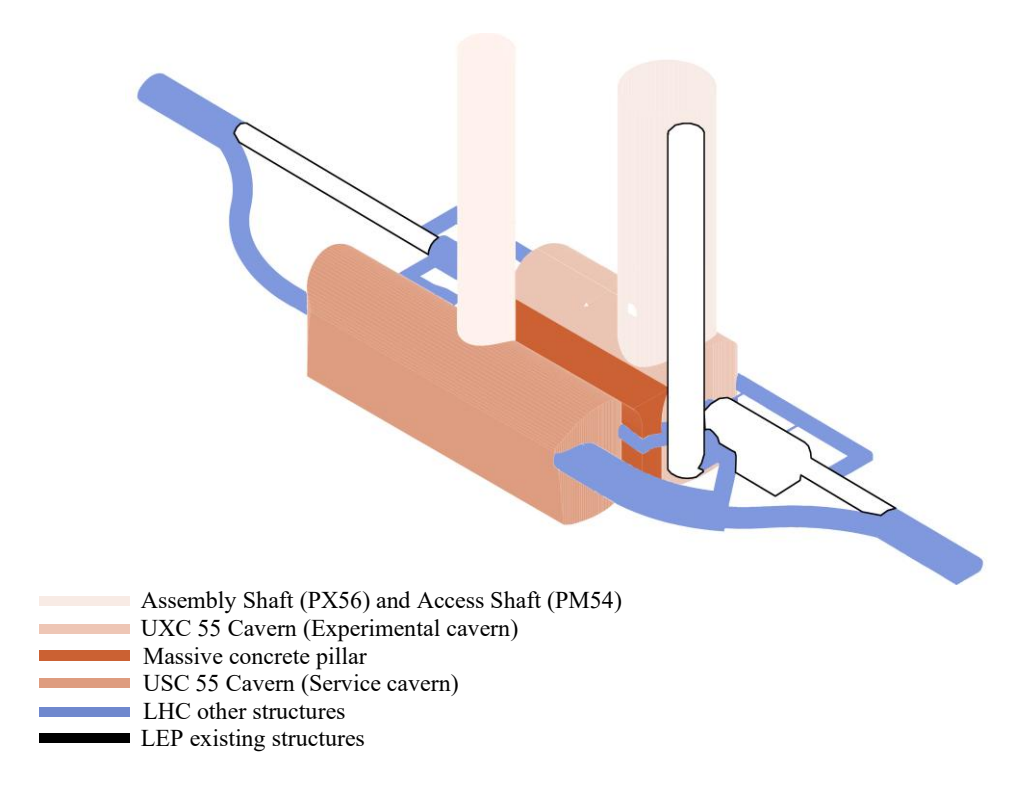


Figure 4.5.2 Point 5: 3D model representing LHC underground facilities, compared to LEP existing structures.

Each of the caverns is connected to the surface by a central shaft in the cavern roof. The permanent access shaft above the Service cavern has a diameter of 12 m. The ventilation and detector installation shaft above the experimental cavern has a diameter of 21 m. The size of this shaft is guided by requirements of the largest size of detector rings, which have been preassembled at the surface and then descended the shaft into the cavern in parts of up to 2000 tons. The remaining elements of Point 5 include supplementary facilities such as junctions, cryogenic chambers, personal access tunnels and survey galleries for monitoring and measuring purposes - utilized during construction as well as for the operational phase.

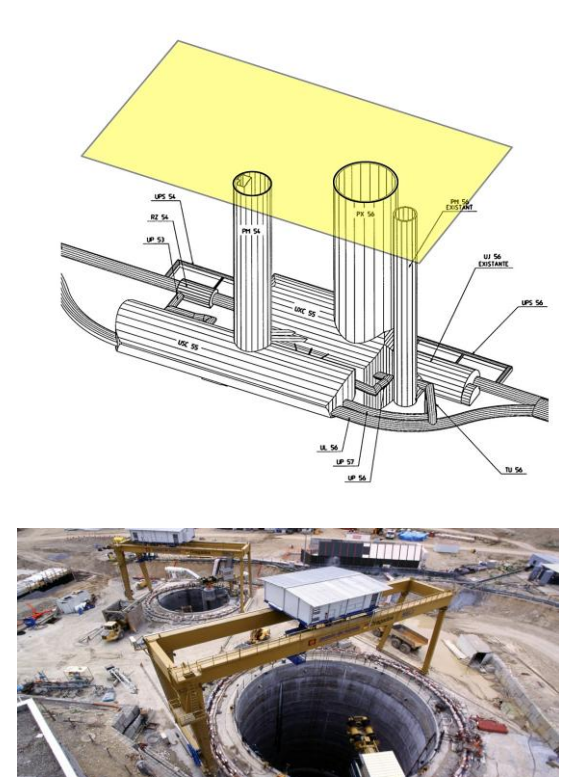


Figure 4.5.3 Point 5: access by means of PM54 and PX56 Shafts [72].

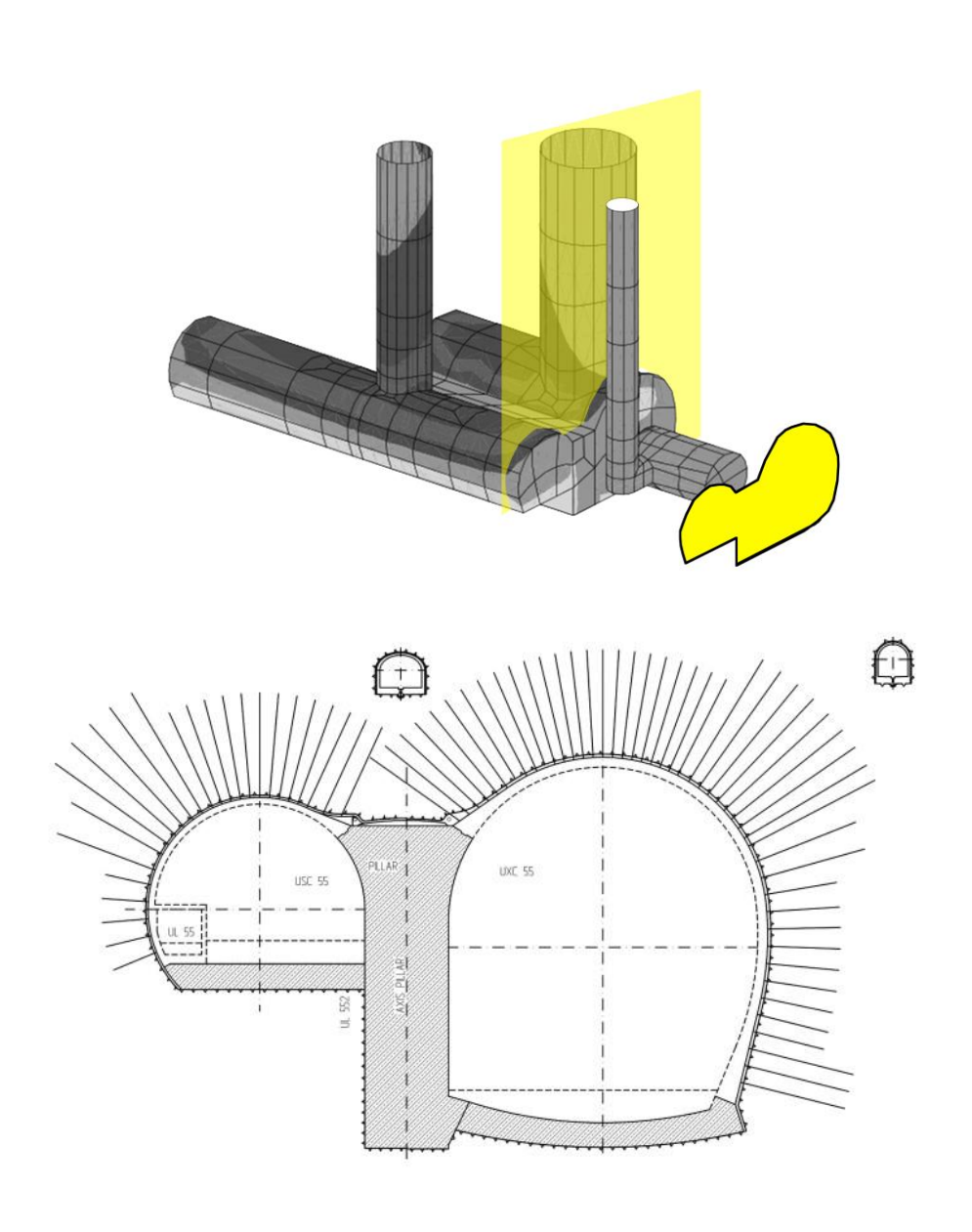


Figure 4.5.4 Point 5: type section of Experimental and Service caverns [69].

In order to maintain scientific progress and exploit its full capacity, High Luminosity LHC is a project aiming to upgrade the LHC after 2026 (Figure 4.5.5).

The main underground structures included in the HL-LHC project at Point 5 can be briefly summarized as follows:

- A new shaft (PM57), approximately 90 m deep and having 9.8 m internal diameter.
- A cryogenic cavern (divided into US57 and UW57 units, separated by a masonry wall), approximately 46 m long.
- Power converter tunnel UR55, to link the US57 cavern with the service tunnels, envisaged to be approximately 300 m long.
- Service tunnels (UA57, UL57, UA53; UL53), approximately 50 m long, to connect the power converter tunnel to existing LHC tunnel via vertical linkage cores.
- Escape tunnels (UPR53 and UPR57) connected to the existing LHC infrastructure.

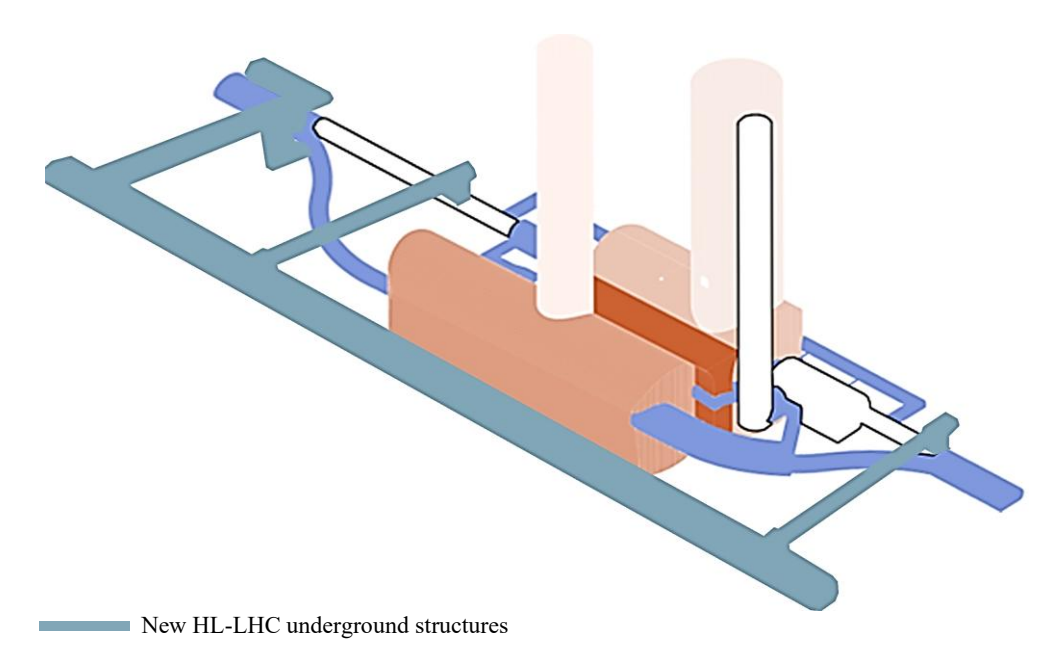


Figure 4.5.5 HL-LHC at Point 5: scheme of the underground structures.

0 DIS Assembly Shaft (PX56) and Access Shaft (PM54) UXC 55 Cavern (Experimental cavern) Massive concrete pillar USC 55 Cavern (Service cavern)

4.5.1 Construction method and rock support

Figure 4.5.6 CMS plan view and its upper drainage gallery.

Drainage gallery

A significant geological impact was encountered at Point 5 during excavation of the access shafts of the CMS facility.

The design called for the use of ground freezing to support excavation of the shafts through the water-bearing moraine at the base of the Jura range. Despite a program of grout injection prior to freezing in order to reduce the permeability of the moraine, the volume of groundwater was greater than anticipated. As a result, the original freezing installation had to be augmented. Additional freeze pipes and grout holes were placed around the shaft circumference, and liquid nitrogen was introduced to boost the brine freezing systems. This secured a ring of frozen ground and allowed safe excavation of the shafts to the molasse interface.

Shafts sunk through the upper 50 m of water bearing moraine utilizing ground freezing for shaft wall support and ground water control. Shafts were excavated sequentially down and primary concrete rings were cast progressively to form a 1.4 m thick primary lining ring. Below the moraine within the molasse, fibre-reinforced shotcrete and rock bolts were used for primary support. Once the shaft excavation was completed and the primary lining ring was in place, a secondary 80 cm thick concrete lining was slip formed from shaft bottom up, separated from the primary lining by a plastic membrane with fleece backing, which is connected to the extensive drainage system designed around the whole cavern complex, (Figure 4.5.6). A major requirement to shaft construction was that no water ingress from the moraine into the molasse is initiated by construction. Consequently, the shafts had to be sealed off at the transition moraine / molasse by an extensive grouting operation, creating a tight grout plug around the shafts.

Since even the excavation of the caverns is again complicated due to the sheer size of the caverns, their very limited distance apart, and the generally poor geological conditions, the cavern end walls are curved rather than straight to create an inherently more stable, circular profile on all sides. Despite this, computer modelling confirmed that excavation of the two caverns so close together could not be supported on such a narrow pillar of rock. The adopted was to excavate this pillar zone and replace it with mass concrete (Figure 4.5.7).

The walls and crown of the 7m thick, 31m high and 50m long pillar excavation are heavily supported with 8m long fiberglass and steel dowels and layers of steel-fiber-reinforced shotcrete. The wet mixed shotcrete is dosed

with steel fibre and a non-alkali liquid accelerator is introduced to the sprayed concrete at the nozzle. A geotextile waterproofing membrane system is also being applied to selected surfaces in the pillar area before it is backfilled with concrete. The shotcrete and the membranes in the pillar excavation will be linked into the two adjacent caverns while rock bolts extending into the profile of the caverns will be cut out during excavation.

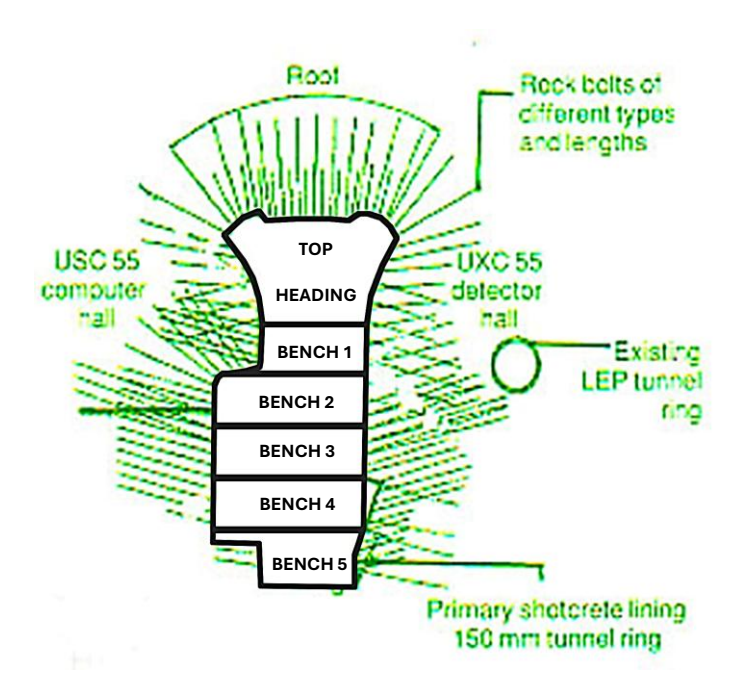


Figure 4.5.7 Excavation of the concrete pillar support wall for the CMS caverns [73].

After concrete pillar construction was completed, the caverns were excavated by road headers. The caverns were excavated with top heading and 2 to 4 benches plus invert, depending on the height of the caverns. Their excavation had followed the NATM construction technique (Figure 4.5.8).

Primary support consists of 30 to 50 cm fibre-reinforced shotcrete and systematic, fully grouted rock bolts with up to 12 m length. Typical rock support for the main caverns is shown in Figure 4.5.8. To account for the potential swelling rock underneath the cavern invert, and the weight of the

extremely heavy CMS detector, a massive highly reinforced concrete invert arch was constructed, providing a stiff foundation for the experimental cavern and horizontal support for the concrete pillar. The three-dimensional transition from shafts to cavern roofs is additionally supported by a shotcrete collar and anchored back into the rock mass with pretensioned high load rock anchors.

The reinforced secondary concrete lining has a thickness of 80 cm in the Experimental and 50 cm in the Service Cavern. [73].

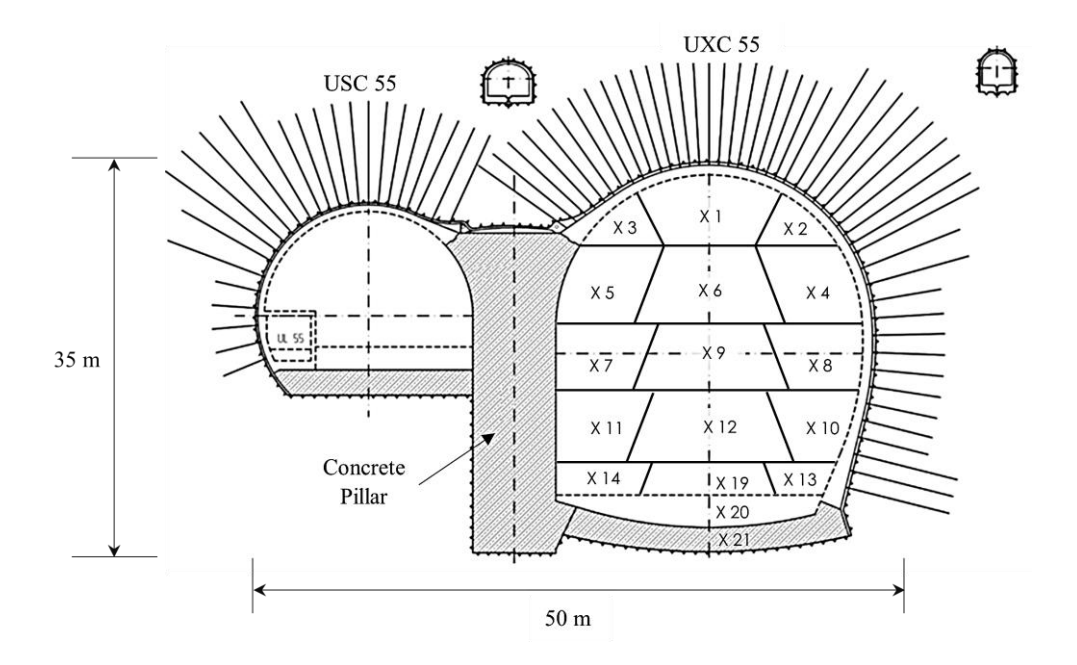


Figure 4.5.8 Sequence of the excavation for the UXC55 Experimental cavern [55].

4.5.2 UXC 55 Experimental cavern: construction sequence

With specific reference to the excavation and construction sequence of the UXC 55 Experimental cavern (Figure 4.5.9), there are several chronological phases that need to be considered.

From December 2001 to February 2002 [74]: excavation of Bench 1 of the UXC 55 cavern working westwards from Shaft PX56 was completed to the west headwall in mid-January. Excavation of Bench 2 started in the second week of January and was completed up to the west headwall by end of February. The excavation of Bench 3 started in the area below shaft PX 56 near the east headwall of the cavern before the end of February. Primary support was installed in each of the above excavation stages followed the excavation round by round.

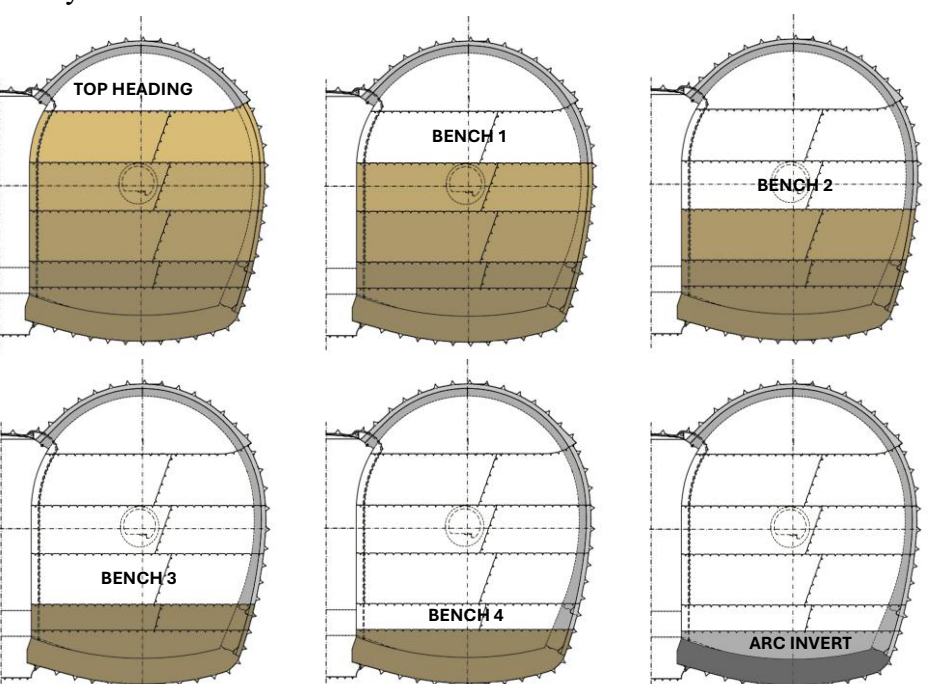


Figure 4.5.9 UXC55 Experimental cavern: excavation sequence.

From March to June 2002 [75]: excavation and primary support for the third bench down to arc invert started in February from the area below the PX 56 shaft and was completed up to the west headwall early in May. Excavation and primary support for the invert in Bay 1 started at the end of April and were completed in May, and the invert concrete in Bay 1 was poured in mid-June. Excavation and primary support for the invert in Bay 2 followed the completion of the invert concrete in Bay 1 and was completed by end of June, followed by the placing of blinding concrete, works for the drainage system and reinforcement fixing. The invert concrete in the same bay was poured at the end of July (Figure 4.5.10).

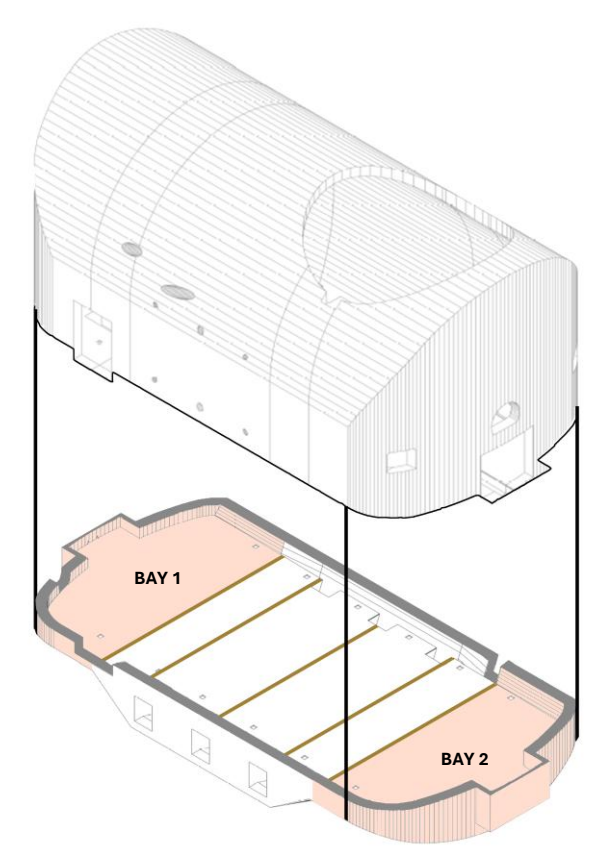


Figure 4.5.10 UXC55 Experimental cavern: arc inverts' excavation sequence.

From July to October 2002 [76]: excavation for the invert in Bay 5 and Bay 6 started after the completion of the invert in Bay 2. The invert concrete was poured in mid-September and end of September for Bay 5 and Bay 6 respectively. Excavation for the invert in Bay 3 and Bay 4 started after the completion of the invert in Bay 6. The invert concrete in Bay 3 was poured at the end of October. All the excavation operations were followed by the placing of blinding concrete, works for drainage system and reinforcement fixing (Figure 4.5.11).

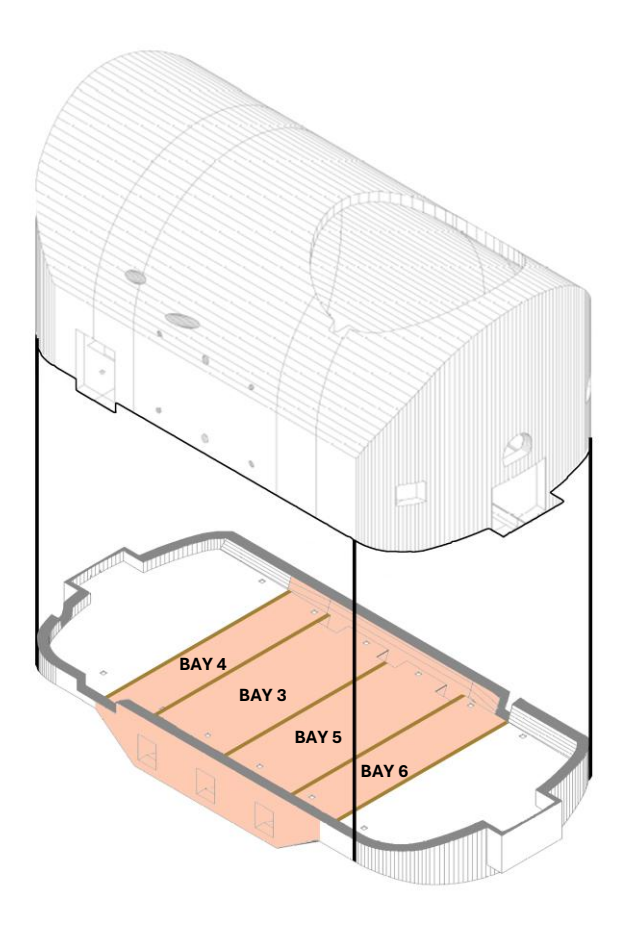


Figure 4.5.11 UXC55 Experimental cavern: arc inverts' excavation sequence.

From November 2002 to November 2004 [77]: to maintain the long – term stability of the Experimental and Service cavern, thick reinforced concrete a lining was executed, more in detail in the western, northern and eastern sidewalls, respectively, as well as at the crown, until to cavern / shaft connection. The cavern lining is assumed to be impermeable. This was a strict pre-requisite by CERN to ensure the safety of the sensitive equipment. A plastic membrane with fleece backing was built around the whole cavern wall to ensure the water tightness, which relates to an extensive drainage system to prevent any hydraulic pressure to build up behind the linings (Figure 4.5.12).

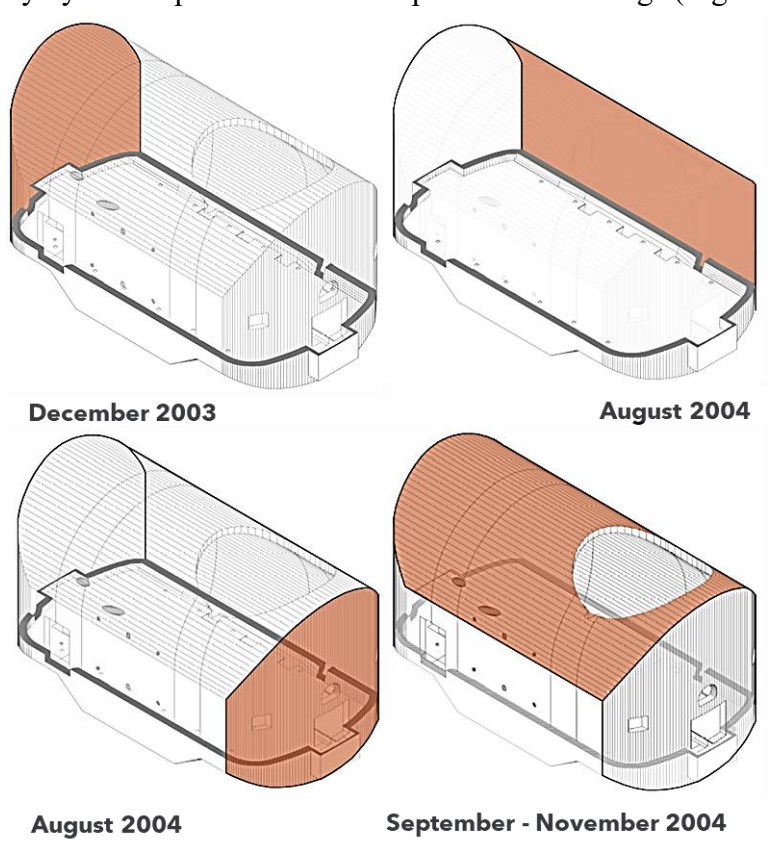


Figure 4.5.12 UXC55 Experimental cavern: linings construction sequence.

4.5.3 UXC 55 Experimental cavern: the CMS detector

Understanding the physical universe by breaking it down into its smallest constituents and studying the interactions between them represents an approach that has been established since the ancient Greeks, who introduced the concept of the atom as the fundamental building block of matter in the fifth century B.C. The atomic theory of the ancient Greeks sought to reduce components of the cosmos to matter and empty space, proposing that the fundamental constituents of matter were indivisible, and providing a natural explanation for the diversity of matter as resulting from atoms of different properties forming complex arrangements.

This early reductionist philosophy was remarkably ahead of its time, and although ancient atomic theory and its concepts fell into obscurity after being rejected by later Greek philosophers, they were rediscovered by Enlightenment scientists in the early nineteenth century and laid the foundation for modern atomic theory, which forms the basis for understanding the structure of matter and the nature of chemical reactions.

By the end of the nineteenth century, with the discoveries of the electrons, atoms were understood to not be indivisible and indestructible, and therefore could not be elementary constituents of matter, and, after discovering atomic number, a periodic table that led to a better understanding of the electron structure of atoms was developed. In the same period, the atomic nucleus and the concept of the proton were formulated, and, to account for the missing mass discrepancy between atomic weight and atomic number measurements, the existence of neutrons was theorized, leading to the important conclusion that protons, neutrons and electrons constituted the fundamental particles of matter.

In the twentieth century, the development of a quantum mechanical framework provided a deeper understanding of the behaviour of atomic and subatomic particles, clarifying that protons, neutrons, and many other species in the particle zoo did not constitute fundamental particles, but were instead composed of combinations of elementary quarks bound together by a strong nuclear force.

Through the 1960s and early 1970s, a quantum field theory that incorporated the four fundamental forces at work in the universe, i.e. strong, weak, electromagnetic and gravitational forces was developed to reduce the

complex and diverse behaviour of all atomic and subatomic particles to the elementary particles and the fundamental interactions between them.

In accordance with such theory, referred to as the Standard Model (SM) (Figure 4.5.13), composite particles of matter are differentiated in terms of their constituent elementary particles of half – integer spin, called fermions, which are the building blocks of matter. Fermions are bound together by the exchange of fundamental, force-carrying particles of integer spin, called bosons, and are themselves further categorized into the quark and the leptons subgroups:

- quarks belong to the "first generation" of the lightest and most stable particles, and all stable matter in the universe is made from particles that belong to this one.
- leptons, instead, belong to the "second and third generations" of the heavier and less-stable particles that quickly decay to more stable ones.

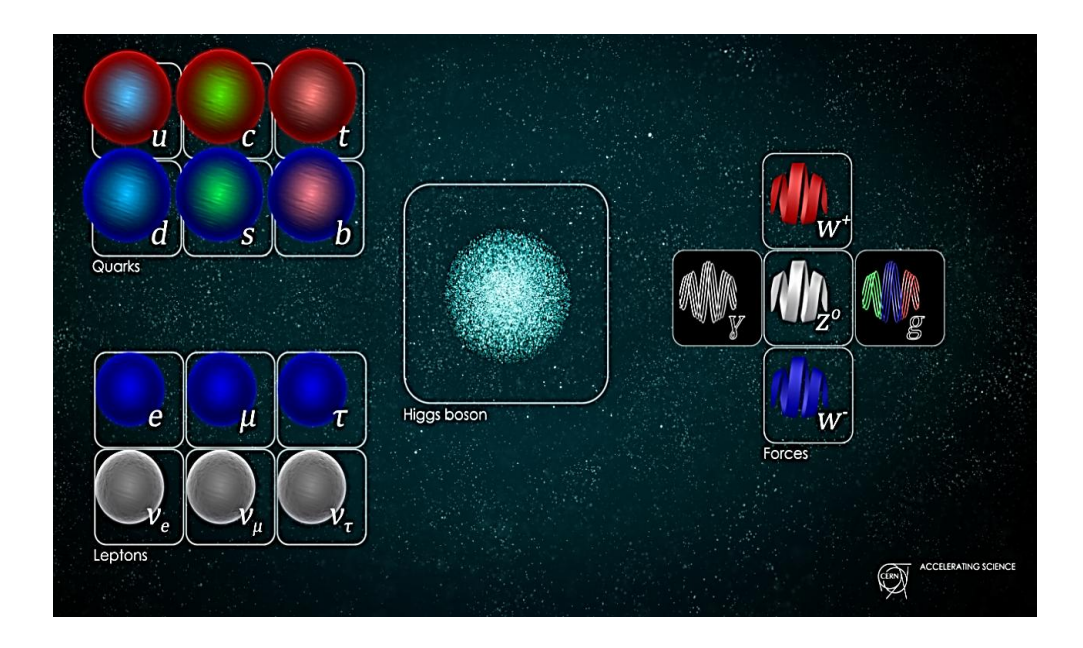
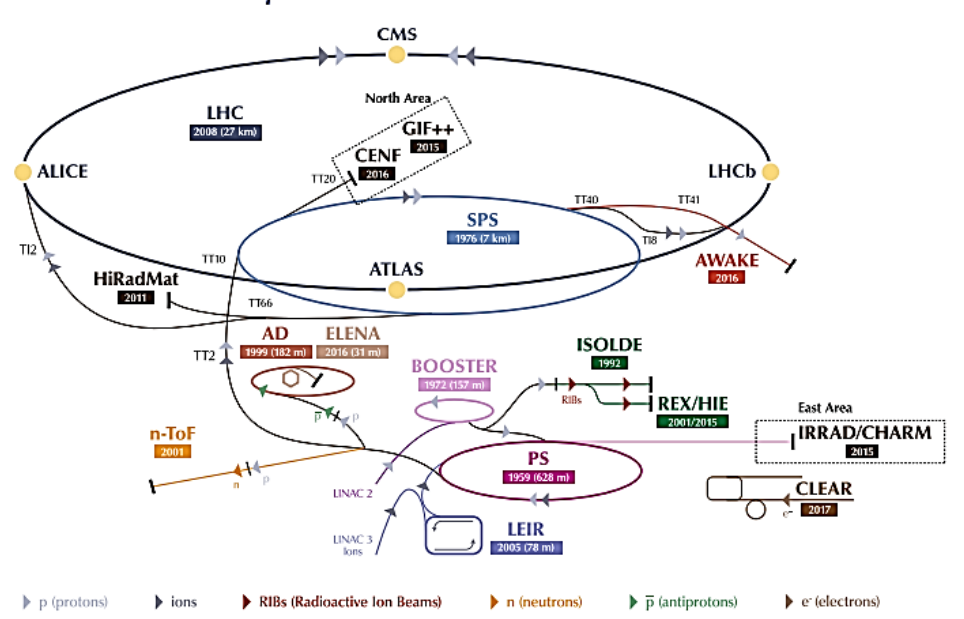


Figure 4.5.13 Particles of the Standard Model of Particle Physics [78].

In this context, experiments to discover and determine the properties of SM particles are performed at particle accelerator facilities located at CERN (Figure 4.5.14), designed to accelerate two counter-rotating proton beams to energies up to 6.8 TeV (Tera electron Volts), i.e. 99.999999% the speed of light, and collide them at designated interaction points, in order to measure electrical signals and collect scintillated light produced by such particles interacting with the material of the detector.

The CERN accelerator complex Complexe des accélérateurs du CERN



LHC - Large Hadron Collider // SPS - Super Proton Synchrotron // PS - Proton Synchrotron // AD - Antiproton Decelerator // CLEAR - CERN Linear Electron Accelerator for Research // AWAKE - Advanced WAKefield Experiment // ISOLDE - Isotope Separator OnLine // REX/HIE - Radioactive Experiment/High Intensity and Energy ISOLDE // LEIR - Low Energy Ion Ring // LINAC - LINear ACcelerator // n-ToF - Neutrons Time Of Flight // HiRadMat - High-Radiation to Materials // CHARM - Cern High energy AcceleRator Mixed field facility // IRRAD - proton IRRADiation facility // GIF++ - Gamma Irradiation Facility // CENF - CErn Neutrino platForm

Figure 4.5.14 A schematic of the LHC at CERN's accelerator complex in Geneva at the border of Switzerland and France [78].

For LHC project, the Compact Muon Solenoid (CMS) is a general – purpose detector built around a huge solenoid magnet, takes the form of a cylindrical coil of superconducting cable that generates a field of 4 tesla, about 100,000 times the magnetic field of the Earth. The field is confined by a steel "yoke" that forms the bulk of the detector's 14,000-tonne weight. (Figure 4.5.15, Figure 4.5.16). Its magnetic field, exerting a force perpendicular to a charged particle's transverse momentum and measuring a transverse momentum magnitude from the curvature of its trajectory, bends the paths of charged particles as they move through the detector, enabling the silicon inner tracker, with which high – energy charged particles ionize the silicon leaving trails of position measurements that are used to reconstruct the particle trajectories with sophisticated tracking algorithms, to make such measurements with a good resolution. Surrounding the silicon inner tracker is the electromagnetic calorimeter (ECAL) that measures the energy of particles, such as electrons, positrons, and photons, that primarily interact electromagnetically.

Among most particles directly detected by CMS, another type of them representing the final leptonic state of decay, so named muons, leave tracks in the silicon inner tracker, their trajectories are curved due to the presence of the magnetic field of the solenoid, and penetrate through the calorimeters and solenoid to leave ionization trails in the chambers of the muon system, placed at the very outer layers of the experiment in the steel flux-return yoke. The muon system is aligned with the inner tracker for the detectors to work together to identify muons and reconstruct their trajectories (Figure 4.5.17) [78].

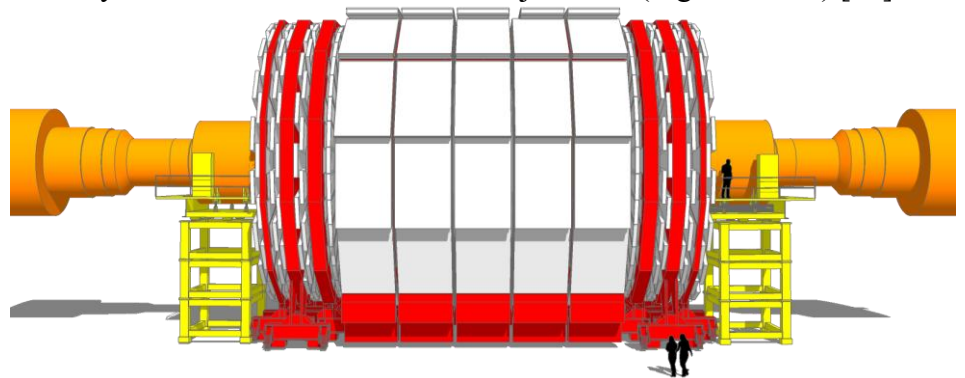


Figure 4.5.15 Compact Muon Solenoid Detector: front view.

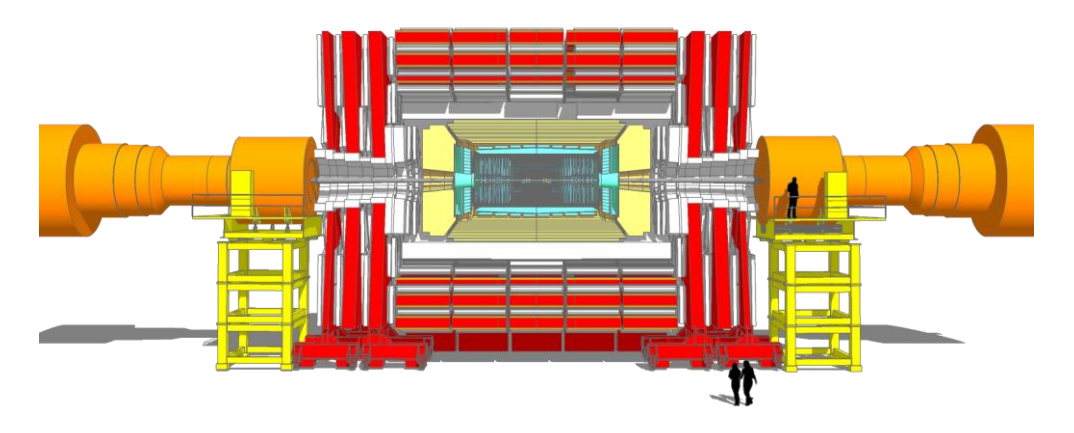


Figure 4.5.16 Compact Muon Solenoid Detector: section view.

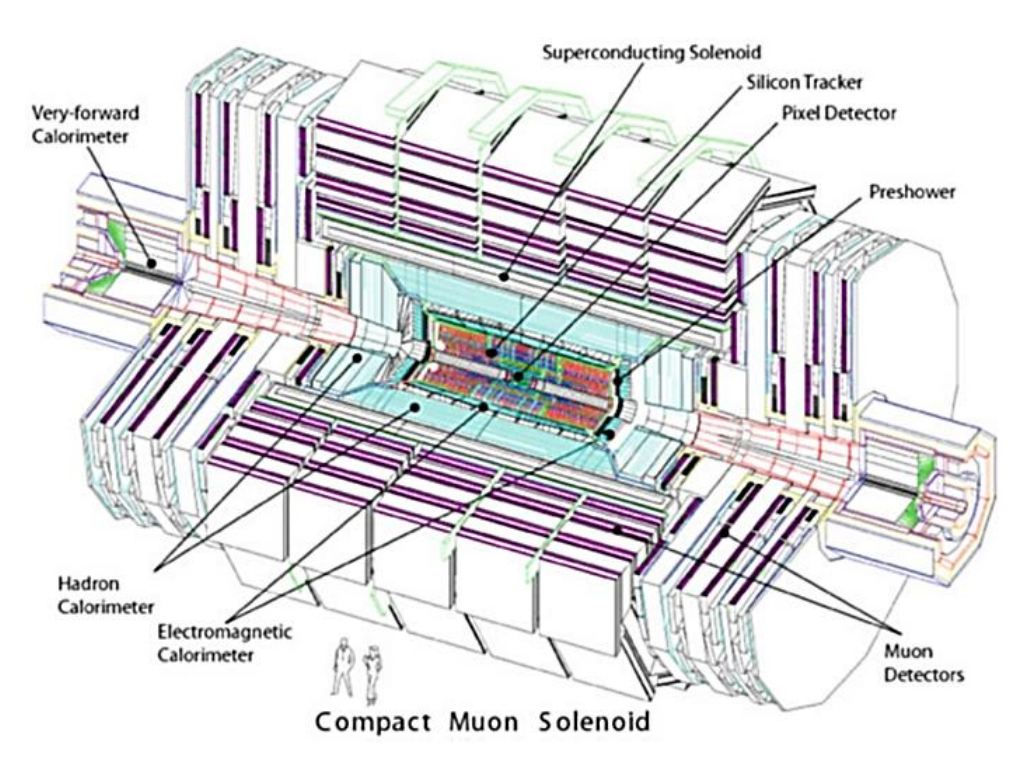


Figure 4.5.17 An exploded view of the CMS detector layout with labelled sub-detectors [78].

4.6 Preliminary study for seismic assessment of the underground facilities at Point 5

To estimate the response of the large underground cavities under seismic excitations, several fully dynamic analyses have been carried out through the software PLAXIS v20 [33] and [34], where non-linear material properties for each soil layer were assigned. The caverns' lining was modelled with elastic plate elements. The width of the model $x = 1000 \text{ m} \approx 20 \cdot W_{caverns}$ (caverns' width) as well as the vertical boundaries were set at five times the caverns' depth to reduce the effect of boundary wave reflection in the area of interest [79] (Figure 4.6.1).

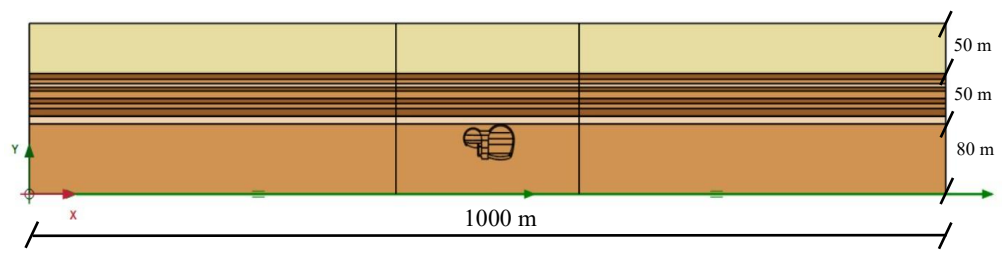


Figure 4.6.1 LHC project: layout of the Point 5 model built in Plaxis 2D [40].

Once the materials models were defined, a mesh of 15-noded elements was generated (Figure 4.6.5) in conformity with the most common element sizing criteria [80]. Five preliminary plastic calculation stages were computed to achieve a realistic stress state in the ground, which included cavities excavation and temporary supports system, following the New Austrian Tunnelling Method (NATM), was simulated using the load reduction method (θ – method), according to the available documentation (Figure 4.6.2, Figure 4.6.3, Figure 4.6.4).

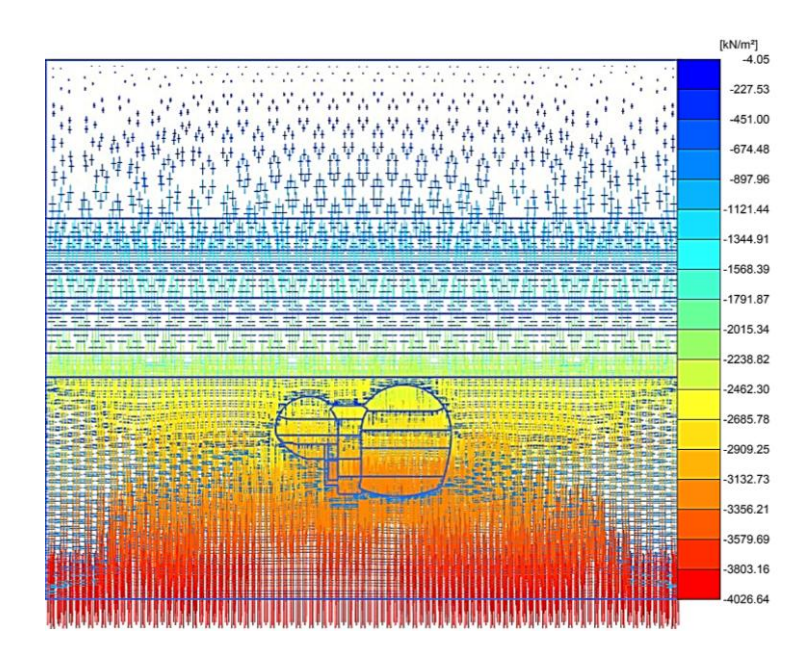


Figure 4.6.2 Plaxis 2D: effective principal stresses in free field lithostatic conditions [40].

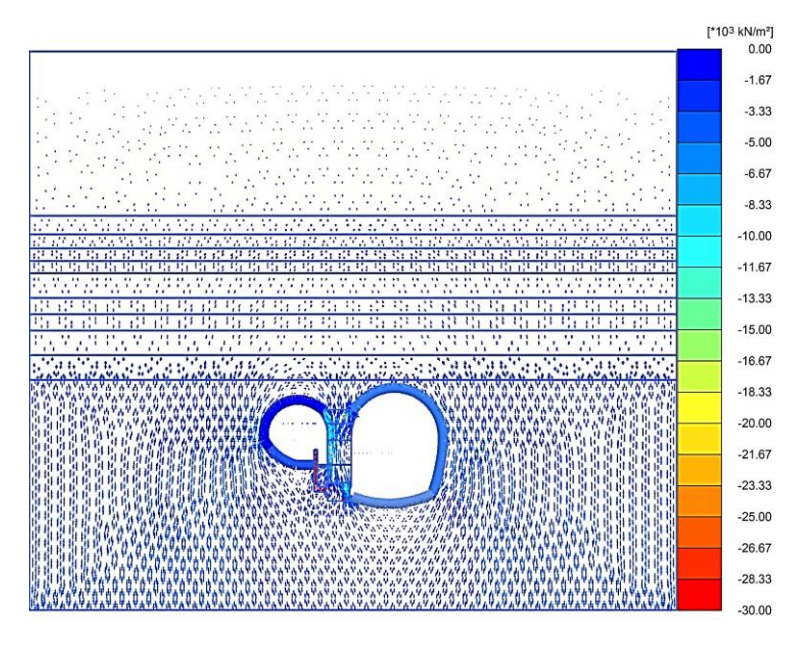


Figure 4.6.3 Plaxis 2D: effective principal stresses in post – cavities conditions [40].

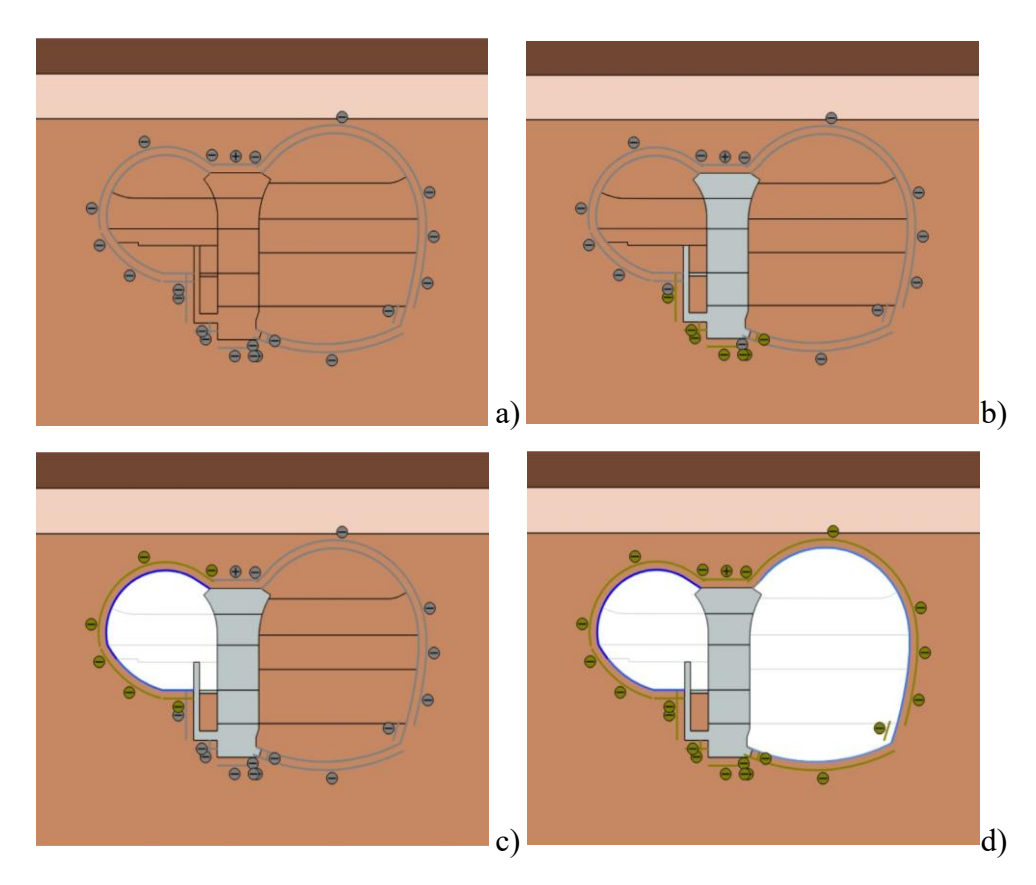


Figure 4.6.4 Plaxis 2D: main plastic calculation stages of the underground cavities: a) free – field conditions; b) pillar construction; c) USC55 Service cavern excavation; d) UXC55 Experimental cavern excavation.

4.6.1 FE model description

The model is ideally divided into three major layers, starting from the top: a Moraine deposits layer, extending from ground level to 50 m depth; an underlying Molasse rock layer, extending to 100 m depth, divided into sublayers by stiffness; and a medium stiff Molasse rock layer extending a further 70 m to the base of the model (Figure 4.6.5).

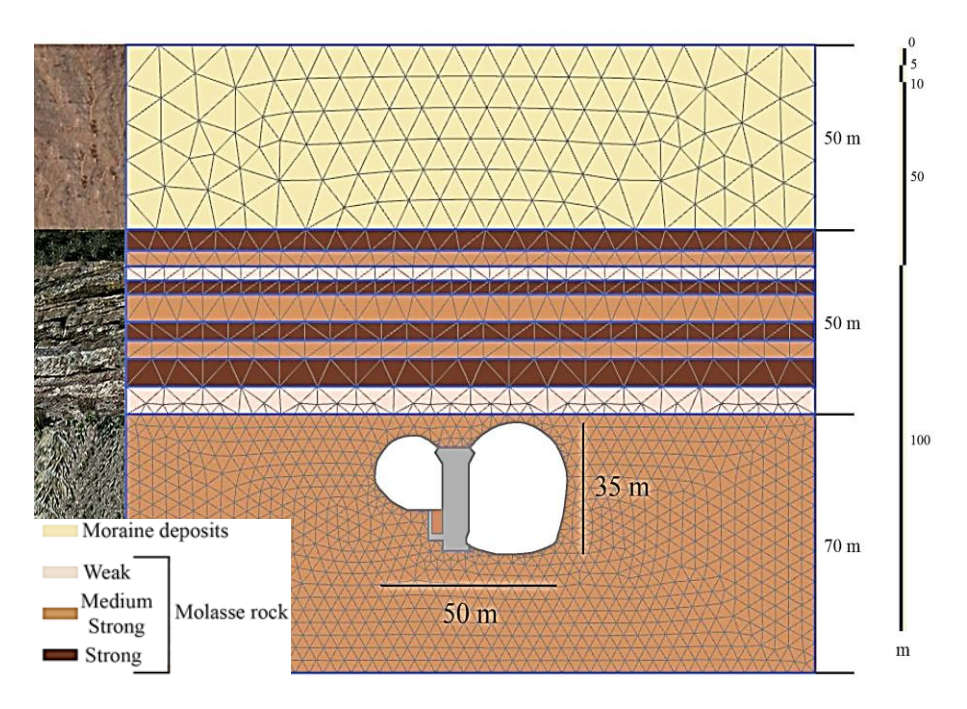


Figure 4.6.5 LHC Point 5: stratigraphic and mesh layout [40].

Static boundary conditions were defined by restraining the horizontal and vertical displacements at the base and the horizontal displacements at both sides. During the dynamic stages, the input acceleration time history was applied at the base of the model and the lateral boundary conditions were set as equivalent to a free-field condition.

The stress-strain behaviour of the various materials was modelled using the non-linear elastic-plastic isotropic hardening hysteretic model, known as Hardening Soil model with small strain stiffness (HS small) [81]. HS small model parameters used for the different geotechnical units are: γ_{sat} , the saturated unit weight; E_{50ref} , E_{oedref} , E_{urref} the reference secant normal, oedometer and unloading-reloading stiffness moduli respectively, defined at mean effective reference confining pressure of 100 kPa; G_{0ref} , the reference shear modulus; $\gamma_{0,7}$, the shear strain at $G=0.7~G_0$; v, the Poisson's ratio; m, the exponent for stress-level dependency of stiffness; c'ref, the cohesion; ϕ ', the friction angle; ψ , the dilatancy angle (Table 3).

It's worth nothing that there are differences between Table 3 and the table present in Mubarak in [55], as for the first simulations done in Plaxis, preliminary data received from CERN were considered and then reworked by [55].

The model incorporates the increase of damping ratio with strain, D (γ) through its hysteretic formulation, while the damping at very small strain level (D₀) has been modelled using a Rayleigh approach with double frequency control.

More in detail, by employing HS-small model, soil material damping is not shown, whereas soils stiff generally show a bit of viscous damping. Hence, additional damping is needed to model realistic damping characteristics, by means of Rayleigh damping. In PLAXIS, Rayleigh damping was first implemented by assuming two target frequencies: the first one is assumed to be the first natural frequency of a soil deposit f_l .

Regarding a soil of thickness H, frequency is related to its geometry and stiffness, according to the following equation:

$$f = V_s/4H \tag{36}$$

Vs represents the shear wave velocity in the soil deposit, that is a function of the shear stiffness modulus G: according to the previous equation, the first target frequencies for Moraine deposits and Molasse rock were, respectively:

$$f_{1 Moraine} = 1.25 Hz$$

$$f_{1 Molasse} = 4.5 Hz$$

The second target frequency is the predominant frequency of input motion f_2 , over the soil natural frequency, and was obtained by the following equation:

$$f_2 = n \cdot f_1 \tag{37}$$

In the equation, n represents an odd multiplier, approximated to excess and equal to:

$$n = f_2 / f_1 \tag{38}$$

In addition to frequencies, another important parameter to be implemented was the damping ratio ξ , expressed in percentage terms. According to Table 2, two values for Moraine deposits and Molasse rock were defined, respectively.

In Table 4 the mechanical properties adopted for UXC55 cavity's linings and basement, as soon as for concrete massive pillar, were defined.

For the determination of the mechanical properties of the concrete linings and basements in Table 4, the documents and data provided by CERN were consulted from plans/explanatory plans/sections on cavity design. Specific weight (γ) and Young's modulus (E) were considered from the mechanical properties of the concrete classes given in the CERN documents and related to each lining, while axial and flexural stiffnesses were obtained by considering a typical rectangular section:

- For area A was made b x h x 1m area influence of a lining (C35/45 lining layer walls and C50/60 cavity basement).
- For inertia I, the classical formulation b3h/12 x 1m influence area was considered.
- The values of EA and EI related to C40/50 and C50/60 refer to the basement and, therefore, to an important section thickness (4.5m for the USC55 cavity and 6m for the UXC55 cavity). These values can be traced in several representative sections of CERN cavities.

Control analyses were carried out in which an elastic - plastic model (concrete model) was adopted for the pillar and bedrock of the experimental

cavity, incorporating the same mechanical properties adopted by Ahmed in his thesis work, while the mechanical properties of the soil are the same as those adopted for the first simulations carried out in Plaxis (HS - small). A strong signal (i.e., Friuli earthquake of 1976) was inserted at the bedrock of the model.

Comparing the results with those obtained considering global elastic - linear behavior for the concrete, it was observed that although there is the absence of significant plasticization, the response observed at the UXC55 cavity basement is affected by non - linearities of the concrete that could be considered downstream of an appropriate characterization of the concrete in place.

Modelling of the central pillar was done by always considering the illustrative tables provided by CERN, as well as the material used for construction, i.e. C20/25. EA and EI values were appropriately entered and calculated along the lines of what was done for the cavities' linings and basements.

Invert arch was modelled as a plate element for preliminary analysis. Subsequently, the model was refined, and the plate elements were replaced with volume elements, both in Plaxis and in subsequent verification analysis steps with Real - ESSI. Verification analyses were carried out to evaluate the influence of the detector mass, distributed entirely on the base plate. By making a comparison with analyses in which the detector mass is not considered, the difference in terms of cavity response is negligible, so this was not considered in subsequent analyses.

Parameter	Unit	Moraine	Molasse
ξ	%	0.5	2.5
f_1	Hz	1.25	4.5
f_2	Hz	3.75	13.5
Rayleigh α	-	0.0589	1.06
Rayleigh B	-	0.3183 ·10-3	$0.4421 \cdot 10^{-3}$

Table 2 LHC Point 5: definition of Rayleigh damping [40].

The Generalized Newmark Method was adopted, with time integration parameters $\alpha_N = 0.3025$ and $\beta_N = 0.6$ to ensure the stability of the numerical solution and where the time step was constant [49]. A critical time step for

dynamic analyses was estimated to accurately model wave propagation and reduce the error due to the integration of time history functions, based on the material properties and the element size [33] and [34]. The calculation time step is adjusted to this value through sub-stepping.

Parameter	Unit	Moraine		Molasse rock	
			Weak	Medstrong	Strong
γ_{sat}	kN/m ³	23	24	24	24
$\mathrm{E}^{\mathrm{ref}}_{50}$	kN/m ²	30×10^{3}	340×10^3	1.2×10^6	2.42×10^6
$\mathrm{E}_{\mathrm{oed}}^{\mathrm{ref}}$	kN/m ²	30×10^{3}	340×10^3	700×10^3	1.8×10^6
E _{ur} ref	kN/m ²	60×10^3	680×10^3	2.4×10^6	4.84×10^6
G_0^{ref}	kN/m^2	92×10^{3}	2.24×10^6	2.72×10^6	4.1×10^6
$\gamma_{0.7}$	[-]	0.09×10^{-3}	1.2×10^{-3}	1.2 x 10 ⁻³	1.2 x 10 ⁻³
c'ref	kN/m ²	0	140	792	1660
φ'	[°]	35	18	50	53
Ψ	[°]	0	0	0	0
v	[-]	0.3	0.25	0.25	0.25
m	[-]	0.5	0	0.7	0.7

Table 3 LHC Point 5: mechanical properties and model parameters for the different layers, after [55] and employed in [40].

Parameter	Unit	Concrete C25/30 Pillar	Shotcrete C35/45 Linings	Concrete C50/60 Arc invert
γ	kN/m ³	25	25	25
Е	kN/m^2	31.45×10^6	34.63×10^6	37.24×10^6
EA	kN/m	61.63 x 10 ⁸	45×10^6	230×10^6
EI	kN m ² /m	57.5 x 10 ⁹	6.34×10^6	739 x 10 ⁶

Table 4 LHC Point 5: mechanical properties for cavities' linings and for massive concrete pillar.

4.6.2 Seismic input motions and analyses setup

Table 5 and Table 6 list the seismic input signals and its fundamental characteristics retrieved from the Engineering Strong-Motion Database (ESM) [82], in order to be compatible with the horizontal design spectrum foreseen by the Eurocode 8 for a type-A ground, assuming nominal life of 100 years (Figure 4.6.6). Hence, the reference peak ground acceleration considered by preliminary studies of the area was set equal to 0.15g [83]. After appropriate frequency and baseline correction operations (Table 7), such signals were employed to perform dynamic analyses in Plaxis by imposing them on the model bedrock to evaluate their effects at significant points in the soil and rock layers, as well as at the perimeter of the UXC55 experimental cavity.

As an example, the first adopted input time history (Friuli earthquake) and the related Fourier spectrum are shown in Figure 4.6.7.

Figures 4.6.8, 4.6.9, 4.6.10, 4.6.11 show all the other input signals employed. Figure 4.6.12 shows the PSA response spectra.

Accelerogram	Event date	Accelerometer registration	Peak Ground Acceleration	Arias Intensity	Bracketed Duration
		component	[g]	[m/s]	[s]
Friuli	15/09/1976	HNN	0.128	0.095	2.85
Centre Italy	30/10/2016	HNE	0.146	0.183	7.255
Iceland_1	17/06/2000	HN2	0.123	0.165	3.595
Iceland_2	17/06/2000	HN3	0.155	0.192	3.795
Iceland_5	29/05/2008	HN2	0.13	0.112	3.935

Table 5 Seismic records selected [40].

Event name	Event date	Event time	Magnitude Mw	Focal Mechanism	Station code
Friuli	15/09/1976	09:21	6.0	Thrust faulting	SRCO
Centre Italy	30/10/2016	06:40	6.6	Normal faulting	T1256
Iceland_1	17/06/2000	15:40	6.5		108
Iceland 2	17/06/2000	15:40	6.5		108
Iceland 5	29/05/2008	15:46	6.3		306

Table 6 Seismic records properties.

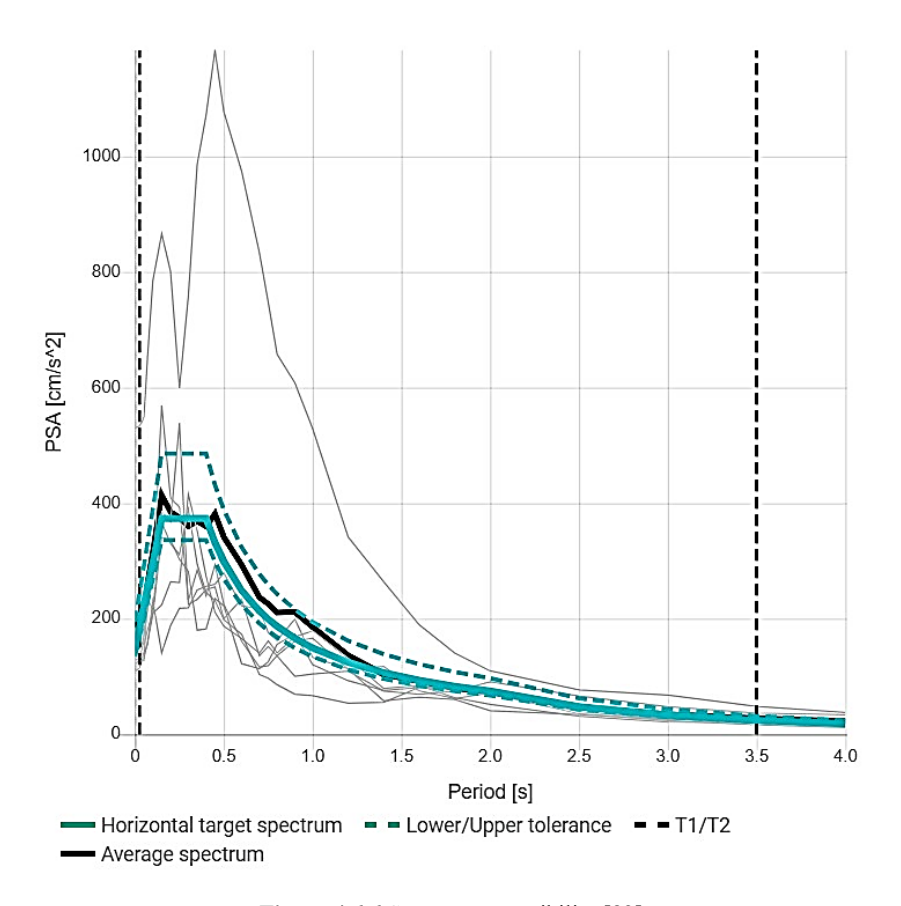


Figure 4.6.6 Spectro-compatibility [82]

Event name	Event date	Baseline correction	Filter type	Filter order	Low cut frequency [Hz]	High cut frequency [Hz]
Friuli	15/09/1976	Removed	Butterworth	2	0.10	29
Centre Italy	30/10/2016	Removed	Butterworth	2	0.04	40
Iceland_1	17/06/2000	Removed	Butterworth	2	0.010	40
Iceland_2	17/06/2000	Removed	Butterworth	2	0.010	40
Iceland_5	29/05/2008	Removed	Butterworth	2	0.010	40

Table 7 Seismic input motions: filtering and baseline corrections.

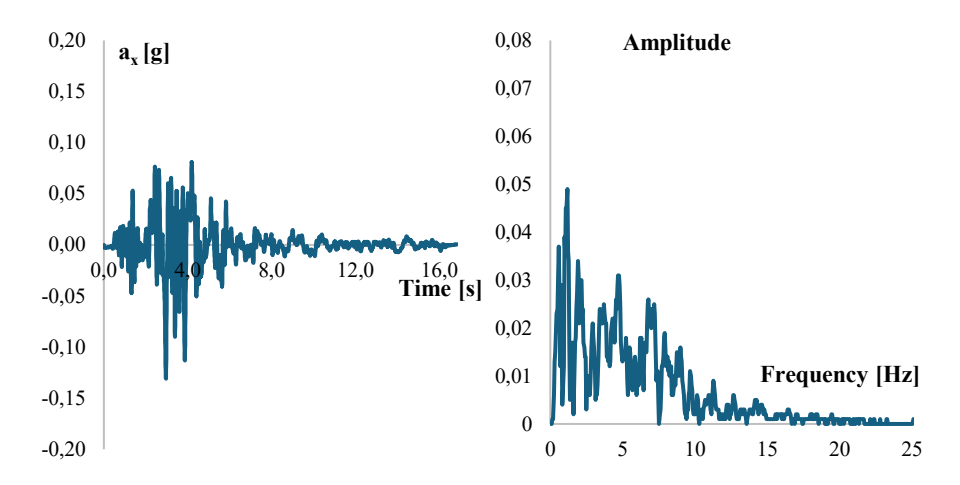


Figure 4.6.7 Friuli earthquake (1976): acceleration time history (on the left); the related Fourier spectrum (on the right) [40].

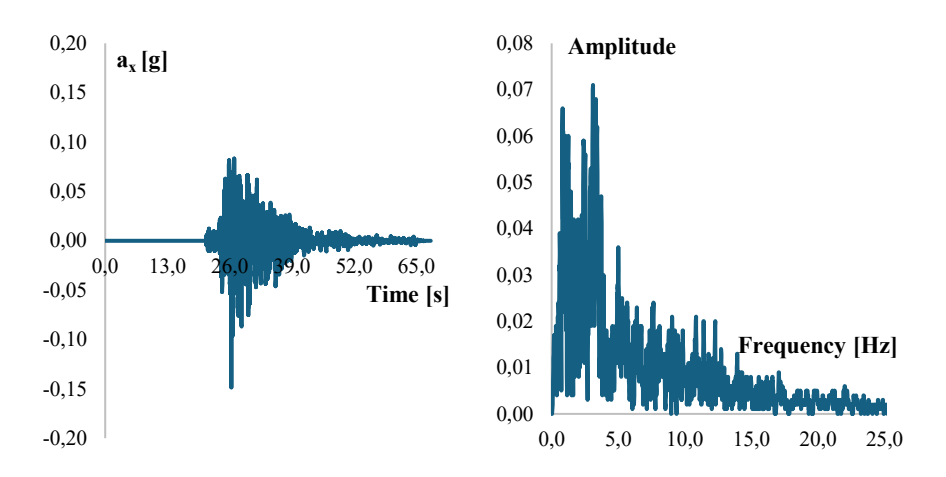


Figure 4.6.8 Centre Italy earthquake (2016): acceleration time history (on the left); the related Fourier spectrum (on the right)

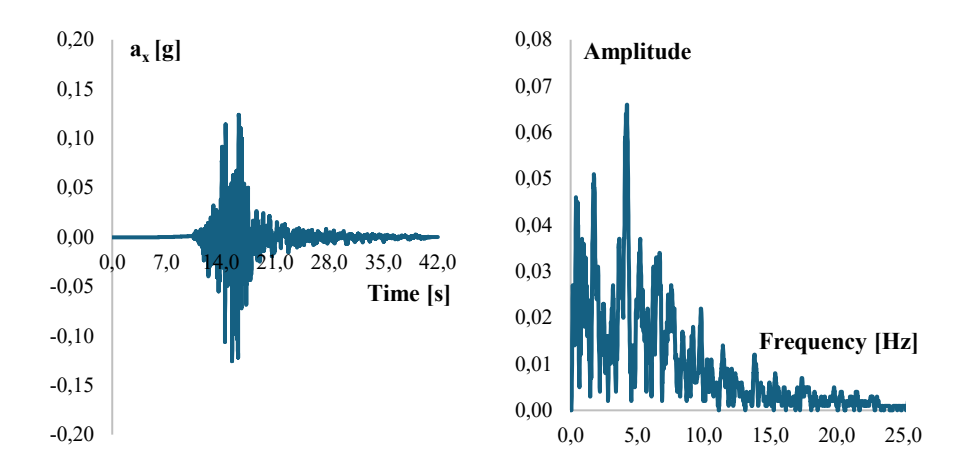


Figure 4.6.9 Iceland earthquake (2000): acceleration time history (on the left); the related Fourier spectrum (on the right).

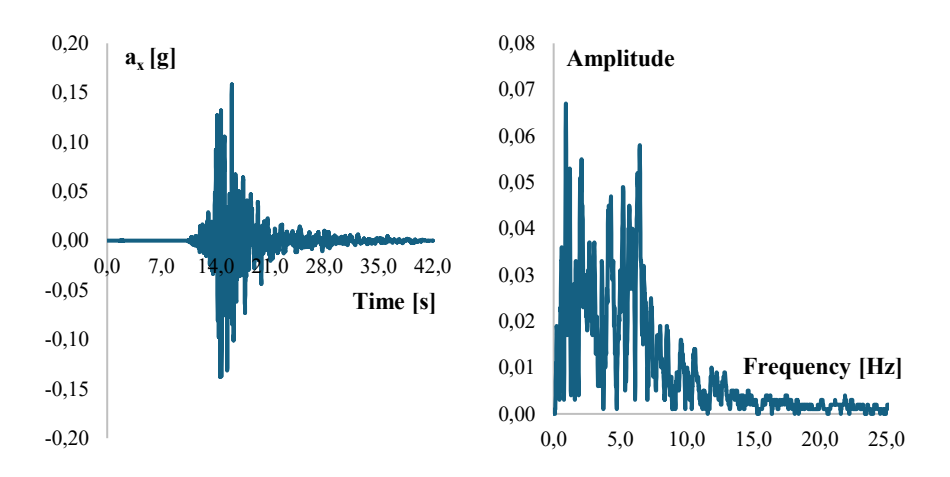


Figure 4.6.10 Iceland earthquake (2000): acceleration time history (on the left); the related Fourier spectrum (on the right).

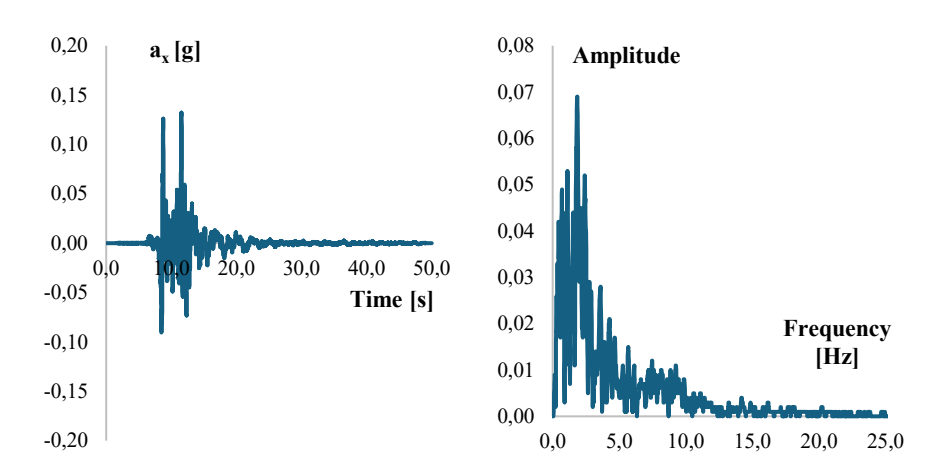


Figure 4.6.11 Iceland earthquake (2008): acceleration time history (on the left); the related Fourier spectrum (on the right).

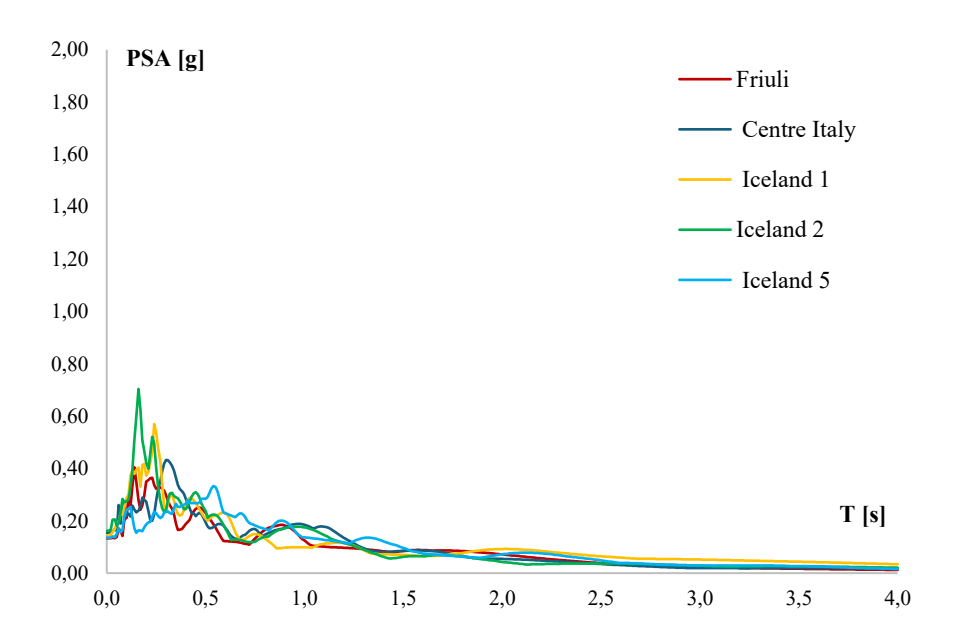


Figure 4.6.12 PSA response spectra.

4.6.3 Results and comments: the Friuli earthquake (1976)

For the sake of brevity, the details of the first seismic input in this study (i.e., Friuli earthquake of 1976) is considered. A comparison with the results obtained using the other inputs is presented later.

Figure 4.6.13 shows a comparison in terms of Pseudo-Spectral Acceleration (PSA) computed along three vertical axes: across the main experimental cavern, 90 m away and 300 m away from it. Acceleration amplification, compared to the bedrock, is calculated towards the ground surface, within the underlying molasse layer (see "Bottom border molasse-molasse"), the layered molasse sequence (see "Upper border moraine-molasse") and the uppermost moraine layer (see "Ground level). The two central axes (0 and 90m) are affected by the presence of the caverns. The basement of the UXC55 cavern shows larger amplification than the surrounding rock at very low periods (peak at 0.15s). Comparing with the point at the roof of UXC55 it seems clear that the response spectra change with the position along the perimeter of the cavern cross-section.

Figure 4.6.14 shows PSA values along horizontal axes (ground level, upper border of the layered molasses, bottom border of the layered molasses). It confirms that amplifications larger than under free-field conditions are generally computed around the cavities, within a horizontal distance from the cavern wall of at least two times the value of the cavity height.

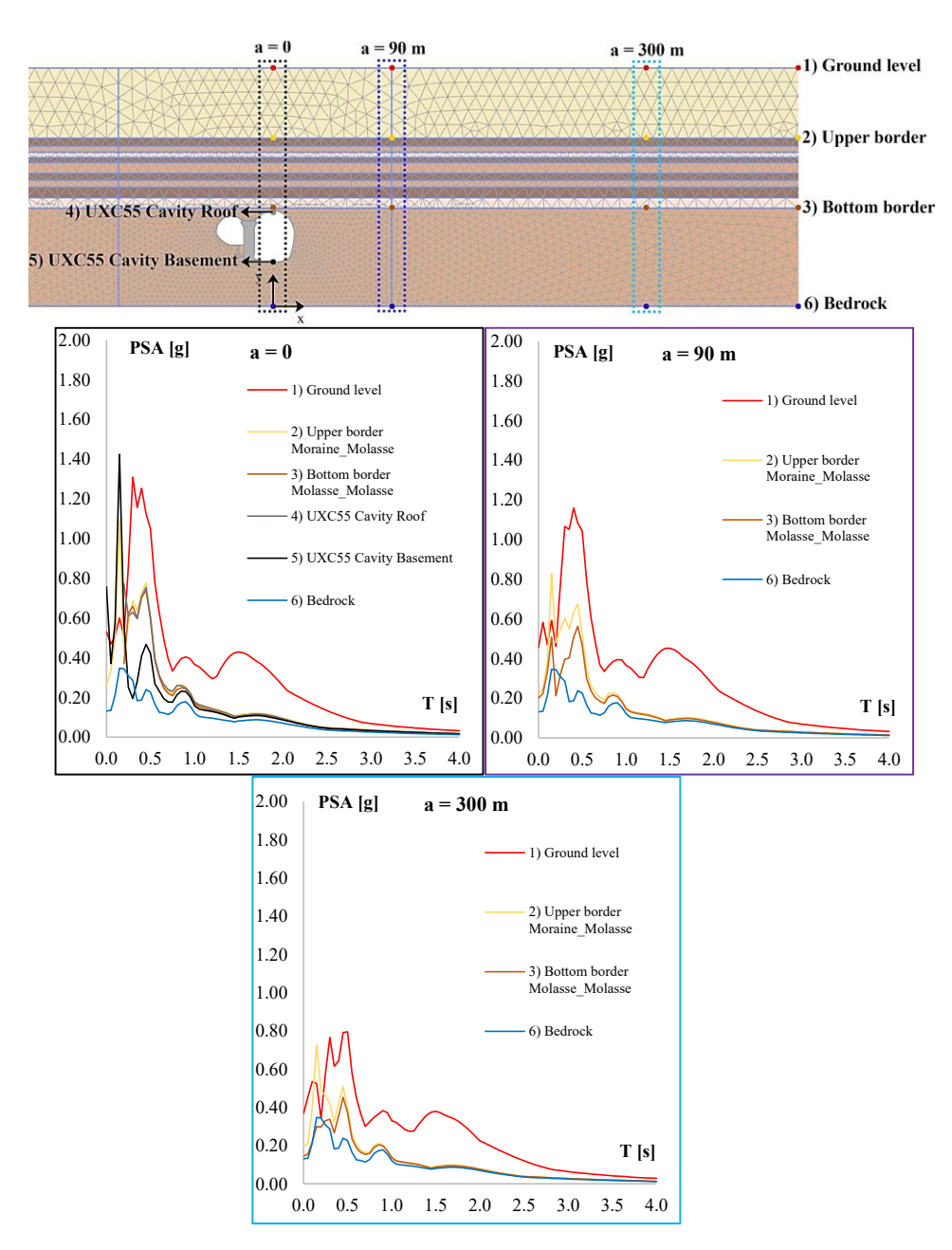


Figure 4.6.13 PSA values along vertical arrays, related to Friuli signal, in significative points of the model [40].

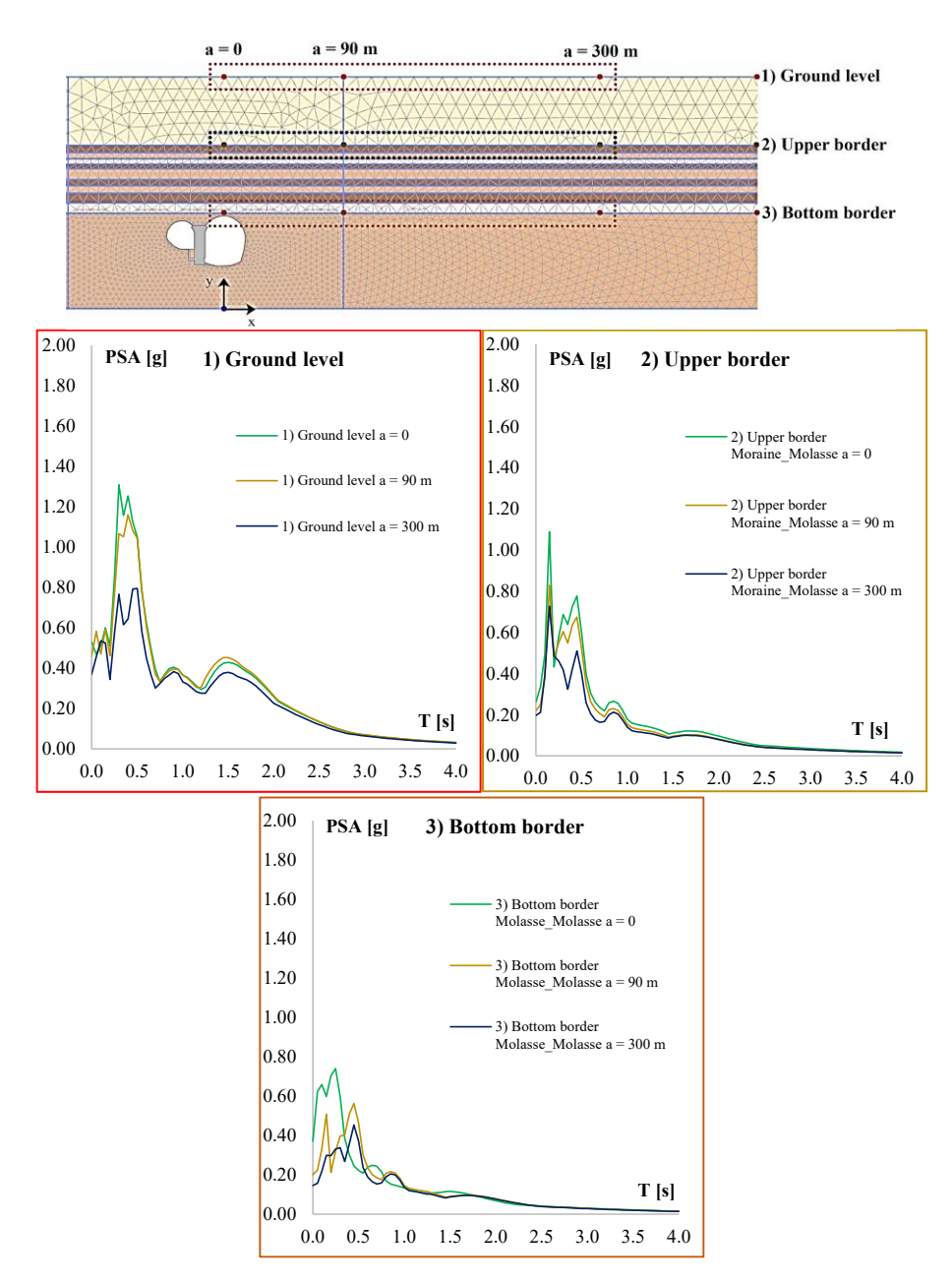


Figure 4.6.14 PSA values along horizontal arrays, related to Friuli signal, in significative points of the model [40].

4.6.4 Results and comments: the other input motions

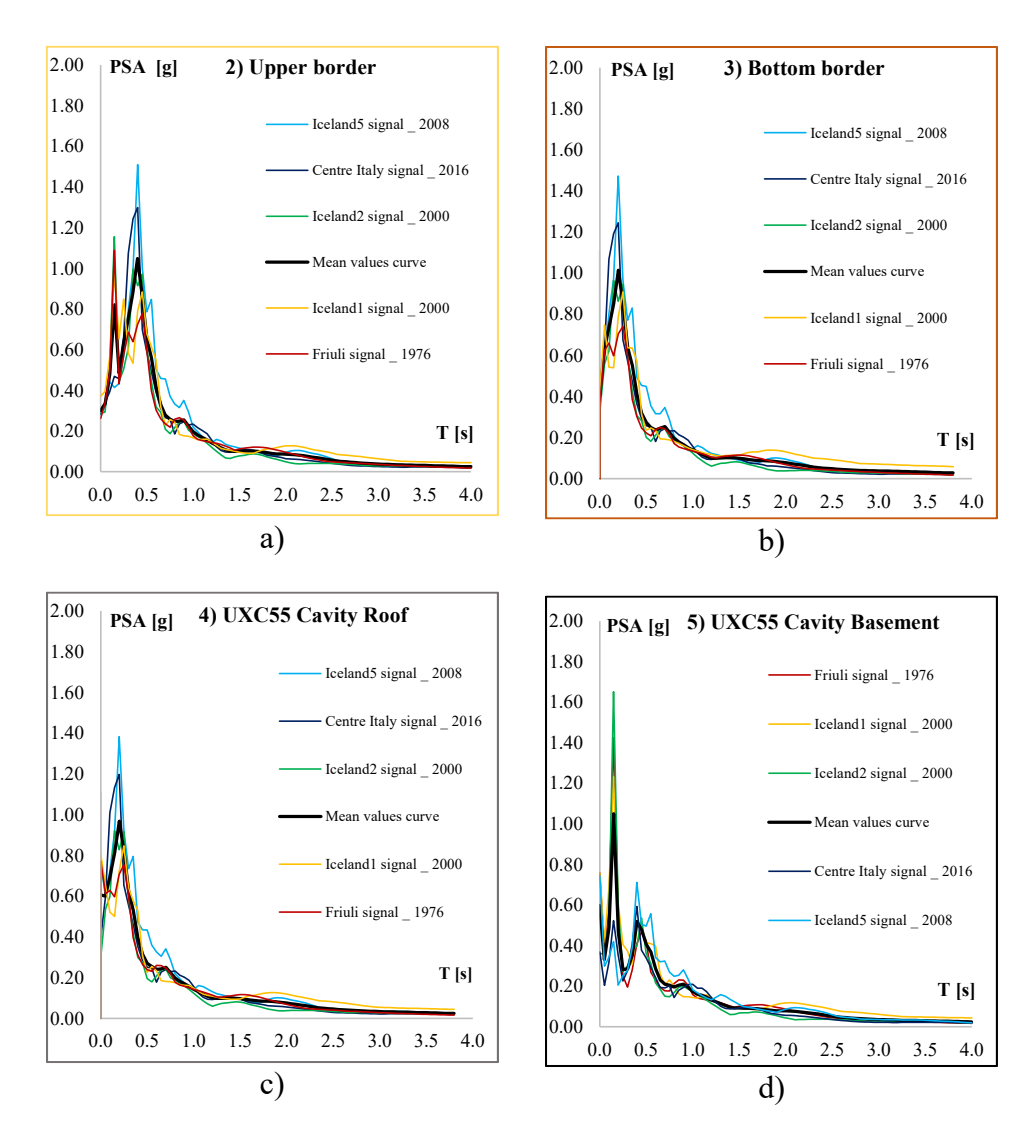


Figure 4.6.15 PSA values for the considered seismic inputs at different locations [40].

The results using the whole set of input signals are plotted in Figure 4.6.15 in terms of response spectra. On the cavity perimeter (both basement and roof) the response spectra show a larger peak at around 0.15s, which corresponds to the predominant period of the input signals; a second peak, around 0.5s, appears predominant in the response of the rock layers (upper border' and 'bottom border'). This seems to indicate a rather rigid response of the cavern system, that could be influenced by the stiff behaviour of high concrete pillar that separates the two cavities.

A direct comparison between the mean spectra for the cavity basement and the cavity roof confirms that the spectral response is affected by the position along the perimeter of the cavity cross-section.

4.7 Evaluation of the seismic behaviour of the underground facilities using Real – ESSI Simulator

Understanding the seismic behaviour of underground structures is essential to assess the response of critical equipment for scientific experiments, such as those housed in the cutting-edge infrastructure of CERN. In the field of seismic geotechnical engineering, the code Real-ESSI (Realistic modelling and simulation of Earthquakes, Soils, Structures and their Interaction) permits simulating the behaviour of underground infrastructure when subjected to seismic waves, integrating advanced finite element modelling techniques with high-performance computing capabilities. In this perspective, Real-ESSI Simulator represents a tool capable of properly achieving a performance level through the verification of the software correctness and numerical accuracy of the solution to a given computational model, as well as the validation of a model based on comparisons between computational simulation and experimental data.

Real-ESSI was used for assessing the seismic performance of the underground cavities hosting the Compact Muon Solenoid experiment, as part of the Large Hadron Collider complex.

By considering several different seismic input motions applied at the model base, dynamic Finite Elements Analyses (FEA) have been carried out to benchmark results using Real-ESSI against analyses using the PLAXIS FEA software [33] and [34], in order to assess the amplification of the ground shaking through the layers up to ground level, as well as to identify the effect of seismic excitations on the cavern's boundaries under plane-strain conditions.

4.7.1 Real-ESSI verification on the free-field response: results and comments

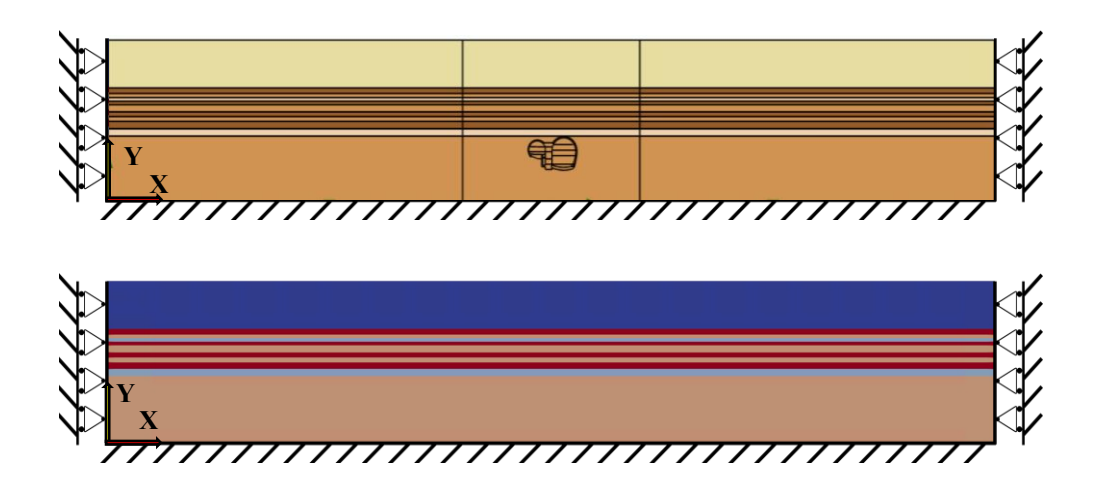


Figure 4.7.1 Comparison between model built by PLAXIS (top) and Real – ESSI (bottom) [53].

Parameter	Unit	Moraine	Molasse rock	Molasse rock	Molasse rock
	11310		Weak	Medstrong	Strong
γ_{sat}	kN/m ³	23	24	24	24
Е	kN/m ²	5.51 x 10 ⁶	4.96 x 10 ⁶	8.81×10^6	13.76 x 10 ⁶
G	kN/m ²	2.12×10^{5}	1.98 x 10 ⁶	3.52×10^6	5.51×10^6
V_s	m/s	300	900	1200	1500
V	[-]	0.3	0.25	0.25	0.25

Table 8 Mechanical properties defined for different soil layers in both software.

By employing Real-ESSI software to build the same model built in PLAXIS (Figure 4.7.1), in order to compare them in terms of the stratigraphic and lithological profile as done in Mubarak [55], a verification phase has been initially carried out by considering a free-field conditions (i.e. without the presence of CMS cavities).

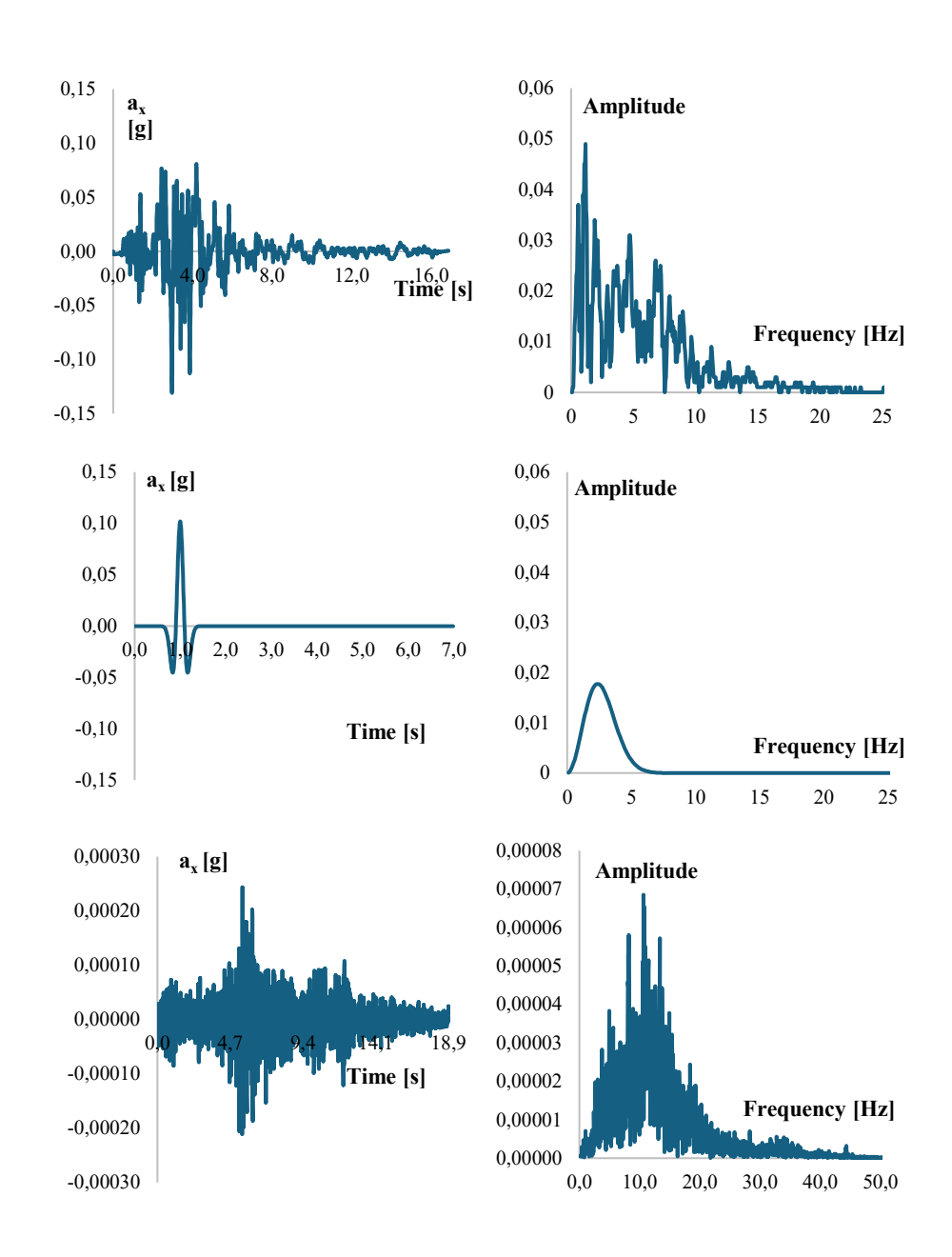


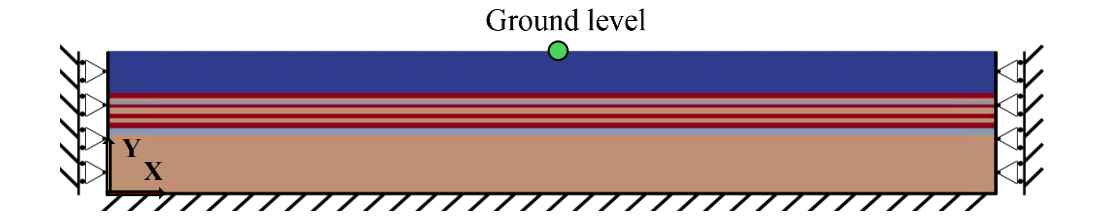
Figure 4.7.2 Acceleration time histories and related Fourier spectra of Friuli earthquake of 1976 (top), Ricker Wavelet (centre) and event recorded at CERN on November 1°, 2022 (bottom), respectively.

In Table 8, there are the parameters used to verify that the Plaxis software and the Real.ESSI software returned the same output.

More specifically, the values of γ , v and V_s are the same as those used for the first simulations in Plaxis with the HS - small model: from these parameters, the mass density ρ and the stiffness moduli E and G were derived. The choice of a linear - elastic constitutive model is dictated by the need for comparison and verification of the results.

As done in U. Carmando et al. in [40] the vertical boundaries of the model were set at five times the caverns' depth to minimize the effect of boundary wave reflection in the area of interest. A 1-km-length model has been created in Real-ESSI, by defining a regular mesh size of 8-node-brick elements, a linear visco-elastic behaviour and the same materials for soil layers, the same boundaries conditions, i.e. a full fixity at the base of geometry was generated, whereas roller supports to the vertical boundaries were assigned, as well as the same damping ratios initially equal to approximately 5% for all soil layers via Rayleigh approach with double frequency control were adopted.

For further comparison, a third software capable of computing a linearelastic one-dimensional wave propagation through a layered medium, namely Strata, has been employed [84]. By applying a Ricker Wavelet as input motion at the base of the model, and considering a point taken at the ground level, results observed in terms of acceleration time histories show good compatibility level between the two FE analyses in the time domain (Figure 4.7.2, Figure 4.7.3).



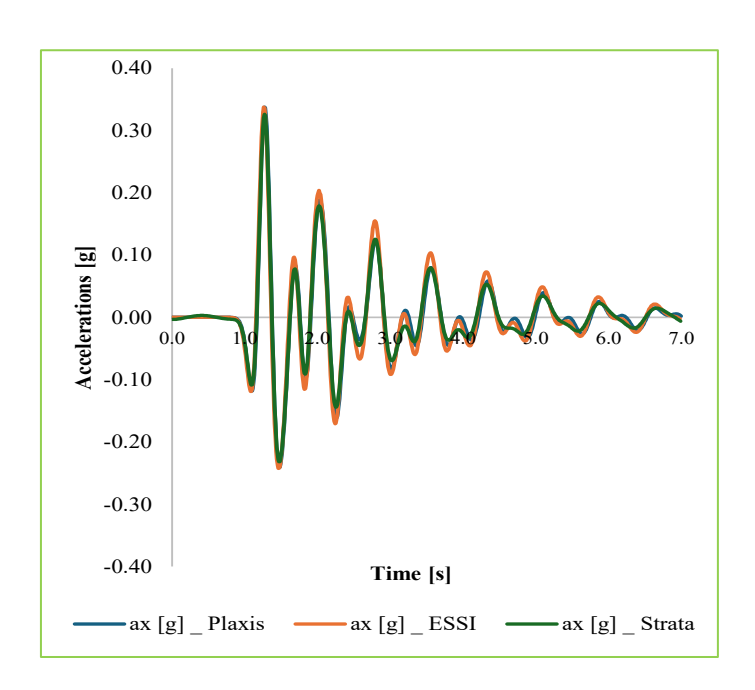


Figure 4.7.3 Free-field conditions: acceleration time history observed at ground level as results of the three-software adopted, by applying Ricker Wavelet at the surface base [53].

4.7.2 Real-ESSI verification on CMS cavities: results and comments

A second further comparison between PLAXIS 2D and Real-ESSI with the presence of the CMS cavities (Figure 4.7.4), with the same ground conditions and having the same Ricker Wavelet as input motion as above Damping ratios have been assumed equal to 0.5% and 2.5% for Moraine deposits and Molasse rock and 5% for the concrete linings of caverns and pillar. The damping considered in the analyses carried out with HS small model and linear viscoelastic model involved choosing different damping levels to calculate the Rayleigh values to be used in the analyses, according to a linear equivalent approach of the expected strain level. Several points of the model have been compared in both models (Figure 4.7.5, Figure 4.7.6). In this case as well, results in terms of accelerations time histories confirm a good numerical accuracy between the two FE tools and allow us to understand how different the effects, in terms of amplifications, are on cavities' boundaries once a pulse has been applied at base as an imposed motion.

Parameter	Unit	Concrete	Shotcrete	Concrete	Concrete
		C25/30	C35/45	C40/50	C50/60
γ	kN/m ³	25	25	25	25
E	kN/m^2	31.5×10^6	34.63 x 10 ⁶	35.55 x 10 ⁶	37.24×10^6
ν	121	0.25	0.25	0.25	0.25

Table 9 Mechanical properties defined for cavities' walls and for the concrete pillar in Real - ESSI.

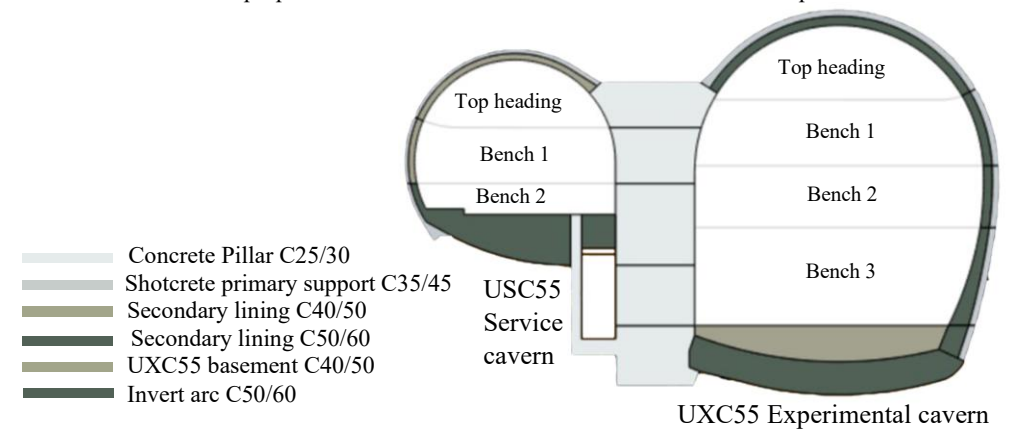


Figure 4.7.4 CMS cavities: section type.

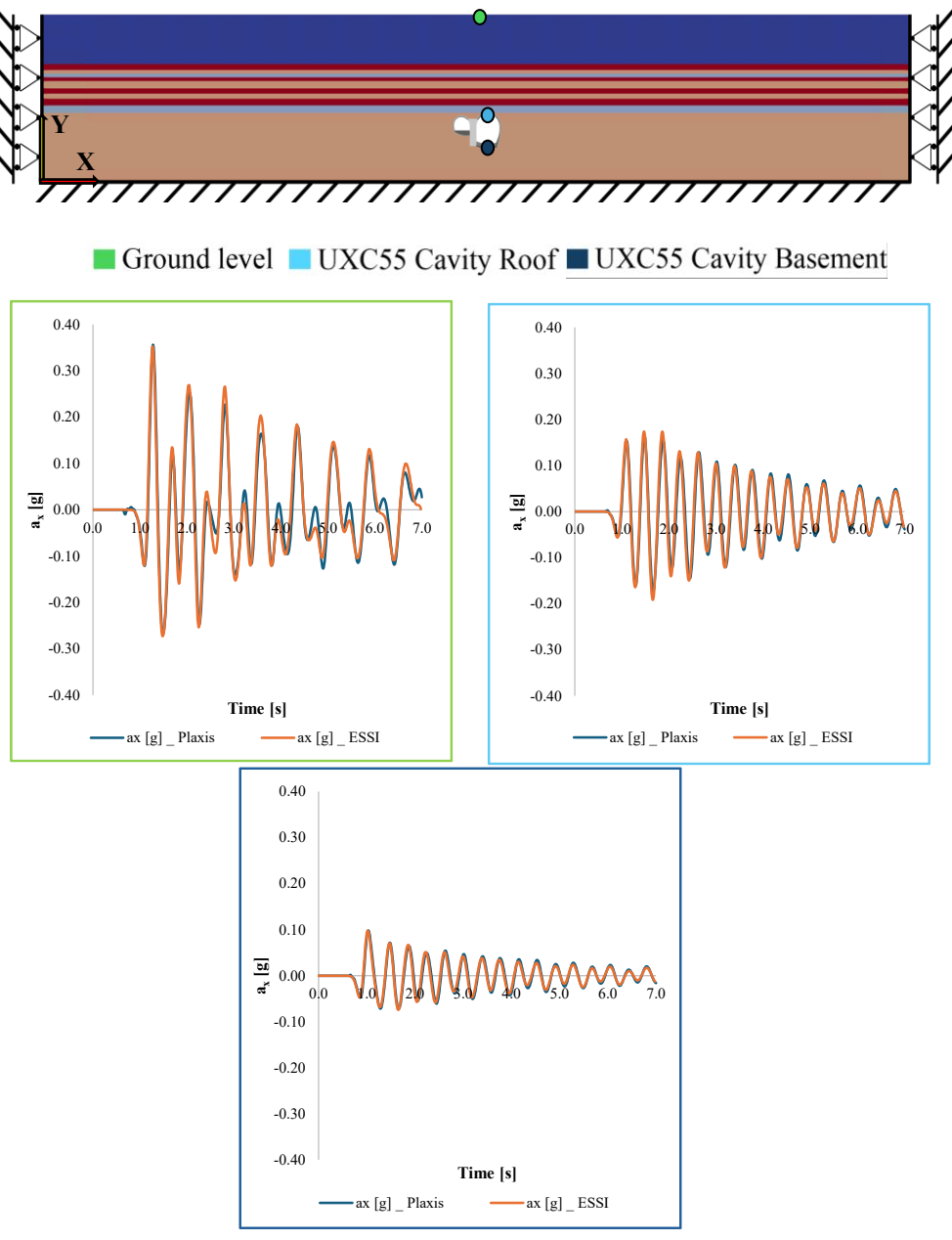


Figure 4.7.5 Comparison between PLAXIS and Real-ESSI models: results in terms of acceleration time histories by applying Ricker Wavelet [53].

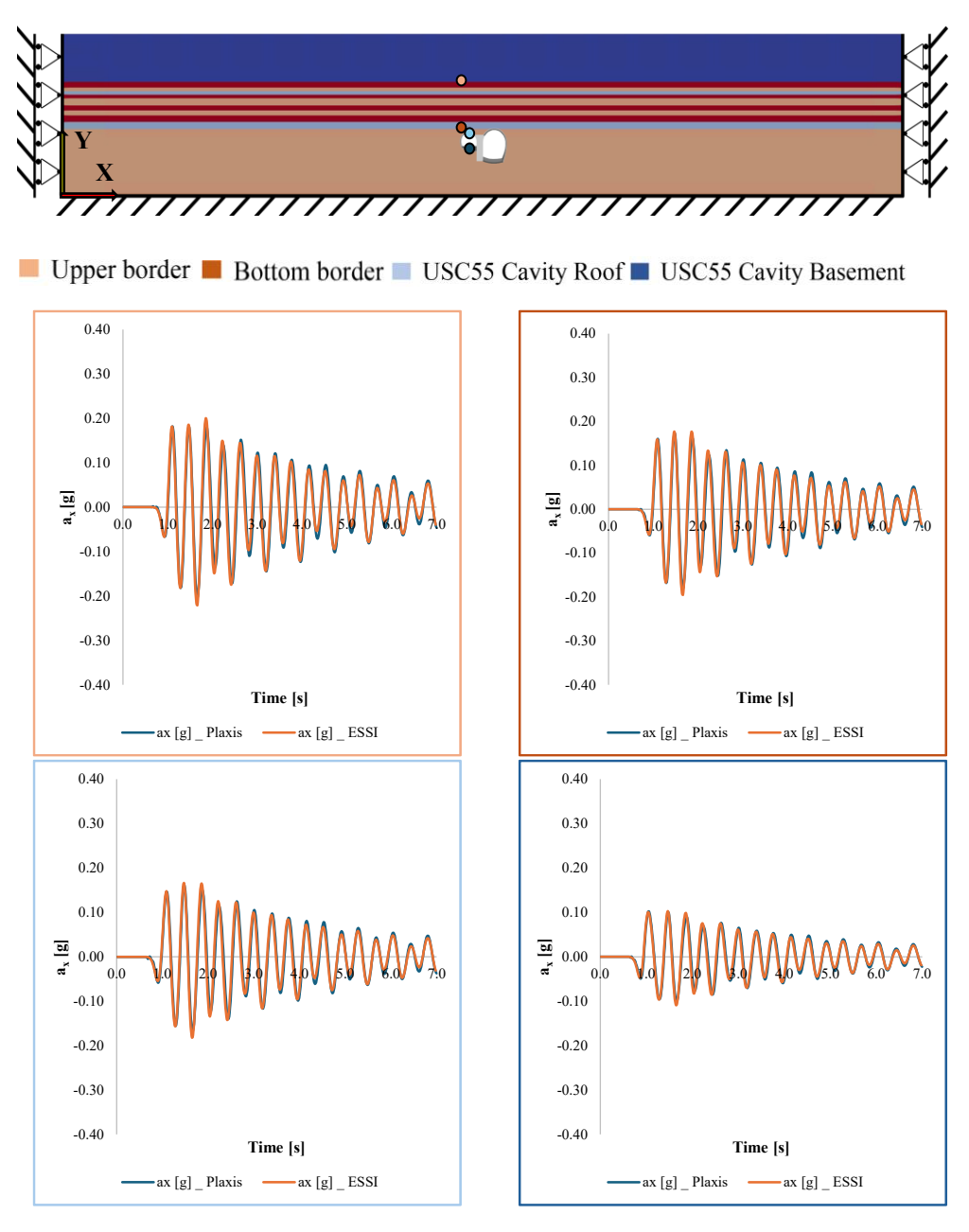


Figure 4.7.6 Comparison between PLAXIS and Real-ESSI models: results in terms of acceleration time histories by applying Ricker Wavelet [53].

To better understand if the model can determine structural response of cavities when subjected to a seismic input motion, instead of the Ricker wavelet input, the recorded time history of acceleration during the Friuli earthquake (1976) and a low intensity event recorded at CERN on November 1st, 2022 (namely CERN5) were employed and applied at the surface base of the model. Such event, as described in the Chapter 5, had a PGA recorded at ground surface by a seismic station installed by CERN equal to 0.0002 g, with a duration of 180 s and a bracketed duration of 18.864 s has been considered. (Figure 4.7.2).

Results of a comparison between them have been produced in terms of amplification functions. While in free-field conditions they are almost overlapped, consistently with the linear elastic framework, differences in the peak amplitude are due to possible diversities in the damping ratio among codes. Considering the presence of cavities (Errore. L'origine riferimento n on è stata trovata.), the low intensity CERN signal produces very large amplifications, possibly due to numerical issues that need further investigation.

It's worth noting that, between the group of preliminary analyses done in Plaxis and the group of analyses concerning the verification processes of Real - ESSI by means of Plaxis and Strata, as well as its subsequent application for all the analyses carried out in Chapter 5, there are differences:

- In the first group of analyses in Plaxis, as described in Section 4.6, linings and basements were modelled as plate elements.
- For the inter-code response verification process, the model built in Plaxis was integrated with linings and basements appropriately modeled as volume elements. A similarly complete model, identical to the appropriately integrated Plaxis model, was built in Real-ESSI, and all inter-code comparisons were made considering, therefore, the updated and appropriately refined models (Section 4.7).
- In Chapter 5, all analyses in Real-ESSI performed, employing the DRM methodology and the input parameters generated by the LHS algorithm, always involved the updated and appropriately refined model.

Thus, plate elements were not employed in Real-ESSI. All comparisons with Plaxis and analyses using DRM methodology were performed employing the integrated and appropriately refined model.

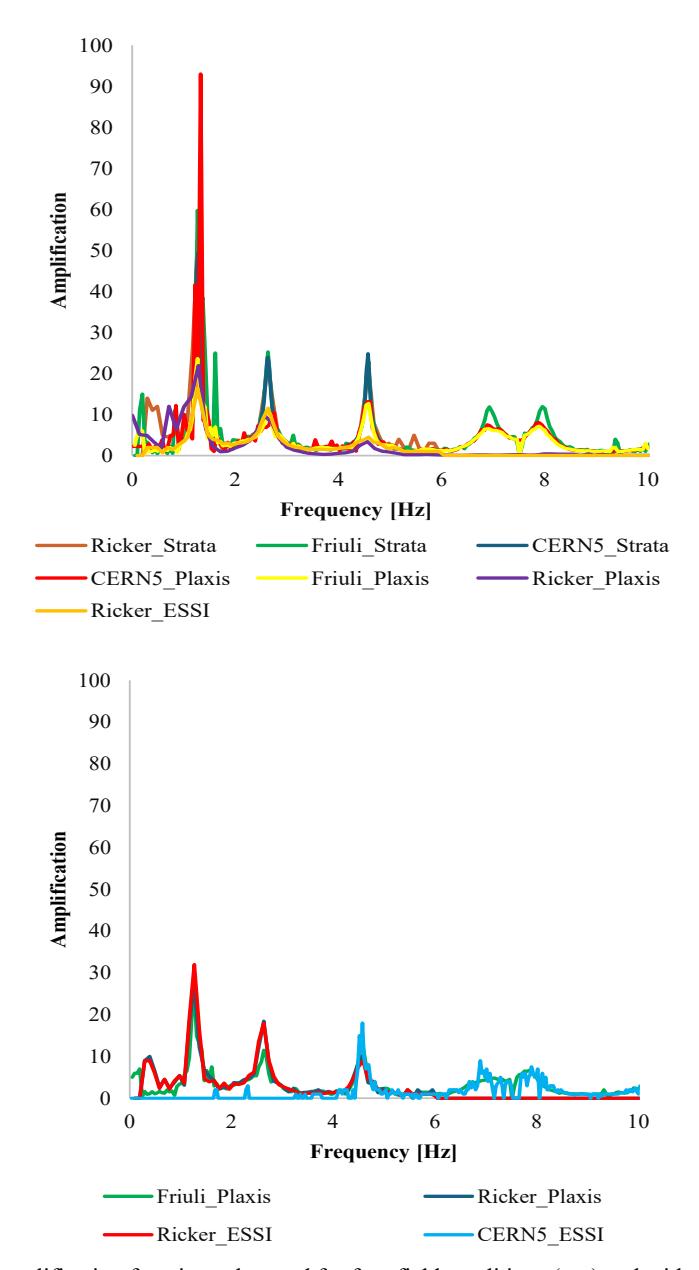
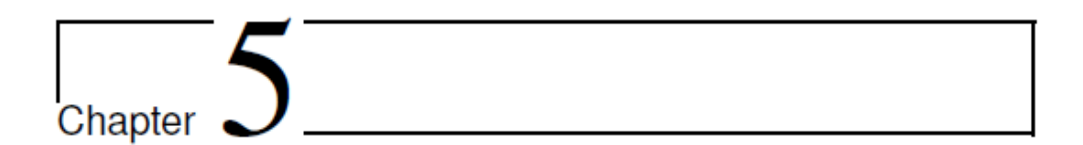


Figure 4.7.7 Amplification functions observed for free-field conditions (top) and with the presence of CMS cavities (bottom) [53].





5 Uncertainties treatment

In statistics, Monte Carlo simulation is a powerful tool which is frequently used to analyse random phenomena using computers. In a random problem, statistical or probabilistic information is desired for a random output, which depends upon random input variables, fields, and processes. In Monte Carlo simulation, these random input quantities are represented by sets of deterministic numbers called realizations, observations, or samples.

Sample inputs are used to generate sample outputs, which can yield the desired statistical or probabilistic information about the random output quantity. Monte Carlo simulation is robust, simple to use, and generally faster than full probabilistic approaches, and therefore is often used to solve random problems and to validate other analysis techniques. To reduce the number of samples required for good accuracy in Monte Carlo simulation, other sampling approaches have been developed for specific cases. One of the best small-sample Monte Carlo approaches is Latin Hypercube Sampling (LHS).

Latin hypercube sampling preserves marginal probability distributions for each variable simulated, while matching target correlations between variables. To do this, Latin hypercube sampling constructs a highly dependent joint probability density function for the random variables in the problem, which allows good accuracy in the response parameters using only a small number of samples. There are two stages to Latin hypercube sampling. First, samples for each variable are strategically chosen to represent the variable's probability density function. Then the samples for the variables are ordered to match target correlations between variables. Because correlations are enforced by changing the order of the samples instead of their values, the marginal probability

distributions of the variables remain intact, according to Huntington and Lyrintzis in [85].

In the present Chapter, LHS was employed to define all the possible uncertainties related to the random choice of the geotechnical and mechanical parameters defining the properties of soils, rocks and cavities' materials.

Through a series of analyses, several probabilistic scenarios were studied in which the displacements and accelerations, with reference to the point located at the base of the experimental cavity UXC55, showed a variation, sometimes significant, depending on the aforementioned properties and, above all, on the type of seismic signal considered.

Starting from experimental recordings provided by seismic stations located on the surface and at depth, the calibrations of these parameters were carried out several times with the aim of reducing the state of uncertainty affecting the choice of such parameters.

Considering the dependence of the dynamic response of underground structures on the amount of stiffness mobilized by low strain levels associated with low intensity recordings, the amount of shear stiffness relative to the soil/rock was consequently increased, in accordance with the law of decay of shear stiffness as a function of the level of strain reached.

- In Section 5.1, an overview of the LHC seismic network, whose installation deployed at CERN beginning of 2017 in collaboration with the Swiss Seismological Service (SED).
- In Section 5.2, all the characteristics related to the reference seismic event employed for the analyses were highlighted. More in detail, all the horizontal components recorded by the surface and underground seismic stations, namely CERNS and CERN5 respectively, in their bracketed duration, are reported. In addition, a description of the distribution of the seismic stations with related seismic data has been done, with a reference, essential for the present study, to the attenuation laws to be considered for correctly implementing the input signal CERNS at ground surface and foreseeing, in this sense, an attenuation of the latter and, therefore, of the time histories in terms of displacements and accelerations.
- In Section 5.3 and its subsections, a description of the first application of LHS algorithm to the case study was reported. A data set containing all the random variables chosen on the basis of several

Chapter 5: Uncertainties treatment

parameters as the uncertainty weight and the probability distribution functions, has been produced. All the results and comments were reported, describing all the possible causes that produced a high level of uncertainty, highlighted in terms of very high amplifications of the responses in terms of displacements and accelerations that may produce conditions of serious damage due to the nature of the systems and equipment present in the cavities and, therefore, may negatively affect the safety requirements and structural integrity.

• In Section 5.4 and its subsections, a description of the second application of LHS algorithm to the case study was reported. In this sense, a second data set was produced on the basis of the mean values of all the analyses that, in the first stage, produced appreciable results, since the state of uncertainty around the variables recalibrated had less effects, in terms of large amplifications, on the responses produced. This second application achieved satisfactory results, confirming a reduced state of uncertainty around all the parameters randomly chosen.

5.1 LHC seismic stations

Switzerland needs a seismic network to monitor background seismicity and understand the effects of rare, large – scale earthquakes that cause extensive damage. This is important even in a country with a seismic hazard as moderate as Switzerland's. A dense network that monitors seismic activity in real time fulfils this role and rapidly notifies the authorities, the media and the public about earthquakes in the wake of significant seismic events and provide highquality data for hazard studies and fundamental earthquake research. Switzerland's dense seismic network consists of sophisticated, modern, lownoise stations with real-time communication to distributed processing hubs at ETH Zurich. Data were analysed and events were detected within tens of seconds after their occurrence, as done in Cabon et al. in [86].

The Global Seismographic Network (GSN) has more than several thousand stations, globally distributed, state-of-the-art digital seismic network that provides free, real – time, open access data. The Swiss Seismological Service (SED) at ETH Zurich is the federal agency for earthquakes in Switzerland. Its activities are integrated in the federal action plan for earthquake precautions.

Over 150 seismic monitoring stations operated by the Swiss Seismological Service monitor the seismic activity in Switzerland and its neighbouring countries in real-time. The stations are spread all over the country and are installed at various sites like caves, tunnels, and even boreholes.

In view of current sensitive projects and those to be realized in the future, CERN in collaboration with the Swiss Authorities decided to deploy a seismic network, at surface and underground positions.

A large ground vibration or a seismic wave striking the LHC might induce beam position (orbit) changes partially or all along the circumference. The ground movement is transmitted to the beam through LHC quadrupole magnets. The main effect of ground is the change in the beam position along the entire ring due to the displacement of the quadrupoles. This effect can be amplified by the LHC magnet structure. Two basic elements must be considered to measure the stability of the beam: the dynamic behaviour of the structure, as a ground motion can be strongly amplified at the magnetic centre if certain magnet natural frequencies are excited, and the environmental conditions, in the location where the structure is installed, that can be affected

by stationary (ground motion) or transitory vibrations (earthquakes, nearby shocks).

Due to LHC sensitivity to vibrations, seismic stations were installed directly next to the experiments to measure ground vibrations in terms of displacement, velocity or acceleration, and represent a precious information for monitoring the equipment at the surface or at several depths, as well as allowing to anticipate some vibratory effects on the beam stability.

The three first stations of the seismic network have been installed one at the surface near LHC, namely CERNS, and two in LHC tunnels, namely CERN1 near ATLAS and CERN5 near CMS experiments respectively (Figure 5.1.1).

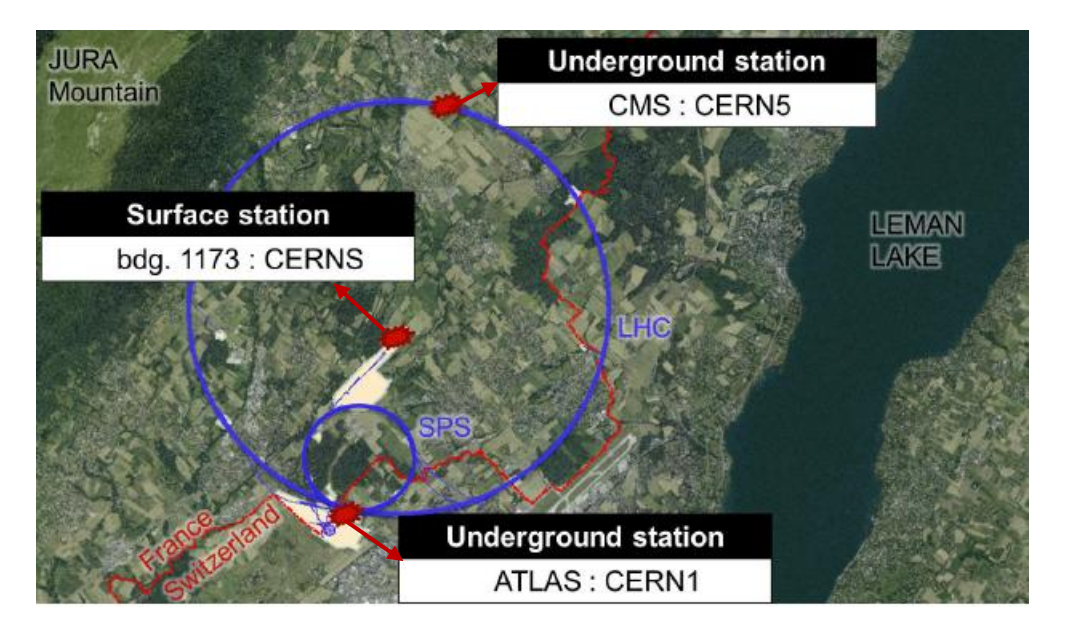


Figure 5.1.1 Position of the seismic stations [86].

	Latitude [WGS84]	Longitude [WGS84]	Altitude [Nf02]	Distance to surface [m]
Surface	46.266947	6.066212	463,2	-0.5
Point 1	46.235876	6.054836	356.3	-83.7
Point 5	46.309893	6.076080	418.2	-90.2

Table 10 Coordinates of the CERN seismic stations.

For achieving seismic signals of good quality, two conditions were met in their positioning and alignment:

- As far as possible from any human activity, buildings with deep foundations, electrical lines and airports.
- To the depth of bedrock: the depth of sediments should be as small as possible, the ground should be stable, and the sensor should not be installed on an artificial hill which would have a poor coupling with the ground. If no bedrock is available, a seismic vault should be installed.
- The stations' sensors at surface are aligned towards the North, while the underground sensors (EW, NS, V) are aligned to fit the anti-clockwise beam coordinates (X, Y, Z) (Figure 5.1.2).

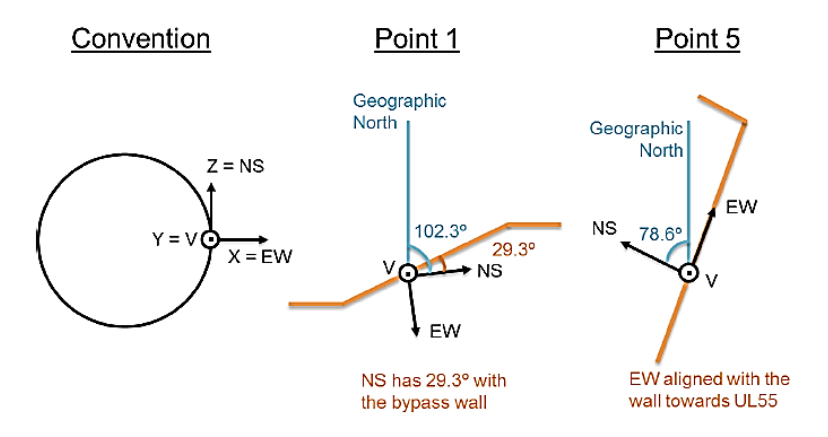


Figure 5.1.2 Convention for alignment of the underground stations [86].

The station in point 5 aims at monitoring the levels of vibration near CMS experimental cavern. The sensors and the control rack are separated by a sector door that should only be open in case of emergency. The corridor where the sensors are installed is thus rarely used. The rack is on the other side of the sector door, in USC55, easily accessible from the surface (Figure 5.1.3).

Chapter 5: Uncertainties treatment

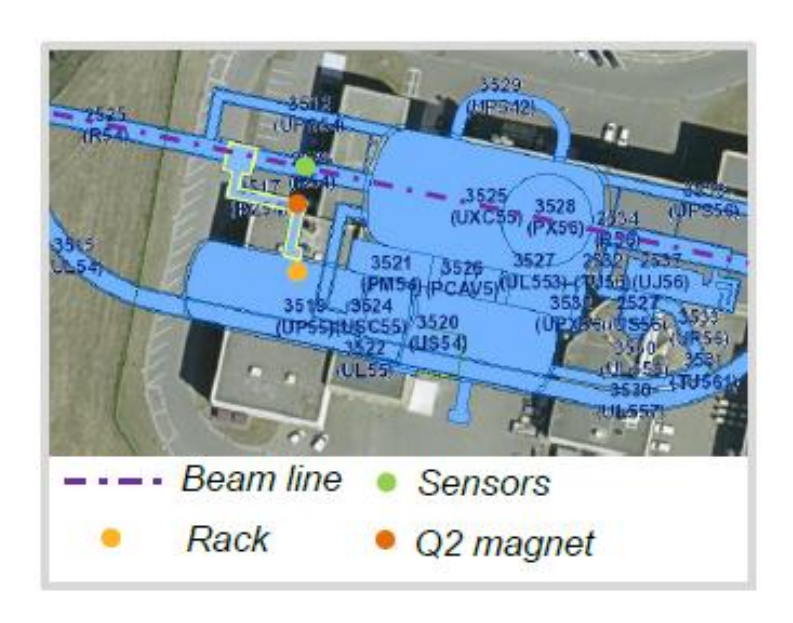


Figure 5.1.3 Point 5: location of the CERN5 sensors (green) in the CMS cavern area [86].

5.2 The earthquake event of 1st November 2022

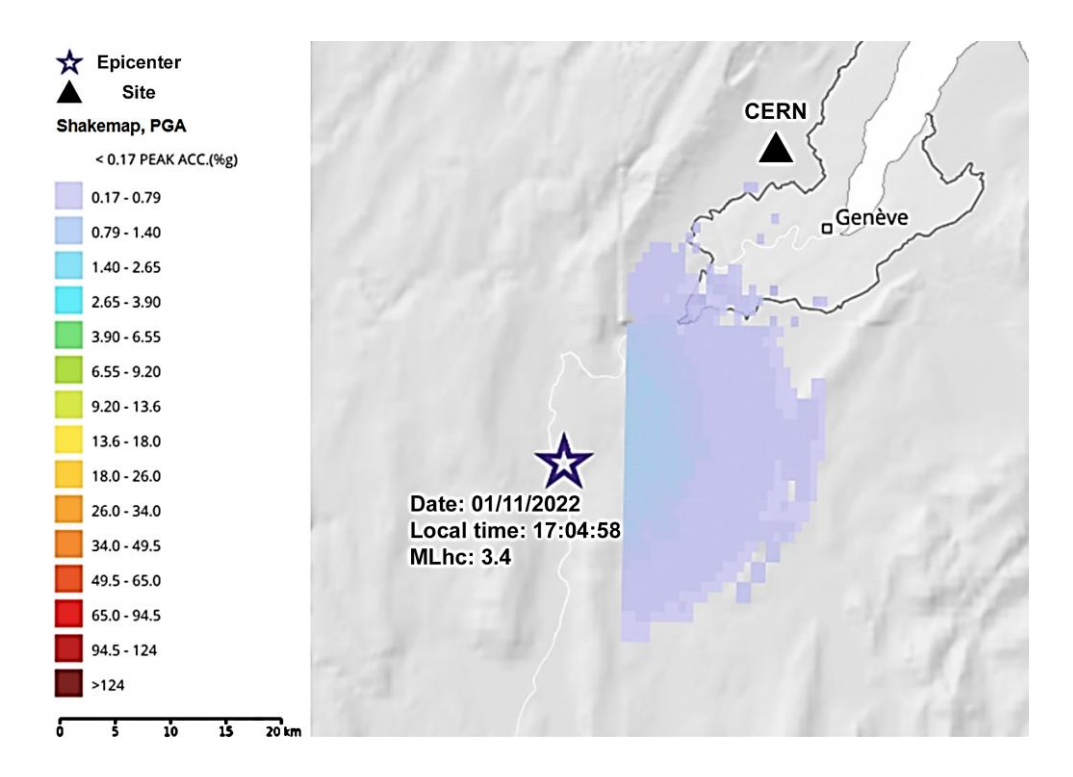


Figure 5.2.1 Earthquake event of 1st November 2022: PGA distribution [87].

Local time	01/11/2022 17:04:58
UTC time	01/11/2022 16:04:58
Latitude / Longitude	46.02 / 5.83
Magnitude	3.4
Magnitude type	MLhc
Location	Bellegarde – sur – Valserine (France)
Depth [km]	9.5

Table 11 Earthquake event of 1st November 2022: summary description.

For benchmarking Real-ESSI simulations and evaluating the seismic structural safety of the underground facilities at Point 5 in terms of vibration assessment and monitoring, a real earthquake event recorded at CERN has been employed.

Regarding this event, occurred approximately 30 km South-West of the CERN area on 1st November 2022, having Local Magnitude (ML) of 3.4 on the Richter scale, in Figure 5.2.1 is shown a map [87] with the definition of the epicentre position, respect to CERN site, as well as a PGA distribution detected by the Swiss Seismological Service at the ETH Zurich. In this context, being CERN5 seismic station of considerable interest, as installed in the proximity of the UXC55 experimental cavern at Point 5, as well as CERNS station, thanks to which having available PGA surface records for evaluating earthquake – induced effects in terms of amplifications, their respective vertical and horizontal components, were taken as the reference for this study. Figure 5.2.2 shows, in detail, the horizonal components of the records of such stations.

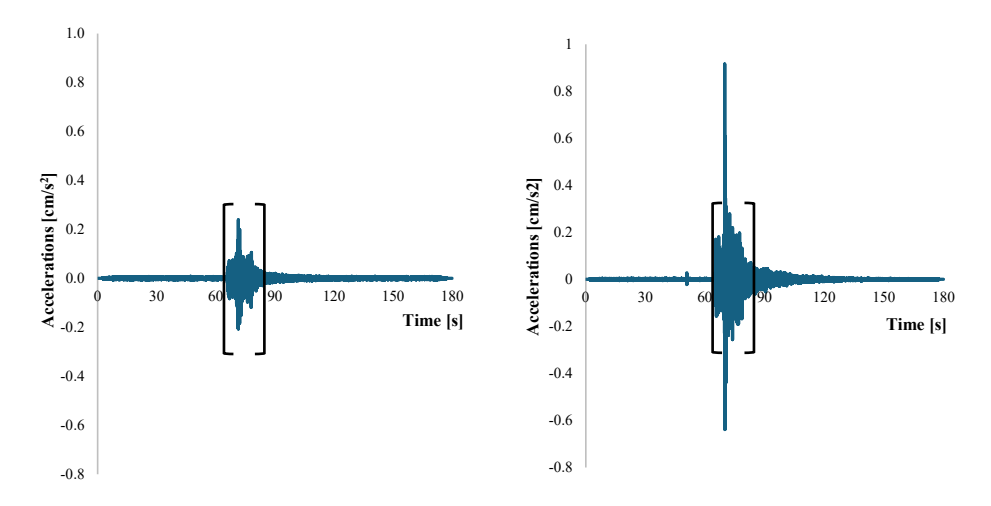


Figure 5.2.2 Horizontal components of the CERN5 underground acceleration (left) and CERNS surface acceleration time histories (right), with indication of bracketed duration considered.

Because of the excessive length of the records, quantified as 180 seconds and because for most of these signals, accelerations and displacements are almost zero, a bracketed duration of 18.9 seconds was determined and

implemented in the software for all the comparison studies (Figure 5.2.3, Figure 5.2.4).

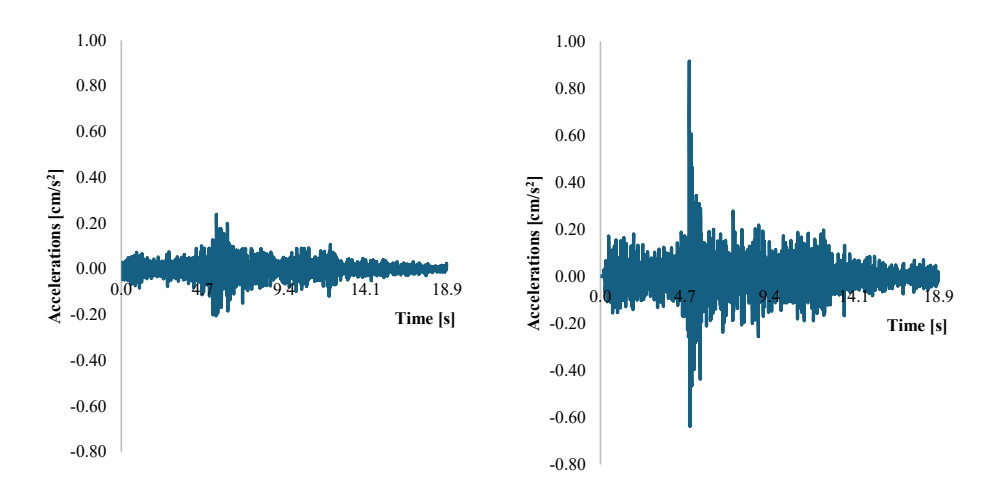


Figure 5.2.3 Horizontal components of CERN5 underground accelerations (left) and CERNS surface accelerations (right) time histories: bracketed durations.

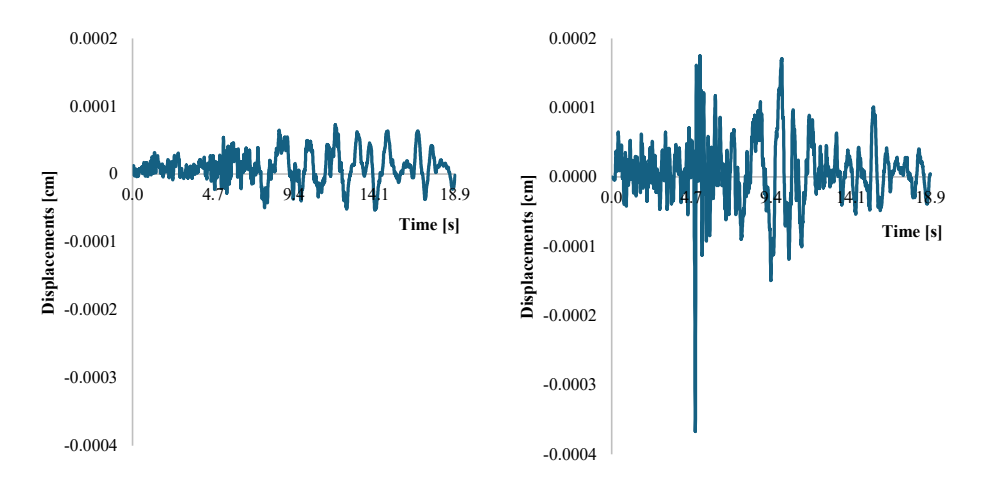


Figure 5.2.4 Horizontal components of CERN5 underground displacements (left) and CERNS surface displacements (right) time histories: bracketed durations.

According to Alakbarli et al. in [88], the accelerations detected are a function of the Euclidean distance from the epicentral area. In Figure 5.2.5 a ground vertical section indicating the recorded accelerograms is given, while Table 12 contains the seismic data referring to the CERNS and CERN5 stations aligned in the 75° East direction, in occasion of the 1st November 2022 earthquake.

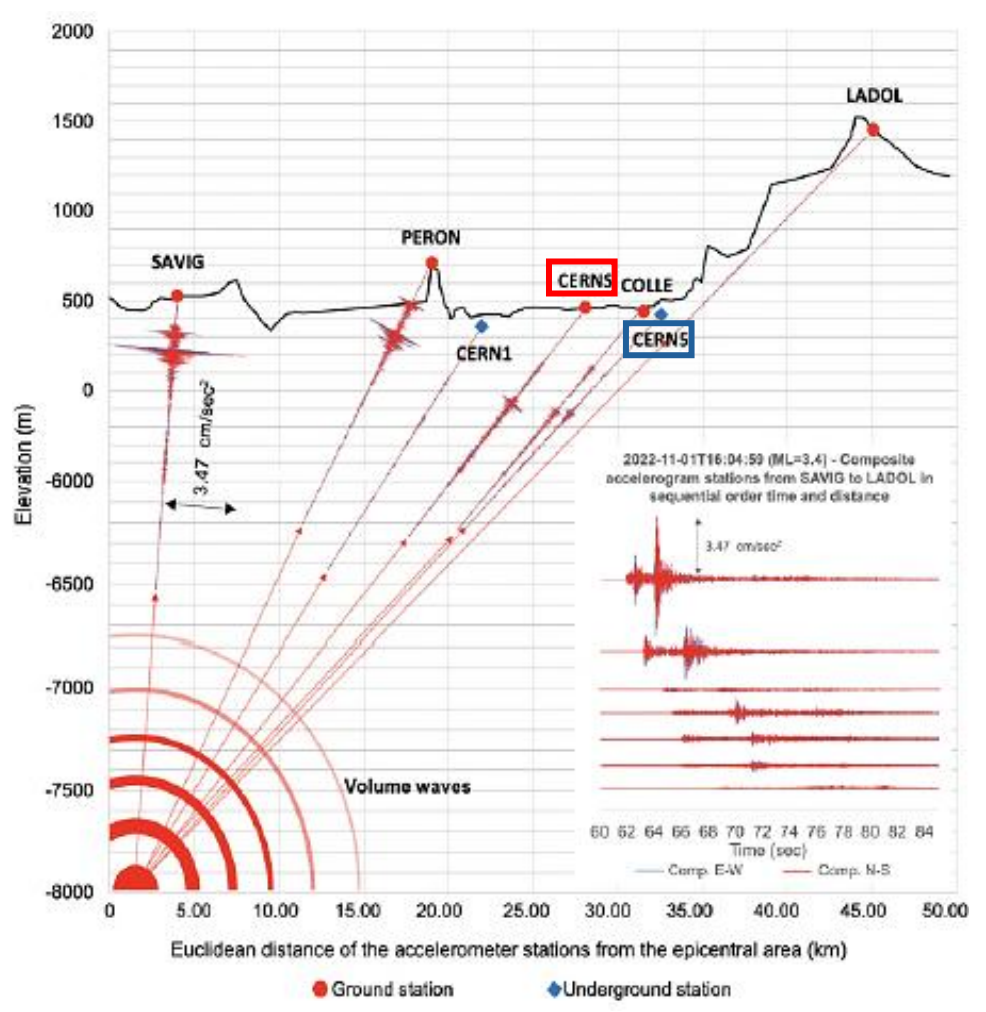


Figure 5.2.5 Earthquake event of 1st November 2022: seismic stations distribution and related accelerograms recorded [88].

Station Code	Elevation	Epicentral distance	Direction	Onset time of the seismic motion	Peak acceleratio n in first second	Speed between pairs of stations	PGA arrival	PGA	Speed between pairs of stations	PGA damping compared to epicentral PGA
	(m)	(km)	*East	(sec)	(cm/sec²)	(km/sec)	(sec)	(cm/sec ²)	(km/sec)	(%)
CERNS	463	27,5897	73.00	65.268	0.1539	4.17	69.956	0.865	2.38	18.40
CERN1	356	24.03	73.00	64.70	0.1193		65.376	0.1193		
CERN5	418	32.36	73.00	65.88	0.0873	7.06	71.208	0.2483	1.43	

Table 12 Earthquake event of 1st November 2022: CERNS and CERN5 seismic data [88].

The accelerograms recorded by the surface and underground stations during the event clearly show that such linear dependence, as evident from the SAVIG station (epicentral distance equal to 4.66 km) and the LADOL station (epicentral distance equal to 46.62 km), is due as much to the onset time of the ground motion, generated by the volume waves rising from the deeper layers of the geo-stratigraphic configuration, i.e. P and S waves, as to the PGA arrival time generated by the surface waves, i.e. Rayleigh and Love waves, confirming that, moving away from the epicentre zone, the amplitudes of the surface waves become predominant compared to the amplitude of the longitudinal (P) and transversal (S) volume waves, until the ground motion tends to dampen.

Focusing on CERNS surface station and CERN5 underground station recordings and comparing them with the CERN1 underground station (located in proximity of ATLAS experiment, at Point 1), CERN1 is closest to the epicentral area of about 8.33 km respect to CERN5, but an increase of accelerations recorded by CERN5 five seconds after the arrival time of the volume waves respect to the CERN1 accelerogram could be probably due to the propagation phenomena of wall waves in the LHC tunnel.

CERN1 recording presents an acceleration peak value in the first second of the seismic motion equal to 0.1193 cm/s² and is similar to that recorded by the same station five seconds after the peak. By considering, instead, CERNS and CERN5 stations, the acceleration peaks, equal to 0.8650 cm/s² and 0.2483 cm/s² respectively and recorded with a delay of five seconds, are greater than the accelerations recorded during the first second of the seismic motion. This aspect suggests that while the seismic motion recorded by the CERN1 station can be due only to volume waves, the acceleration peaks recorded in the other two CERN stations can be attributed to the seismic motion generated by waves,

as triggered by volume waves respectively in the surface layer of the geostratigraphic configuration and in the rocks around the LHC tunnel.

Since the CERN5 underground station is located about 5 km away from the CERNS surface station, by means of the figure below in which the attenuation curves for volume waves and surface waves are shown, as well as the positioning of the seismic stations with respect to the epicentre area, in order to employ a correct input signal for subsequent analysis, it is necessary to attenuate it by an amount equal to the ratio of the acceleration value recorded at CERN5 but read in projection on the surface wave curve (PGA_{CERN5}) to the value recorded at CERNS but read in projection on the same (PGA_{CERNS}) (Figure 5.2.6).

Being PGA_{CERN5} = 0.50 cm/s^2 and PGA_{CERNS} = 0.60 cm/s^2 , the above ratio is:

$$r = \frac{PGA_{CERN5}}{PGA_{CERNS}} \sim 0.83 \tag{39}$$

Consequently, the CERNS accelerations and displacement time histories to be considered must be reduced by about 20% (Figure 5.2.7), by means of the following relations:

CERNS attenuated accelerations = $0.83 \cdot \text{CERNS}$ surface acceleration CERNS attenuated displacements = $0.83 \cdot \text{CERNS}$ surface displacements

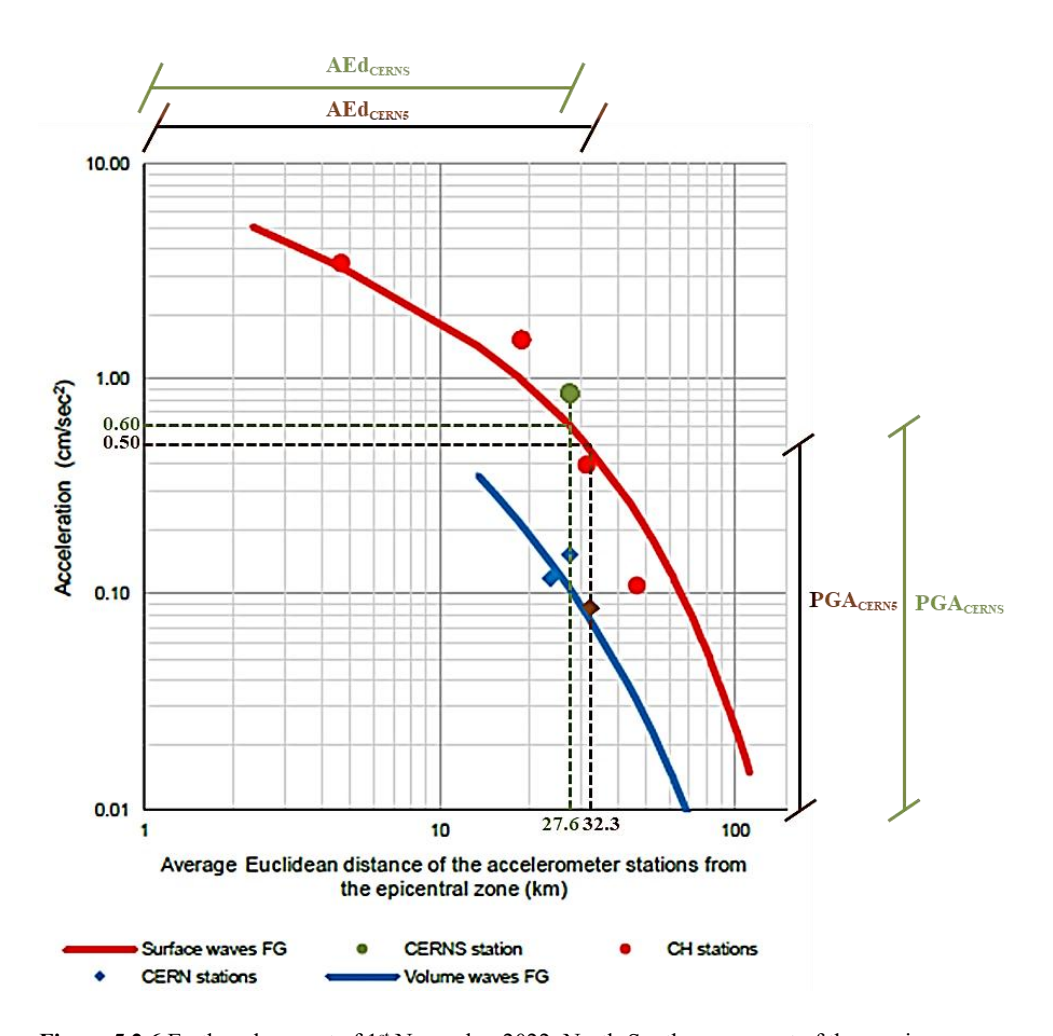


Figure 5.2.6 Earthquake event of 1st November 2022: North-South component of the maximum acceleration of the sole volume waves recorded in the first second in CERN stations (blue) and the PGA recorded in surface stations (red) [88].

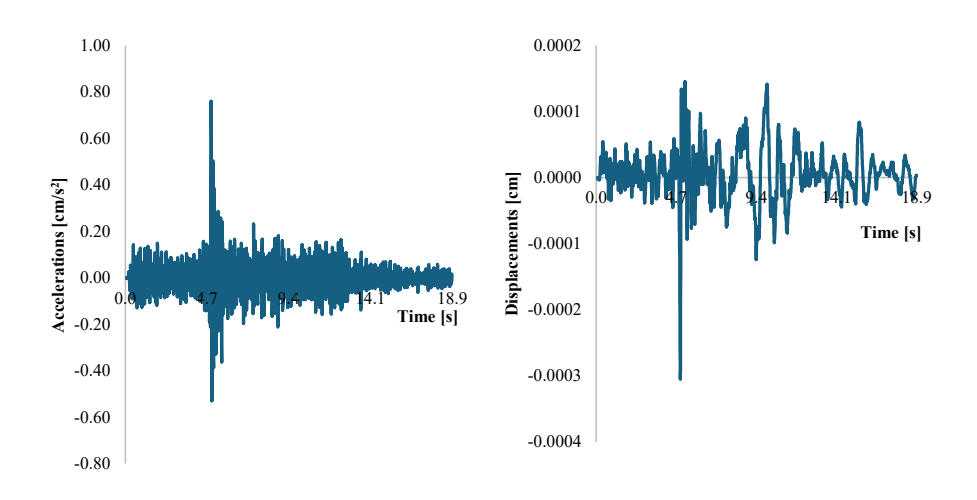
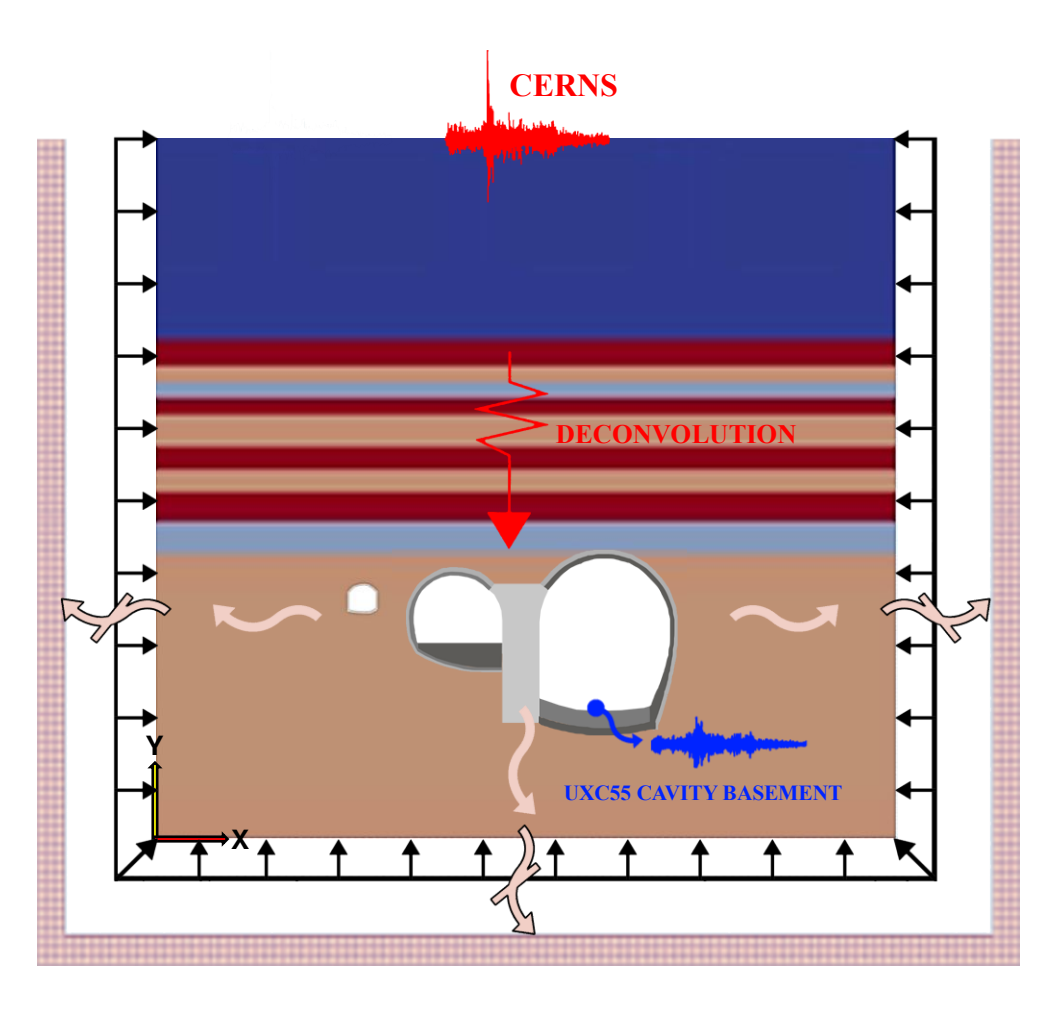


Figure 5.2.7 Horizontal components of CERNS surface acceleration (left) and displacement (right) time histories properly attenuated.

An explanatory figure of the general performance of the DRM methodology is shown below (Figure 5.2.8). More in detail, the deconvolution process is shown, in terms of propagation of the seismic input signal from the ground surface to the underground structures, with the definition of the points of greatest interest for later analyses, as well as how internal waves internally generated by this latter can be radiated until the boundaries' model, before getting artificially damped out by the lateral and bottom damping elements. In this context, in fact, damping elements must be used to damp out such waves, not allowing them to go back into the main domain, so according to [47] [89] while for DRM layer no Rayleigh damping was assigned ($\xi = 0$), it is necessary to provide higher viscous damping values to lateral and bottom damping elements ($\xi = 50\%$).

This latter has been chosen and applied at the boundaries damping elements after consulting several literature studies [48] [89] [90] and [91]: such studies contemplate the application of DRM methodology to soil – structures interaction problems, but not to soil – tunnels interactions, so after several trials the choice of $\xi = 50\%$ allowed the analyses to converge toward a finding worthy of comparison with the available input data.



Free – field input motion: CERNS station.

Output recorded at the UXC55 Cavity Basement: comparison with CERN5 station recordings.

DRM layer: "effective" seismic forces applied by DRM elements on the whole model.

Internal waves internally generated by underground structures and radiated until they get artificially damped out by the lateral and bottom damping elements.

Damping layer: application of high values of Rayleigh viscous damping to damp out internally generated and radiated waves at the boundary of the domain.

Figure 5.2.8 DRM methodology applied to the model realized in Real – ESSI Simulator.

5.3 LHS application to DRM model: first comparison

Based on the study presented in Section 4.5 on the preliminary characterization of the response of large underground cavities located in Point 5 under seismic excitations, most of the parameters contained in Table 3 were taken to be properly implemented in the Latin Hypercube Sampling algorithm to obtain the mean values and the standard deviation values, respectively.

More in detail, being the CERNS and CERN5 recordings of low intensity as they refer to the earthquake od 1st November 2022, all the parameters characterizing a linear visco – elastic behaviour for both soils and concrete linings were considered (Table 14, Table 14).

Soils/Rock	Parameters	Unit	Model	Mean	STD
	γ_{soil}	kN/m3	LN	23	0.5
Moraine	E_{soil}	MPa	LN	30	15
deposits	V _{soil}	[-]	Beta [0,0.5]	0.3	0.05
	$\xi_{\rm soil}$	[-]	LN	5	2.5
	γ_{soil}	kN/m3	LN	24	0.4
Weak	Esoil	MPa	LN	340	240
Molasse	V _{soil}	[-]	Beta [0,0.5]	0.25	0.05
	$\xi_{\rm soil}$	[-]	LN	5	2.5
	γ_{soil}	kN/m3	LN	24	0.4
Medium	E_{soil}	MPa	LN	1200	620
Strong Molasse	V _{soil}	[-]	Beta [0,0.5]	0.25	0.05
	$\xi_{\rm soil}$	[-]	LN	5	2.5
Strong Molasse	γ_{soil}	kN/m3	LN	24	0.4
	E _{soil}	MPa	LN	2420	1500
	V _{soil}	[-]	Beta [0,0.5]	0.25	0.05
	$\xi_{\rm soil}$	[-]	LN	5	2.5

Table 13 LHS: probability distributions of the input parameters (soils and rock).

Concrete linings and basements	Parameters	Unit	Model	Mean	STD
	γcls	kN/m3	LN	24.5	0.5
C25/20	$f_{ m cls}$	MPa	LN	33	5
C25/30	V _{cls}	[-]	Beta [0,0.5]	0.25	0.05
	ξ_{cls}	[-]	LN	5	2.5
	$\gamma_{ m cls}$	kN/m3	LN	24.5	0.5
G25/45	$f_{ m cls}$	MPa	LN	43	5
C35/45	V _{cls}	[-]	Beta [0,0.5]	0.25	0.05
	$\xi_{\rm cls}$	[-]	LN	5	2.5
	γcls	kN/m3	LN	24.5	0.5
040/50	$f_{ m cls}$	MPa	LN	48	5
C40/50	V _{cls}	[-]	Beta [0,0.5]	0.25	0.05
	$\xi_{\rm cls}$	[-]	LN	5	2.5
	$\gamma_{ m cls}$	kN/m3	LN	24.5	0.5
C50/60	$f_{ m cls}$	MPa	LN	58	5
	V _{cls}	[-]	Beta [0,0.5]	0.25	0.05
	ξ _{cls}	[-]	LN	5	2.5

Table 14 LHS: probability distributions of the input parameters (concrete linings and basements).

Once the mean and standard deviation values were set, LHS algorithm was employed to obtain a random distribution of the above geo-mechanical parameters and define a set of fifteen simulations.

During the first simulations carried out, of which in Figure 5.3.1 an example is shown by applying CERNS record at the ground surface and evaluating the output at the UXC55 cavity basement, very amplified displacements were observed in the points of greatest interest, i.e. the ground surface and the UXC55 cavity basement. This anomaly can be traced back to the fact that, considering the soils/rock values in the tables above, the E_{soil} stiffness, the soil

layers appeared much more deformable, since the shear wave velocity values (Vs) obtained from the following relations:

$$G = \frac{E_{\text{soil}}}{2(1 + v_{\text{soil}})}; \quad \rho_{\text{soil}} = \frac{\gamma_{\text{soil}}}{g}; \quad v_{\text{s}} = \sqrt{\frac{G}{\rho}}$$
 (40)

were equal to 70 m/s for Moraine deposits, 235 m/s for Weak Molasse, 443 m/s for Medium Strong Molasse, 629 m/s for Strong Molasse, respectively.

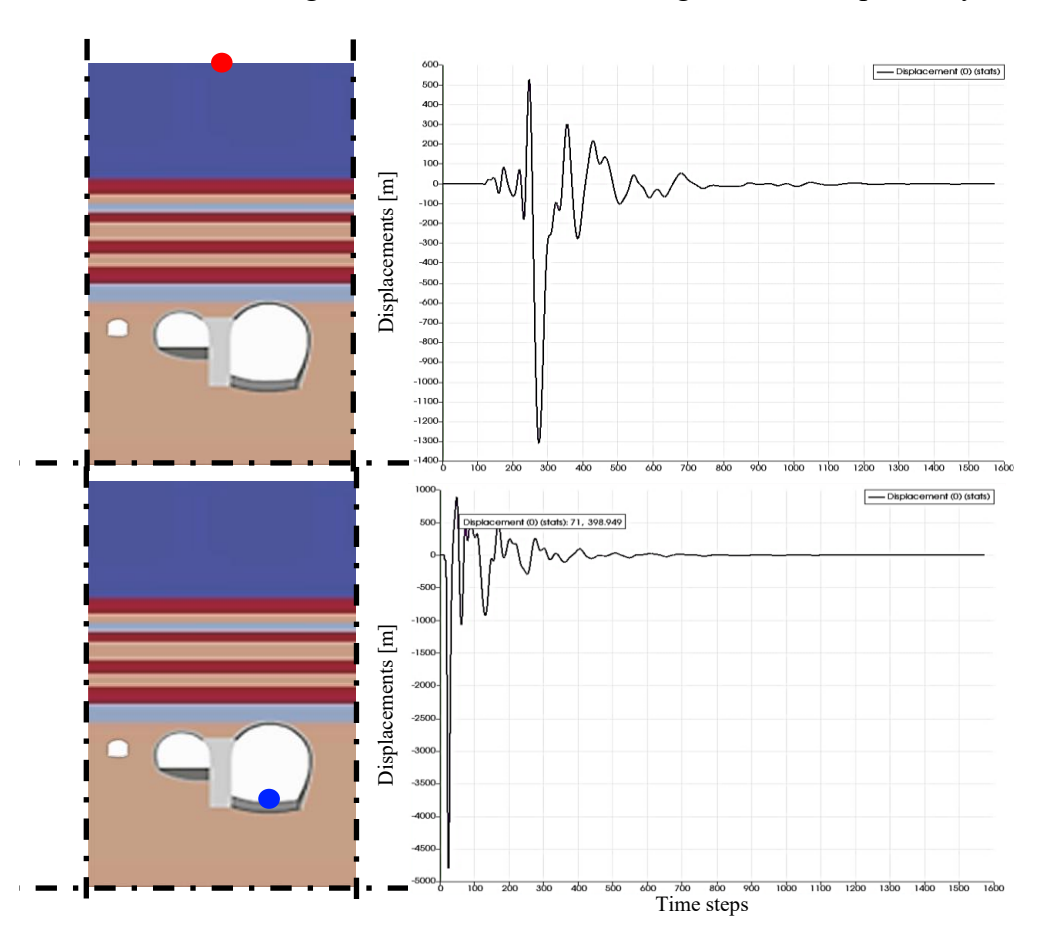


Figure 5.3.1 DRM model: displacement time history, in [m] unit, recorded at the ground surface (top) and at the UXC55 cavity basement (bottom), by employing the parameters of Tables 11-12 and applying the deconvolution considering CERNS input at the ground surface.

This anomaly can also be traced back to the type of seismic signal that is being used, since being of very low intensity, a low level of deformation is consequently mobilized which corresponds, according to the stiffness decay curve described above, to high shear stiffnesses.

According to [71], to consider the low deformation level of the recorded signal, in a subsequent calibration of the above tables, shear stiffnesses were increased approximately to eight times in the Moraine and four times in the Molasses (Table 15). The results obtained below, compared to those obtained as a test and visible in Figure 5.3.1, demonstrate how the dynamic response depends on the mobilized stiffness. The mean Vs profile obtained from this recalibration, as well as all the profiles generated by the LHS algorithm application, is shown below (Figure 5.3.2).

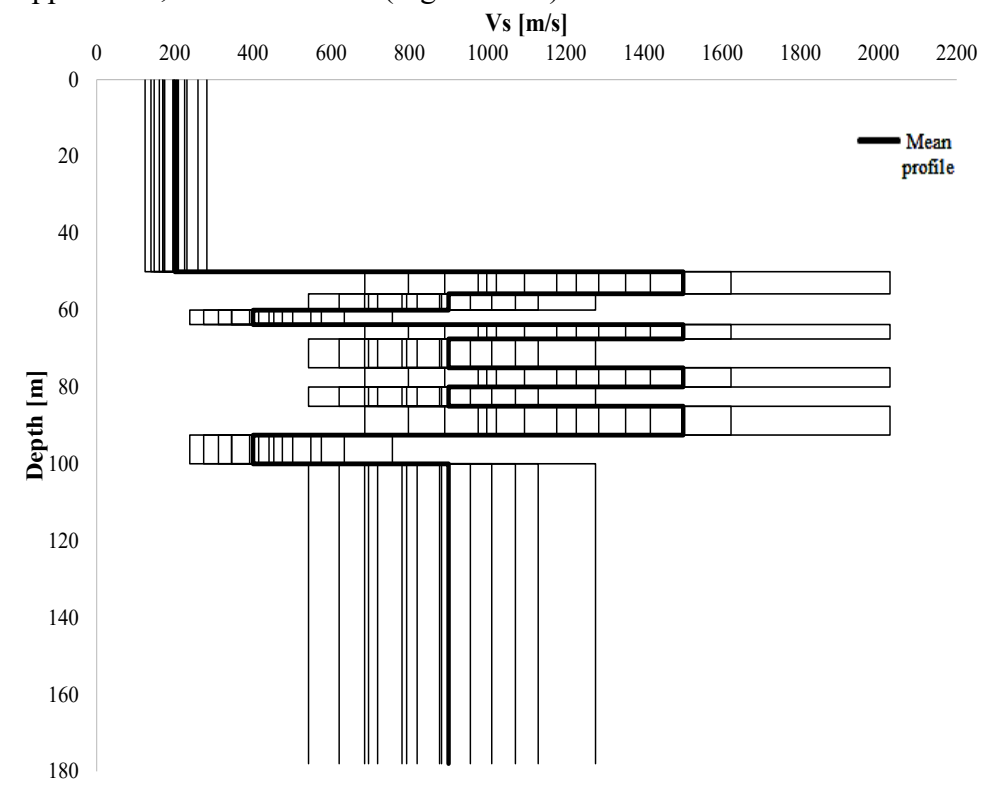


Figure 5.3.2 Vs profiles generated by LHS algorithm by implementing Vs mean profile.

Soils/Rock	Parameters	Unit	Model	Mean	STD
	γ_{soil}	kN/m3	LN	23	0.5
	Esoil	MPa	LN	240	15
	V _{soil}	[-]	Beta [0,0.5]	0.3	0.05
Moraine	ξ _{soil}	[-]	LN	5	2.5
	G	MPa		92	
	ρ_{soil}	kg/m3		2345	
	V_s	m/s		198	
	γ_{soil}	kN/m3	LN	24	0.4
	Esoil	MPa	LN	1360	240
	V _{soil}	[-]	Beta [0,0.5]	0.25	0.05
Weak Molasse	ξ _{soil}	[-]	LN	5	2.5
	G	MPa		544	
	$\rho_{\rm soil}$	kg/m3		2446	
	V_s	m/s		472	
	γ_{soil}	kN/m3	LN	24	0.4
	E _{soil}	MPa	LN	4800	620
M- 1' C4	V _{soil}	[-]	Beta [0,0.5]	0.25	0.05
Medium-Strong Molasse	$\xi_{\rm soil}$	[-]	LN	5	2.5
	G	MPa		1920	
	$\rho_{\rm soil}$	kg/m3		2446	
	V_s	m/s		886	
	γ_{soil}	kN/m3	LN	24	0.4
	Esoil	MPa	LN	13649	1500
	V _{soil}	[-]	Beta [0,0.5]	0.25	0.05
Strong Molasse	ξ _{soil}	[-]	LN	5	2.5
	G	MPa		5460	
	$\rho_{\rm soil}$	kg/m3		2446	
	V_{s}	m/s		1494	

Table 15 LHS: recalibration of the probability distributions for the soils and rock parameters.

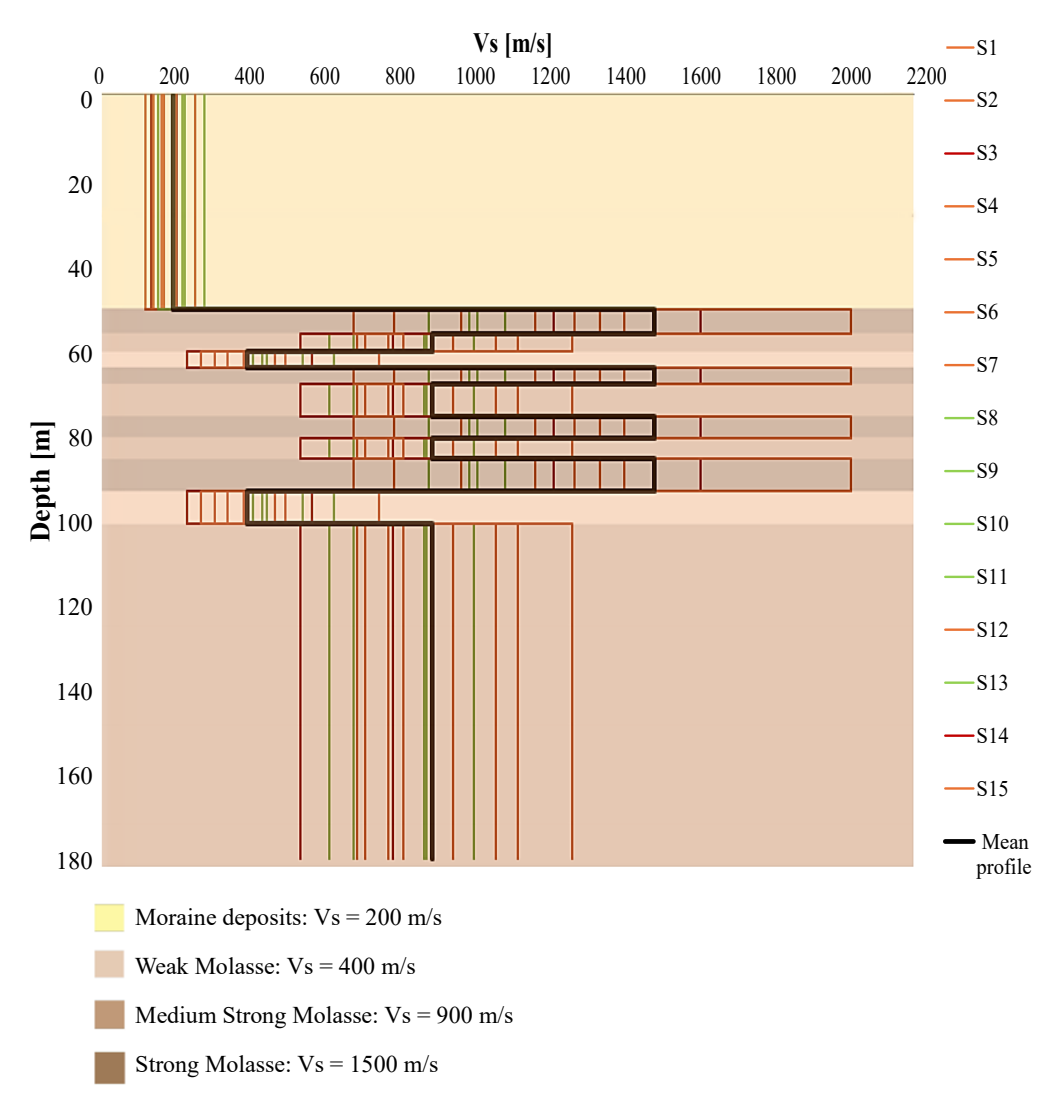


Figure 5.3.3 DRM section model highlighting the Vs mean profile and all the fifteen profiles associated to the fifteen analyses within the first simulations process.

5.3.1 Evaluation of the displacements and accelerations

The treatment of uncertainties problem, applied to this study, has been widely discussed to characterize the seismic response of the underground facilities at point 5, particularly the UXC55 cavity hosting the main equipment and installations, when excited by an earthquake, by means of the execution of a set of fifteen analyses, for which all the data generated by LHS algorithm were employed.

More in detail, in order to characterize several possible scenarios defined in a stochastic way, therefore containing all the uncertainties related to a generation of a random distribution of the geo – mechanical parameters to be inserted in FE software Real - ESSI, displacement and acceleration time histories compared to CERNS and CERN5 seismic signals taken as a reference time histories, were obtained.

As the parameters chosen for the response check between Plaxis and Real-ESSI were used in relation to the signal intensity employed, i.e., medium-high intensity and therefore related to high deformation field, the main problem investigated in the present study was that of focused on the response to low intensity signals such as those recorded in various events that occurred in the area of the cavity system for which records were available (CERN5 and CERNS). Accordingly, the stiffness parameters were modified, scaling them according to the decay curves of the materials, in order to reproduce the behavior at low deformation levels.

The methodology used to obtain the mean and standard deviation values is taken from the test results available from the geotechnical characterization reports provided by CERN [92] [93] [94] [95].

The choice of the parameter fc for concrete in Table 13 is dictated by the availability of more information regarding the values that could be used, so the relevant formula for determining the modulus E was derived.

As shown in Figure 5.3.3, that highlight the Vs profiles defined for each simulation compared to the mean profile, all the FEM simulations related to them were initially marked with a colour, more specifically green, orange and red, to illustrate which and how many of analyses achieved a good level of comparison or mismatch with the ground surface – applied and appropriately attenuated CERNS input signal, as well as a later comparison of the CERN5

recording with the software-generated output data at the UXC55 cavity basement.

For a greater clarity in understanding the results, five analyses perfectly compared with the input data have been subsequently marked with green colour, while all other analyses, generally inconsistent with the input data and highlighting very large amplifications, have been marked with grey colour.

Therefore, for both displacement and acceleration time histories, the results reported consider firstly the "better performed" analyses, then subsequently the results relating to all the analyses carried out to explain which and how many possible scenarios, from the best to the worst, have been stochastically defined.

Focusing on the displacement time histories (Figure 5.3.4, Figure 5.3.5, Figure 5.3.6) the five green analyses appear perfectly comparable at the ground surface, also to confirm the exact implementation of the CERNS input signal in the software in order to operate the deconvolution, while the output results recorded at the UXC55 cavity basement, compared to CERN5 recording, show an almost similar trend especially in the second part of the signal, while in the first part, up to about 5 seconds, the obtained response presents peaks congruent with those observed for the ground surface – applied input signal.

Secondly, focusing on the acceleration time histories, as observed in the results in terms of displacement, the five analyses highlighted in green present comparable results in both control points (Figure 5.3.9, Figure 5.3.10, Figure 5.3.11) while considering all the fifteen analyses results compared one to another, in particular for the control point at the UXC55 cavity basement, it is possible to appreciate the variety of possible scenarios established by the LHS algorithm and understand how much the choice of certain parameters, if dictated by a causal distribution, can significantly affect the dynamic response of the cutting – edge infrastructures in terms of structural safety (Figure 5.3.7, Figure 5.3.8, Figure 5.3.12, Figure 5.3.13).

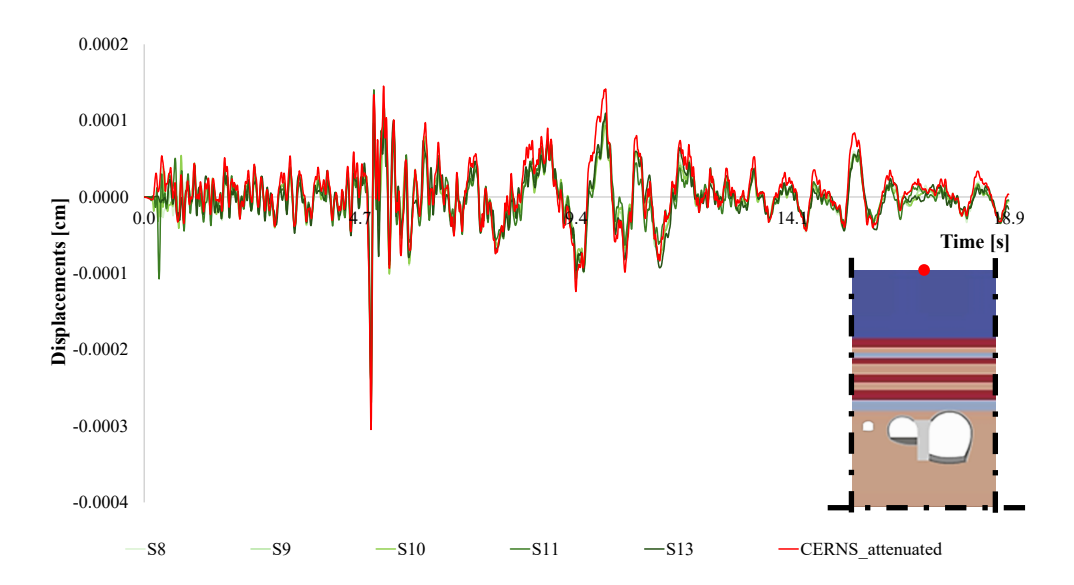


Figure 5.3.4 DRM model: comparison between displacement time histories recorded by CERNS surface station and five "comparable" results recorded at ground surface.

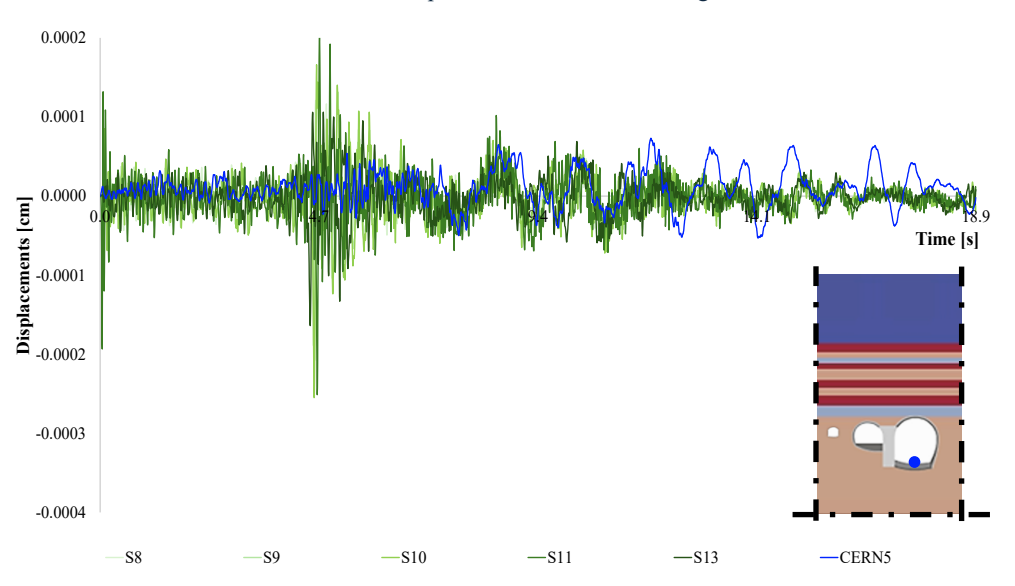


Figure 5.3.5 DRM model: comparison between displacement time histories recorded by CERN5 underground station and five "comparable" results recorded at the UXC55 cavity basement.

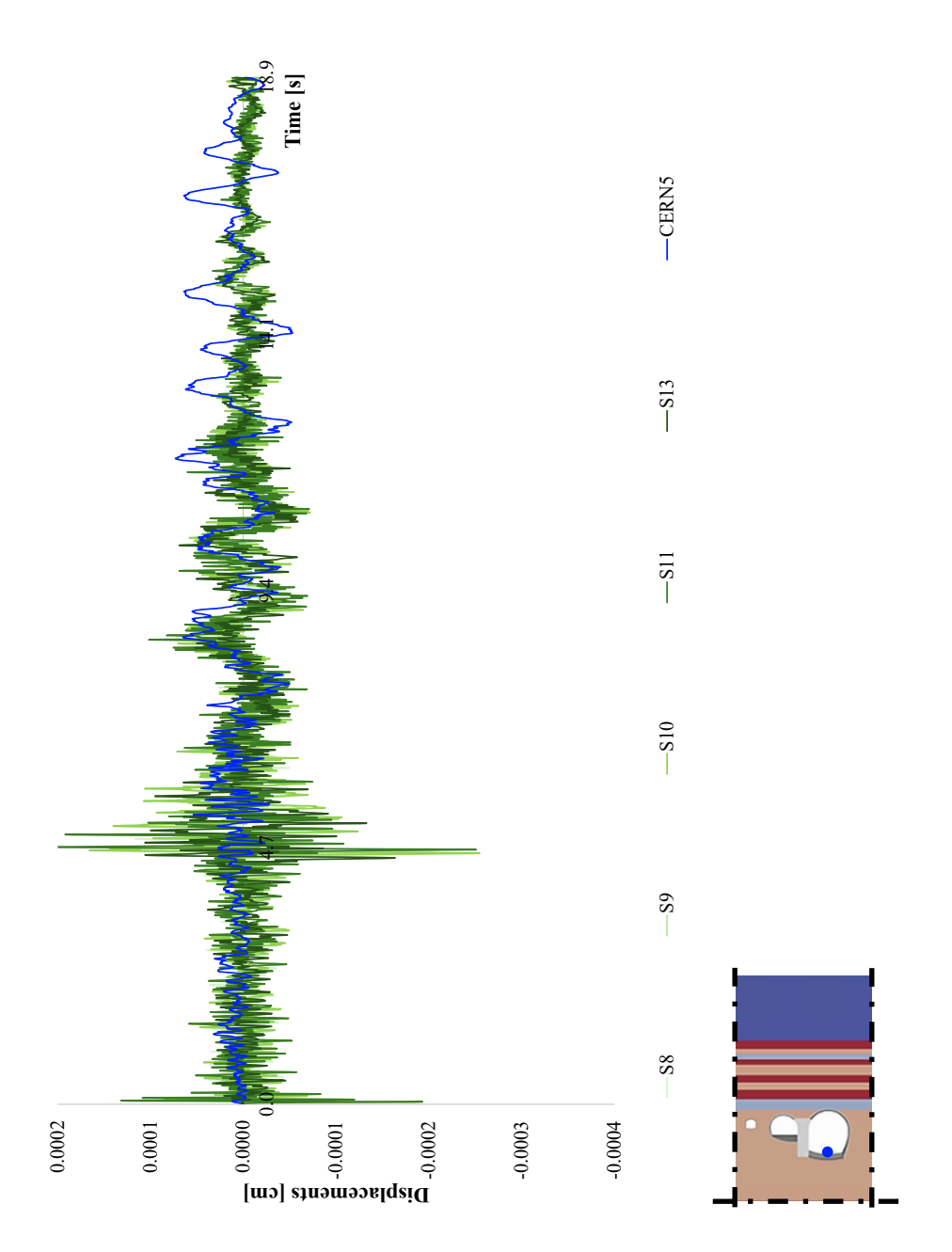


Figure 5.3.6 DRM model: comparison between displacement time histories recorded by CERN5 underground station and five "comparable" results recorded at the UXC55 cavity basement.

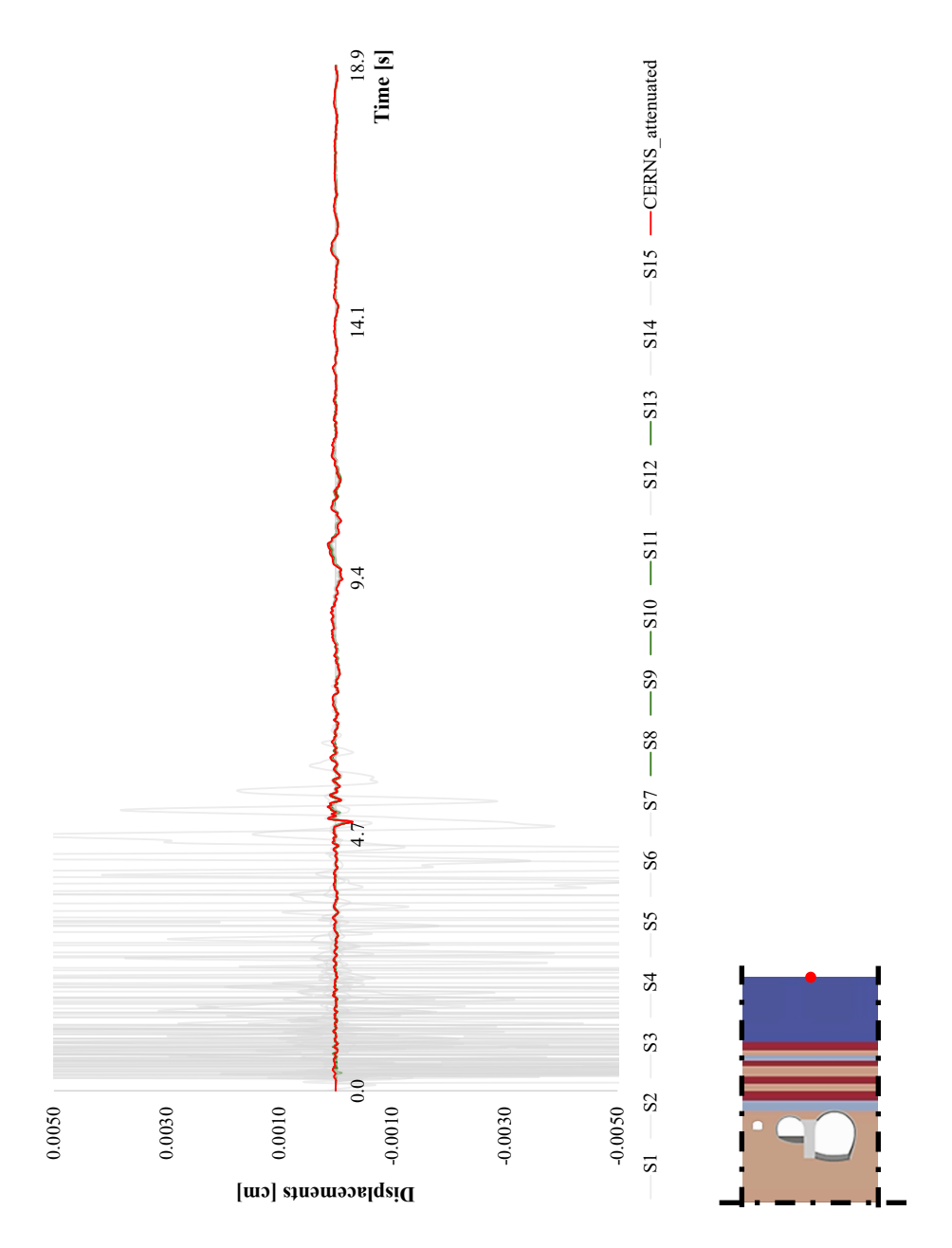


Figure 5.3.7 DRM model: comparison between displacement time histories recorded by CERNS surface station and all the fifteen output results recorded at ground surface.

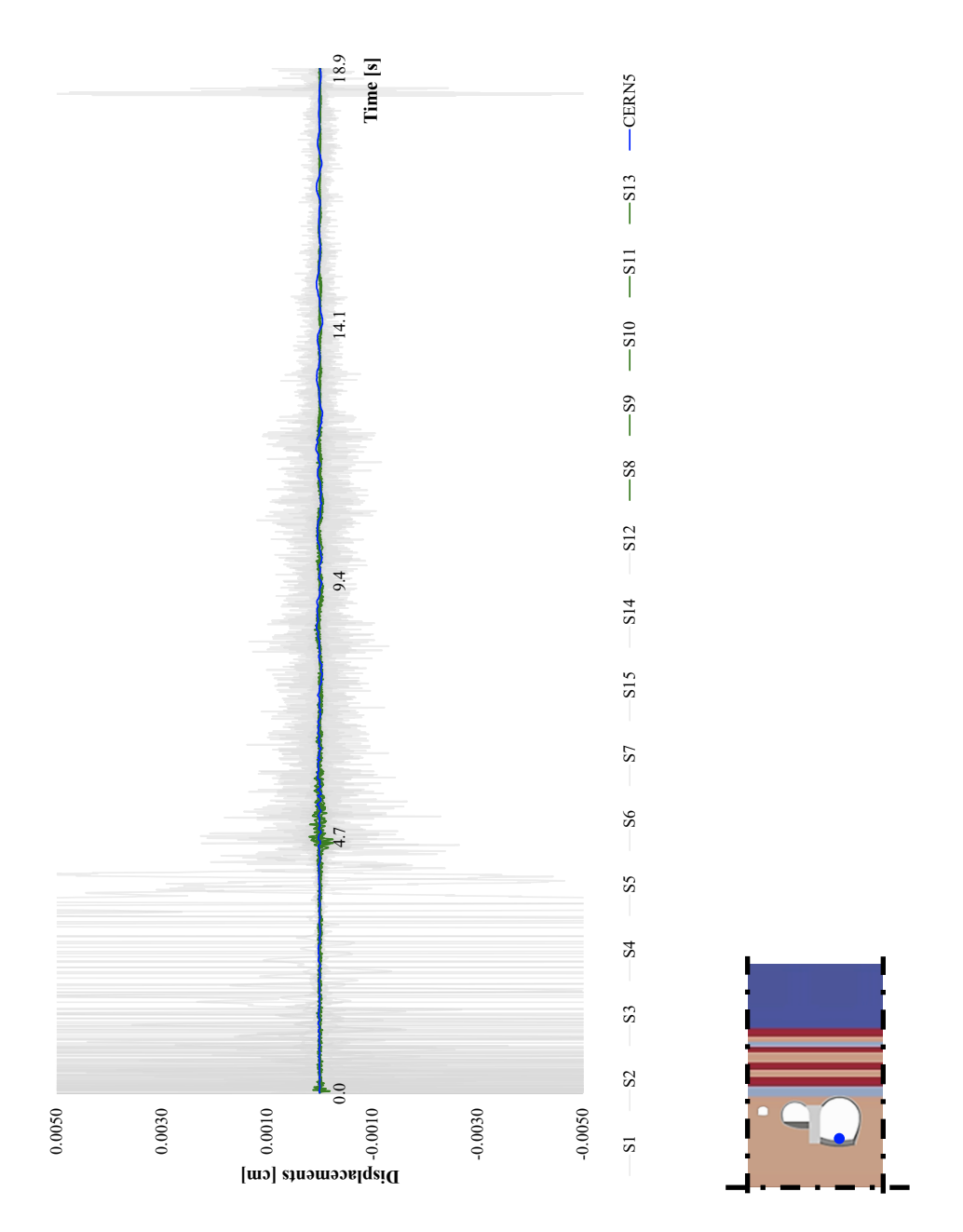


Figure 5.3.8 DRM model: comparison between displacement time histories recorded by CERN5 underground station and all the fifteen output results recorded at the UXC55 cavity basement.

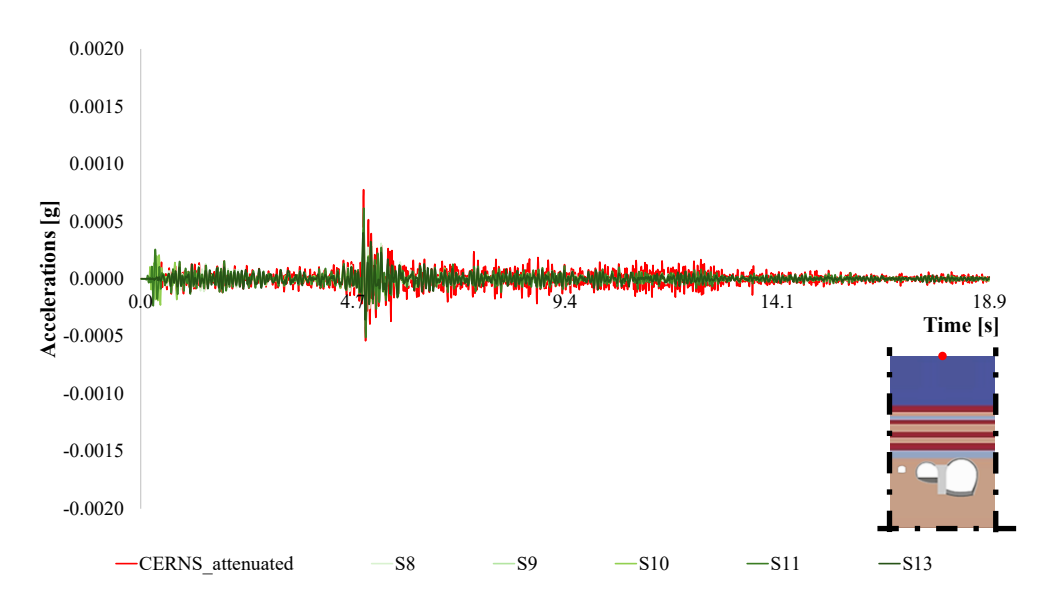


Figure 5.3.9 DRM model: comparison between acceleration time histories recorded by CERNS surface station and five "comparable" results recorded at ground surface.

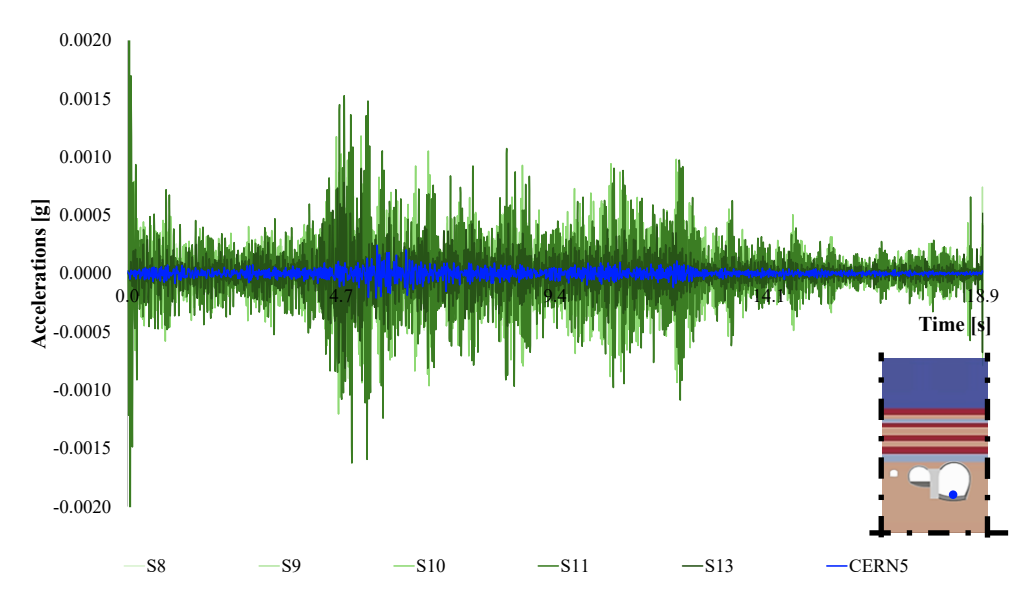


Figure 5.3.10 DRM model: comparison between acceleration time histories recorded by CERN5 underground station and five "comparable" results recorded at the UXC55 cavity basement.

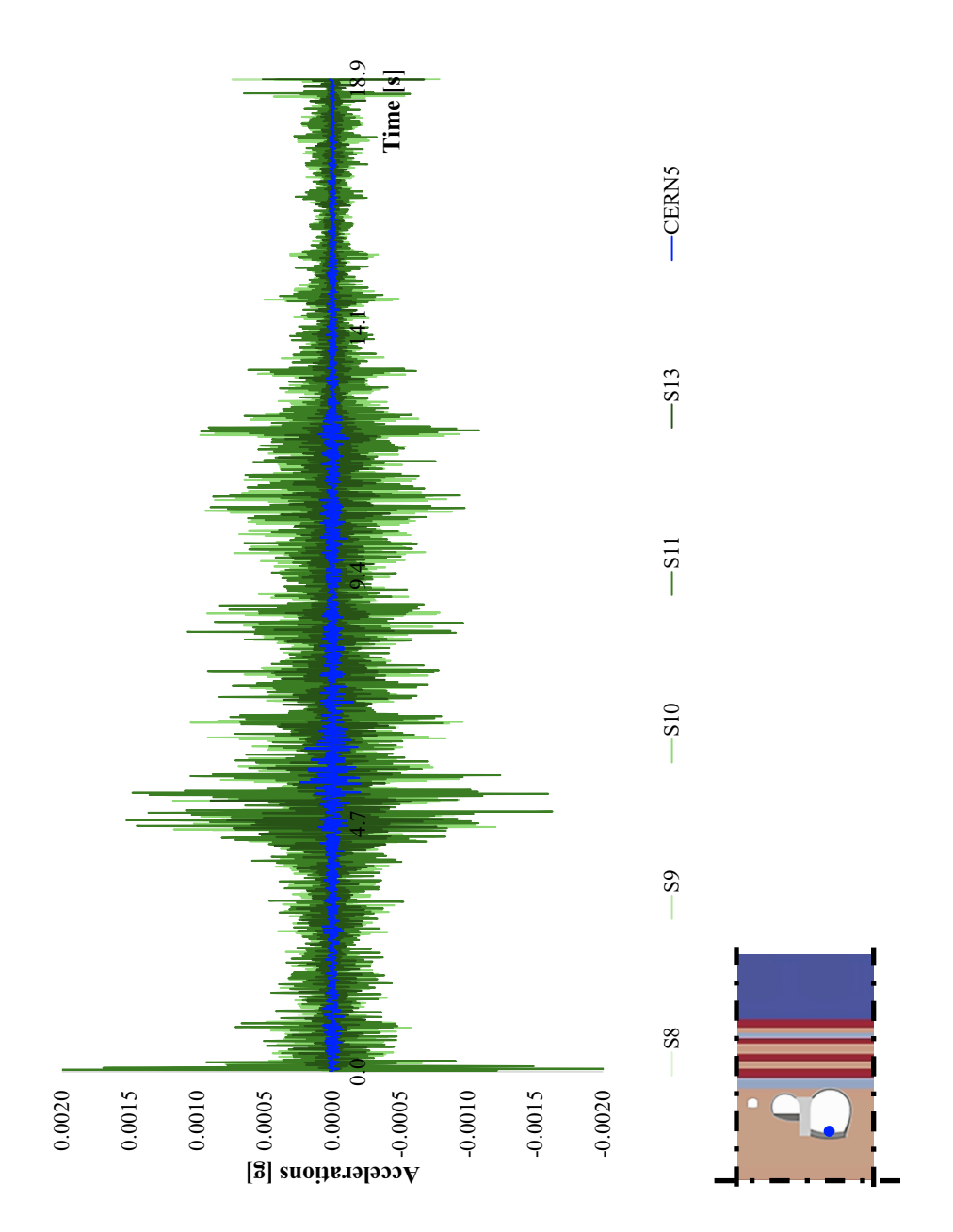


Figure 5.3.11 DRM model: comparison between acceleration time histories recorded by CERN5 underground station and five "comparable" results recorded at the UXC55 cavity basement.

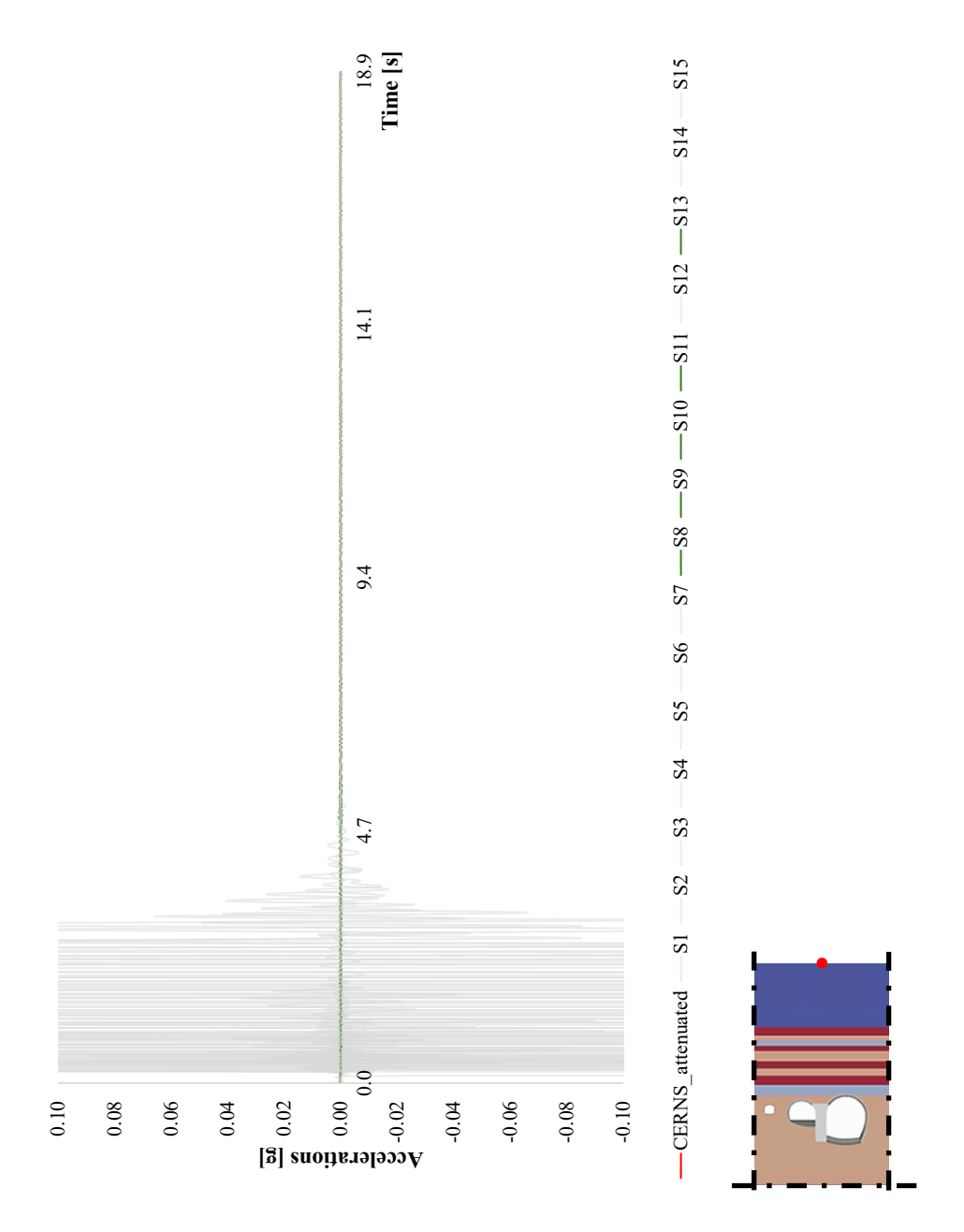


Figure 5.3.12 DRM model: comparison between acceleration time histories recorded by CERNS surface station and all the fifteen output results recorded at ground surface.

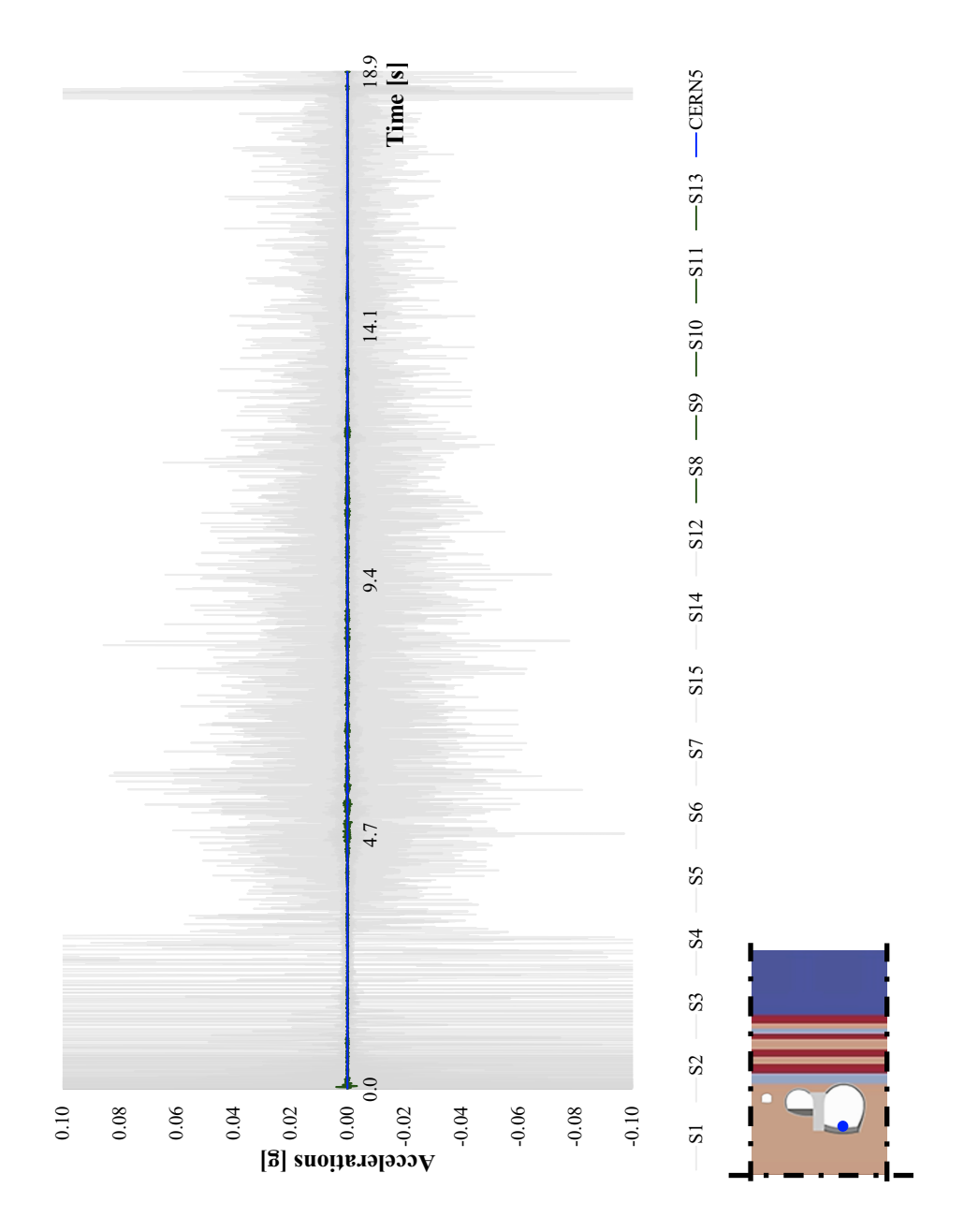


Figure 5.3.13 DRM model: comparison between acceleration time histories recorded by CERN5 underground station and all the fifteen output results recorded at the UXC55 cavity basement.

5.3.2 Results and comments

As explained before, the results in terms of displacement and acceleration time histories provided by Real-ESSI, compared to the available input data, generally showed a good level of compatibility at the ground surface, as well as at the control point at the main experimental UXC55 cavity basement, for five analyses, while focusing on the complete data set, a more obvious "variation" dictated by a casual choice of parameters to be implemented in the LHS algorithm, can be better appreciated.

A common feature of all the analyses conducted and the consequent results obtained is characterized by the presence of large resonance amplifications, approximately in the first five seconds of the time histories under consideration, for most of the analyses conducted (specifically, those connoted by the colours orange and red). In order to understand its causes, more attention was directed to the problem of seismic impedance contrasts detected between one soil layer and another, by considering the random input data generated by the algorithm and related to soil mass density (ρ) and shear wave propagation velocities (V_s), respectively (Figure 5.3.14).

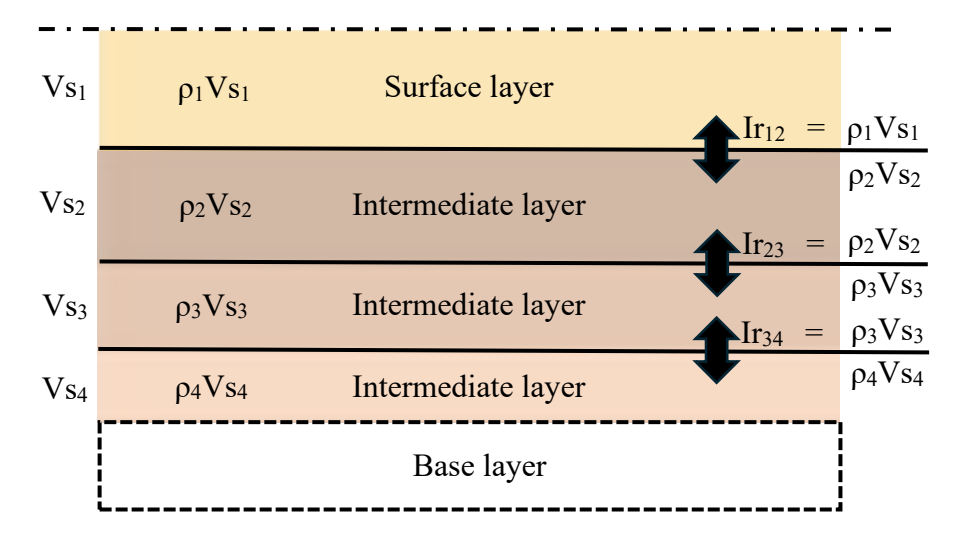


Figure 5.3.14 Definition of the impedance ratio between adjacent layers.

Obtained as the product of the mass density calculated for a soil / rock layer by the shear wave propagation velocity, the seismic contrast of impedance generally affects how seismic energy propagates from one medium to another, so large amplifications phenomena depend not only on the mechanical properties of the soil layers, but also on those of the rock layers interposed between them through the impedance ratio, calculated as the ratio of impedance contrasts assessed between two adjacent layers and, therefore, at the interface between them, as carefully described in Kokusho and Ishizawa in [96].

As shown in the Figure 5.3.15, greater impedance contrasts were detected at a certain depth, more specifically at the interface between the Strong Molasse layer and the Weak Molasse layer: being that amplification phenomena are all the more pronounced the greater the impedance contrast detected between adjacent soil/rock layers, in this study a greater impedance contrast can be justified by the excessive difference found in stiffness that may have affected the dynamic response recorded at the both points of control considered in the model.

Another aspect to be discussed regards the exploring of the effects of randomly variable damping coefficient ratios. To better explain this aspect, a comparison between two analyses, among the fifteen carried out, more specifically S3 and S8 simulations, was done. The choice of the latter, as highlighted in the Figure 5.3.16 and Figure 5.3.17, is motivated by the fact that S3 analysis presents seismic impedance contrasts stronger than S8, as demonstrated also by the variation of Vs with depth that is, in S3, smoother than S8. According to Boaga et al. in [97], a detailed identification of soil material damping becomes important or unimportant in relation to the impedance contrasts observed at the interface between each soil layers. More in detail, going to replace in the S3 analysis the randomly chosen damping ratios for the S8, the results in terms of displacements and acceleration show a significant reduction in the amplifications found especially at the beginning of the response, so as to align more closely with the data recorded from the reference stations (Figure 5.3.18, Figure 5.3.19, Figure 5.3.20, Figure 5.3.21, Figure 5.3.22, Figure 5.3.23, Figure 5.3.24).

Substituting, on the other hand, in the S8 analysis the randomly chosen damping ratios for the S3 analysis, it can be seen that by varying the range of damping, the observed responses show a good degree of matching, so it can be

concluded that the uncertainty on damping generally has a limited impact in the presence of low impedance contrasts compared to the case where, in the presence of strong impedance contrasts, the effect of damping is much more pronounced, due to its strong effect on the resonance amplitude (Figure 5.3.25, Figure 5.3.26, Figure 5.3.27, Figure 5.3.28).

Concluding, it was considered that some results show a high-frequency component that cannot be propagated by the numerical model. This suggests, for future applications, the need to filter the recordings by limiting them to the range of frequencies significant for the specific application.

Such results containing displacement/acceleration responses in grey belong to the first-attempt analyses, so all analyses that produced "worse" results have been represented in grey to better distinguish, instead, that group of analyses that produced "good" results, in the context of comparison with experimental data.

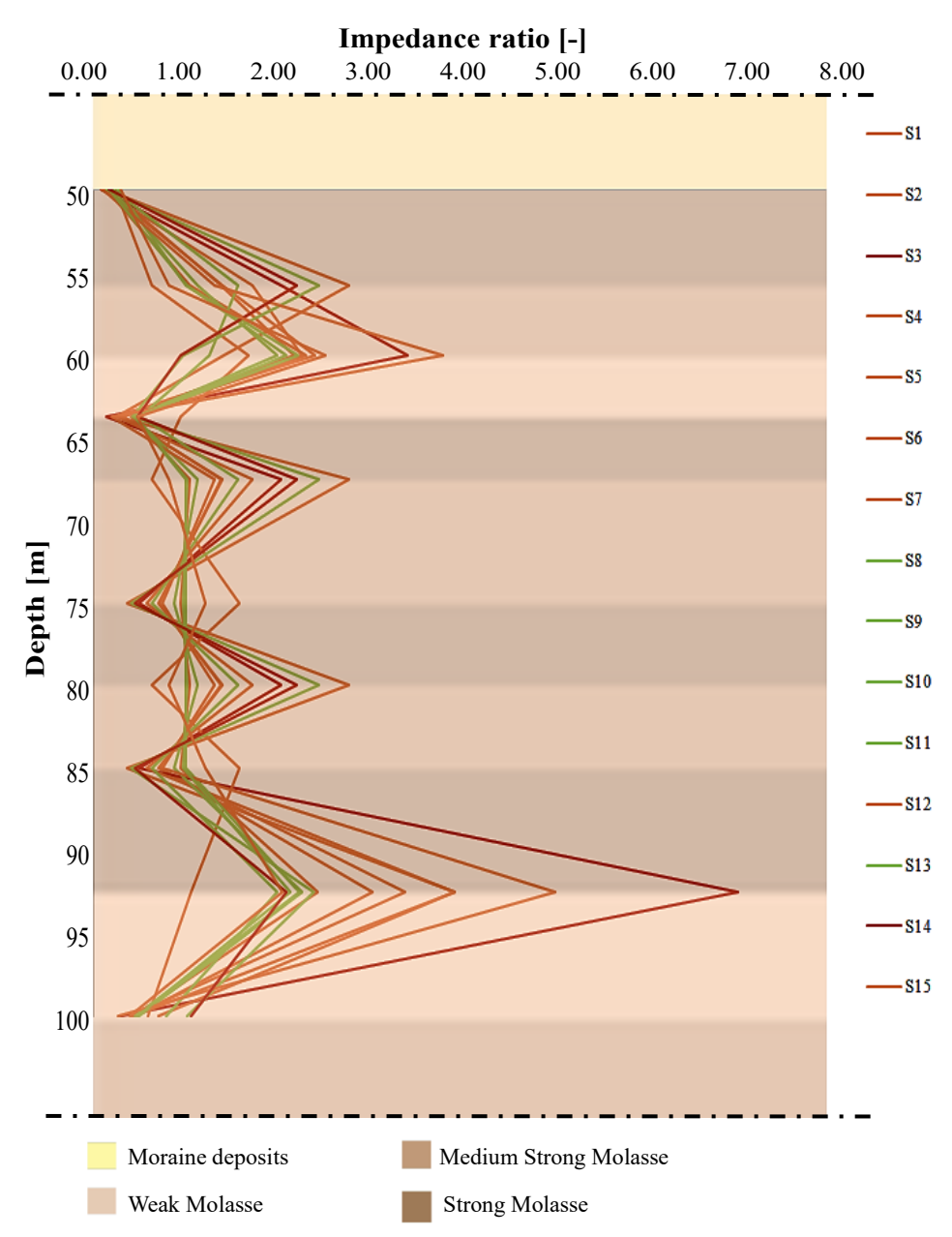


Figure 5.3.15 DRM section model showing the variation of the seismic impedance ratios, as depth changes, calculated at the interface between one soil layer and another.

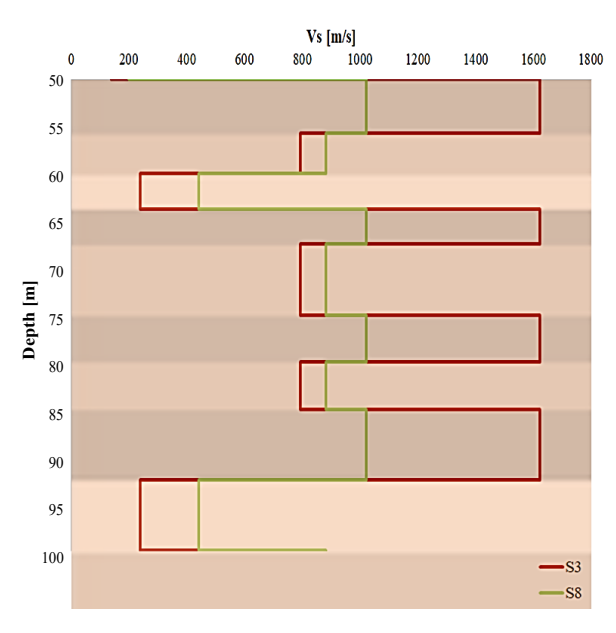


Figure 5.3.16 Vs profiles compared for the central packet of soil layers in S3 and S8 simulations.

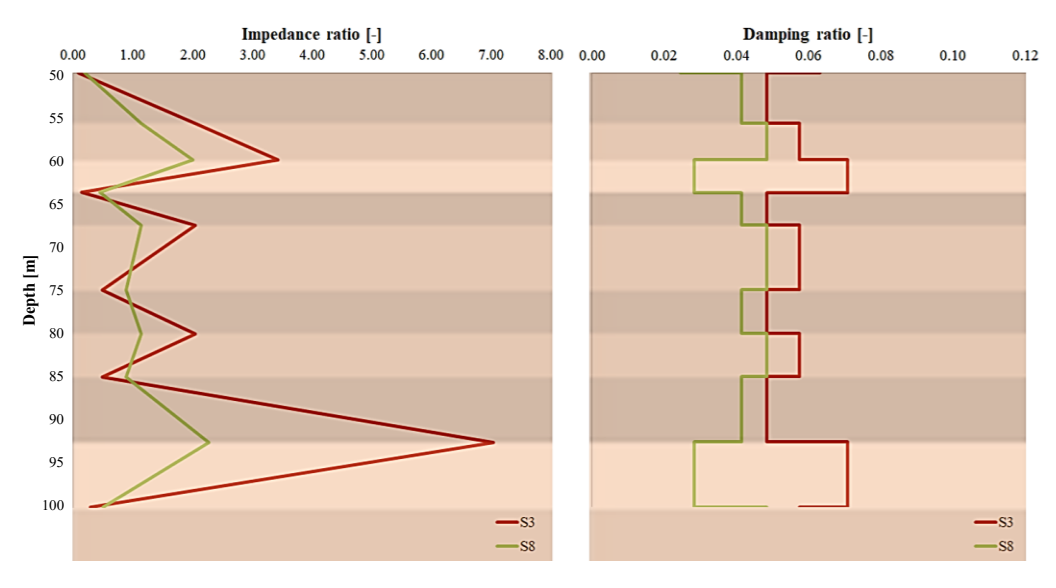


Figure 5.3.17 Comparison between S3 and S8 simulations in terms of impedance and damping ratios.

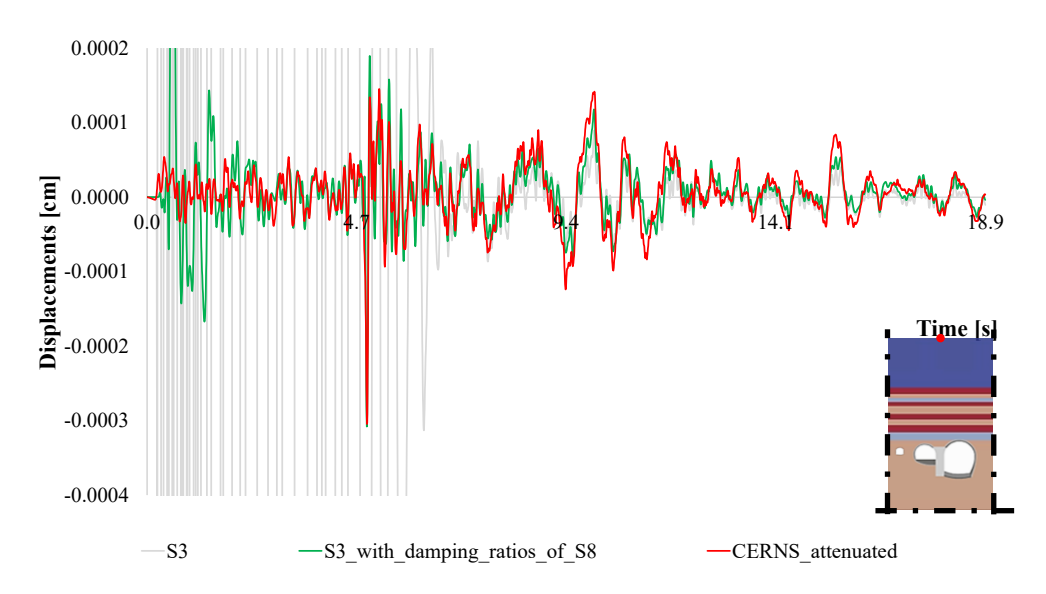


Figure 5.3.18 DRM model: comparison between displacement time histories recorded by CERNS, S3 and S8 simulations at ground surface, by substituting in S3 the damping ratios considered for S8.

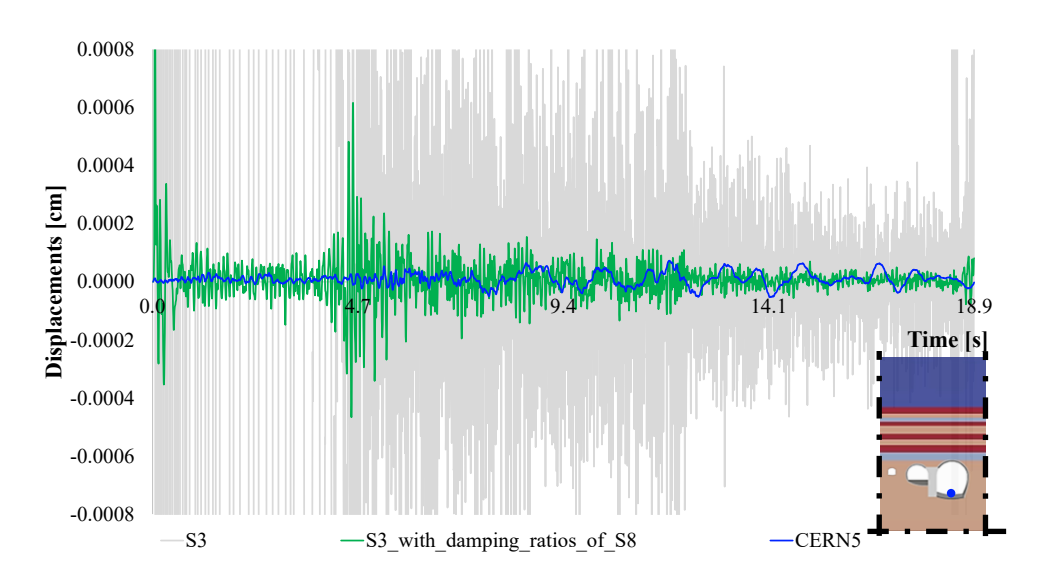


Figure 5.3.19 DRM model: comparison between displacement time histories recorded by CERN5, S3 and S8 simulations at UXC55 cavity basement, by substituting in S3 the damping ratios considered for \$8.8

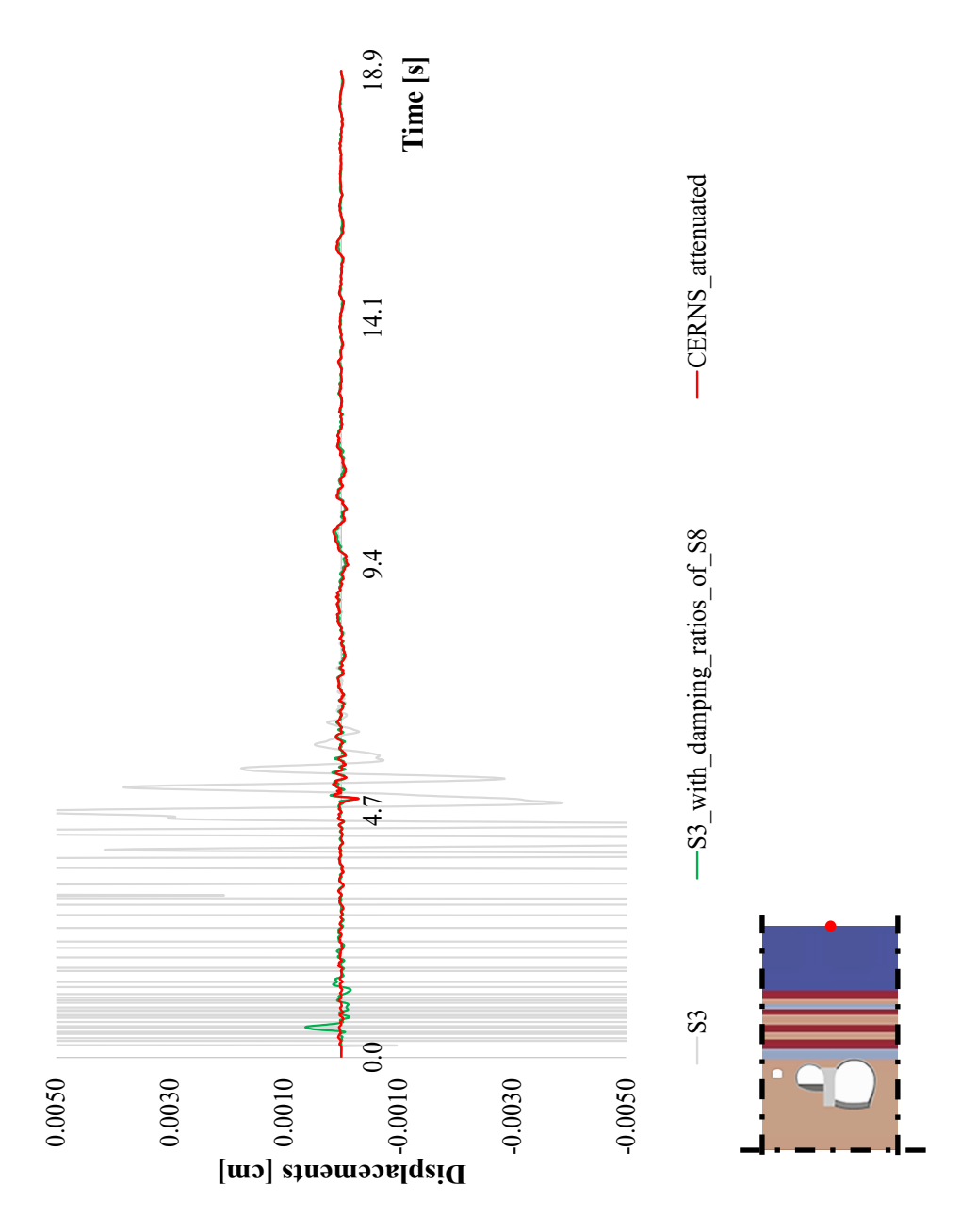


Figure 5.3.20 DRM model: comparison between displacement time histories recorded by CERNS, S3 and S8 simulations at ground surface, by substituting in S3 the damping ratios considered for S8.

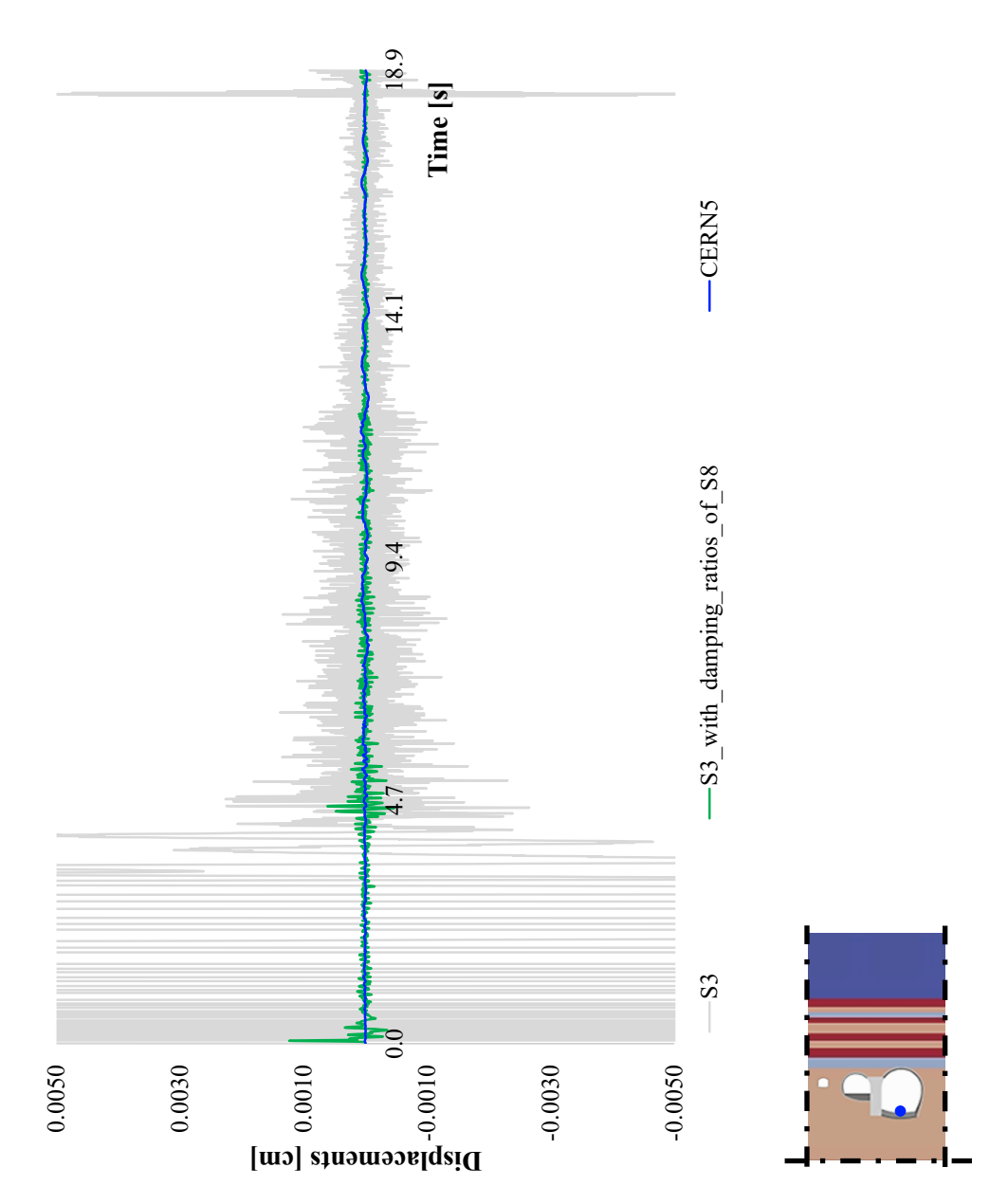


Figure 5.3.21 DRM model: comparison between displacement time histories recorded by CERN5, S3 and S8 simulations at UXC55 cavity basement, by substituting in S3 the damping ratios considered for S8.

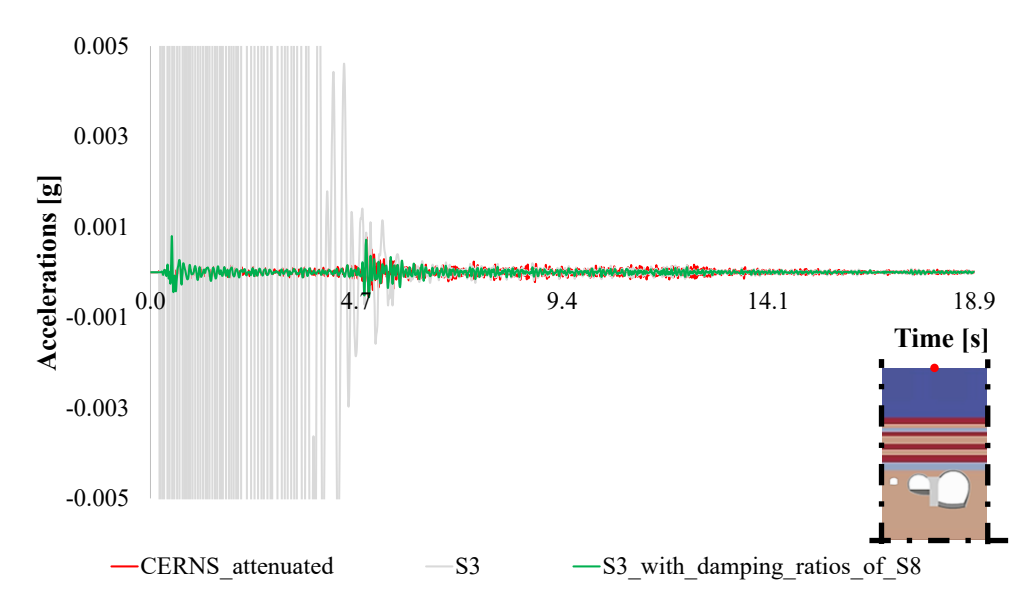


Figure 5.3.22 DRM model: comparison between acceleration time histories recorded by CERNS, S3 and S8 simulations at ground surface, by substituting in S3 the damping ratios considered for S8.

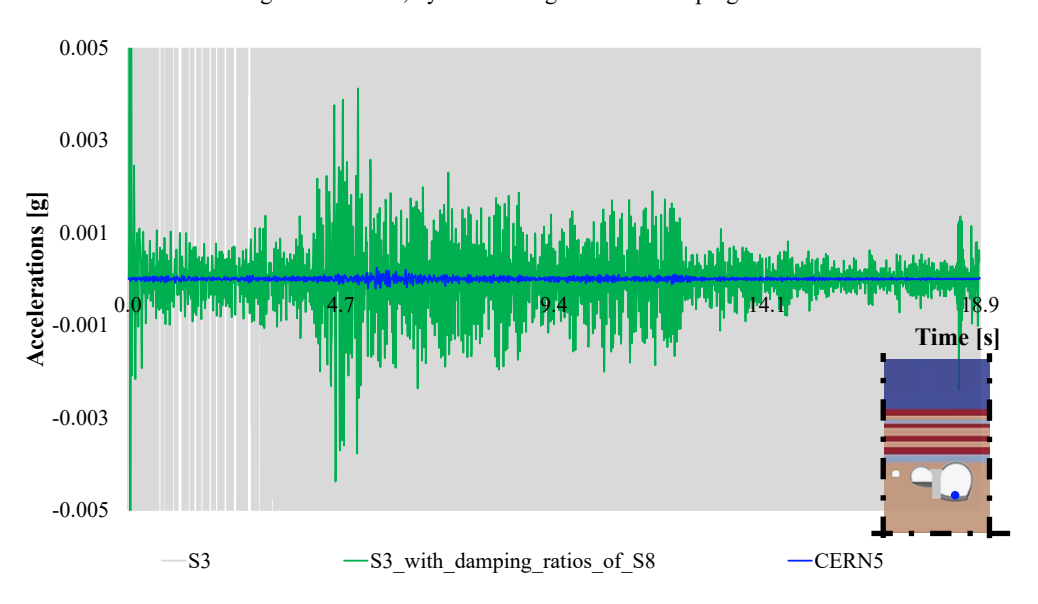


Figure 5.3.23 DRM model: comparison between acceleration time histories recorded by CERN5, S3 and S8 simulations at UXC55 cavity basement, by substituting in S3 the damping ratios considered for \$8\$

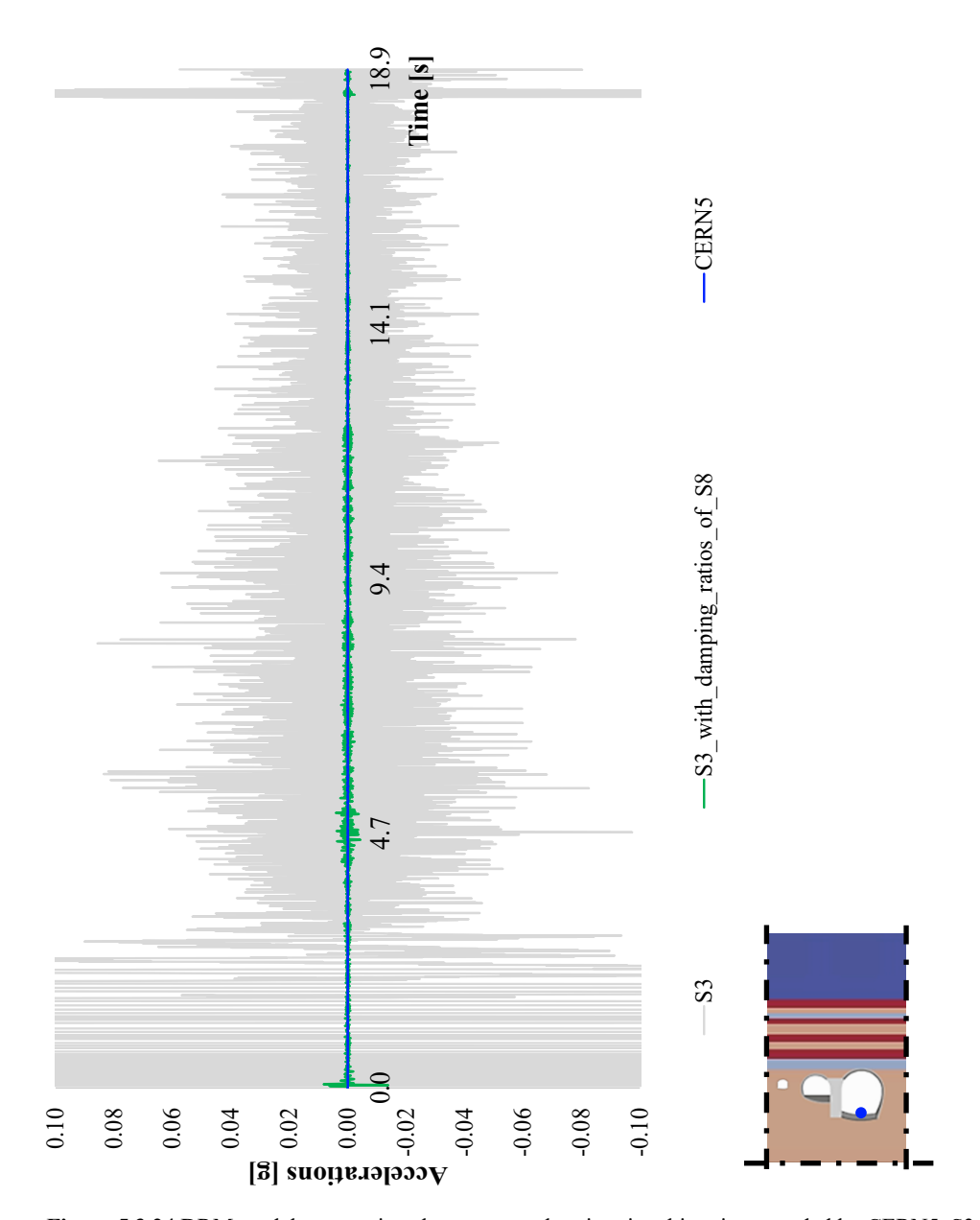


Figure 5.3.24 DRM model: comparison between acceleration time histories recorded by CERN5, S3 and S8 simulations at UXC55 cavity basement, by substituting in S3 the damping ratios considered for S8.

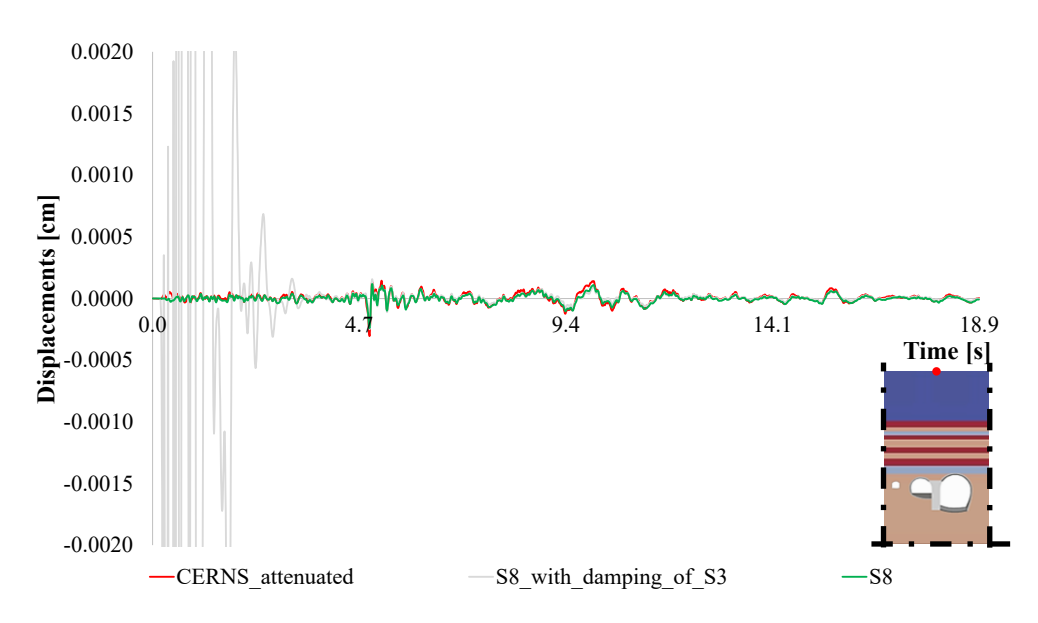


Figure 5.3.25 DRM model: comparison between displacement time histories recorded by CERNS, S3 and S8 simulations, by substituting in S8 the damping ratios considered for S3.

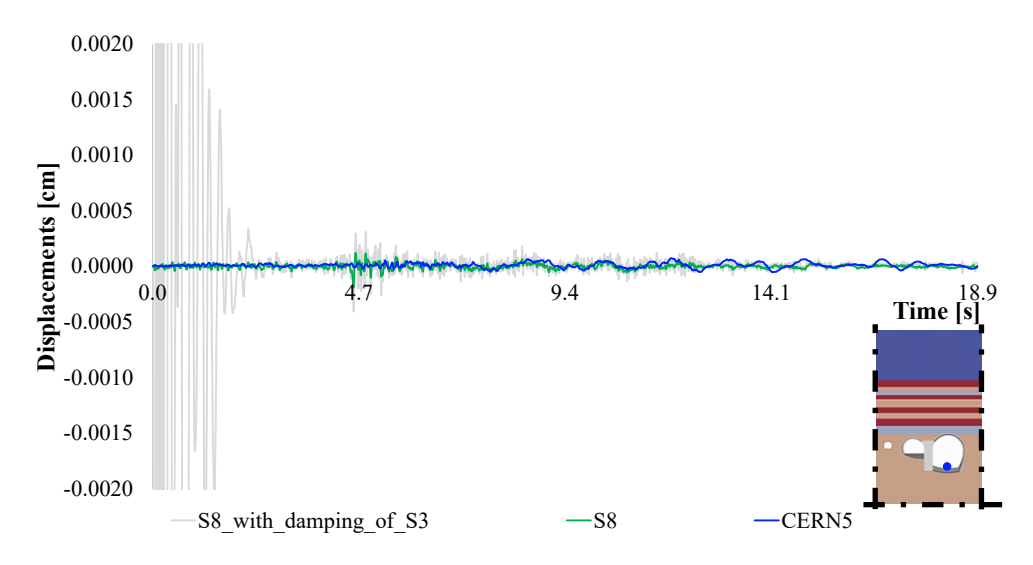


Figure 5.3.26 DRM model: comparison between displacement time histories recorded by CERN5, S3 and S8 simulations, by substituting in S8 the damping ratios considered for S3.

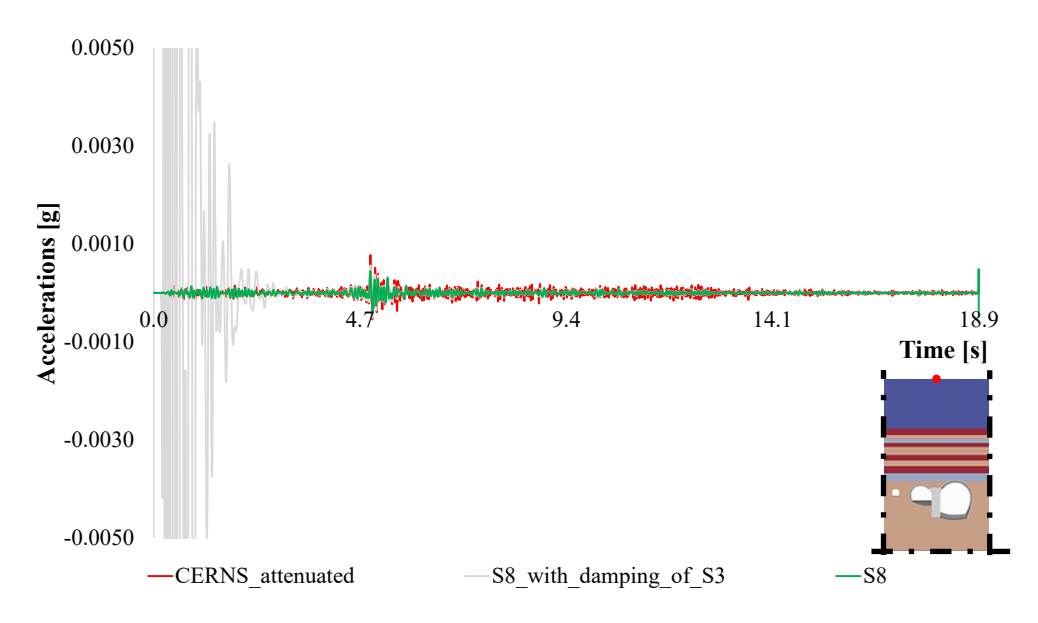


Figure 5.3.27 DRM model: comparison between acceleration time histories recorded by CERNS, S3 and S8 simulations, by substituting in S8 the damping ratios considered for S3.

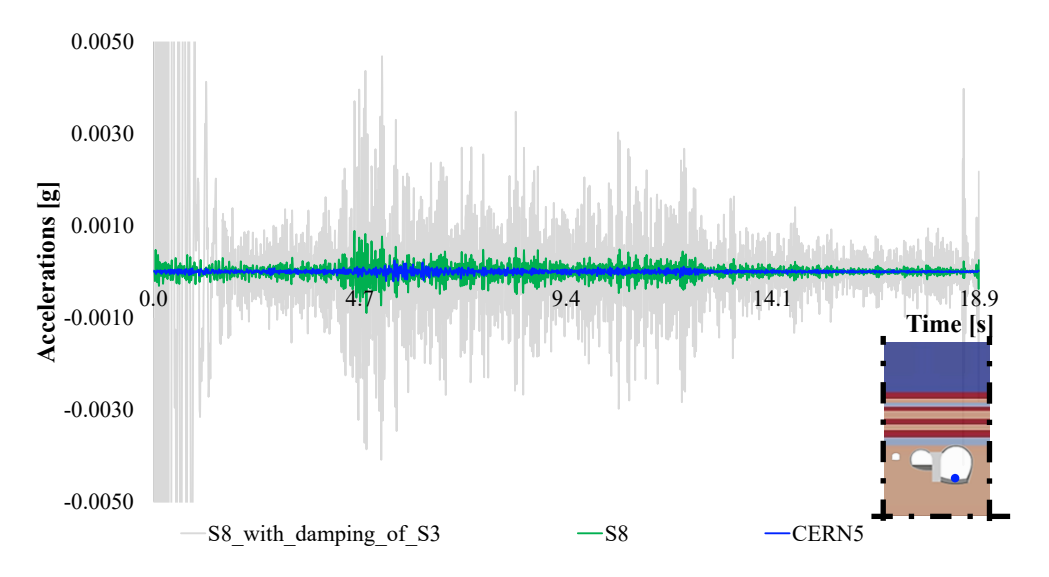


Figure 5.3.28 DRM model: comparison between acceleration time histories recorded by CERN5, S3 and S8 simulations, by substituting in S8 the damping ratios considered for S3.

5.4 LHS application to DRM model: second comparison

Based on the results obtained, a recalibration of all parameters for soils and rocks in terms of mean values and standard deviations was carried out using the LHS algorithm (Table 16), starting from those first-attempt analyses with which a good result was achieved (green results), since red and orange analyses were discarded because they provided physically unrealistic results.

Accordingly, a new data set table was prepared, and further FE simulations were carried out. Such recalibration involved the definition of a new smooth Vs mean profile (Figure 5.4.1, Figure 5.4.2).

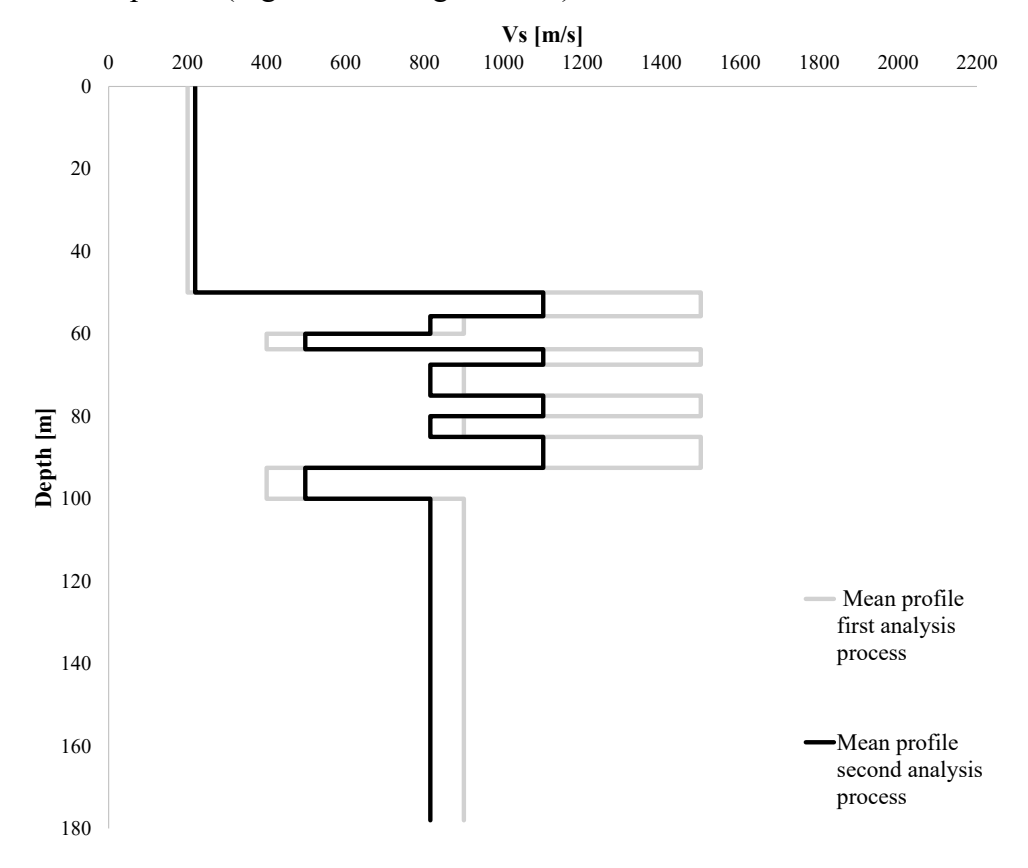


Figure 5.4.1 Vs mean profile defined for the second analysis process and compared to the previous one.

Soils/Rock	Parameters	Unit	Model	Mean	STD
	γ_{soil}	kN/m3	LN	23	0.7
	Esoil	MPa	LN	307	134
	V _{soil}	[-]	Beta [0,0.5]	0.3	0.5
Moraine	$\xi_{\rm soil}$	[-]	LN	3	1.2
	G	MPa		116	47
	$\rho_{\rm soil}$	kg/m3		2321	72
	V_s	m/s		219	45
	γsoil	kN/m3	LN	24	0.4
	Esoil	MPa	LN	1360	240
	V _{soil}	[-]	Beta [0,0.5]	0.22	0.05
Weak Molasse	$\xi_{\rm soil}$	[-]	LN	4	2.4
	G	MPa		619	226
	$\rho_{\rm soil}$	kg/m3		2440	24
	V_s	m/s		498	91
	γsoil	kN/m3	LN	24	0.4
	Esoil	MPa	LN	4800	620
Medium-Strong	V _{soil}	[-]	Beta [0,0.5]	0.28	0.05
Molasse	$\xi_{\rm soil}$	[-]	LN	5	1.2
	G	MPa		1676	640
	$\rho_{\rm soil}$	kg/m3		2442	30
	V_{s}	m/s		815	159
	γ_{soil}	kN/m3	LN	24	0.4
	Esoil	MPa	LN	13649	1500
	V _{soil}	[-]	Beta [0,0.5]	0.28	0.05
Strong Molasse	$\xi_{ m soil}$	[-]	LN	4	1.4
	G	MPa		3068	1401
	$ ho_{ m soil}$	kg/m3		2443	27
	$V_{\rm s}$	m/s		1101	235

Table 16 LHS: recalibration of the probability distributions for the soils and rock parameters, done as the mean of the five analyses with better results obtained in the first analysis process.

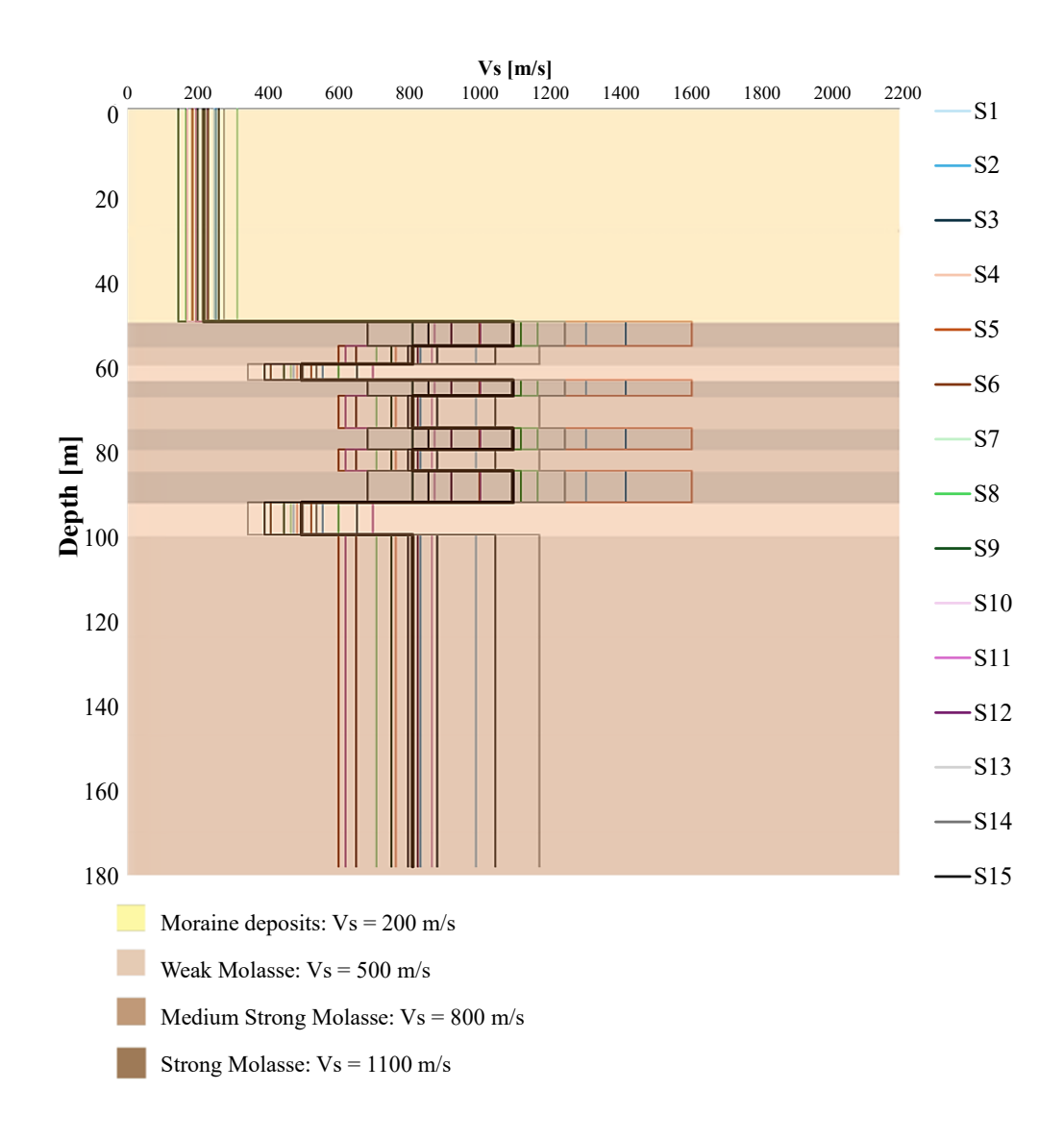


Figure 5.4.2 DRM section model highlighting the Vs mean profile and all the fifteen profiles associated to the fifteen analyses within the second simulations process.

5.4.1 Evaluation of the displacements and accelerations

As highlighted in Figure 5.4.3, Figure 5.4.4, Figure 5.4.5, Figure 5.4.6, Figure 5.4.7 and Figure 5.4.8, an overall recalibration of the data set, again performed at random, contributed to the determination of results more closely matching the inputs taken as reference.

As for the first – attempt analyses carried out, standard deviations were obtained from data in geotechnical characterization reports of the site under study [92] [93] [94] [95].

More in detail, in Table 16, statistical parameters were obtained by eliminating analyses that had provided responses in terms of displacements and accelerations that were worse (red), so mean and standard deviation were recalculated based on parameter sets that had provided better responses (green). With the new parameters, the sampling process was re-executed to obtain a new set of parameters. The procedure does not necessarily produce new statistical parameters that are more representative of the actual material property variations; however, it was used to quantify the effect that greater uncertainty on parameter determination, related to higher standard deviation values, affected the dispersion of analysis results.

Apart from the first temporal instants in which, in all graphs, peaks of amplification, although limited, are still evident, most likely due to numerical issues, in all the graphs showing displacement and acceleration time histories, it is possible to appreciate a generally uniform trend and above all it is highlighted how the choice of parameters to implement represents a fundamental step to determine a stochastic variability translated into operational scenarios in which the dynamic response of the infrastructures under study is carefully evaluated, even when stressed by seismic events of a moderate nature, but this means that, in any circumstance, it is imperative to preserve their structural safety since the equipment and systems present therein, designed for scientific and experimental purposes of absolute international importance, are sensitive to every minimal vibration and/or displacement.

Chapter 5: Uncertainties treatment

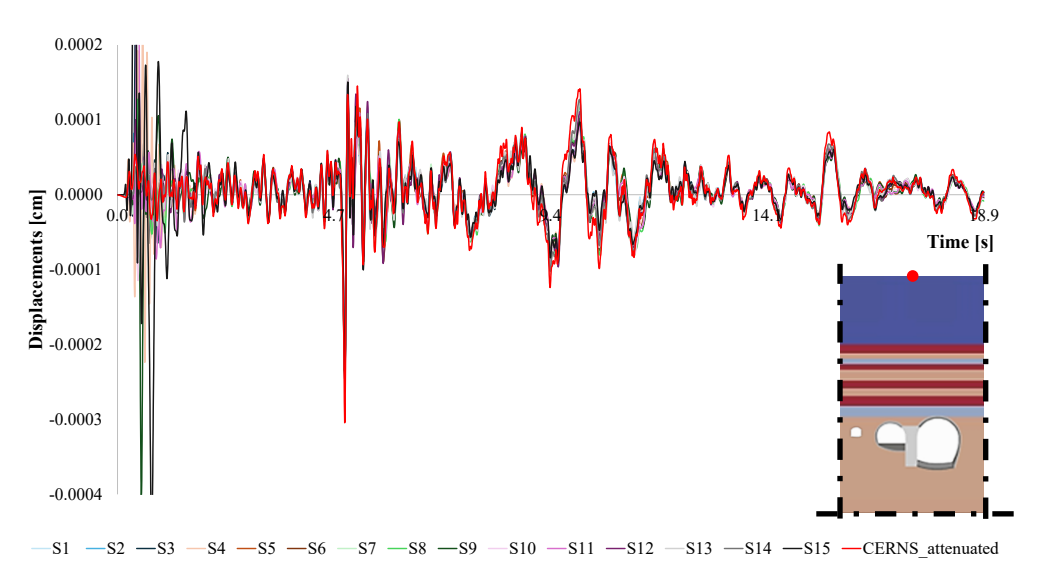


Figure 5.4.3 DRM model: comparison between displacement time histories recorded by CERNS surface station and all the fifteen output results recorded at ground surface.

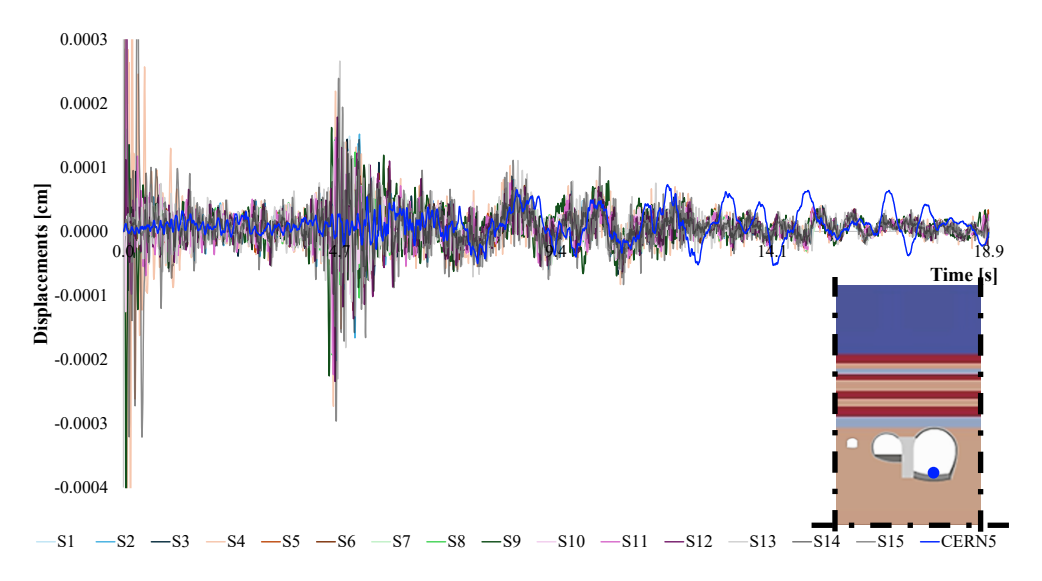


Figure 5.4.4 DRM model: comparison between displacement time histories recorded by CERN5 underground station and all the fifteen output results recorded at the UXC55 cavity basement.

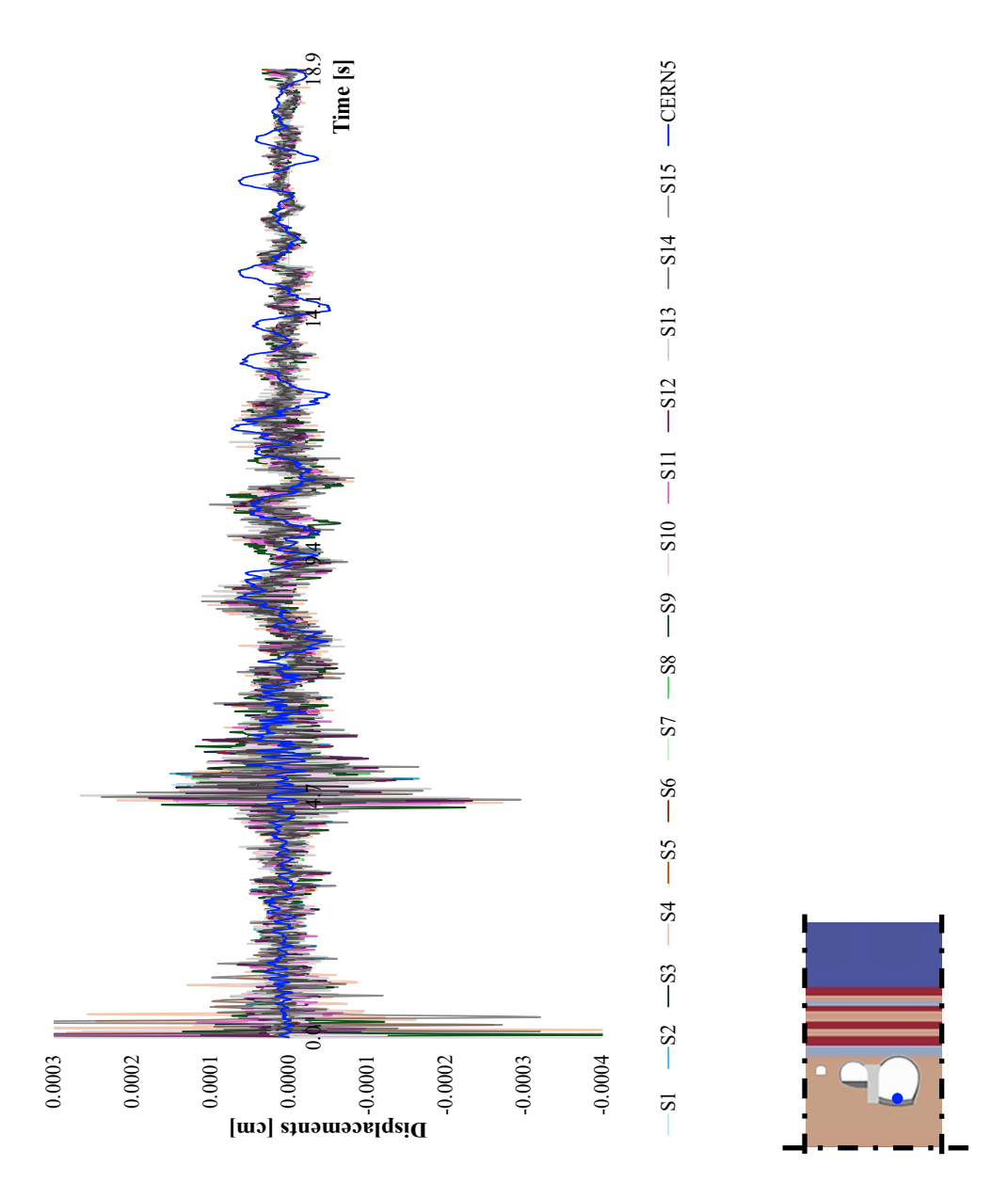


Figure 5.4.5 DRM model: comparison between displacement time histories recorded by CERN5 underground station and all the fifteen output results recorded at the UXC55 cavity basement.

Chapter 5: Uncertainties treatment

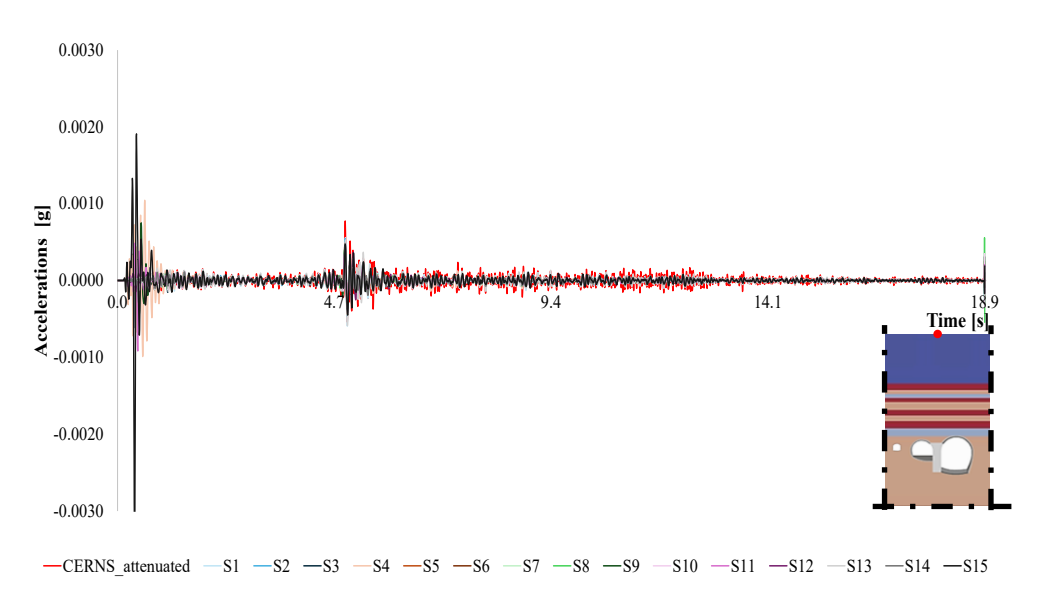


Figure 5.4.6 DRM model: comparison between acceleration time histories recorded by CERNS surface station and all the fifteen output results recorded at ground surface.

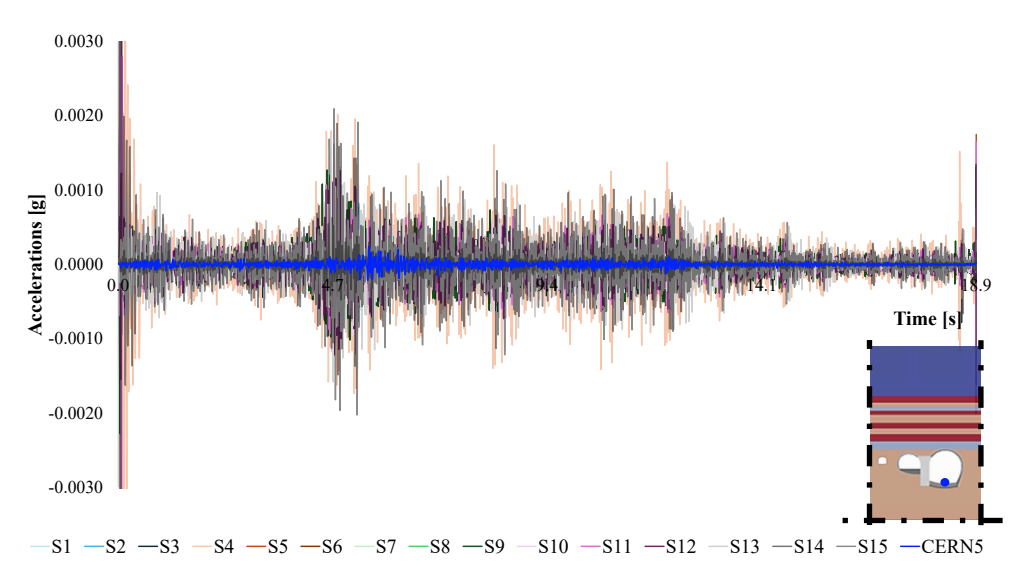


Figure 5.4.7 DRM model: comparison between acceleration time histories recorded by CERN5 underground station and all the fifteen output results recorded at the UXC55 cavity basement.

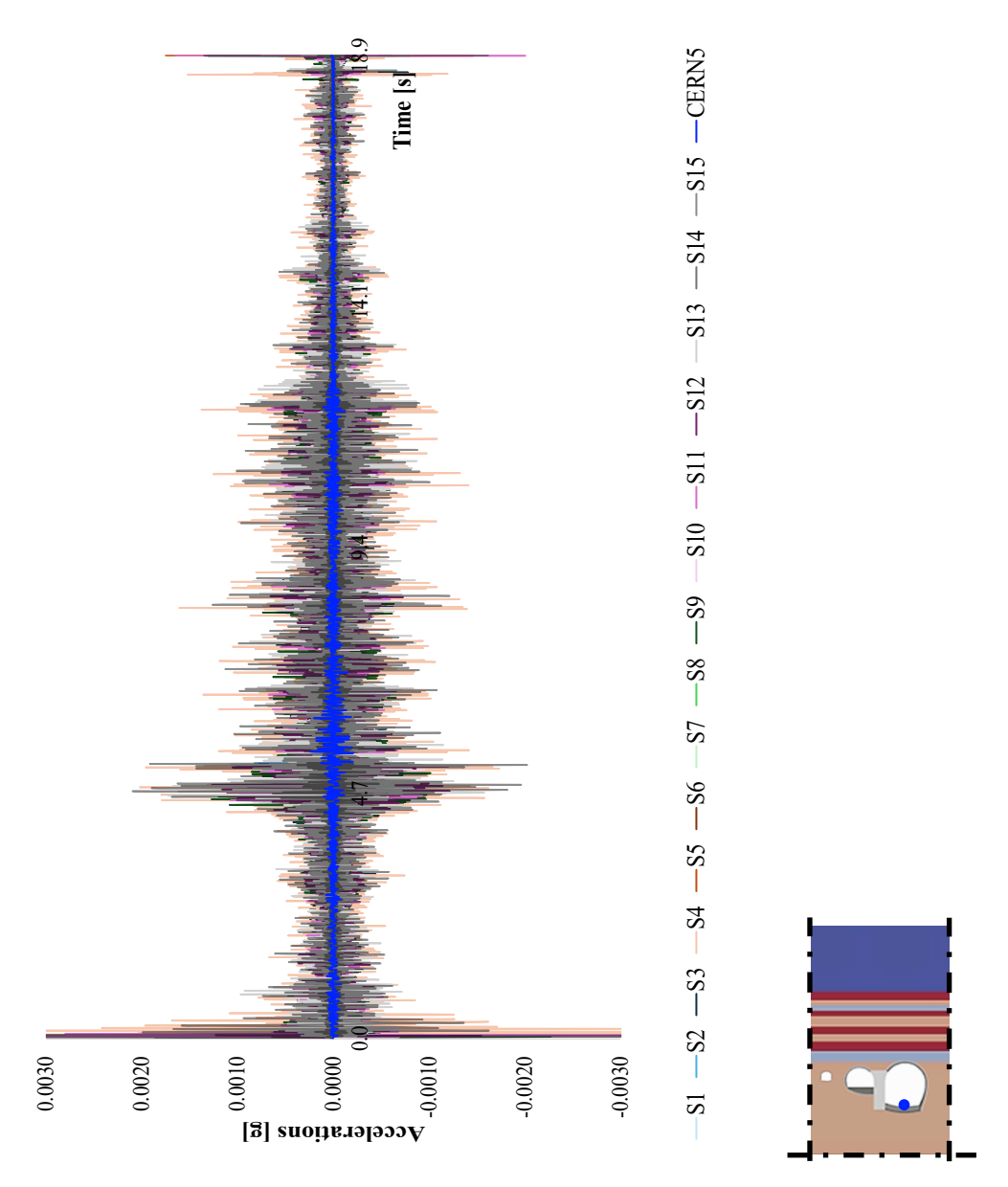


Figure 5.4.8 DRM model: comparison between acceleration time histories recorded by CERN5 underground station and all the fifteen output results recorded at the UXC55 cavity basement.

5.4.2 Results and comments

As shown in Figure 5.4.9 and Figure 5.4.10, in which the impedance contrasts following random recalibration of all values were observed, the results in terms of displacement and acceleration time histories show a general homogeneous trend comparable to the data provided by the reference stations.

More in detail, no significant contrast in shear wave velocity is found between the soil layers, since in this second analysis process the Vs profile of the entire model is smoother than the Vs profile adopted in the first process, and this is why the uncertainty scenarios generated by a random recalibration of all the parameters under consideration contemplate a more acceptable variation of the results within limited displacement and/or acceleration values and in line with the structural safety requirements to be constantly monitored for the existing installations.

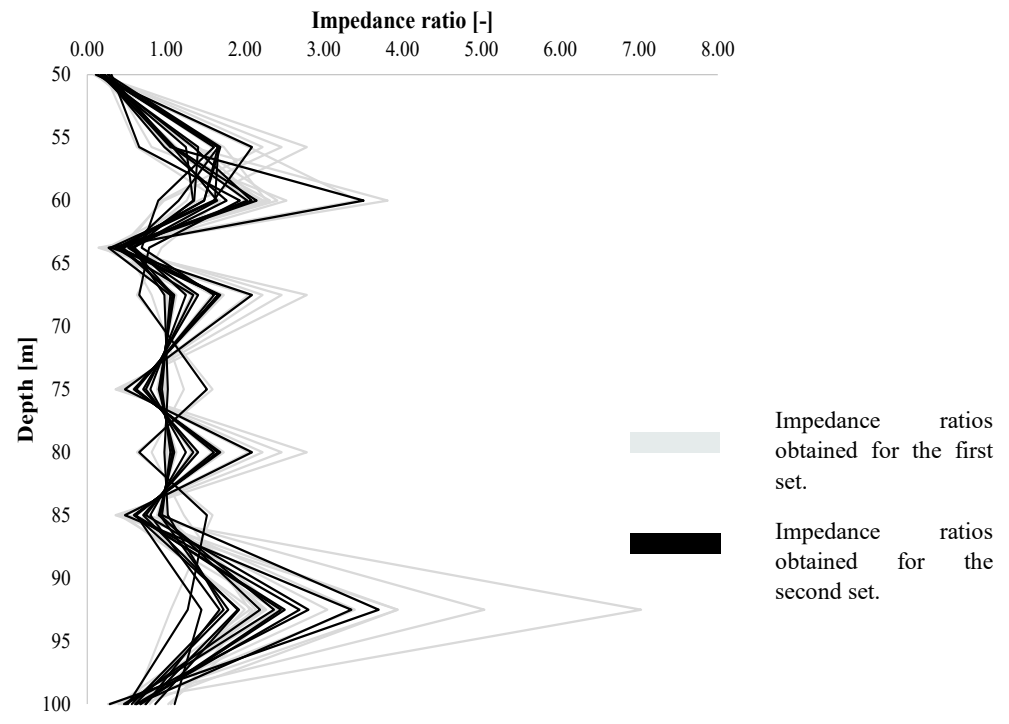


Figure 5.4.9 Impedance ratios: comparison between first and second process analyses.

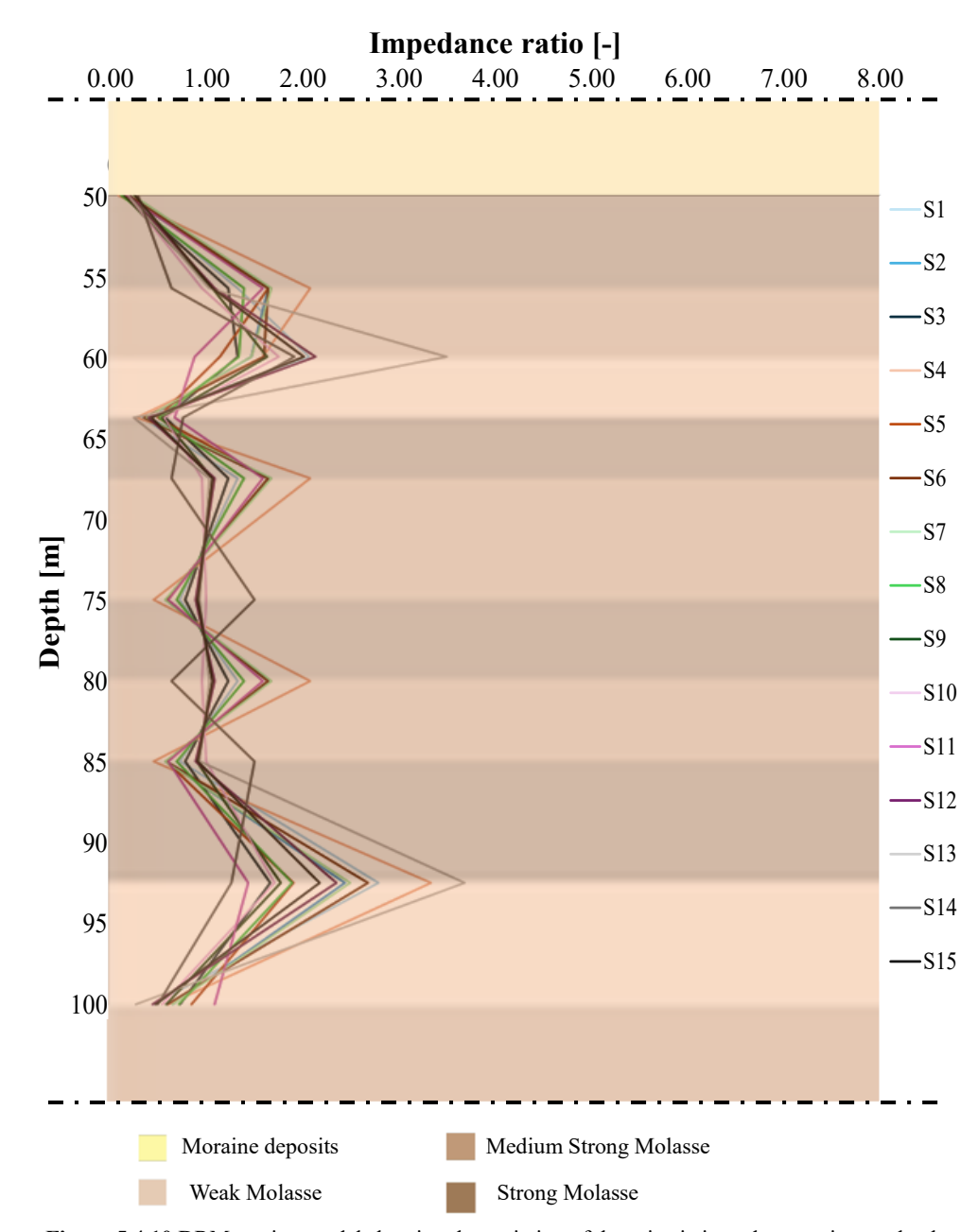
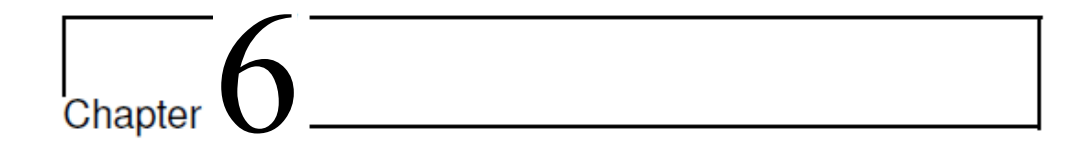


Figure 5.4.10 DRM section model showing the variation of the seismic impedance ratios, as depth changes, calculated at the interface between one soil layer and another.

Chapter 5: Uncertainties treatment





6 Conclusions and future developments

The research presented in this thesis addresses the seismic behaviour of underground structures, with particular focus on tunnels and subterranean facilities. The work explored various aspects influencing seismic performance, starting from the most relevant design and construction methodologies used in modern engineering practice, and highlighting the importance of integrating tectonic considerations into these processes.

Furthermore, fundamental geotechnical concepts, such as soil stiffness and damping characteristics, were introduced, given their significant influence on the dynamic response of underground structures, particularly when soil-structure interaction (SSI) is considered. In this context, existing regulatory frameworks and their practical implications for underground infrastructure were critically reviewed, revealing areas of potential improvement in current standards and guidelines.

Finally, numerical methods were discussed, applied and validated on measured data, illustrating their effectiveness in predicting seismic responses for contributing to improved resilience of underground infrastructures.

The analyses conducted in this research have allowed for an exploration and deeper understanding of the seismic behaviour of underground structures, specifically focusing on the emblematic case study of the Large Hadron Collider (LHC) at CERN's Point 5 site.

In particular, the study demonstrated how the combined application of advanced numerical methodologies, such as the Domain Reduction Method

(DRM), and high-performance software like the Real-ESSI Simulator, facilitates an accurate representation of complex phenomena characterizing soil-structure interaction (SSI).

- The use of DRM, previously employed in other soil-structure interaction applications but not for underground structures when treated within the Real-ESSI simulator, has been analysed in detail and validated across various seismic scenarios.

It was proven especially effective in significantly reducing the computational domain size while maintaining a high level of accuracy in dynamic responses using appropriate boundary and initial conditions, including a damping layer.

Results obtained through this technique clearly highlighted operational and computational advantages, especially when handling large and complex underground structures, as illustrated by the CERN case.

- Numerical simulations conducted using the Real – ESSI Simulator allowed for a comparison between experimentally recorded dynamic responses from CERN's monitoring network installed in the experimental cavities and those predicted by numerical models.

Such comparisons demonstrated that the employed approach can captures the real system's responses (accelerations and displacements) both under free-field conditions and in the presence of underground structures.

- It was possible to clearly identify the critical influence of local stratigraphy and geotechnical soil characteristics on the seismic behaviour of the cavities.

Numerical simulation results indicated that minor variations in geological layer properties could significantly amplify or attenuate the stresses transmitted to underground structures, impacting structural safety and long-term durability.

- The adoption of the Latin Hypercube Sampling (LHS) algorithm for uncertainty management further strengthened the robustness of the analyses.

Probabilistic analysis using LHS highlighted how realistic variations in soil mechanical properties and cavity support parameters significantly influence structural dynamic responses. This underscores the importance of incorporating uncertainty into structural modelling and design, particularly in seismic contexts, where combined effects of various parameters can lead to vastly different system responses.

The uncertainty associated with the combined effects of the various mechanical and geotechnical parameters generated several scenarios in which very large resonance amplifications were found. By means of a focused study on the possible generative causes of these amplifications, the seismic impedance contrasts existing between one soil layer and another were assessed.

As was observed, in the first-attempt process, red and orange analyses provided were discarded because they provided physically unrealistic results, since greater impedance contrasts at a certain depth, above all at the interface between the Strong Molasse layer and the Weak Molasse layer, were detected, while green analyses provided lower impedance contrasts.

Since amplification phenomena are the more pronounced the greater the impedance contrast detected between adjacent soil/rock layers, a greater impedance contrast is justified where there is an excessive difference found in terms of stiffness such as to have affected the dynamic response recorded at the two control points considered in the model.

A first consideration concerns the uncertainty associated with ground damping and how its random choice may affect the observed amplification phenomena.

Also based on the studies in the literature, when a strong impedance contrast is present, the impact of variation in the damping characteristics of the ground is not negligible, since it exerts a strong effect on the amplitude of resonance, so a proper calibration of the damping ratio itself is necessary. In contrast, if the variation of Vs with depth is

relatively smooth, the choice of damping coefficient has a limited impact on the amplification predictions.

In more detail, going to replace in the worst analysis (S3) performed at the first attempt the randomly chosen damping ratios for the best one (S8), the results show a significant reduction in the amplifications found especially at the beginning of the response, so as to align more closely with the data recorded by the reference stations.

The above results and considerations confirm that, where probabilistic analyses contribute to generate a scenario in which strong impedance contrasts in the ground determine equally strong resonance phenomena, greater attention must be paid to the knowledge of the correct attenuation characteristics of the damping ground.

Instead of acting on the damping parameter, which has a very high inherent uncertainty, it is convenient to recreate an analysis dataset generated on updated parameter distributions based on an evaluation of analysis results obtained from the first-attempt dataset.

In this context, carrying out a recalibration of all parameters for soils and rocks, in terms of mean values and standard deviations, on the basis of the parameters randomly chosen for green analyses, a second random variation of the parameters generated probabilistic scenarios in which the observed impedance contrasts were smaller than in the first-attempt case study analysed, and the uncertainty associated with them had less effect in terms of amplifications, therefore a less impact on the structural safety and long - term durability of the structures studied.

From a regulatory perspective, the research highlighted the necessity of adopting an integrated approach in defining design standards and guidelines for the seismic design of underground structures.

The methodologies proposed provide effective and reliable tools for implementing advanced numerical analyses, suggesting their incorporation into international regulatory codes, thus ensuring safer and economically sustainable designs.

In conclusion, this thesis has significantly contributed to understanding seismic dynamics in underground structures, providing original scientific outcomes and practical insights. The advanced numerical techniques applied, combined with robust uncertainty analysis, represent a fundamental starting point for further theoretical and practical advancements in structural engineering, geotechnics, and seismic risk management.

Future research should focus on refining these techniques, further integrating numerical models with experimental data obtained from advanced real-time monitoring systems. This integration will not only enhance numerical prediction reliability but also enable the development of monitoring and early-warning systems capable of mitigating seismic risks in major underground infrastructures. Such a multidisciplinary approach is essential to successfully addressing the challenges posed by the design and maintenance of strategic subterranean structures, ensuring greater safety and resilience against seismic events.

The studies conducted considered a 3D section. A future advancement could involve developing a more accurate full three-dimensional model to analyse behaviour along the tunnels' longitudinal direction, as well as shaft-cavity interactions. Considering the potential use of additional accelerograms, future analyses should also incorporate nonlinear constitutive models, as until now a linear visco-elastic model was adopted due to the low seismic intensity signal typical of the study area considered in this thesis.

Chapter 6: Conclusions and future developments



7 Reference List

- [1] C. G. di Prisco, D. Peila, and A. Pigorini, "Introduction," in *Handbook on Tunnels and Underground Works Concept Basic Principles of Design*, CRC Press., vol. 1, E. Bilotta, R. Casale, C. G. Di Prisco, S. Miliziano, D. Peila, A. Pigorini, and E. M. Pizzarotti, Eds., London: CRC Press, 2022. doi: 10.1201/9781003256175.
- [2] M. Karakuş and R. J. Fowell, "Bölgesel Kaya Mekaniği Sempozyumu / ROCKMEC'2004-VIIth Regional Rock Mechanics Symposium," 2004.
- [3] Y. Zhang, X. Zhuang, and R. Lackner, "Stability analysis of shotcrete supported crown of NATM tunnels with discontinuity layout optimization," *Int J Numer Anal Methods Geomech*, vol. 42, no. 11, pp. 1199–1216, Aug. 2018, doi: 10.1002/nag.2775.
- [4] D. Peila, C. Todaro, A. Carigi, D. Martinelli, and M. Barbero, "Construction methods," in *Handbook on Tunnels and Underground Works Concept Basic Principles of Design*, CRC Press., vol. 1, E. Bilotta, R. Casale, C. G., Di Prisco, S. Miliziano, D. Peila, A. Pigorini, and E. M. Pizzarotti, Eds., 2022, ch. 8.
- [5] L. Scesi, P. Gattinoni, and S. Lo Russo, "Input data: geology and hydrogeology," in *Handbook on Tunnels and Underground Works Concept Basic Principles of Design*, CRC Press., vol. 1, E. Bilotta, R. Casale, C. G. Di Prisco, S. Miliziano, D. Peila, A. Pigorini, and E. M. Pizzarotti, Eds., 2022, ch. 3.
- [6] C. M. Wensrich, E. H. Kisi, and V. Luzin, "Non-contact stress measurement in granular materials via neutron and X-ray diffraction: theoretical foundations," *Granul Matter*, vol. 15, no. 3, pp. 275–286, Jun. 2013, doi: 10.1007/s10035-013-0416-x.

- [7] B. Wu, K. Ito, N. Mori, T. Oya, T. Taylor, and J. Yanagimoto, "Constitutive Equations Based on Non-associated Flow Rule for the Analysis of Forming of Anisotropic Sheet Metals," *International Journal of Precision Engineering and Manufacturing-Green Technology*, vol. 7, no. 2, pp. 465–480, Mar. 2020, doi: 10.1007/s40684-019-00032-5.
- [8] D. Hestroffer *et al.*, "Small Solar System Bodies as granular media," *The Astronomy and Astrophysics Review*, vol. 27, no. 1, p. 6, Dec. 2019, doi: 10.1007/s00159-019-0117-5.
- [9] E. Bilotta, D. Boldini, M. Barbero, D. Martinelli, A. Graziani, and A. Sciotti, "Input data: geotechnics," in *Handbook on Tunnels and Underground Works Concept Basic Principles of Design*, CRC Press., vol. 1, E. Bilotta, R. Casale, C. G. Di Prisco, S. Miliziano, D. Peila, A. Pigorini, and E. M. Pizzarotti, Eds., 2022, ch. 4.
- [10] P. Badry and N. Satyam, "Seismic soil structure interaction analysis for asymmetrical buildings supported on piled raft for the 2015 Nepal earthquake," *J Asian Earth Sci*, vol. 133, pp. 102–113, Jan. 2017, doi: 10.1016/j.jseaes.2016.03.014.
- [11] G. MYLONAKIS and G. GAZETAS, "SEISMIC SOIL-STRUCTURE INTERACTION: BENEFICIAL OR DETRIMENTAL?," *Journal of Earthquake Engineering*, vol. 4, no. 3, pp. 277–301, Jul. 2000, doi: 10.1080/13632460009350372.
- [12] M. E. Aydemir, "Soil structure interaction effects on structural parameters for stiffness degrading systems built on soft soil sites," *Structural Engineering and Mechanics*, vol. 45, no. 5, pp. 655–676, Mar. 2013, doi: 10.12989/sem.2013.45.5.655.
- [13] M. Ciampoli and P. E. Pinto, "Effects of Soil-Structure Interaction on Inelastic Seismic Response of Bridge Piers," *Journal of Structural Engineering*, vol. 121, no. 5, pp. 806–814, May 1995, doi: 10.1061/(ASCE)0733-9445(1995)121:5(806).

- [14] V. Anand and S. R. Satish Kumar, "Seismic Soil-structure Interaction: A State-of-the-Art Review," *Structures*, vol. 16, pp. 317–326, Nov. 2018, doi: 10.1016/j.istruc.2018.10.009.
- [15] K. Pitilakis and G. Tsinidis, "Performance and Seismic Design of Underground Structures," 2014, pp. 279–340. doi: 10.1007/978-3-319-03182-8 11.
- [16] G. Tsinidis *et al.*, "Seismic behaviour of tunnels: From experiments to analysis," *Tunnelling and Underground Space Technology*, vol. 99, May 2020, doi: 10.1016/j.tust.2020.103334.
- [17] Y. M. A. Hashash, J. J. Hook, B. Schmidt, and J. I-Chiang Yao, "Seismic design and analysis of underground structures," *Tunnelling and Underground Space Technology*, vol. 16, no. 4, pp. 247–293, Oct. 2001, doi: 10.1016/S0886-7798(01)00051-7.
- [18] K. Kawashima, "Seismic Analysis of Underground Structures," *Journal of Disaster Research*, vol. 1, no. 3, pp. 378–389, Dec. 2006, doi: 10.20965/jdr.2006.p0378.
- [19] G. Norman, "EARTHQUAKE ENGINEERING OF LARGE UNDERGROUND STRUCTURES," 1981.
- [20] J.-N. Wang' and G. A. Munfakhz, "Seismic design of tunnels," 2001. [Online]. Available: www.witpress.com,
- [21] J. Penzien, "Seismically induced racking of tunnel linings," *Earthq Eng Struct Dyn*, vol. 29, no. 5, pp. 683–691, May 2000, doi: 10.1002/(SICI)1096-9845(200005)29:5<683::AID-EQE932>3.0.CO;2-1.
- [22] C. M. St John and T. F. Zahrah, "Aseismic design of underground structures," *Tunnelling and Underground Space Technology*, vol. 2, no. 2, pp. 165–197, Jan. 1987, doi: 10.1016/0886-7798(87)90011-3.

- [23] A. Bobet, G. Fernandez, H. Huo, and J. Ramirez, "A practical iterative procedure to estimate seismic-induced deformations of shallow rectangular structures," *Canadian Geotechnical Journal*, vol. 45, no. 7, pp. 923–938, Jul. 2008, doi: 10.1139/T08-026.
- [24] C. Jeremy Hung, J. Monsees, N. Munfah, and J. Wisniewski, "TECHNICAL MANUAL FOR DESIGN AND CONSTRUCTION OF ROAD TUNNELS – CIVIL ELEMENTS," Washington D.C., U.S., 2009.
- [25] "ISO 23469: Bases for design of structures Seismic actions for designing geotechnical works, International Standard ISO TC98/SC3/WG10," Geneva, Switzerland, 2005.
- [26] G. Lanzano, E. Bilotta, G. Russo, and F. Silvestri, "Experimental and numerical study on circular tunnels under seismic loading," *European Journal of Environmental and Civil Engineering*, vol. 19, no. 5, pp. 539–563, May 2015, doi: 10.1080/19648189.2014.893211.
- [27] E. Bilotta, G. Lanzano, S. P. G. Madabhushi, and F. Silvestri, "A numerical Round Robin on tunnels under seismic actions," *Acta Geotech*, vol. 9, no. 4, pp. 563–579, Aug. 2014, doi: 10.1007/s11440-014-0330-3.
- [28] C. Di Prisco *et al.*, "Assessment of excavation related hazards and design of mitigation measures," in *Handbook on Tunnels and Underground Works.*, CRC Press., vol. 1, E. Bilotta, R. Casale, C. G. Di Prisco, S. Miliziano, S. Peila, A. Pigorini, and E. M. Pizzarotti, Eds., 2022, ch. 10.
- [29] "Eurocode 8: Design of structures for earthquake resistance," 2004.
- [30] J. Peiró and S. Sherwin, "Finite Difference, Finite Element and Finite Volume Methods for Partial Differential Equations," in *Handbook of Materials Modeling*, Dordrecht: Springer Netherlands, 2005, pp. 2415–2446. doi: 10.1007/978-1-4020-3286-8_127.

- [31] T. Vyzikas and D. Greaves, "Numerical modelling," in *Wave and Tidal Energy*, wiley, 2017, pp. 289–363. doi: 10.1002/9781119014492.ch8.
- [32] V. G. Terzi and G. D. Manolis, "Basic numerical modelling issues in dynamic soil-tunnel interaction," Sep. 01, 2023, *Elsevier Ltd.* doi: 10.1016/j.soildyn.2023.108060.
- [33] R. B. J. Brinkgreve, "PLAXIS 2D Manuals. General Information, Tutorial Manual, Reference Manual, Material Models Manual, Scientific Manual," 2018.
- [34] "Plaxis. Material Models Manual and Reference Manual," 2021, *Bentley*.
- [35] B. O. Hardin and V. P. Drnevich, "Shear Modulus and Damping in Soils: Design Equations and Curves," *Journal of the Soil Mechanics and Foundations Division*, vol. 98, no. 7, pp. 667–692, Jul. 1972, doi: 10.1061/JSFEAQ.0001760.
- [36] A. Gomes Correia *et al.*, "Scholars' Mine Scholars' Mine to 10-2-2 Strain Levels Strain Levels Recommended Citation Recommended Citation AN APPROACH TO PREDICT SHEAR MODULUS OF SOILS IN THE RANGE OF 10" TO lo-* STRAIN LEVELS," 2001. [Online]. Available: https://scholarsmine.mst.edu/icrageesd/04icrageesd/session01/18
- [37] R. B. J. Brinkgreve, M. H. Kappert, and P. G. Bonnier, "Hysteretic damping in a small-strain stiffness model," in *Proceedings of the 10th International Symposium on Numerical Models in Geomechanics NUMOG 10 Numerical Models in Geomechanics NUMOG 10*, 2007, pp. 737–742. doi: 10.1201/noe0415440271.ch106.
- [38] J. H. Atkinson and G. Sallfors, "Experimental determination of soil properties. General Report to Session 1," in *10th ECSMFE*, J. H. Atkinson and G. Sallfors, Eds., Florence, 1991.

- [39] S. Suwal, A. Pagliaroli, and G. Lanzo, "Comparative study of 1D codes for Site Response Analyses," *INTERNATIONAL JOURNAL OF LANDSLIDE AND ENVIRONMENT*, vol. 2, Nov. 2014, [Online]. Available: https://www.researchgate.net/publication/299559701
- [40] U. Carmando et al., "PRELIMINARY STUDY FOR SEISMIC ASSESSMENT OF THE UN-DERGROUND FACILITIES AT POINT 5 OF THE LARGE HADRON COLLIDER (LHC) AT CERN.," in 9th ECCOMAS Thematic Conference on Computational Methods in Structural Dynamics and Earthquake Engineering, COMPDYN 2023, Athens, Greece.: ECCOMAS Proceedia, 2023, pp. 4197–4205.
- [41] B. Jeremić et al., Nonlinear finite elements: Modeling and simulation of earthquakes, soils, structures and their interaction. Davis, CA: Univ. of California, and Lawrence Berkeley National Laboratory., 2025.
- [42] J. Abell, Y. Feng, H. Yang, H. Wang, and B. Jeremic, *Real-ESSI Simulator Domain Specific Language*. CA, Davis: University of California, Davis, 2025.
- [43] K. S. Sinha, Y. Feng, H. Yang, H. Wang, and B. Jeremic, *Real-ESSI Simulator Model Development and Mesh Generation Manual.* Davis, CA: University of California, Davis., 2025.
- [44] J. Abell, K. S. Sinha, Y. Feng, H. Yang, H. Wang, and B. Jeremic, Real-ESSI Simulator Results Postprocessing and Visualization Manual. Davis, CA: University of California, Davis., 2025.
- [45] J. Bielak, K. Loukakis, Y. Hisada, and C. Yoshimura, "Domain Reduction Method for Three-Dimensional Earthquake Modeling in Localized Regions, Part I: Theory," 2003. [Online]. Available: http://pubs.geoscienceworld.org/ssa/bssa/article-pdf/93/2/817/2715684/817.pdf
- [46] C. Yoshimura, J. Bielak, Y. Hisada, and A. Fernández, "Domain Reduction Method for Three-Dimensional Earthquake Modeling in

- Localized Regions, Part II: Verification and Applications," 2003. [Online]. Available: http://pubs.geoscienceworld.org/ssa/bssa/article-pdf/93/2/825/2715764/825.pdf
- [47] C. Bolisetti and A. S. Whittaker, *Site Response, Soil-Structure Interaction and Structure-Soil-Structure Interaction for Performance Assessment of Buildings and Nuclear Structures.* State University of New York at Buffalo, 2015. [Online]. Available: http://mceer.buffalo.edu
- [48] C. Kanellopoulos, B. Jeremic, I. Anastasopoulos, and B. Stojadinovic, "Use of the Domain Reduction Method to simulate the seismic response of an existing structure protected by resonating unit cell metamaterials.," in *EURODYN 2020 23-26 November 2020, XI International Conference on Structural Dynamics. Proceedings*, Athens, Greece: European Association for Structural Dynamics (EASD), 2020. doi: 10.3929/ethz-b-000462587.
- [49] N. M. Newmark, "A Method of Computation for Structural Dynamics," *Journal of the Engineering Mechanics Division*, vol. 85, no. 3, pp. 67–94, Jul. 1959, doi: 10.1061/JMCEA3.0000098.
- [50] M. Vořechovský and D. Novák, "Correlation control in small-sample Monte Carlo type simulations I: A simulated annealing approach," *Probabilistic Engineering Mechanics*, vol. 24, no. 3, pp. 452–462, Jul. 2009, doi: 10.1016/j.probengmech.2009.01.004.
- [51] M. D. Mckay, F. J. Beckman, and W. J. Conover, "A Comparison of Three Methods for Selecting Values of Input Variables in the Analysis of Output From a Computer Code."
- [52] A. Olsson, G. Sandberg, and O. Dahlblom, "On Latin hypercube sampling for structural reliability analysis," *Structural Safety*, vol. 25, no. 1, pp. 47–68, Jan. 2003, doi: 10.1016/S0167-4730(02)00039-5.
- [53] U. Carmando *et al.*, "Evaluation of the seismic behaviour of the underground facilities hosting CMS experiment at the Large Hadron

- Collider at CERN using Real ESSI Simulator," in 2024 International Workshop Computational Dynamic Soil-Structure Interaction CompDSSI, Assisi, 2024.
- [54] E. J. Fern, V. Di Murro, K. Soga, Z. Li, L. Scibile, and J. A. Osborne, "Geotechnical characterisation of a weak sedimentary rock mass at CERN, Geneva," *Tunnelling and Underground Space Technology*, vol. 77, pp. 249–260, Jul. 2018, doi: 10.1016/j.tust.2018.04.003.
- [55] A. Mubarak, "A. Numerical simulation of large tunnel systems under seismic loading conditions: CERN infrastructure as a case study," University of Dundee (UoD), United Kingdom, 2022.
- [56] "https://home.cern/science/accelerators."
- [57] J. C. Gaborit, M. Silari, and L. Ulrici, "Radiation levels in the CERN Large Electron Positron collider during the LEP 2 phase (68–105GeV)," *Nucl Instrum Methods Phys Res A*, vol. 565, no. 2, pp. 333–350, Sep. 2006, doi: 10.1016/j.nima.2006.05.049.
- [58] Z. Xiao, V. Di Murro, J. A. Osborne, H. Zhu, and Z. Li, "Distributed fibre optic sensing and novel data processing method for tunnel circumferential deformation A case study of an ageing tunnel at CERN," *Tunnelling and Underground Space Technology*, vol. 153, p. 106014, Nov. 2024, doi: 10.1016/j.tust.2024.106014.
- [59] A. Abada *et al.*, "FCC-hh: The Hadron Collider," *Eur Phys J Spec Top*, vol. 228, no. 4, pp. 755–1107, Jul. 2019, doi: 10.1140/epjst/e2019-900087-0.
- [60] A. Moscariello, "Exploring for geo-energy resources in the Geneva Basin (Western Switzerland): opportunities and challenges.," *Swiss Bulletin für angewandte Geologie*, vol. 24, no. 2, pp. 105–124, 2019.
- [61] N. Clerc, E. Rusillon, A. Moscariello, P. Renard, S. Paolacci, and M. Meyer, "Detailed structural and reservoir rock typing characterisation of the Greater Geneva Basin, Switzerland, for geothermal resource

- assessment.," in *Proceedings World Geothermal Congress 2015*, Melbourne, Australia, Apr. 2015.
- [62] V. Antunes *et al.*, "Seismotectonics and 1-D velocity model of the Greater Geneva Basin, France-Switzerland," *Geophys J Int*, vol. 221, no. 3, pp. 2026–2047, 2020, doi: 10.1093/GJI/GGAA129.
- [63] S. S. Service and E. Zürich, "ECOS-09 Earthquake Catalogue of Switzerland Release 2011," 2011.
- [64] F. Thouvenot *et al.*, "The ML 5.3 Épagny (French Alps) earthquake of 1996 July 15: a long-awaited event on the Vuache Fault," *Geophys J Int*, vol. 135, no. 3, pp. 876–892, Dec. 1998, doi: 10.1046/j.1365-246X.1998.00662.x.
- [65] "Décret n°2000-892 du 13 septembre 2000 relatif à la prévention du risque sismique," 2010, *France*.
- [66] "Décret no 2010-1254 du 22 octobre 2010 relatif à la prévention du risque sismique," 2010, *France*.
- [67] Appendix L., Geotechnical Information and Geotechnical Baseline Report. Civil Civil Engineering Works for the High Luminosity LHC project at Point 5. France: European Organization for Nuclear Research (CERN), 2017.
- [68] "Arrêté du 22 octobre 2010 relatif à la classification et aux règles de construction parasismique applicable aux bâtiments de la classe dite 'à risque normal," 2010, *France*.
- [69] H.-C. Kurzweil, "The LHC-Project of CERN-Large Caverns in Soft Rock a Challenge for Scientists and Engineers," 2004.
- [70] A. G. Mubarak, J. A. Knappett, and M. J. Brown, "Influence of modelling approach for reinforced concrete underground structures, with application to the CMS cavern at CERN," *Soil Dynamics and*

- *Earthquake Engineering*, vol. 182, Jul. 2024, doi: 10.1016/j.soildyn.2024.108725.
- [71] M. Dysli, "Use of ADINA in soil mechanics with case studies for excavations," *Comput Struct*, vol. 17(5–6), pp. 635–642, 1983.
- [72] J. Osborne, "CMS Worksite. Civil Engineering and Fitting Out of Experimental Areas," 2006.
- [73] S. Wallis, "Construction of great excavations," *Civil Engineering*, no. 71(8), 34, 2001, [Online]. Available: https://www.tunneltalk.com/CERN-Aug01-Construction-of-great-excavations.php
- [74] "LHC Civil Engineering Works Package 02. Monthly Monitoring Report nr. 06. January to February 2002.," 2002.
- [75] "LHC Civil Engineering Works Package 02 (2002). Monthly Monitoring Report nr. 07. March to June 2002," 2002.
- [76] "LHC Civil Engineering Works Package 02 (2002). Monthly Monitoring Report nr. 08. July to October 2002," 2002.
- [77] "LHC Civil Engineering Works Package 02 (2002). Monthly Monitoring Final Summary Report nr. 09. December 2004," 2004.
- [78] J. R. Thieman, *Top Quark Spin Correlations with the CMS Detector*. Cham: Springer Nature Switzerland, 2024. doi: 10.1007/978-3-031-76117-1.
- [79] C. Visone, E. Bilotta, and F. Santucci de Magistris, "One-Dimensional Ground Response as a Preliminary Tool For Dynamic Analyses in Geotechnical Earthquake Engineering," *Journal of Earthquake Engineering*, vol. 14, no. 1, pp. 131–162, Dec. 2009, doi: 10.1080/13632460902988950.
- [80] R. L. Kuhlemeyer and J. Lysmer, "Finite Element Method Accuracy for Wave Propagation Problems," *Journal of the Soil Mechanics and*

- Foundations Division, vol. 99, no. 5, pp. 421–427, May 1973, doi: 10.1061/JSFEAQ.0001885.
- [81] T. Benz, P. A. Vermeer, and R. Schwab, "A small-strain overlay model," *Int J Numer Anal Methods Geomech*, vol. 33, no. 1, pp. 25–44, Jan. 2009, doi: 10.1002/nag.701.
- [82] L. Luzi et al., "Engineering Strong Motion Database (ESM)," 2020, Istituto Nazionale di Geofisica e Vulcanologia (INGV): 2.0.
- [83] G. Benincasa and R. Schmidt, "Seismic design spectra for ATLAS and CMS," 2000.
- [84] A. R. Kottke, X. Wang, and E. M. Rathje, *Technical Manual for Strata*. Department of Civil, Architectural, and Environmental Engineering, University of Texas, 2013.
- [85] D. E. Huntington and C. S. Lyrintzis, "Improvements to and limitations of Latin hypercube sampling," *Probabilistic Engineering Mechanics*, vol. 13, no. 4, pp. 245–253, Oct. 1998, doi: 10.1016/S0266-8920(97)00013-1.
- [86] M. Cabon, C. Charrondire, K. Develle, P. Fessia, M. Guinchard, and J. Wenninger, "LHC seismic network design, installation and operation. Rep. EDMS, 1549343.," Geneva, Switzerland, 2017.
- [87] "Swiss Seismological Service ETH Zurich, accessed March 10, 2025 http://seismo.ethz.ch/."
- [88] E. Alakbarli *et al.*, "Seismic Hazard Analysis for the TDC2/TCC2 Facility at CERN: A Multivariate Geostatistical Approach," 2024. [Online]. Available: https://www.researchgate.net/publication/382343234
- [89] B. Miladinović, "Domain reduction method: Formulation, possibilities, and examples for analyzing seismic soil-structure interaction,"

- *Gradjevinski materijali i konstrukcije*, vol. 66, no. 3, pp. 177–191, 2023, doi: 10.5937/grmk2300009m.
- [90] B. Jeremic, "Seismic Response of an NPP on Linear and Nonlinear Soil and Contact."
- [91] C. Kanellopoulos, N. Psycharis, H. Yang, B. Jeremi, and I. Anastasopoulos, "Seismic Resonant Metamaterials for the protection of an elastic-plastic SDOF system against vertically propagating seismic shear waves (SH) in nonlinear soil by." [Online]. Available: http://real-essi.info
- [92] GADZ, "Reconnaissances géologiques et géotechniques rapport d'interprétation No 3545/91," Geneva, 1996.
- [93] GADZ, "Reconnaissances de la Molasse Rapport de Synthèse No 3545.97," Geneva, 1997.
- [94] GADZ, "Reconnaissances géotechnique Point 1 No 7222/2," 2016.
- [95] GADZ, "Reconnaissances géotechniques No 7223/2," 2016.
- [96] T. Kokusho and T. Ishizawa, "Site amplification during strong earthquakes investigated by vertical array records," *Geosciences (Switzerland)*, vol. 11, no. 12, Dec. 2021, doi: 10.3390/geosciences11120510.
- [97] J. Boaga, S. Renzi, R. Deiana, and G. Cassiani, "Soil damping influence on seismic ground response: A parametric analysis for weak to moderate ground motion," *Soil Dynamics and Earthquake Engineering*, vol. 79, pp. 71–79, Dec. 2015, doi: 10.1016/j.soildyn.2015.09.002.

8 Author's publications

- U. Carmando et al., "PRELIMINARY STUDY FOR SEISMIC ASSESSMENT OF THE UN-DERGROUND FACILITIES AT POINT 5 OF THE LARGE HADRON COLLIDER (LHC) AT CERN.," in 9th ECCOMAS Thematic Conference on Computational Methods in Structural Dynamics and Earthquake Engineering, COMPDYN 2023, Athens, Greece.: ECCOMAS Proceedia, 2023, pp. 4197–4205.
- U. Carmando *et al.*, "VALUTAZIONE PRELIMINARE DELLA RISPOSTA SISMICA DELLE OPERE SOTTERRANEE PRESSO IL PUNTO 5 DEL CERN," in *XII Incontro Annuale dei Giovani Ingegneri Geotecnici. IAGIG 2023*, Padova, 2023.
- U. Carmando *et al.*, "Evaluation of the seismic behaviour of the underground facilities hosting CMS experiment at the Large Hadron Collider at CERN using Real ESSI Simulator," in 2024 International Workshop Computational Dynamic Soil-Structure Interaction CompDSSI, Assisi, 2024.